To the Graduate Council:

I am submitting herewith a dissertation written by James Edgar Parks II entitled "Photon Scanning Tunneling Microscopy in the Ultraviolet and Soft X-Ray Regions." I have examined the final copy of this dissertation for form and content and recommend that it be accepted in partial fulfillment of the requirements for the degree of Doctor of Philosophy, with a major in Physics.

Dr. Tom Callcott, Major Professor

We have read this dissertation and recommend its acceptance:

Accepted for the Council:

Associate Vice Chancellor
and Dean of The Graduate School

Photon Scanning Tunneling Microscopy in the Ultraviolet and Soft X-Ray Regions

A Dissertation

Presented for the

Doctor of Philosophy

Degree

The University of Tennessee, Knoxville

James Edgar Parks II

August 1995

Copyright © James Edgar Parks II, 1995
All rights reserved

Acknowledgments

I would like to thank Dr. Ed Arakawa, Dr. Tom Callcott, Dr. Tom Ferrell, and Dr. Bruce Warmack for their advice and support. I would also like to thank the staff, students, and PostDocs with whom I've had the pleasure of working with at Oak Ridge National Laboratory and the National Synchrotron Light Source. In particular, I would like to thank Page Tuminello, Dr. Sherrie Sharp, and Dr. Ken Miyano. A special thanks goes to my wife, Cheryl, and my dog, Mollie, who many times waited past midnight for their nightly kiss and walk.

Abstract

Photon scanning tunneling microscopy in the ultraviolet and soft x-ray regions is investigated. In the ultraviolet region a photon scanning tunneling microscope (PSTM) has been created by slightly modifying the visible PSTM. Improvements in resolution with decreasing wavelength are shown in images obtained with constant probe size. Comparisons between signals in the visible and ultraviolet region are discussed, and probe geometries beneficial to increasing signal-to-background and signal-to-noise ratios are introduced. The ultraviolet PSTM expands the capability of the PSTM by improving resolution and making a larger photon spectrum available for spectroscopic and experimental applications.

In the soft x-ray region a PSTM has been constructed, and experiments have been performed to investigate the feasibility of creating a soft x-ray PSTM capable of imaging with subwavelength resolution. Special PSTM components were developed for the soft x-ray region. A freestanding thin-film grating provides a method of creating total internal reflection at the L_{23}-shell absorption edge of aluminum, and phosphor-coated fiber optic probes permit submicron area detection of soft x rays. With synchrotron radiation a periodic soft x-ray evanescent field was created on the surface of the thin-film grating and mapped with the soft x-ray probe. The demonstration of total internal reflection in the thin-film grating and frustrated total internal reflection to the soft x-ray probe provides a basis for further research in the soft x-ray region.

The spectroscopic potential of the PSTM increases as the PSTM operates over a wider photon range. Elemental spectroscopy with the scanning electron microscope (SEM) has been investigated for comparison with and consideration of spectroscopy with the PSTM. The elemental spectroscopic range of the SEM has been extended by observing soft x-ray emission from light elements. During normal SEM operation the concentration of light elements is spatially mapped by monitoring the emission of characteristic soft x rays with a grazing-incidence spectrometer. Experimental soft x-ray yields for the light elements are given and compared with theoretical calculations.

Table of Contents

I. Introduction 1

II. Ultraviolet Photon Scanning Tunneling Microscopy 7
A. Introduction 7
B. Visible Photon Scanning Tunneling Microscopy Review 7
1. Frustrated Total Internal Reflection 8
2. Frustrated Total Internal Reflection Induced by a Fiber Optic Probe 13
3. Imaging with Frustrated Total Internal Reflection 15
C. UVPSTM Components and Resulting Spectra 20
1. Mercury Arc Lamp Light Source 20
2. Fiber Optic Probe 24
3. Light Spectra of the UVPSTM 34
D. Evanescent Field Detection 37
1. Wavelength and Incident Angle Effects on Tunneling Signals 39
2. Probe and Sample Effects on Tunneling Signals 46
E. Imaging 55
F. Discussion 68
G. Conclusion 84

III. Progress Toward a Soft X-Ray Scanning Tunneling Microscope 87
A. Introduction 87
B. SXPSTM Concept 88
C. SXPSTM Apparatus 96
1. Vibration Isolation System 96
2. Aluminum Thin-Film Grating 99
3. Soft X-Ray Probe Detector 100
D. Total Internal Reflection in the Thin-Film Grating 111
1. Theoretical Transmission through the Thin-Film Grating 113
2. Experimental Transmission through the Thin-Film Grating 120
E. Probing the Evanescent Field 126
1. Theoretical Generation of Signals from Probe Scans 128
2. Experimental Data from Probe Scans 137
F. Conclusion 148

List of References 151

Appendix A. Scanning Electron Microscope Soft X-Ray Spectrometry 154
A. Introduction 154
B. Soft X-Ray Spectrometer for the Scanning Electron Microscope 158
C. Soft X-Ray Yield from Electron Bombardment 160
1. Element Spectra and Yield Measurements 162
2. Theoretical Calculation of Yield 170
3. Discussion of Soft X-Ray Emission Mechanism 174
D. Microanalysis Images 179
E. Conclusion 186

Appendix B. Optical Theory of Layered Thin Films 187

Appendix C. Transmission through a Wedge-Shaped Gap 198

Vita 206

List of Figures

II.1. Frustrated Total Internal Reflection....9
II.2. Evanescent Field Intensity vs. Transmission by FTIR....12
II.3. Fiber Optic Probe....14
II.4. Fiber Optic Probe Induced FTIR....16
II.5. Scan Modes....18
II.6. UVPSTM Apparatus....21
II.7. Aluminum Coating....26
II.8. Long- and Short-Taper Probes....28
II.9. Extreme-Taper Probe....29
II.10. Short-Taper Probe Finish Etch....32
II.11. Extreme-Taper Probe Finish Etch....33
II.12. Tip Regions of Long-Taper Probes....35
II.13. Tip Regions of Short- and Extreme-Taper Probes....36
II.14. UVPSTM Light Spectra....38
II.15. Evanescent Field Decay Length Variation....40
II.16. Tunneling Signals for Varying Wavelength Spectra....41
II.17. UVA Tunneling Signals for Varying Angle of Incidence....42
II.18. UVB Tunneling Signals for Varying Angle of Incidence....43
II.19. UVA Tunneling Magnitude for Varying Angle of Incidence....44
II.20. UVB Tunneling Magnitude for Varying Angle of Incidence....45
II.21. Evanescent Field Decay Length Variation Over Incident Angle Distribution....47
II.22. Data from Long-Taper Probe with Aluminum Shielding....49
II.23. Data from Long-Taper Probe without Aluminum Shielding....51
II.24. Data from Extreme-Taper Probe with Aluminum Shielding....52
II.25. Probe-Sample Contact in Tunneling Signals....54
II.26. SEM Image of Silver-Coated Quartz Cross Grating....56
II.27. AFM Image of Quartz Cross Grating....57

II.28. Variation of Wavelength I....58
II.29. Variation of Wavelength II....59
II.30. Variation of Wavelength III....60
II.31. Variation of Wavelength IV....61
II.32. Red and Blue Image Cross Sections....63
II.33. UVA and UVB Image Cross Sections....64
II.34. Red and Blue Slope Measurements....65
II.35. UVA and UVB Slope Measurements....66
II.36. Variation of Incident Angle....67
II.37. Variation of Probe-Sample Separation Distance I....69
II.38. Variation of Probe-Sample Separation Distance II....70
II.39. λ_e Evanescent Wave on Step Surface....72
II.40. $\lambda_e/2$ Evanescent Wave on Step Surface....73
II.41. Model Surface....74
II.42. λ_e Evanescent Wave on Model Surface....75
II.43. $\lambda_e/2$ Evanescent Wave on Model Surface....76
II.44. Wavefronts of Incident and Evanescent Waves....80
II.45. Evanescent Wave Action at Discontinuities in the Interface....81
II.46. Evanescent Wave Diagram for Experimental Conditions....83
II.47. Probe Map of Evanescent Wave for Different Wavelengths....85

III.1. Total Internal Reflection in the Visible Spectrum....89
III.2. Index of Refraction of Aluminum....90
III.3. Soft X-Ray Interactions with Thin Films....92
III.4. SXPSTM Overview....95
III.5. Evanescent Field Intensity....97
III.6. Thin-Film Grating Photograph....101
III.7. Thin-Film Grating Production....102
III.8. Optical Fiber Etching Techniques....105
III.9. Soft X-ray Microprobe Photograph....108
III.10. Probe Material Comparison....110
III.11. Probe Size Calculation....112
III.12. Thin-Film Grating Regions....115
III.13. Theoretical Thin-Film Grating Transmission....118
III.14. Aluminum Oxide Suppression....119

III.15. Experimental Thin-Film Grating Transmission....122
III.16. Bruggeman Approximation....125
III.17. Typical Transmission Data....127
III.18. Evanescent Field Decay Length....129
III.19. Theoretical Tunneling Signal for Z Scans....131
III.20. Theoretical Periodic Signal of X Scans....134
III.21. Spreading of Evanescent Field Region....135
III.22. Theoretical Signals for Experimental Conditions....136
III.23. X Scan Data I....139
III.24. X Scan Data II....140
III.25. X Scan Data III....141
III.26. X Scan Data IV....142
III.27. X Scan Data V....143
III.28. Z Scan Data I....146
III.29. Z Scan Data II....147

A.1. Soft X-Ray Spectrometer....159
A.2. Channeltron Electron Multiplier Efficiency....161
A.3. Si Soft X-Ray Emission....163
A.4. Al Soft X-Ray Emission....164
A.5. Mg Soft X-Ray Emission....165
A.6. C Soft X-Ray Emission....166
A.7. B Soft X-Ray Emission....167
A.8. Be Soft X-Ray Emission....168
A.9. Li Soft X-Ray Emission....169
A.10. Gryzinski Cross Section....172
A.11. Yield Theory with Feldman Expression....175
A.12. Yield Theory with Thomas and Pattison Expression....176
A.13. Yield Theory with Fitting Expression....177
A.14. Si Soft X-Ray Signal from Si with C Overlayer....181
A.15. SEM and Li Images....182
A.16. SEM and Mg Images....183
A.17. SEM, Mg, and Al Images....184
A.18. SEM and Al Images....185

B.1. Two-Media System.....189
B.2. Three-Media System.....192
B.3. Four-Media System.....195

C.1. Geometry of the Wedge-Shaped Gap.....199
C.2. Transmission for Varying Wedge Angle.....204

Chapter I

Introduction

Science is an idea of how the world works. The action of forming and constantly reshaping our idea occurs in many ways, but throughout history the most common way of figuring out how the world works has been by taking things apart. Dissection has shown man that the world is composed of a seemingly endless series of smaller pieces that interact and join together to form larger pieces, and with each level of dissection new information is revealed. The process of dissection continues today as man attempts to unravel DNA and search for particles that make up quarks.

The microscope has played a critical role in the dissection process. Dissection allows isolation of the individual pieces so that the pieces can be studied by observation and experiment. The microscope has made observation possible as the size of the dissected particles grows smaller, and the capability to observe particles has made many experiments possible.

Three major revolutions in the field of microscopy have occurred thus far. The first revolution involved the study of optics which led to the traditional optical microscope. The importance of the invention of the optical microscope cannot be overestimated. Scientists were able to see the structure of cells and even see live microorganisms that are invisible with the naked eye. Even today the optical microscope performs many tasks in a wide range of laboratories. The simple operation, low cost, and

minimal components of the optical microscope form a quick and reliable instrument for magnified inspection.

The second revolution was the invention of the scanning electron microscope (SEM). The theory of quantum mechanics, which evolved in the early twentieth century, showed that all particles have wave properties and that the wavelength of a particle is associated with its mass. The wavelength of electrons that have the same energy as visible photons is much smaller than the wavelength of visible light. The SEM operates in essentially the same way as the traditional optical microscope except that electrons are used in place of visible light. In a vacuum a relatively high-energy beam of electrons is focused onto a sample and the scattered electrons are detected. As the electron beam is scanned across the sample the backscattered electron signal shows the structure of the sample. The smaller wavelength of the high-energy electrons($\approx$1-500 keV) results in better resolution for the SEM.

In addition to outstanding resolution the SEM offers the capability of performing many types of spectroscopy. Spatial compositional analysis and electronic characterization can be obtained by monitoring the electronic interactions that occur between the sample and electron beam. The types and limits of spectroscopy that can be done with the SEM are still being pursued today. One pursuit of limits to elemental soft x-ray emission spectroscopy is presented in **Appendix A.** This technique offers much better spectroscopic resolution than electron energy-loss spectroscopy.

Although the resolution of the SEM is superior to the traditional optical microscope, there are some disadvantages to the SEM. Unless it is an electrical conductor, the sample must have a conducting outer layer, and it must be placed under vacuum to be examined with the electron beam. Additionally, the sample may be damaged by the electron bombardment. These factors make the observation of biological samples difficult. The SEM sample preparation may alter the structure of a biological sample, and the SEM is not capable of imaging live biological samples in their native

environment. Furthermore, SEMs are costly instruments, and sample preparation and operation of the SEM takes considerable time and expertise. Thus, the traditional optical microscope is still used a great deal, with SEMs being used when the need for better resolution or certain spectroscopic information outweighs the expense. Today in biology the SEM is used less frequently than the transmission electron microscope(TEM) for highest resolution work. The TEM is similar to the SEM except the electrons scatter through the sample and are detected instead of being backscattered from the sample as in the SEM. The resolution of TEMs is slightly better than the resolution of SEMs; however, TEMs are very expensive and suffer from many of the same difficulties described above.

The most recent revolution in microscopy occurred in 1982 when a microscope called the scanning tunneling microscope (STM) designed by Bennig *et al.* obtained images of individual atoms.[I-1] The STM utilizes the quantum mechanical process of tunneling to image conducting samples. Contrary to the traditional optical microscope and the SEM the STM uses a probe instead of a beam of particles to image a sample.

For the STM the probe is an extremely sharp conducting wire. The probe is positioned in very close proximity ($\leq$1 nm) to the sample surface but not touching the sample. When a bias is applied between the probe and the sample, electrons will tunnel from the sample through the classically forbidden vacuum or air region to the probe (or in reverse order depending on the bias direction). The magnitude of this "tunneling signal" is dependent on the bias potential, the electrical properties of the sample and probe, the size of the extreme tip of the probe, and the separation distance between the probe tip and sample. The dependence of the tunneling signal on the probe-sample separation distance is extremely strong and critical to the operation of the STM. The tunneling signal is an exponential function of the probe-sample separation distance with a decay length of $\approx$1 nm. In the operation of the STM the probe is scanned across the surface of the sample at a probe-sample separation distance that allows tunneling to occur. A three dimensional

image of the sample surface is constructed from the tunneling signal that is recorded during the probe scan.

The introduction of the STM started a new class of microscopes called scanning probe microscopes (SPMs). The main characteristic of SPMs is that an extremely small probe acts as the detector of a signal relating to the structure or other characteristic of the sample. Typically, the signal that the probe detects is generated by a force or field that is confined to an extremely small area originating from the sample surface. The combination of the nanometer size probe and extreme dependence of the detected signal on the probe-sample separation distance results in sensitive microscopes.

In 1989 Reddick, Warmack, and Ferrell introduced a new type of SPM called the photon scanning tunneling microscope (PSTM).[I-2,I-3] The PSTM is essentially an optical version of the STM. However, instead of electrons tunneling from a sample to a metal probe, in the PSTM photons tunnel from a sample to a fiber optic probe. The process of photon tunneling occurs by frustrated total internal reflection (FTIR). A prism is used to create total internal reflection (TIR) at a dielectric-air interface, and the sample is placed on the dielectric-air interface so that TIR occurs inside the sample. When the fiber optic probe is positioned close to the sample, FTIR occurs and photons tunnel from the sample to the fiber optic probe. As in the case of the STM, the signal detected by the probe is strongly dependent on the probe size and probe-sample separation distance. Scanning the probe across the surface of the sample and monitoring the tunneling signal allows a three dimensional image of the surface to be obtained. The resolution of the PSTM breaks the diffraction limit and surpasses the resolution of the traditional optical microscope. PSTM images have been obtained with lateral resolutions of $\lambda/10$, where λ is the wavelength of light.[I-4] However, the lateral resolution is dependent upon the sample. The vertical resolution is typically <1 nm and limited only by noise.

Although the resolution of the STM is superior to the PSTM, the PSTM has several advantages. The PSTM requires no sample preparation or alteration, and any

material can be imaged with no vacuum required. In addition, biological samples can be imaged in their natural liquid environment. Since the probe is not in direct contact with the sample, soft and fragile samples can be imaged, and no damage occurs to the sample since a small number of photons are the only penetrating particles. The only sample requirement is that the sample must be transparent at the wavelength used or must be thinner than the wavelength of light. The "sample friendly" aspect of the PSTM makes it ideal for microscopy of biological samples.

The greatest potential capability of the PSTM may be in performing spectroscopy on samples with the same resolution. The same fiber optic probe that detects the tunneling signal can send and receive light to and from locations on the sample for spectroscopic investigation. In theory any spectroscopy done on the macroscopic level can be done on a submicron level with the PSTM; however, practical limitations exist that preclude some types of spectroscopy from being done with the PSTM. The main spectroscopic limitation of the PSTM is signal strength. Since the PSTM probe collects an extremely small area of light, certain types of spectroscopy that detect inefficient processes may not be possible. However, even the relatively weak Raman spectroscopic signal has been acquired by the PSTM probe.[I-5,I-6]

The PSTM is still being developed, and as the understanding of the PSTM increases the capabilities of the PSTM will expand. The future offers better spatial resolution, more spectroscopic analysis techniques, and new experimental applications of the PSTM. The dissertation presented here is a study of the performance of the PSTM at different photon energies. In particular, photon scanning tunneling microscopy in the ultraviolet and soft x-ray regions is investigated. Since the resolution of the PSTM appears to be related to the wavelength of light, photon scanning tunneling microscopy in the ultraviolet and soft x-ray regions should improve the resolution of the PSTM. An additional benefit to photon scanning tunneling microscopy in the ultraviolet and soft x-

ray regions is that a larger photon spectrum is available for spectroscopy, microanalysis, and other experimentation.

Since optics in the soft x-ray region differ greatly from optics in the ultraviolet and visible regions of light, the studies of the PSTM in the ultraviolet and soft x-ray regions are presented separately. First, studies related to photon scanning tunneling microscopy in the ultraviolet region are presented. A review of photon scanning tunneling microscopy in the visible region is included for comparison purposes. Then, studies related to photon scanning tunneling microscopy in the soft x-ray region are presented. One possible spectroscopic analysis capability of the soft x-ray version of the PSTM is soft x-ray emission spectroscopy. A study of the efficiency of soft x-ray emission spectroscopy performed with the SEM is presented in **Appendix A.** for future reference.

Just as science has discovered that the world is made up of smaller pieces, science is made up of smaller pieces of science that ultimately bind the complete picture of the world together. Photon scanning tunneling microscopy has added and will continue to add to the understanding of the submicron part of this world. This study adds to the understanding of photon scanning tunneling microscopy by investigating the performance of the PSTM in two additional photon regions where photon scanning tunneling microscopy has not previously been explored. The resulting information expands the understanding of photon scanning tunneling microscopy and creates new opportunities for the PSTM to contribute to the never-ending endeavor of science.

Chapter II

Ultraviolet Photon Scanning Tunneling Microscopy

A. Introduction

The visible Photon Scanning Tunneling Microscope (PSTM) has been improved by creating an Ultraviolet Photon Scanning Tunneling Microscope (UVPSTM). The improvements are twofold. The smaller wavelength of ultraviolet light allows the UVPSTM to image samples with better lateral and vertical resolution, and the ultraviolet spectrum expands the versatility of the PSTM by permitting imaging and spectroscopy over a larger light spectrum. The modifications needed to form an UVPSTM from a PSTM are simple and relatively inexpensive, and like the PSTM, the UVPSTM operates in a simple manner with no vacuum or sample alteration required. The visible PSTM is reviewed below, and the ultraviolet components of the UVPSTM is presented. Subsequently, data obtained with the UVPSTM and PSTM is presented.

B. Visible Photon Scanning Tunneling Microscopy Review

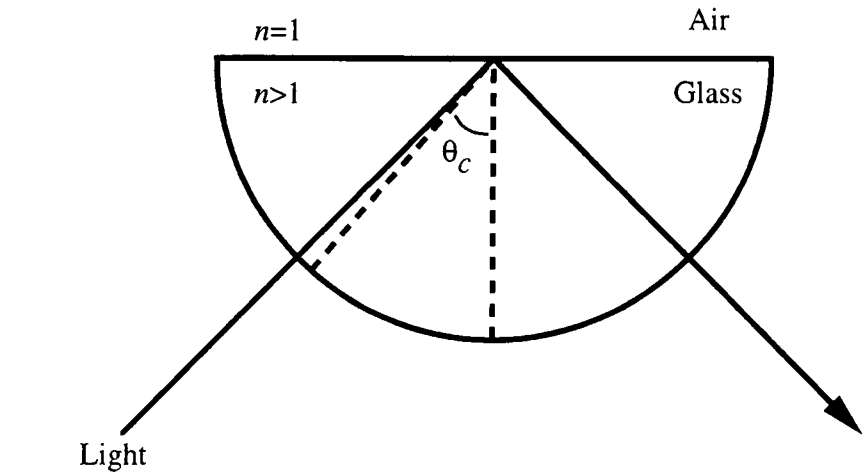
The main components of the visible PSTM are the light source, prism, and fiber optic probe. A computer interfaced with scanning electronics that drive piezoelectric ceramics provides a means of controlling the fiber optic probe and acquiring data;

however, these components are similar to components in most scanning probe microscopes and will not be reviewed. Instead, the main components of the PSTM are introduced as the theory of operation of the PSTM is discussed.

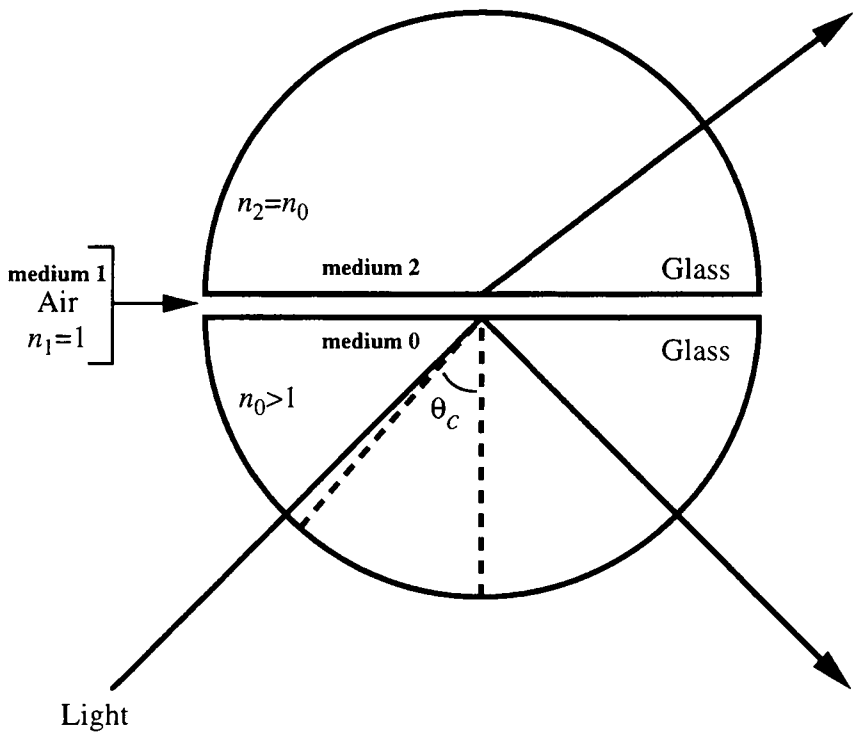
B.1. Frustrated Total Internal Reflection

The PSTM operates on the principle of frustrated total internal reflection (FTIR). Total internal reflection (TIR) occurs when light incident on the interface between two media is reflected back into the medium from which it came with no energy lost. The typical scenario for TIR involves the interface between two insulating dielectrics with different refractive indices with TIR occurring in the medium with the larger real part of the index of refraction (n). The medium with the larger n is referred to as medium 0, and the medium with the smaller n is referred to as medium 1. For example TIR can occur at the interface between glass (n_{glass}=1.46 at λ=546 nm) and air ($n_{air}\approx$1 at λ=546 nm).[II-1] When light traveling through the glass (medium 0) is incident on the glass-air interface at an angle, θ_i, greater than the critical angle, θ_c, all of the light is reflected back into the glass medium and no light is transmitted into the air (medium 1). A prism provides a convenient method of inserting the light into the glass medium such that any θ_i can be obtained (**Figure II.1.a.**). The critical angle, θ_c, is obtained using Snell's law and is dependent on the indices of refraction of the two media at the wavelength of interest.

Two processes hinder TIR at an interface to create FTIR. One process that leads to FTIR is the scattering of light from the interface. Complete TIR at an interface only occurs for a perfectly smooth interface. If any roughness exists on the interface surface some of the incident light will scatter from the rough surface and not be totally internally reflected. The other process leading to FTIR involves coupling to the evanescent wave created on the surface of the interface. The PSTM operates by frustrating TIR with the



(a)



(b)

Figure II.1. Frustrated Total Internal Reflection. Total internal reflection **(a)** and frustrated total internal reflection **(b)** at a glass-air interface.

process of evanescent wave coupling. FTIR due to light scattering at the interface is a competing process that is important to the PSTM but not distinctive of its operation.

The evanescent wave is a surface wave that travels on the TIR interface with its wavevector in the same plane as that of the incident light. The evanescent wave has the same frequency (ω) of light as the incident light, but the electric field strength of the evanescent wave decays exponentially with increasing distance from the TIR interface. The decay length of the exponential field intensity is on the order of the wavelength (λ) of light. The intensity of the evanescent field (I) as a function of distance from the interface (z) is given as:

$$I(z) \propto e^{-\left(\frac{4\pi}{\lambda}\right)\left[\left(\frac{n_0}{n_1}\right)^2 \sin^2\theta_i - 1\right]^{1/2} z}. \qquad \textbf{(II.1.)}$$

The electric field of the evanescent wave is referred to henceforth as the evanescent field, and the region where the evanescent field has significant strength is referred to as the evanescent field region.

FTIR occurs when another material (medium 2) with n greater than medium 1 is inserted into the evanescent field region. When this occurs, light can be transmitted from medium 0 to medium 2 by the evanescent wave. The same process that causes an evanescent wave to be produced by light incident at $\theta_i > \theta_c$ (on the interface of media 0 and 1) causes light to be produced by the evanescent wave at the interface between media 1 and 2. This process of light traveling through medium 1 into medium 2 when it presumably would be totally reflected back into medium 0 is also known as photon tunneling because of the similarity to the quantum mechanical tunneling of particles such as electrons through seemingly forbidden regions. Indeed, if the term "index of refraction" is defined in terms of the ratio of wavevectors rather than as the ratio of velocities, the DeBroglie relation,

$$\vec{p} = \hbar\vec{k}, \qquad \textbf{(II.2.)}$$

where $\bar{p}$ is the momentum vector, $\hbar$ is Planck's constant, and $\bar{k}$ is the wavevector, leads to precisely the same transmission coefficient for s-polarized photons as electrons in the same geometry.[II-2]

The simplest case showing FTIR from evanescent wave coupling involves two parallel planar interfaces. For example two glass prisms arranged as shown in **Figure II.1.b.** create the possibility for FTIR to occur. One glass prism is medium 0, and the other glass prism is medium 2. The air gap between the two prisms is medium 1. The amount of FTIR occurring will depend on the separation distance between the two prisms, or the width of the air gap (medium 1). The evanescent wave provides the transport mechanism for the photons to tunnel from medium 0 to medium 2. Therefore, FTIR can only measurably occur when medium 2 is close enough to medium 0 to be in the sizeable the evanescent field region. When the separation distance is on the order of the decay length of the evanescent field, FTIR will occur, and some light is transmitted into medium 2 with the rest of the light being totally internally reflected back into medium 0. The transmission of light due to FTIR for the case of two planar interfaces can be calculated using standard electromagnetic plane wave theories **(Appendix B.)**. The transmission of light from medium 0 to medium 2 as a function of separation distance is shown in **Figure II.2.** For comparison the evanescent field strength as a function of distance from the prism-air interface is also shown in **Figure II.2.** Two extreme cases of the separation distance show familiar conditions. When the separation distance is zero, all of the light is transmitted from medium 0 to medium 2. Of course, this is the same scenario as light traveling through solid glass. When the separation distance is much larger than the decay constant of the evanescent field, negligible FTIR will occur, and the familiar case of TIR at a single interface will happen (with no measurable transmitted light into medium 2).

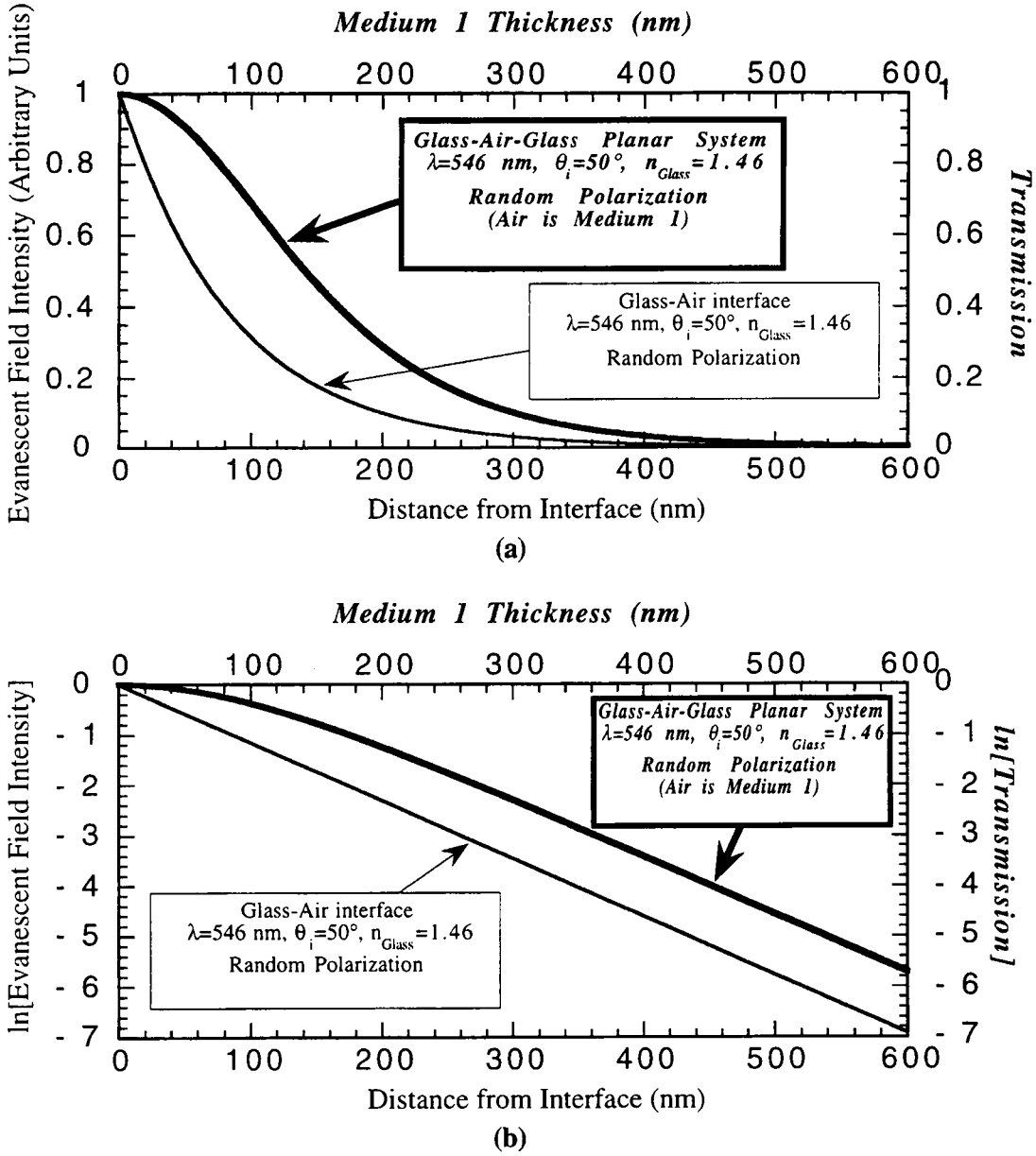


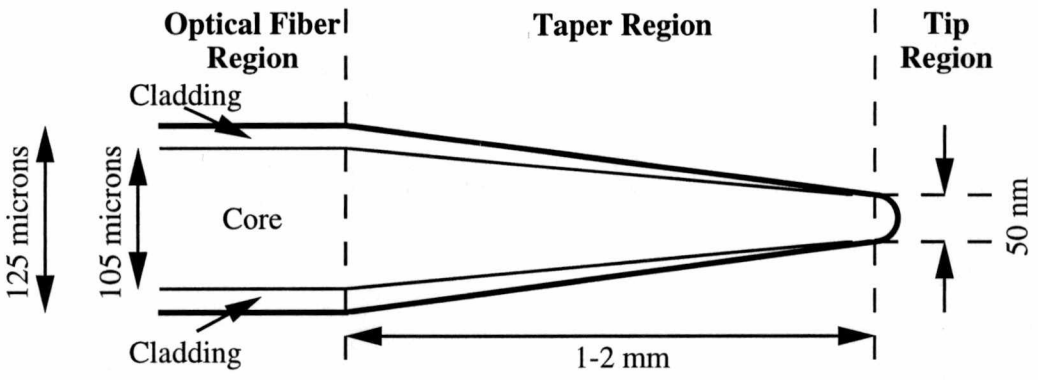
Figure II.2. Evanescent Field Intensity vs. Transmission by FTIR. **(a)** The evanescent field intensity as a function of distance from the prism-air interface shown in **Figure II.1.a**., and the transmission of light from one prism (medium 0) to another (medium 2) as a function of separation distance (thickness of medium 1) for the scenario shown in **Figure II.1.b.** **(b)** A semi-log graph of the same curves in **(a)**. Note that the slope of the log curves are the same except when the separation distance is <150 nm.

B.2. Frustrated Total Internal Reflection Induced by a Fiber Optic Probe

The interface between media 1 and 2 does not have to be a plane for FTIR to occur. The PSTM operates by creating FTIR with a sharpened fiber optic acting as medium 2. The sharpened fiber optic, which is referred to as the fiber optic probe or probe, is an optical fiber that has one end of the optical fiber pulled or etched to a sharp point. Although the actual shape and size of the fiber optic probe will vary according to manufacturing conditions, **Figure II.3.** shows the general size, shape, and symmetry of a fiber optic probe. The probe is symmetric about the central axis of the optical fiber with three distinct regions called the optical fiber or wave guide region, the taper region, and the tip region as demonstrated in **Figure II.3.** The diameter of the tip region ranges from 50 to 100 nm.

As in the previous example, a prism is used as medium 0 in the PSTM. TIR is created at the prism-air interface with a laser typically used as the light source. The fiber optic probe is positioned so that the axis of the probe is normal to the prism-air interface. The normal axis to the prism-air interface is referred to as the z-axis. When the fiber optic probe is moved into the evanescent field region, FTIR will occur. Since the probe is not a perfectly smooth planar surface, FTIR will occur by the evanescent wave scattering from the probe and by the evanescent wave coupling to the probe to create light in the probe. Some of the light escaping the prism by the process of FTIR will travel into the fiber optic where it can be carried by the fiber optic to a photo multiplier tube (PMT) detector. This signal is called the tunneling signal and directly relates to the probe-prism separation distance.

All of the light escaping the prism by FTIR will not be channeled into the fiber optic wave guide. Only light that enters the conducting region of the optical fiber with an angle of incidence less than the acceptance cone angle ($\approx\pm 14°$) of the optical fiber is conducted down the optical fiber. When light enters the optical fiber with this condition, the light is "launched" into the fiber. Light scattering and reflections in the tip and taper



(a)



(b)

Figure II.3. Fiber Optic Probe. **(a)** Diagram of a typical fiber optic probe with the three distinct regions labeled. **(b)** SEM image of a typical fiber optic probe.

regions of the fiber optic probe play a role in determining how much light is launched into the wave guide region of the optical fiber. Light scattered at the tip region of the probe will travel in all directions. Only a portion of the scattered light is transmitted through the taper region to the conducting optical fiber. Additionally, the Huyghen's principle suggests only some of the light created in the tip region of the probe during FTIR is suitably reflected and scattered in the tip and taper regions for launch into the wave guide region.(**Figure II.4.**) However, in regions small compared to the wavelength it is difficult to assess the optical transmission paths.

Although all of the light undergoing FTIR is not carried by the optical fiber to the detector, the tunneling signal is an accurate representation of the amount of light undergoing FTIR. The PSTM uses the tunneling signal to determine the probe position relative to the prism-air interface. The tunneling signal does not relate to the probe-prism separation distance exactly as the transmission between two planar interfaces does, and the tunneling signal is not an exact map of the evanescent field intensity. Instead, the tunneling signal's dependence on the probe-prism separation distance represents a compromise between the planar transmission and the evanescent field intensity. However, the exponential dependence of the tunneling signal on the probe-prism separation distance results in an extremely sensitive method of determining the probe position on the z-axis.

B.3. Imaging with Frustrated Total Internal Reflection

When a sample of interest is placed on the prism, the evanescent wave is modulated according to the shape and optical constants of the sample. By moving the probe close to the sample and inducing FTIR the modulated evanescent wave can be detected. By scanning the probe across the prism, or sample, surface and monitoring the FTIR signal, a three-dimesional map of the modulated evanescent wave can be obtained.

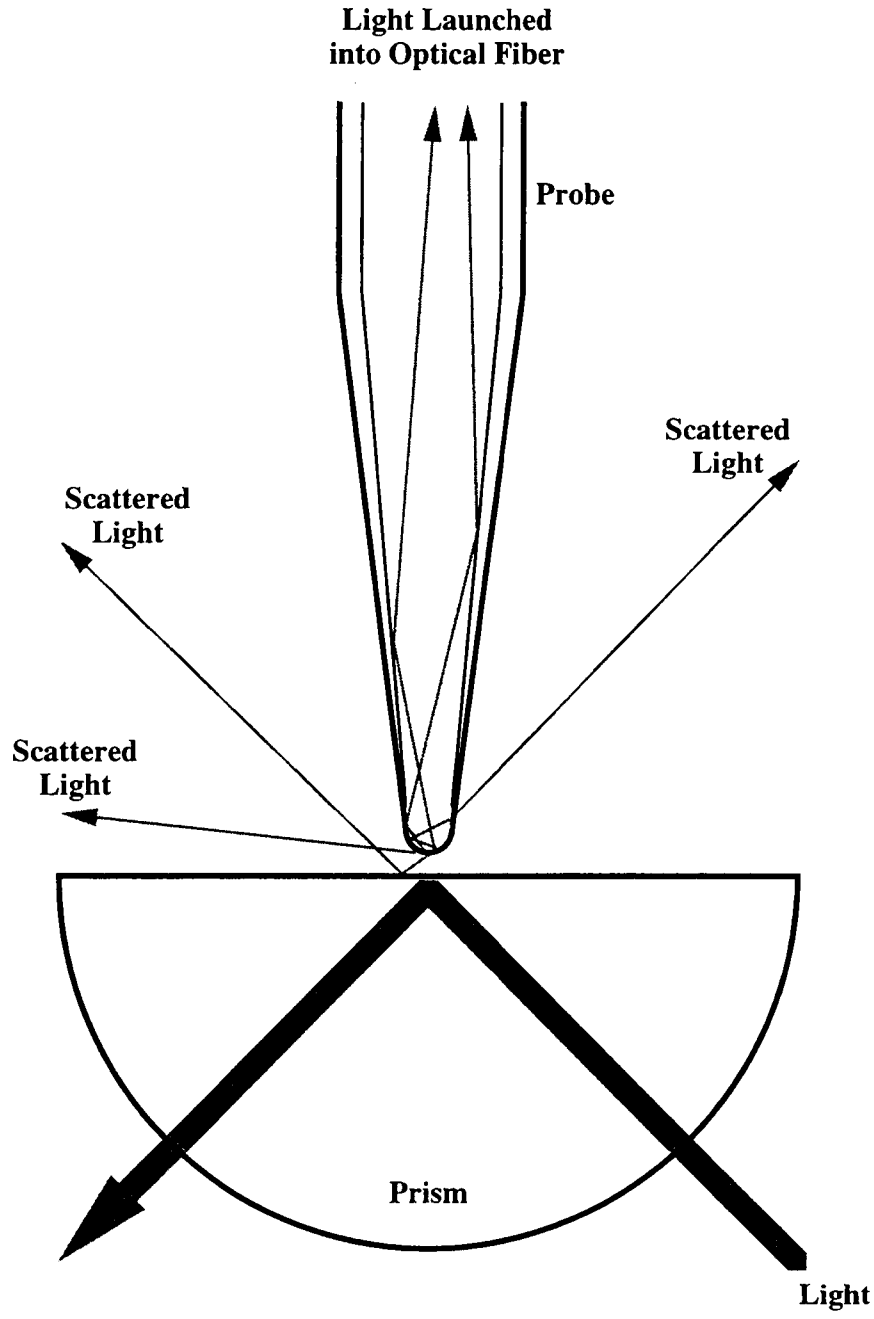


Figure II.4. Fiber Optic Probe Induced FTIR. Diagram of FTIR induced by a fiber optic probe inserted into the evanescent field region near the prism-air interface. Light undergoing FTIR is scattered by the probe tip or collected as the probe tip launches the light into the optical fiber.

This topographical map directly relates to the physical profile of the sample. A three dimensional visual image can be constructed by computer from the tunneling signal data.

Two methods of scanning the probe across the sample exist. When the probe is kept at a constant height on the z-axis during a scan, the scan is called a constant height scan. With electronic feedback the probe can be moved on the z-axis during the scan to keep a constant tunneling signal. This type of scan is called a constant signal scan or a scan in feedback mode. Either type of scan produces a map of the evanescent field intensity.**(Figure II.5.)**

The optical characteristics of the sample will have some effect on the observed tunneling signal. Since many samples observed with the PSTM are thinner than the wavelength of light, the effect of the sample structure on the tunneling signal is greater than the effect of the variation of the sample's optical properties. However, for certain cases the optical properties of a sample will dominate the tunneling signal. Samples with high absorption coefficients at the photon energy that the PSTM is operating can suppress the evanescent field intensity. These samples may give negative image data where the optically thicker points of the sample has smaller evanescent field intensities. Additionally, samples that are flat but are made up of different materials will produce evanescent field intensities that are dependent on the optical characteristics of the sample instead of the structure of the sample. Since the PSTM is sensitive to changes in the optical characteristics of the sample, the PSTM has the capability to do spatial spectroscopy of these samples. Ambiguities can be eliminated by use of dispersion characteristics of the sample if various wavelengths are employed.

The spatial resolution of the PSTM is dependent on several factors. The wavelength of light, incident angle and polarization conditions, signal-to-noise ratio, and probe tip size and shape all affect the resolution of the PSTM. The ultimate vertical resolution (resolution along the z-axis) is primarily dependent on the decay length of the evanescent field intensity which depends on the wavelength of light, angle of incidence,

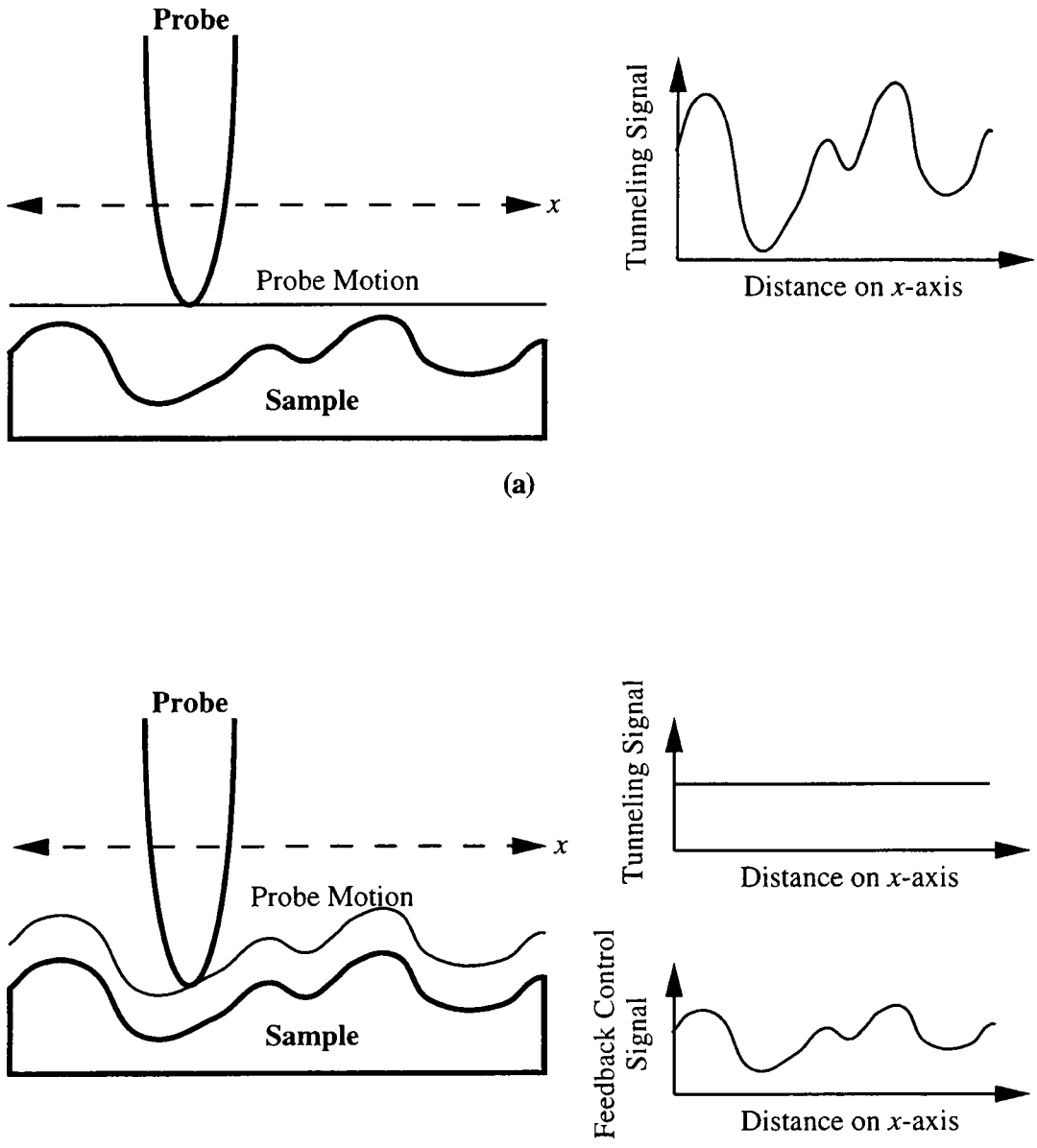


Figure II.5. Scan Modes. (**a**) Constant height scan with the varying tunneling signal producing the image information and (**b**) constant signal scan with the feedback control signal producing the image information.

and optical constants of the prism. Small movements of the probe along the z-axis can be detected since the signal changes exponentially with probe position on the z-axis.

The ultimate lateral resolution (resolution in the plane perpendicular to the z-axis) is primarily dependent on the probe size and shape relative to the sample's local topographic features and the wavelength of light. Photon tunneling to the probe will only occur where the tip of the probe is in the evanescent field. Additionally, the amount of photon tunneling to the extreme tip of the probe is exponentially larger than the amount of photon tunneling to a point on the tip farther away from the sample-air interface. Therefore, the most sensitive area of the probe tip is normally smaller than the physical diameter of the tip, and the lateral resolution is dependent on the most sensitive area of the tip. The wavelength of light affects the lateral resolution since the actual dimensions of the variations in the evanescent wave are related to the wavelength of light.

Noise can impair the resolution of the PSTM by reducing the signal sensitivity to probe movement. Several forms of signal noise occur during PSTM operation. Signal noise from light detection includes light source noise, scattered light from the sample-air interface, and stray light detection by the photo multiplier detector. In practice these noise contributions can be quantified in several ways and used to advantage. Electrical noise picked up by the detector and amplified in the electronics contributes to the signal noise, also. Finally, mechanical vibrations that move the probe in the evanescent field region induce signal noise. While none of these noise sources can be completely eliminated, a carefully designed PSTM can dramatically reduce signal noise so that resolutions close to the ultimate resolutions can be obtained.

C. UVPSTM Components and Resulting Spectra

For ultraviolet light with wavelengths greater than 250 nm the modifications needed to make a UVPSTM from a visible PSTM are simple and straightforward. The UVPSTM presented here uses a 100 W mercury (Hg) arc lamp for the light source.[II-3] Broad band filters are used to select ranges of the total wavelength spectra emitted by the Hg arc. Additional wavelength discrimination occurs by using a solar blind PMT[II-4] that detects ultraviolet radiation but does not detect visible radiation. To prevent absorption of the ultraviolet light a quartz prism and optical fiber made from pure undoped silica[II-5] are employed; this allows transmission of light down to 250 nm. The resulting PSTM is capable of operating as a visible PSTM or a UVPSTM simply by changing filters and/or detectors. By using a beam-splitting arrangement with a visible PMT[II-6] and a solar blind PMT the PSTM can act simultaneously as a visible PSTM and UVPSTM in constant height mode. Thus, comparisons of the operation of the PSTM at different wavelengths can be made. A general schematic of the UVPSTM apparatus is shown in **Figure II.6.**

C.1. Mercury Arc Lamp Light Source

Using a Hg arc lamp as the light source instead of a laser requires some special considerations and introduces some differences from a laser operated PSTM for the UVPSTM. A large part of the light emitted by the Hg arc is collected and focused by a water cooled ellipsoidal mirror to an aperture (diameter ≈1-2 mm). A water filter removes infrared radiation from the beam prior to the aperture to reduce heating of the sample and reduce thermal expansion of components that control the position of the probe. After the light passes through the aperture, a beam splitting quartz slide removes a small portion of the light which is monitored to keep a constant power of light coming through the aperture. The monitored light is focused on a detector that interfaces with the arc lamp power supply to maintain a constant light output with feedback control.[II-7] The

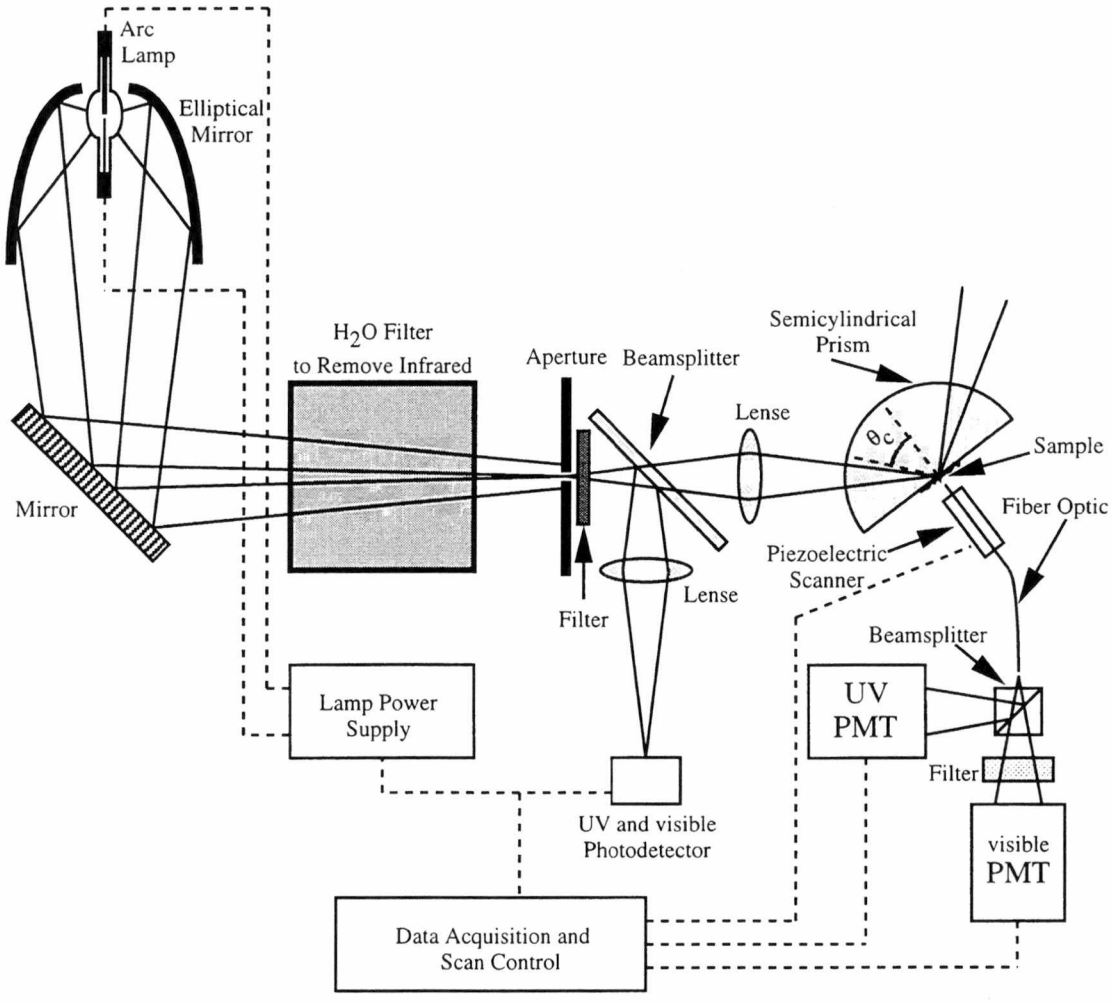


Figure II.6. UVPSTM Apparatus. Schematic showing the components of the UVPSTM.

rest of the light coming through the aperture is refocused by a quartz lens to the prism-air interface. The broad band filters used to select the photon ranges can be inserted before or after the beam-splitting slide removes light in carrying out its duty in the constant power feedback control. The decision of where to put the broad band filter is based on which position in practice maintains a better constant power output.

Using an arc lamp instead of a laser results in one advantage and one disadvantage. The advantage of an arc lamp is that a wide bandwidth of light can be used. This is important to the PSTM because interference effects can reduce the quality of images.[II-8] The narrow bandwidth of lasers results in two main interference effects. The first interference effect is that an interference pattern is produced on the surface of the prism-air interface by the interaction between the light coming into the prism and the light reflected from the exiting surface of the prism. This interference pattern is easily removed by using a coupling prism to redirect the exiting light or by changing the angle of incidence of the laser beam to prevent the reflected light from reaching the same point as the incident light. Since this interference effect is easily removed, it does not present a problem for the PSTM and can even be beneficial for calibration purposes. The more serious interference effects are the interference occurring around the sample and probe tip and the standing waves which may occur at various sites on the sample from reflections of the traveling wave of the evanescent field. Interference occurring at sample boundaries can lead to false modulation of the evanescent wave which leads to false structures in an image. In some cases local interference patterns are beneficial and can be intentionally allowed. These effects have been observed.[II-9]

The disadvantage of an arc lamp is that arc lamps are noisier than lasers. The noise in the light output of an arc lamp evolves from two sources. One source of noise is the electrical noise inherent in a spark gap discharge. Although the arc lamp power supply maintains a constant current output, the light output can vary greatly. Fluctuations

in the vapor pressure of the Hg vapor in the lamp will result in fluctuating light output. This type of noise can be greatly reduced by the aforementioned feedback control.

The second source of noise is arc wander. "arc wander" is a term used to express the movement of the arc discharge relative to the electrodes of the lamp bulb. The movement occurs because the surface of the electrodes becomes corroded and contaminated by the hot Hg vapor reacting with the metal electrode. When corrosion and contamination occur the arc will physically move to a cleaner and less resistive spot on the electrode. The movement in the arc causes a change in light intensity detected by the probe because the light spot at the sample-air interface is essentially an image of the arc. Noise due to arc wander is extremely difficult to control. Although the feedback control can keep the light output from the aperture at a constant power level, the UVPSTM probe detects about one millionth of a percent of that light. Arc wander will result in spatial variations in the light coming through the aperture regardless of whether the total light power is constant or not. These spatial variations in the light beam striking the sample surface will induce noise in the signal detected by the probe. The effects of arc wander can be eliminated by diffusing the light beam, but this results in a significant loss of light flux.

The amount of noise in the light beam is dependent on the wavelength of light. The ultraviolet light is much noisier than the visible light. Additionally, the magnitude of the ultraviolet light is much less than the magnitude of visible light, and larger background signals exist in the ultraviolet signal because the scattering of light from the sample surface in the far zone is inversely proportional to the fourth power of the wavelength. Complications arise in trying to control the ultraviolet light output with feedback control. The small ratio of ultraviolet light to visible light and the larger noise associated with the ultraviolet light require larger fluctuations in the control signal and current output of the power supply. The large fluctuations in the current running through the arc lamp can induce further noise in the system. Although the arc lamp available is

noisy, ultraviolet lasers are pulsed and hence much noisier than continuous-wave visible lasers, and the white light output of arc lamps provides an easy means of selecting different wavelength spectra. Therefore, the arc lamp light source was chosen over an ultraviolet laser.

Another difference between an arc lamp and a laser is the light beam that both produce. Since the light of an arc lamp is emitted in a 4π geometry, the light must be collected and focused to a small spot, and the UVPSTM requires a specific flux of light at the sample-air interface to operate. The optics needed to collect a large solid angle of light and focus the light to a small point without significant loss of light flux consequently produces a strongly converging light beam. The beam incident on the sample-air interface is a light cone with light hitting the sample surface with angles $\pm 7°$ of the angle of incidence of the central axis of the light cone. As a result angles of incidence close to the critical angle cannot be used with the arc lamp source without a reduction in the light flux at the sample surface or some light transmitting through the interface. In general this does not affect the performance of an arc lamp PSTM; however, shorter evanescent field decay lengths must be used.

It should also be noted that samples are generally mounted on a fused silica slide or cleave of mica and then the slide, or cleave, is mounted to the prism. To prevent TIR from occurring at the prism-slide interface, an index matching fluid was inserted into the small air gap between the prism and slide. A special ultraviolet transmitting index matching fluid[II-10] prevents reflections from occurring and prevents absorption of the ultraviolet light in the gap.

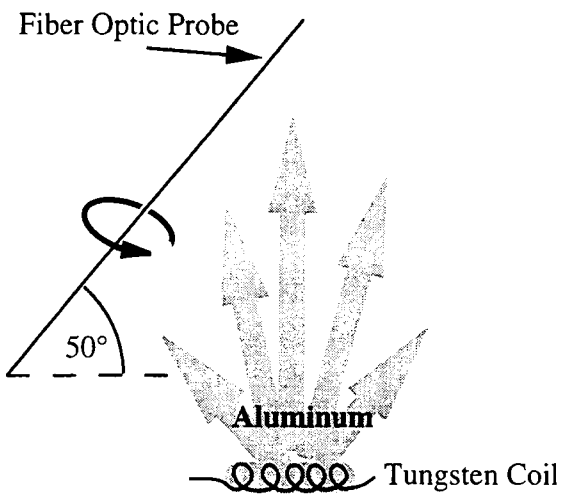
C.2. Fiber Optic Probe

The most critical component of the UVPSTM is the fiber optic probe. The principal compromise involved in probe design is between size and collection efficiency.

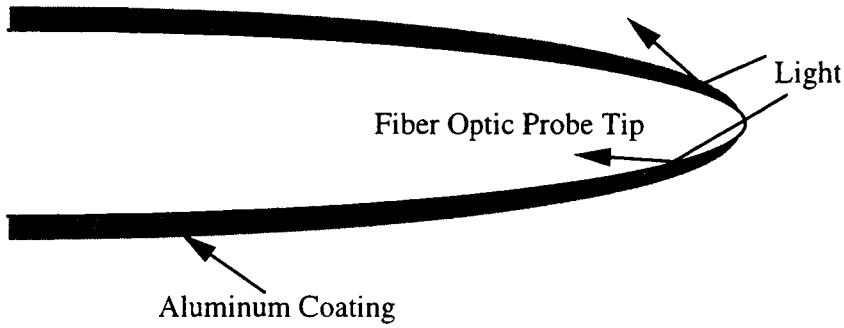
Resolution improves with smaller diameter probes, but the detected signal strength decreases. However, increasing the signal strength is not the only concern related to collection efficiency. The detected signal is comprised of the signal from tunneling light and light scattered by the sample. The ideal probe maximizes the collection of the tunneling signal while minimizing the collection of the scattered light signal; this leads to the largest signal-to-noise and signal-to-background ratios.

Contrary to other forms of scanning probe microscopy the macroscopic shape of the UVPSTM probe critically affects the performance of the probe. As mentioned, light conduction by the optical fiber will only occur if the angle of incidence of light into the optical fiber is less than the acceptance cone angle of the optical fiber. The acceptance cone angle (±14°) is defined by the critical angle of the core-cladding interface of the optical fiber. The shape of the tip and taper regions of the probe must be conducive to channeling the light originating at the probe tip into the optical fiber region. The surface of the probe must be smooth to maximize reflections at the probe walls, and the overall shape must be symmetric to keep the light traveling close to the central axis of the optical fiber.

In addition to controlling the shape and sharpness of the probe with specific production procedures, an aluminum (Al) coating is applied to the outer surface of the probe except the tip region. The purpose of the Al coating is twofold. The Al coating reduces the collection of scattered light by shielding the taper and tip regions, and the Al coating allows lower angle reflections from the core-Al coating interface. This makes a significant difference in maximizing the collection of the tunneling signal and minimizing the collection of the scattered light signal. The optical fiber is mounted and rotated at an angle of 50° relative to the horizontal as the evaporated Al flows in the vertical direction. Therefore, the extreme tip of the probe is shielded from Al (**Figure II.7.**). Coatings of 20 to 50 nm of Al were applied to the outer surface; however, at regions near the tip where the angle of incidence of the Al differs from the mounting angle the coatings were



(a)



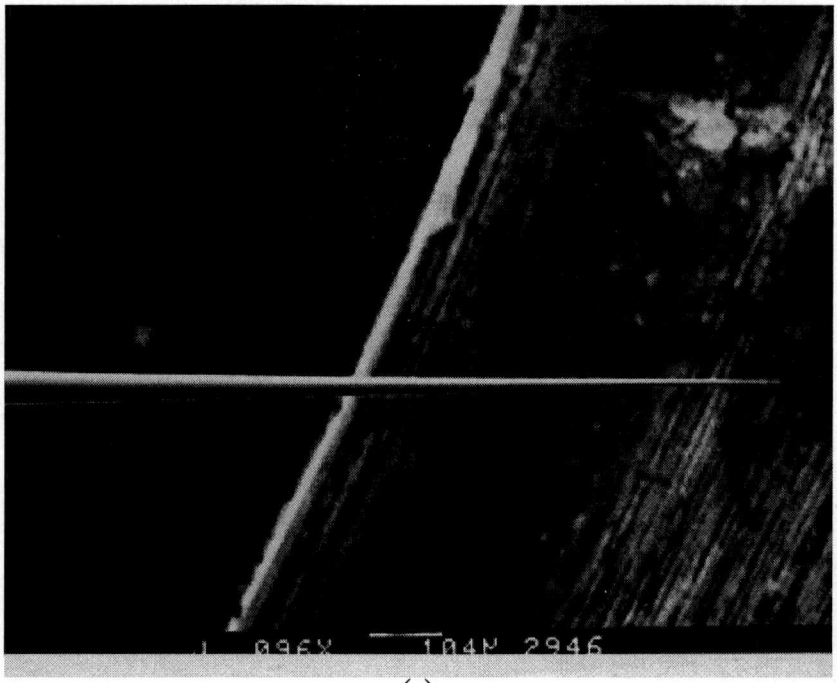
(b)

Figure II.7. Aluminum Coating. **(a)** Evaporation of aluminum onto outer surface of fiber optic probe and **(b)** resulting aluminum coating on probe tip region.

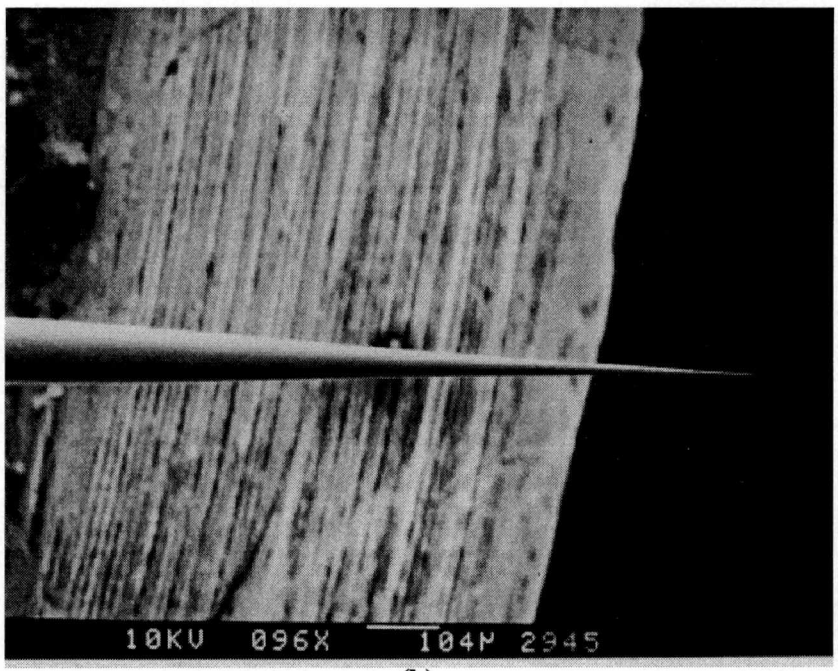
thinner. *It is important to note that the Al shielding does not define an aperture of light collection of the tunneling photons.* The exponential decaying evanescent field combined with the probe tip shape defines the aperture of light collection. Although evaporations made at lower angles (<20°) may create smaller apertures of collection than those created by the evanescent field decay, the probes in this study were confined to aperture definition by the evanescent field to avoid confusion with another optical scanning probe microscope called the Near Field Scanning Optical Microscope that uses apertures defined by Al coatings at angles close to 20°.

Through trial and error, procedures were developed for producing probes suitable for the UVPSTM. Production included a combination of the following processes: pulling the optical fiber, finish etching, and applying an Al shielding. The procedures developed are reviewed; however, it is important to note that in the production of such a small device repeatability is not perfect. Variations in tip shape and size will result from the same carefully followed procedure.

Probes for the study presented here can be separated into three different categories. Probes are referred to as long-taper, short-taper, and extreme-taper probes according to the length of the taper region. **Figures II.8.a., II.8.b., and II.9.a.** show the three different probe types. Different procedures were followed to create the different types of probes. The production of each type of probe began with the pulling of the optical fiber. The long-taper probe was produced with a pulling and Al-shielding process. Short-taper probe production started with the same pulling procedure that produced the long-taper probe, but a finish etching process shortened the taper length of the probe prior to the final Al-shielding process. To produce the extreme-taper probes a pulling procedure with different conditions from the pull for long- and short-taper probes created probes similar to the probe shown in **Figure II.9.b.** Finish etching and Al shielding of the probe shown in **Figure II.9.b.** created the extreme-taper probe (**Figure**

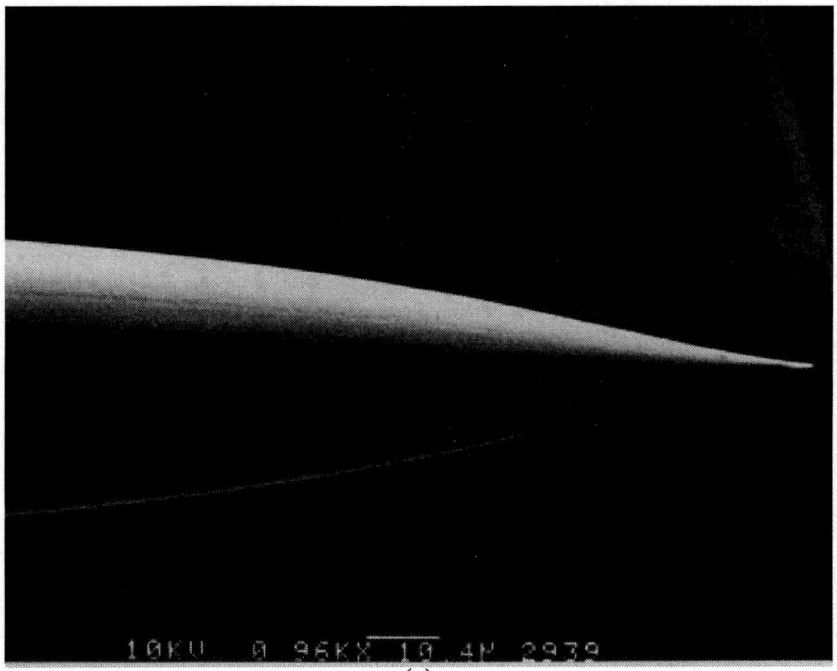


(a)

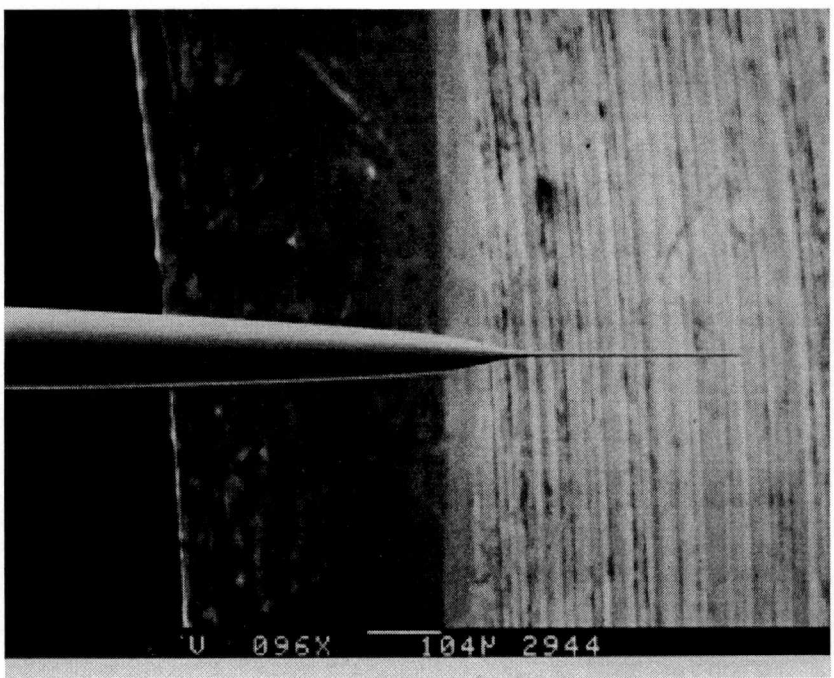


(b)

Figure II.8. Long- and Short-Taper Probes. SEM images of **(a)** long- and **(b)** short-taper probes. The bar corresponds to 104 µm.



(a)



(b)

Figure II.9. Extreme-Taper Probe. SEM image of an extreme-taper probe **(a)** produced from the pulled probe shown in **(b)**. The bar in **(a)** corresponds to 10.4 μm, and the bar in **(b)** corresponds to 104 μm.

II.9.a.). Approximate full cone angles for the long-, short-, and extreme-taper probes are 1.5°, 2.5°, and 10°, respectively.

The first stage in probe production is pulling a bare optical fiber to a sharpened point with heat from a CO_2 laser. This stage of production is performed with a specially designed pulling device manufactured by Sutter Instrument Co. known as the P-2000 Laser Based Micropipette Puller.[II-11] The P-2000 allows programming of five variables that control the heating and pulling of the optical fiber. The five variables are the heat applied with the CO_2 laser (HEAT), the width of the area heated with the laser (FIL), the velocity trigger set point for start of the pull cycle (VEL), the time delay between deactivation of the laser and start of the pull (DEL), and the force of pull applied to the fiber (PULL).

To operate the P-2000 an optical fiber is stripped of insulation and clamped to the pulling device of the P-2000 where tension holds the fiber taut. By running a pull program the CO_2 laser operating at a power associated with HEAT illuminates the optical fiber over a length of the fiber corresponding to the FIL. The P-2000 is capable of detecting small movements of the optical fiber as it begins to melt from the heat of the CO_2 laser. When a velocity corresponding to the VEL is detected, the fiber is pulled with a force corresponding to the PULL setting at a time in relation to the shutdown of the laser determined by the DEL.

The variable settings for the production of the long-taper probe were HEAT=350, FIL=0, VEL=20, DEL=126, and PULL=175. These settings result in pulling the fiber with a large force after a small amount of heating. The settings were chosen to produce probes with sharp tips and short-taper regions. The production of the long-taper probes was completed by coating the probe with Al as discussed before.

The short-taper probes were finish etched in hydrofluoric (HF) acid to further reduce the length of the taper region. The tip region of the probe was placed in HF acid. The level of the HF acid was located at the upper part of taper region of the probe.

Etching was allowed to continue until all of the probe in the HF acid was gone. As the HF acid etched the optical fiber, the meniscus of HF acid around the optical fiber grew smaller until it disappeared when the last part of the optical fiber was etched (**Figure II.10.**). This finish etching procedure produced shorter taper regions on probes without much loss of tip sharpness. The final stage of the short-taper probe production involved applying the Al shielding around the taper region as discussed before.

Extreme-taper probes were produced with a small modification in the pulling stage. The HEAT setting of the pull parameters was reduced to 300. This small reduction in the heat setting produced a different macroscopic shaped probe as seen in **Figure II.9.b.** The small cylindrical section existing at the tip of the strongly converging conical section is etched away in HF acid (**Figure II.11.**). The resulting probe has an extremely short-taper region with a small tip at the tip of the conical section. An Al coating completes the extreme-taper probe production.

The long-, short-, and extreme-taper probes differ in performance and repeatability. Since the long-taper probes do not require the etching procedure, the long-taper probes are the most repeatable probes. The tip size is generally very small, but the long-taper region results in poor light collection capability. In contrast to the long-taper probe, the extreme-taper probe provides excellent light collection because of the high cone angle of the taper region; however, obtaining consistently small tips is difficult. Short-taper probes represent a compromise between long-taper and extreme-taper probes. The etching procedure increases light collection capability while reducing tip size repeatability, but light collection is not as great as light collection with the extreme-taper probe.

The best type of probe for imaging is dependent on the sample type. A sample with a heavy population of high contrast structure produces a large amount of scattered light, but a sample with a sparse concentration of small or low contrast structures does not produce a lot of scattered light. In general, the extreme-taper probes are needed for

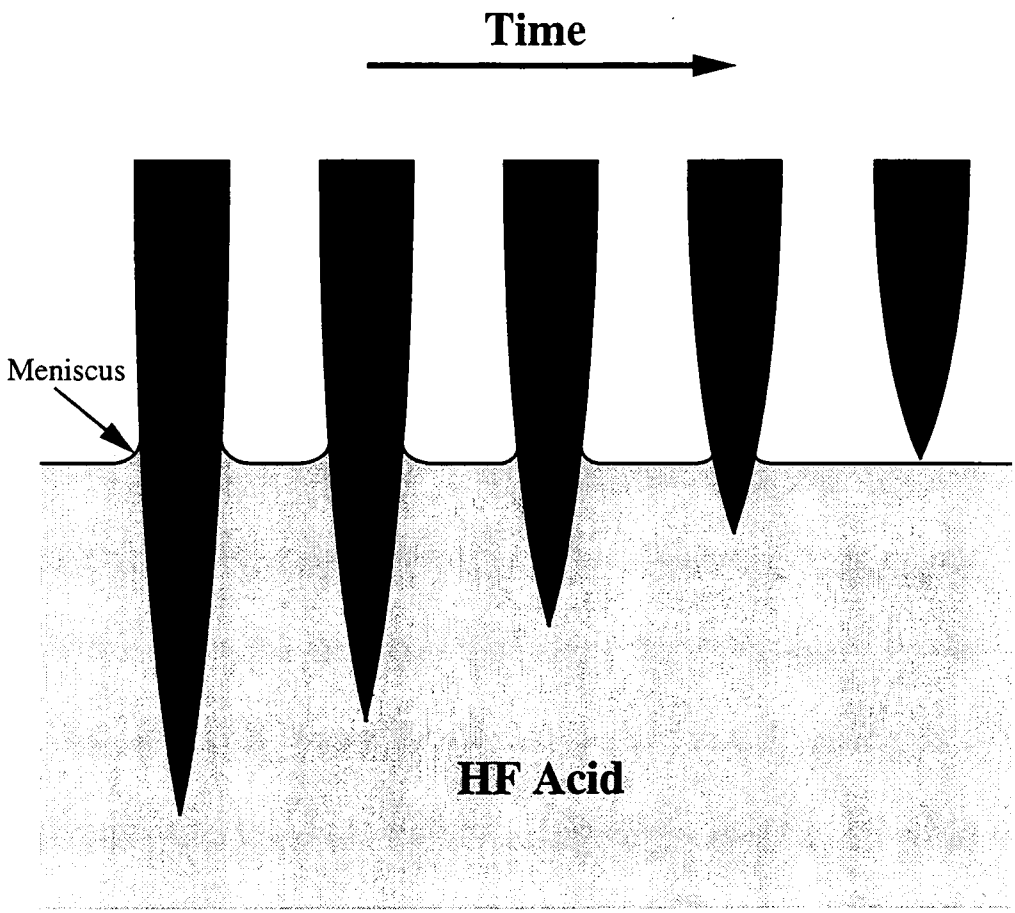


Figure II.10. Short-Taper Probe Finish Etch. Finish etch in hydrofluoric (HF) acid to reduce the probe taper length while maintaining probe tip sharpness.

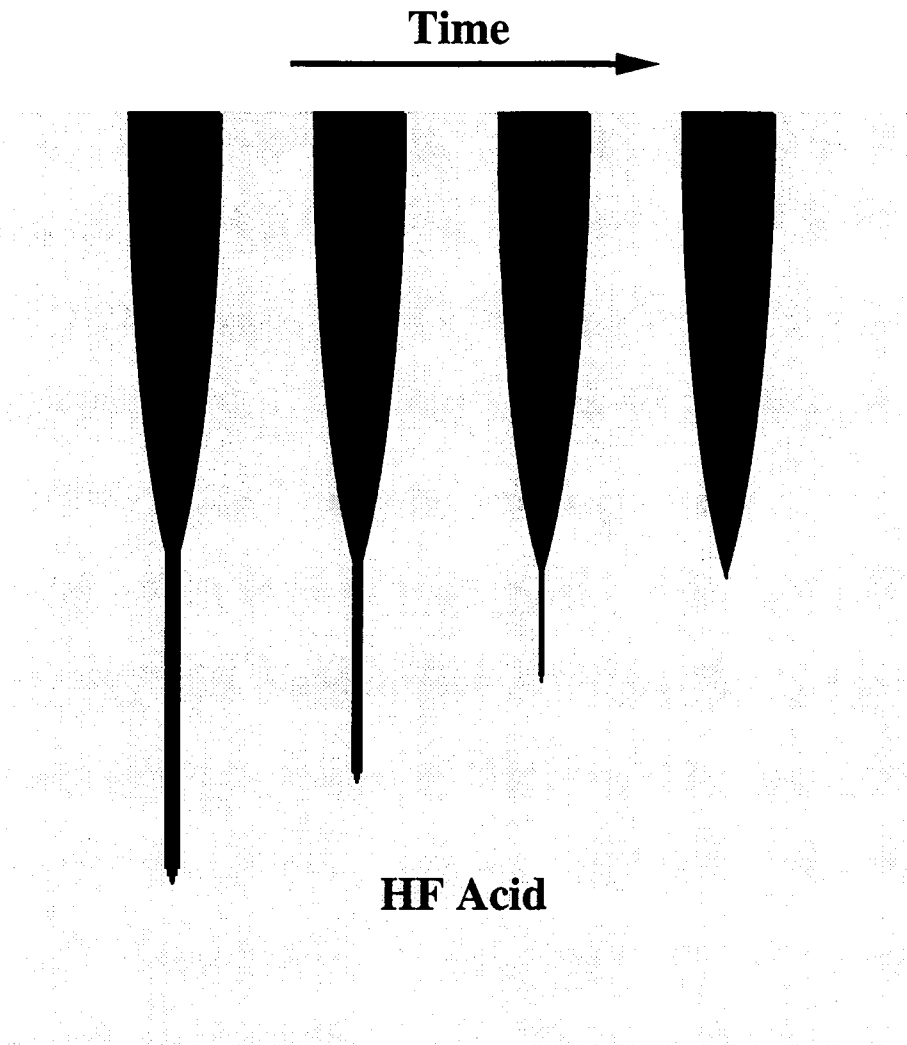


Figure II.11. Extreme-Taper Probe Finish Etch. Finish etch in hydrofluoric (HF) acid to remove the extending cylindrical portion of the probe and create a rapidly converging probe taper region.

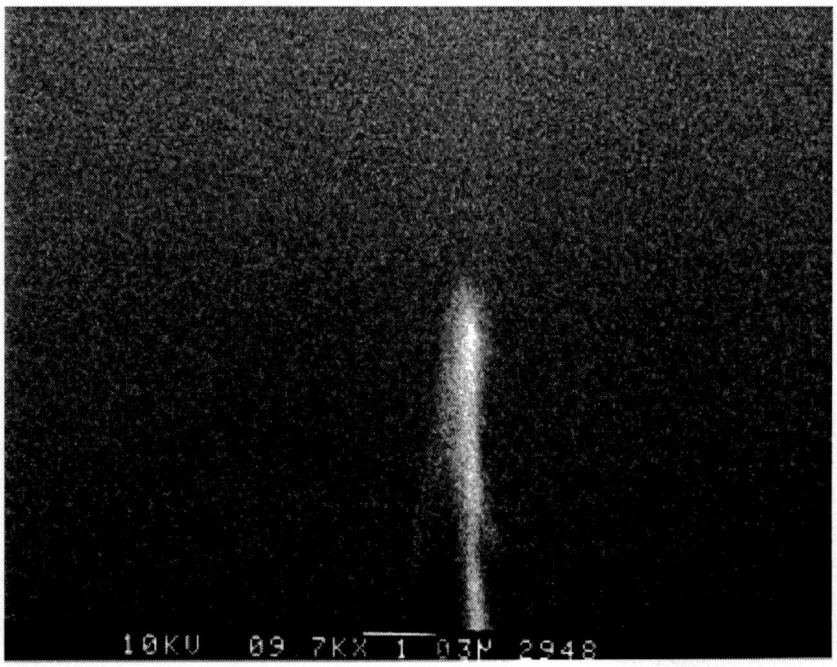
samples where a lot of scattered light is produced. The extreme-taper probes produce a higher signal-to-background noise level which makes locking onto the tunneling signal easier. If only a small amount of scattered light is produced by the sample then the long-taper probes can be used. One other consideration of probe effectiveness involves reducing probe-sample collisions; however, the best type of probe to reduce probe-sample collisions is not well defined since many variables like the shape of the tip region of the probe have to be considered.

The amount of scattered light in the far zone is inversely proportional to λ^4, and the shorter evanescent field decay lengths associated with the ultraviolet result in smaller effective tip sizes when compared to visible tip sizes for the same probe. Thus, the UVPSTM requires extreme-taper probes more often than the visible PSTM to gain signal strength and improve signal-to-background noise levels. In fact, imaging in the UVB region was only possible with short- and extreme-taper probes. The larger collection of extreme-taper probes may also be beneficial to spectroscopic applications of the PSTM.

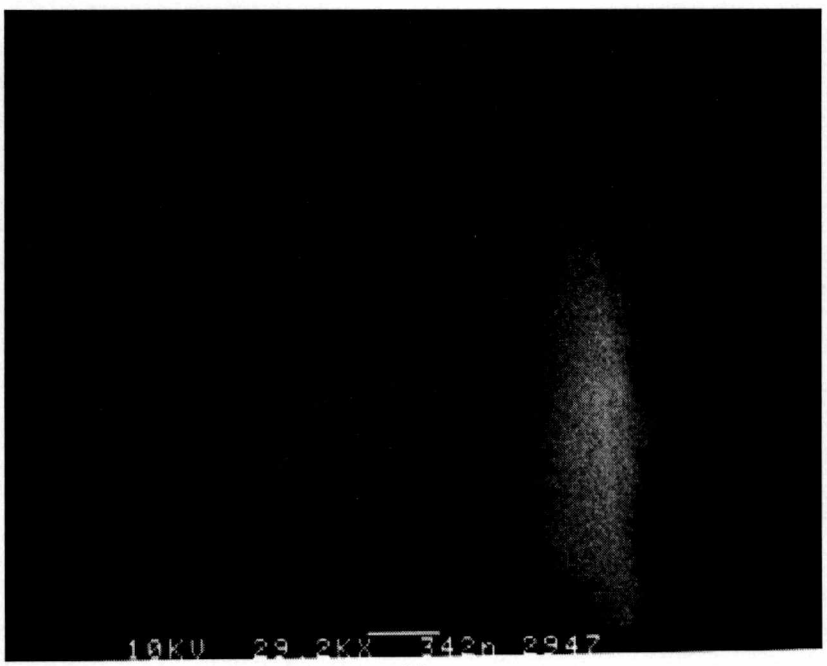
Comparisons between the signals obtained with different probes are shown in **Section II.D.2.** to demonstrate differences in performance. However, it should be noted that the performance of all probes is strongly related to the tip size and structure which is difficult to reproduce consistently. Although SEM imaging of the tip region is difficult due to charging of the probe tip, some typical probe tip regions are shown in **Figures II.12. and II.13.** Typical tip diameters range from 50-150 nm; however, the effective tip diameter depends on several factors including the shape of the probe tip and the decay length of the evanescent field.

C.3. Light Spectra of the UVPSTM

The light spectra obtainable with the UVPSTM are dependent on several factors. The light spectra outputted by the Hg arc lamp is reduced by absorption in the optical

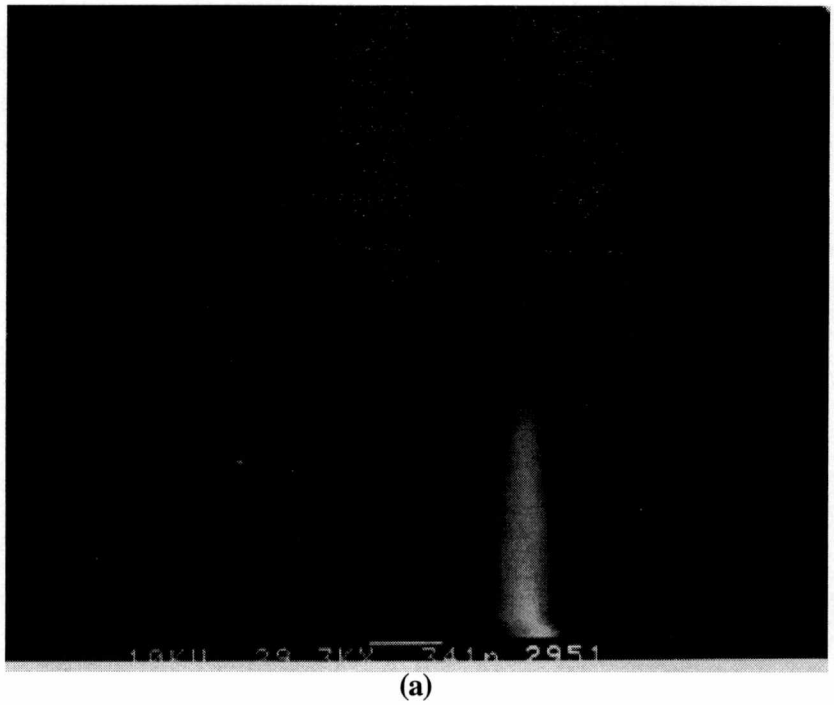


(a)

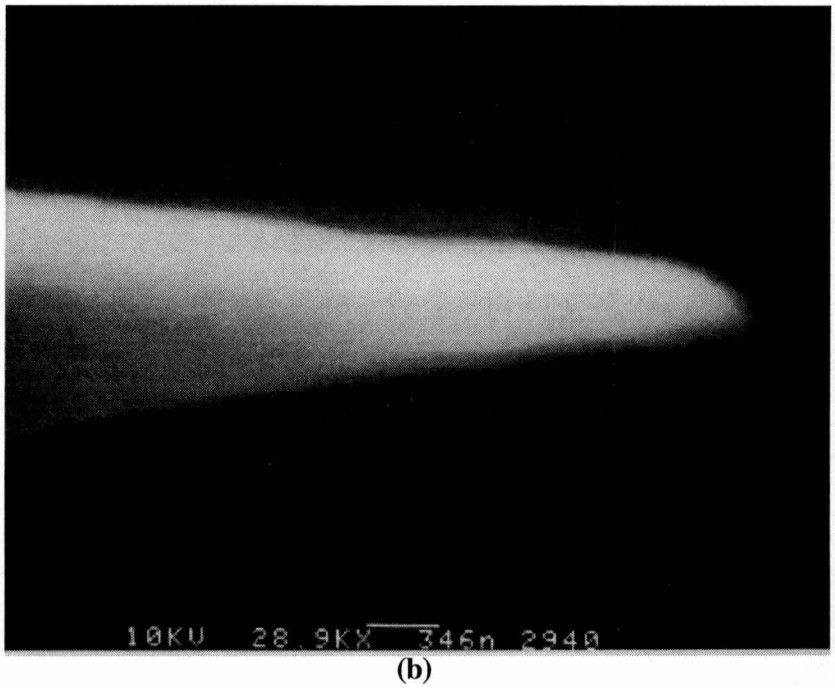


(b)

Figure II.12. Tip Regions of Long-Taper Probes. SEM images of tip regions of long-taper probes. The bar corresponds to 1030 nm in **(a)** and 342 nm in **(b)**.



(a)



(b)

Figure II.13. Tip Regions of Short- and Extreme-Taper Probes. SEM images of tip regions of a short-taper probe(**a**) and an extreme-taper probe(**b**). The bar corresponds to 341 nm in **(a)** and 346 nm in **(b)**.

components and optical fiber. Selection of particular regions of the resulting light spectra is made with broad band filters and the choice of the PMT detector. The resulting spectrum used in the UVPSTM is thus a combination of the spectral output of the Hg arc lamp, the transmission of the optical components, the transmission of the optical fiber, the transmission of any filters, and the quantum efficiency of the PMT detector. The study presented here utilized four different spectra. Three of the four spectra were obtained with three different filters in combination with a PMT (noted as "visible PMT") sensitive to radiation from the absorption edge of glass on through to the visible region. The other spectra was obtained by using a solar blind PMT for wavelength selection. The four spectra are referred to as the red, blue, UVA, and UVB spectra as shown in **Figure II.14.**

D. Evanescent Field Detection

The operation of the UVPSTM centers around the detection of the evanescent field by the fiber optic probe. The vertical resolution of the UVPSTM directly depends on the decay length of the tunneling signal, and the decay length influences the lateral resolution by defining the effective probe size. Additionally, for adequate control of the probe relative to the surface of the sample, a consistent nondrifting signal with a large signal-to-noise ratio is needed. Here examples of tunneling signals obtained under different conditions are shown to demonstrate the variation in the signal obtained during evanescent field detection.

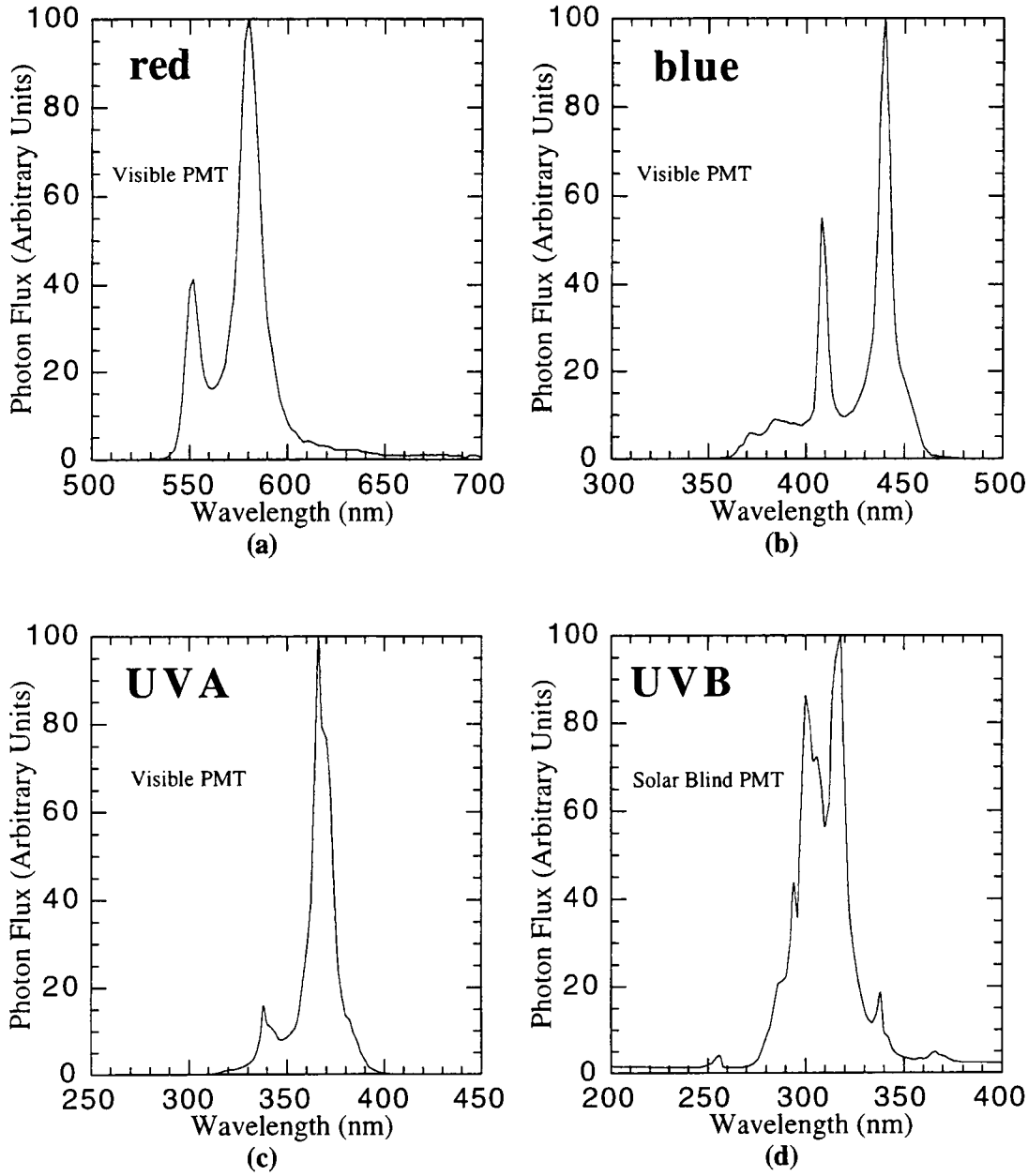


Figure II.14. UVPSTM Light Spectra. **(a)** red, **(b)** blue, **(c)** UVA, and **(d)** UVB light spectra used by the UVPSTM. The peaks represent emission from the Hg vapor of the arc lamp. The spectra are defined by the arc lamp emission, filters, transmission characteristics of the prism and optical fiber, and the spectral response of the photomultiplier tube detector.

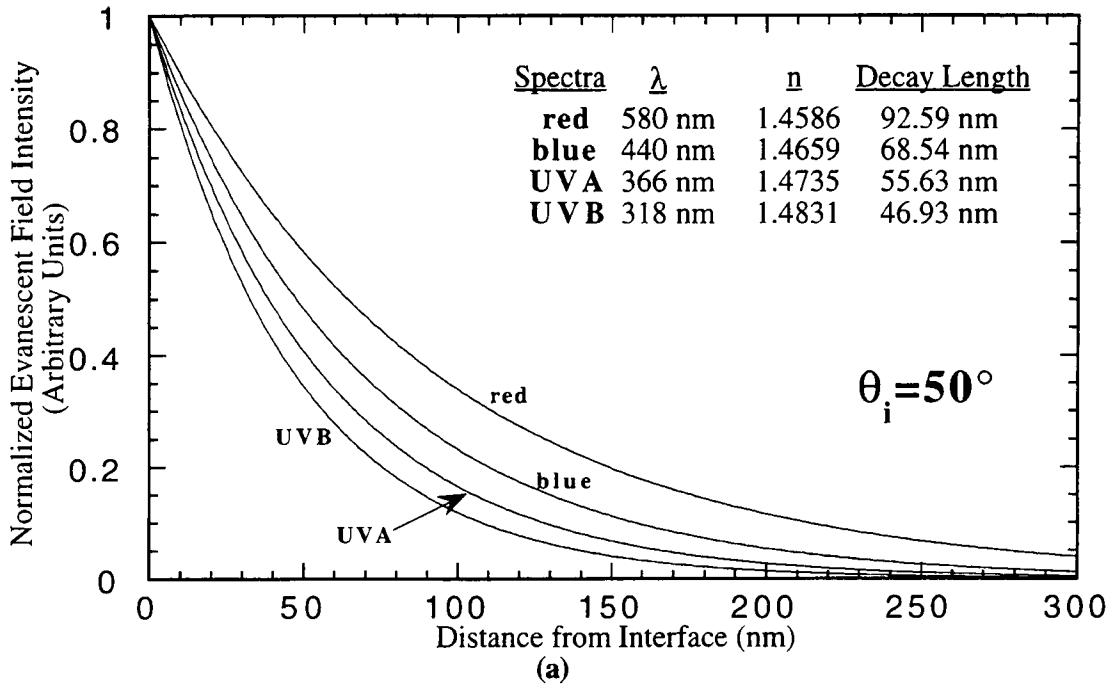
D.1. Wavelength and Incident Angle Effects on Tunneling Signals

The tunneling signal as a function of probe-sample separation is closely related to the evanescent field intensity as a function of distance from the sample-air interface. The decay length of the evanescent field intensity depends on the wavelength of light, angle of incidence to the interface, and indices of refraction of the media making the interface. Therefore, the tunneling signal should have a similar dependence on wavelength, angle of incidence, and indices of refraction. Here data is presented that shows the tunneling signal dependence on wavelength and incident angle variation.

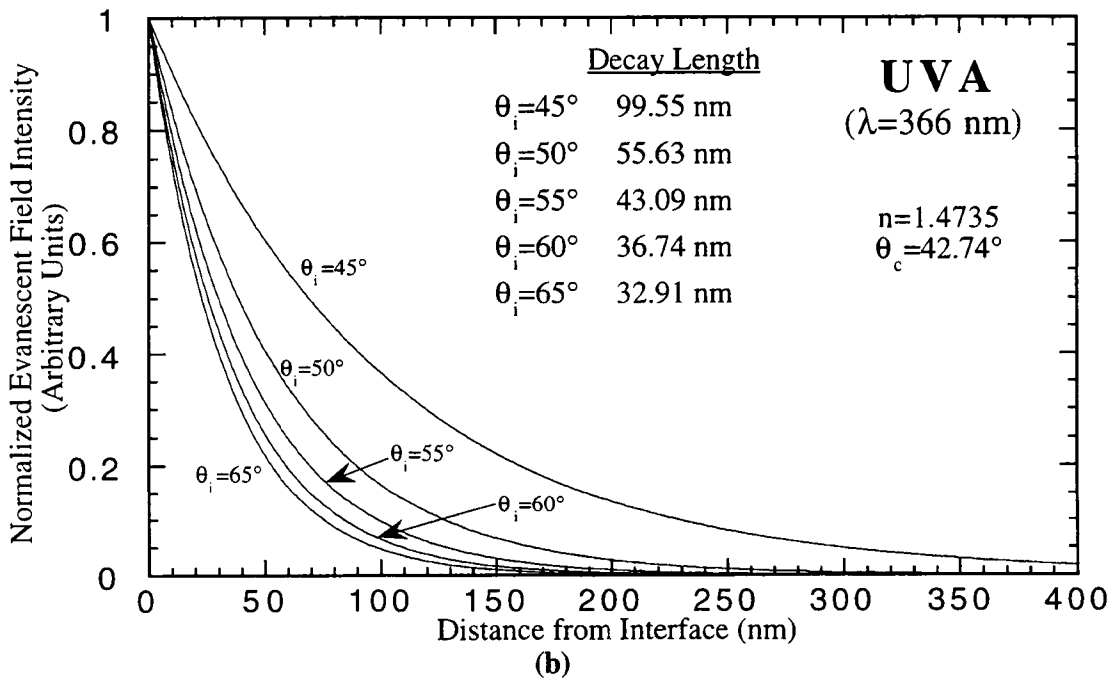
The decay length of the evanescent field intensity will decrease with decreasing wavelength and increasing angle of incidence as expressed in equation **(II.1.)**. **Figure II.15.** shows theoretical evanescent field intensities calculated from equation **(II.1.)** for evanescent waves produced on a fused silica-air interface.[II-12] **Figure II.15.a.** shows the decreasing decay length with decreasing wavelength, and **Figure II.15.b.** shows the decreasing decay length with increasing angle of incidence. Although the red, blue, UVA, and UVB spectra contain a continuum of wavelengths, the decay lengths were calculated with the peak wavelength of each spectrum.

Experimental data showing a decrease in the decay length of the tunneling signal with decreasing wavelength is shown in **Figure II.16.** The decay lengths represent the exponential dependence of the data in the region of strongest curvature. For small (<50-100 nm) probe-sample separation the tunneling signal deviates from an exponential curve as the tunneling signal resembles the transmission through a three-media planar system as shown in **Figure II.2.** For large (>600-1000 nm) probe-sample separation the tunneling signal begins to deviate from an exponential curve as background noise begins to dominate the signal.

The decreasing decay length of the tunneling signal with increasing incident angle is shown experimentally for the UVA and UVB spectral regions in **Figures II.17., II.18., II.19., and II.20.** Additionally, **Figures II.19. and II.20.** show a decrease in the



(a)



(b)

Figure II.15. Evanescent Field Decay Length Variation. Variation of the decay length of the evanescent field with changing wavelength(**a**) and angle of incidence(**b**) for a fused silica-air interface.

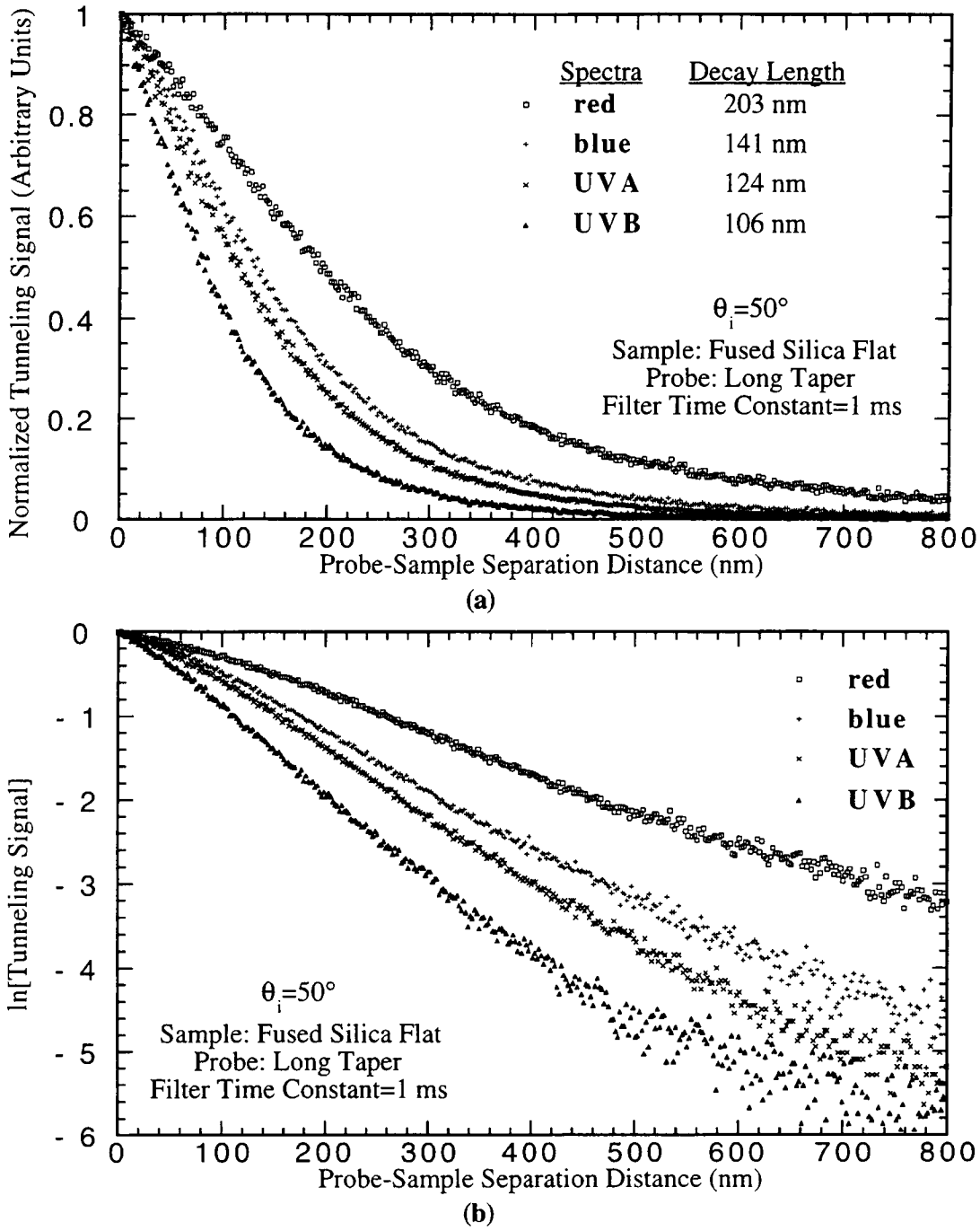


Figure II.16. Tunneling Signals for Varying Wavelength Spectra. **(a)** Linear and **(b)** semi-log plots showing a decrease in the decay length of the tunneling signal as the wavelength decreases. The shorter decay lengths are intimately connected to improved resolution of the UVPSTM.

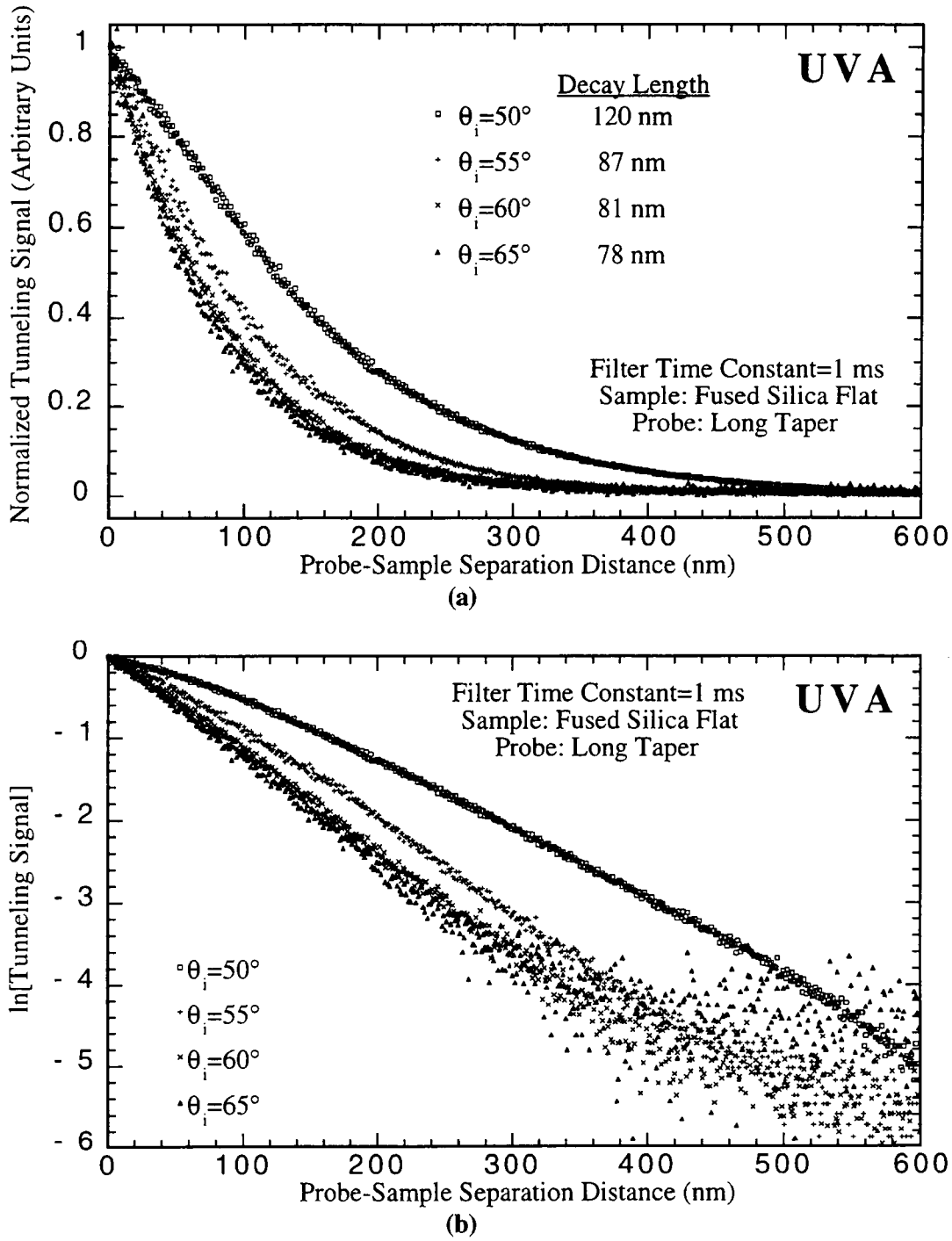


Figure II.17. UVA Tunneling Signals for Varying Angle of Incidence. **(a)** Linear and **(b)** semi-log plots showing a decrease in the decay length of the tunneling signal as the angle of incidence increases.

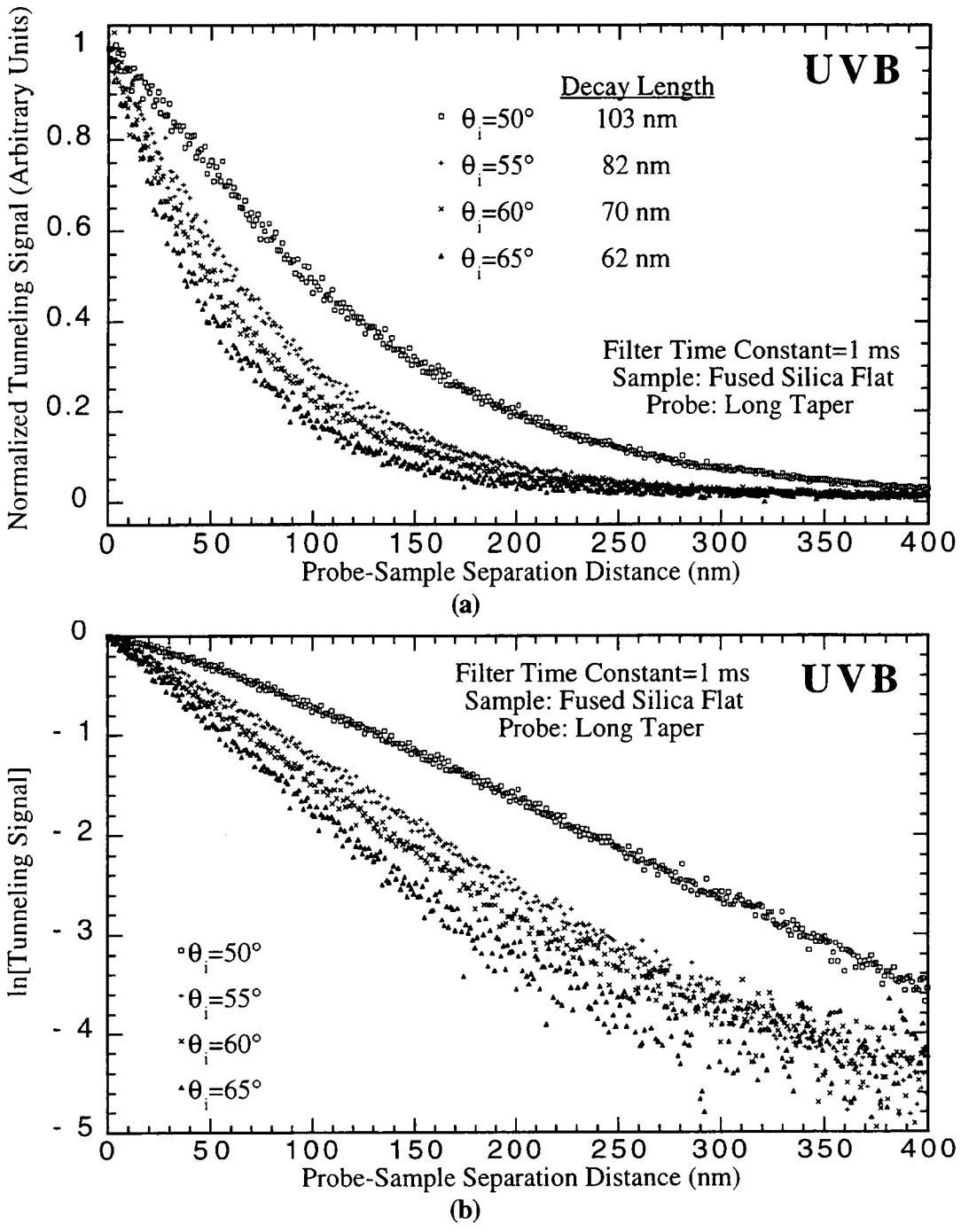


Figure II.18. UVB Tunneling Signals for Varying Angle of Incidence. **(a)** Linear and **(b)** semi-log plots showing a decrease in the decay length of the tunneling signal as the angle of incidence increases.

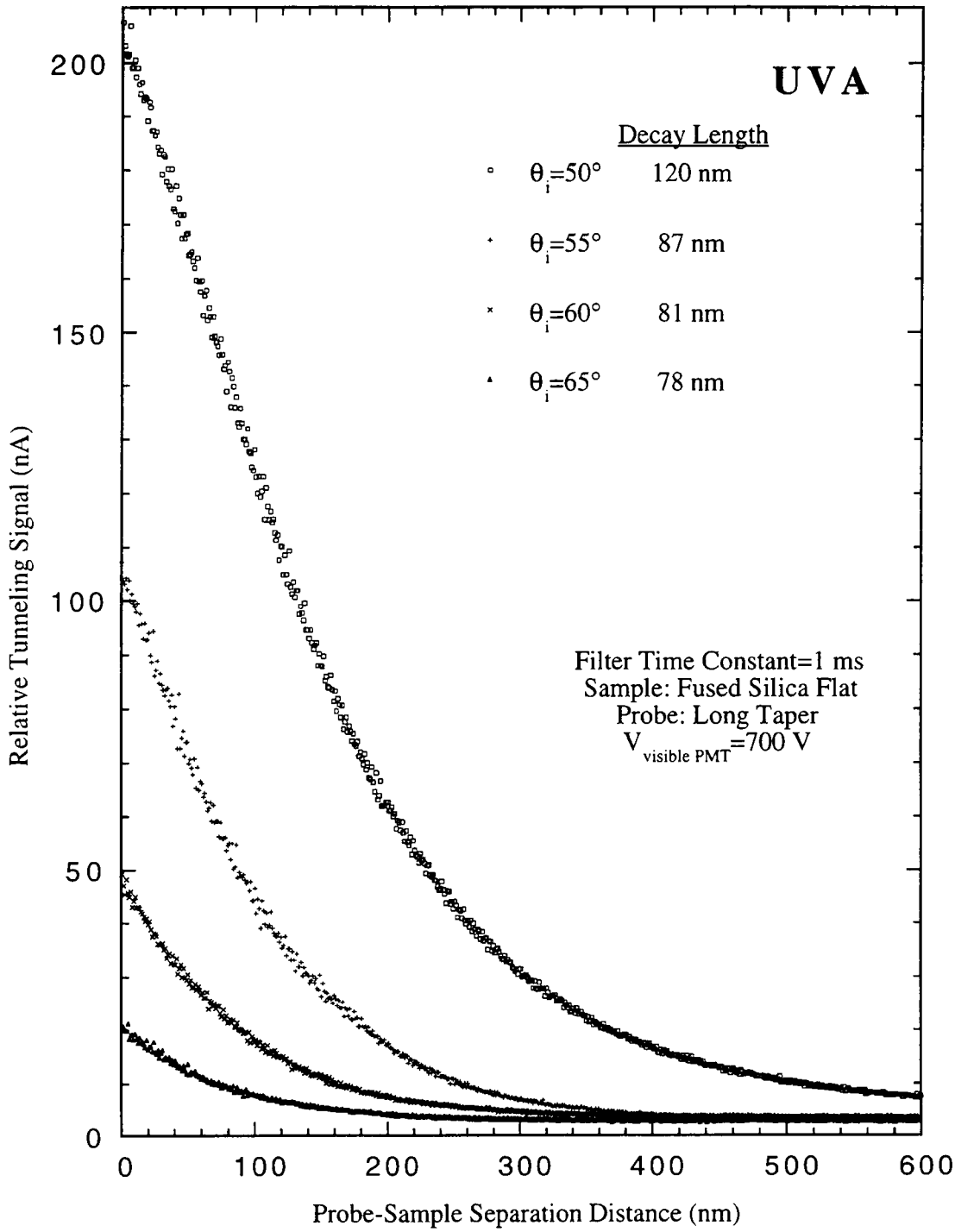


Figure II.19. UVA Tunneling Magnitude for Varying Angle of Incidence. The decay length and magnitude of the tunneling signal decreases with increasing angle of incidence.

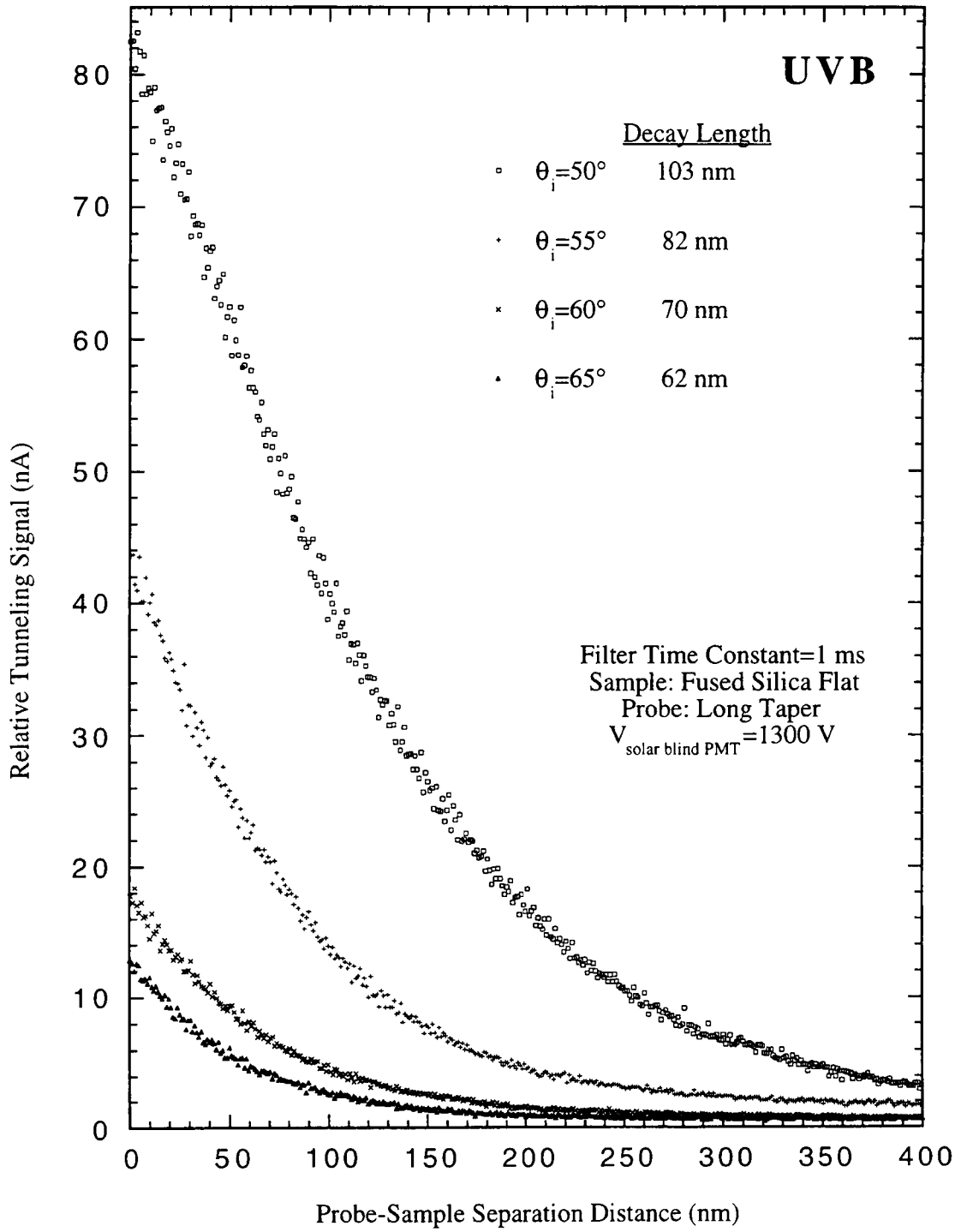


Figure II.20. UVB Tunneling Magnitude for Varying Angle of Incidence. The decay length and magnitude of the tunneling signal decreases with increasing angle of incidence.

magnitude of the tunneling signal with increasing incident angle. Several factors contribute to the decrease in signal magnitude. The flux of light incident on the sample-air interface and the effective detection area of the probe will decrease with increasing incident angle. An additional factor contributing to the decrease in magnitude is the poor launch capability of the fiber optic probe at high angles of incidence. When the probe and prism have similar indices of refraction, light generated in the tip region of the probe will have the same angle relative to the fiber optic axis as the angle of incidence to the sample-air interface. The higher angles of transmitted light are less capable of being gathered by the probe into the acceptance cone of the fiber optic.

Although the theoretical plots in **Figure II.15.a.** and the experimental data in **Figure II.16.** were both generated with θ_i=50°, the theoretical decay lengths are much smaller than the experimental decay lengths. The reason for this discrepancy is that the lens focusing the light onto the prism creates a conical beam of light with a continuum of incident angles. θ_i=50° represents the angle of the central axis of the optical lens focusing system relative to the normal of the sample-air interface. For the geometry of the experimental apparatus the actual incident angles range from θ_i-7° to θ_i+7°, and the observed signal is the sum of the signals measured over this angular range. However, as shown in **Figures II.19. and II.20.**, the magnitude of the tunneling signal is larger for smaller angles of incidence; therefore, the light incident at angles from θ_i-7° to θ_i affects the observed signal more than light incident from θ_i to θ_i+7°. The observed evanescent field decay length is between the evanescent field decay lengths for θ_i-7° and θ_i as shown in **Figure II.21.**

D.2. Probe and Sample Effects on Tunneling Signals

The highly sensitive dependence of the tunneling signal on the probe-sample separation distance makes topographical imaging possible, and the tunneling signal is

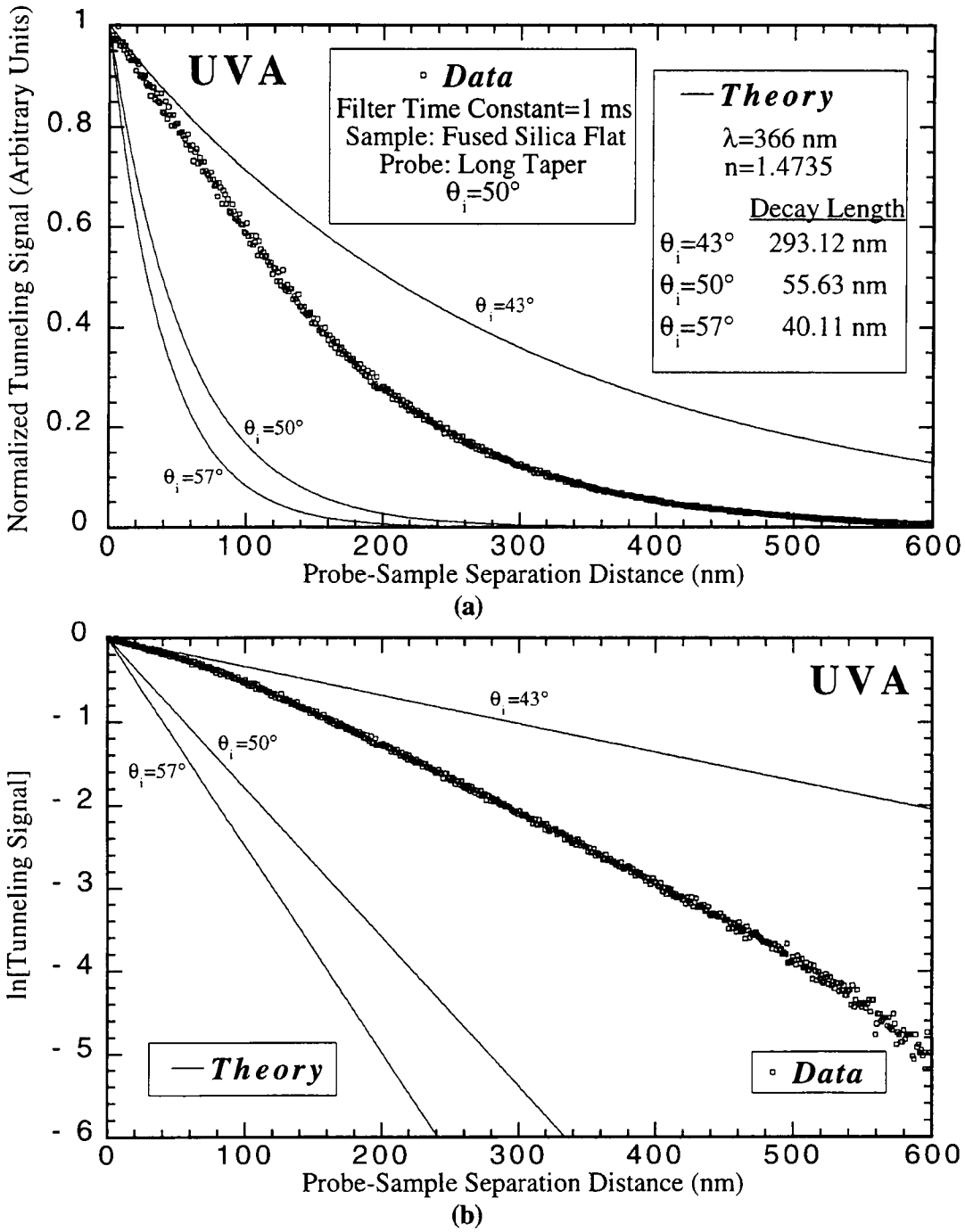
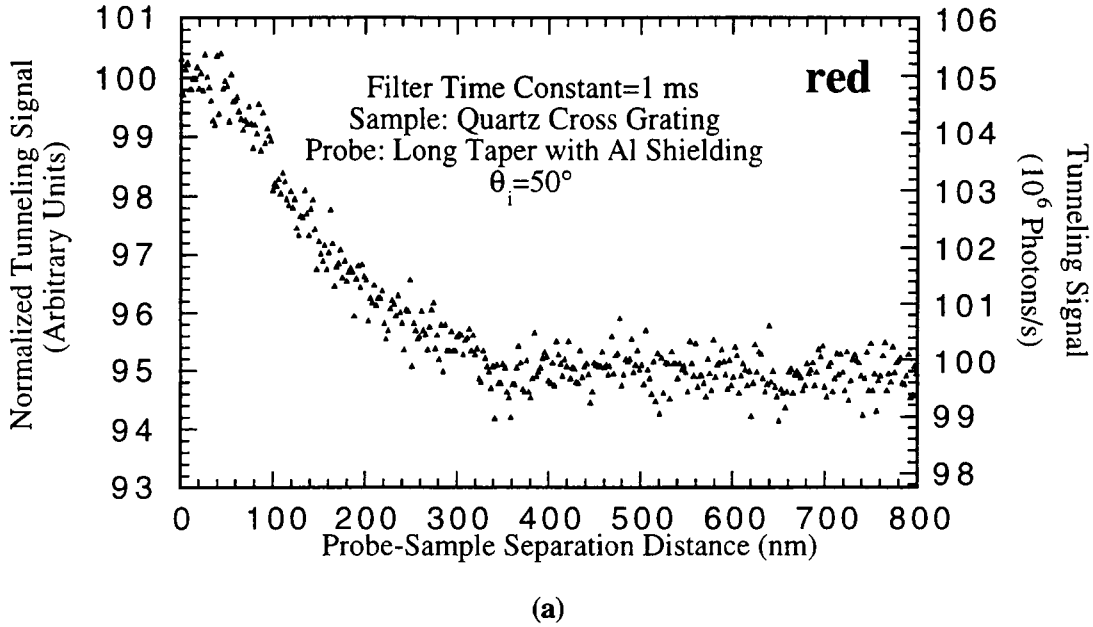


Figure II.21. Evanescent Field Decay Length Variation Over Incident Angle Distribution. **(a)** Linear and **(b)** semilog plots showing the variation in evanescent field decay lengths associated with the distribution of incident angles (θ_i-7° to θ_i+7°) produced by the experimental arrangement. The data show a decay length closer to the decay length of smaller incident angles where the magnitude of the tunneling signal is greater.

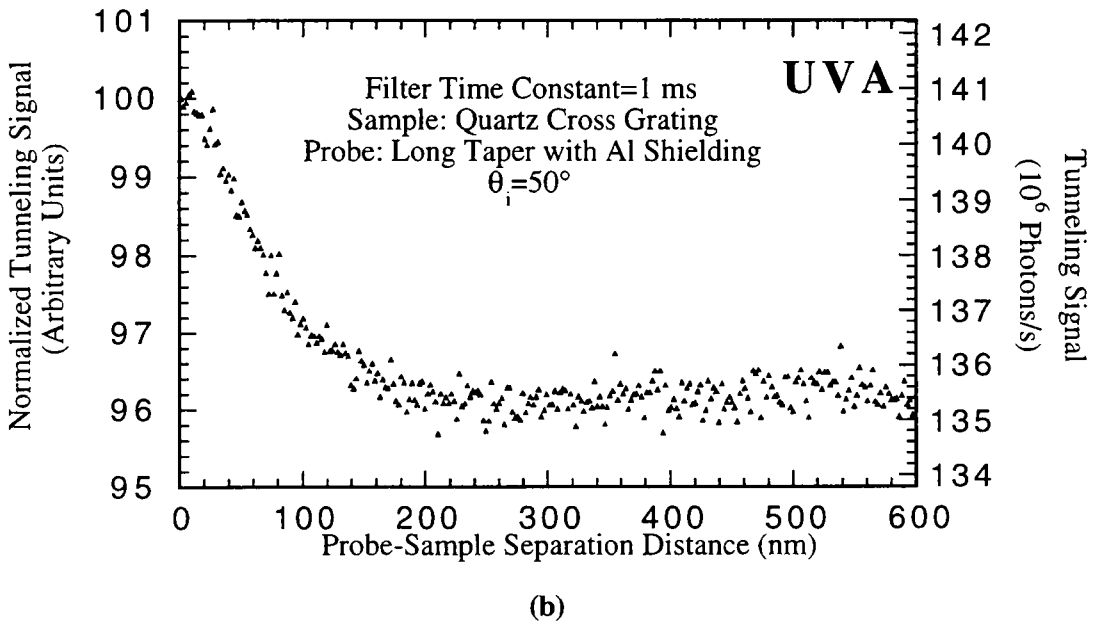
indeed dependent on the sample and probe structure. The shape of the probe will affect the magnitude, decay length, and signal-to-background level of the tunneling signal, and the lateral resolution limits are influenced by the size of the probe tip. The roughness of the sample will affect the signal-to-background level, and the optical properties of the sample will affect the magnitude and decay length of the tunneling signal. Here data is presented to show the contrast between tunneling signals obtained with different probes and samples.

Although the procedures presented in **Section II.C.2.** improve the consistency of probe production, each probe has a unique structure that cannot be reproduced. Because of the variation in tip size and probe structure of probes produced in the same manner, tunneling signals will differ under similar experimental conditions. The data shown in **Figures II.16., II.17., and II.18.** demonstrate a small difference in the tunneling signal obtained by two similar, but not identical, probes. The tunneling signals in **Figure II.16.** were obtained with one long-taper probe, and the tunneling signals in **Figures II.17. and II.18.** were obtained with another long-taper probe. In each case the sample was a fused silica flat. The decay lengths obtained at θ_i=50° with UVA and UVB spectra are slightly different due to the small differences in the two long-taper probes.

A flat fused silica sample has a relatively small amount of surface roughness when compared with other samples more commonly imaged with the PSTM. The amount of surface roughness on a sample affects the background signal detected by the probe. Rough sample structure causes light to scatter at the TIR interface and travel to the probe where the scattered light signal competes with the FTIR signal. **Figure II.22.** shows tunneling signals obtained with a long-taper probe and a quartz cross grating in the red and UVA spectral regions. The cross grating represents the opposite extreme in sample roughness from the fused silica flat, and the background signal detected by long-taper probes is dramatically different. The signal-to-background ratio in **Figure II.19.** is greater than 100:1 for θ_i=50° in the UVA region, but the signal-to-background ratio in



(a)



(b)

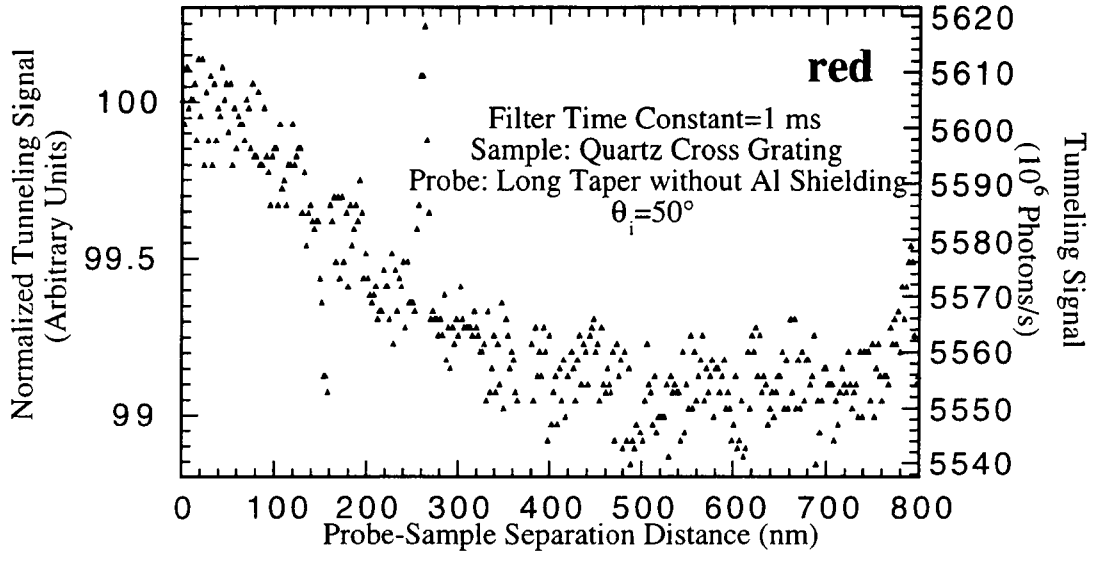
Figure II.22. Data from Long-Taper Probe with Aluminum Shielding. Tunneling signals for red(**a**) and UVA(**b**) spectra collected by a long-taper probe with Al shielding. Note the reduced scatter among data points at gaps less than 100 nm.

Figure II.22. is approximately 4:100. Thus, a factor of 2500 exists between the signal-to-background ratios for a fused silica flat and a quartz cross grating sample.

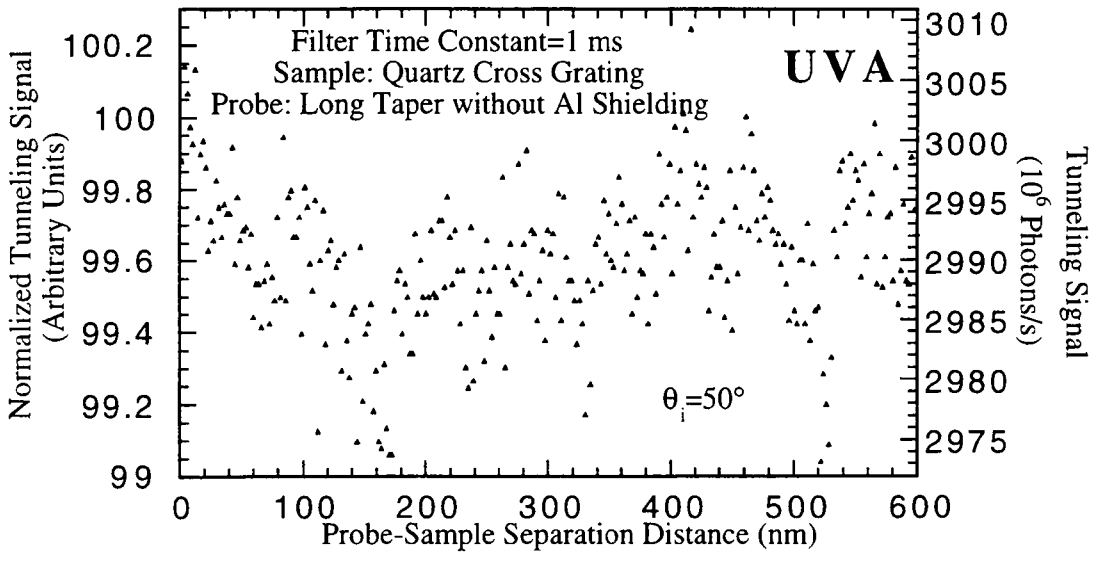
The Al shielding applied to the outer surface of the probe effectively reduces collection of the scattered light and improves the signal-to-background ratio. In contrast to the Al shielded long-taper probe of **Figure II.22.**, **Figure II.23.** shows tunneling signals obtained with the quartz cross grating and a long-taper probe without Al shielding. Although the total amount of photons collected by the probe without Al shielding is much larger than the number of photons collected by the probe with Al shielding, the signal-to-background ratio is much worse.

In addition to the importance of the Al shielding, two important details are demonstrated by **Figures II.22. and II.23.** First, the signal-to-background ratio has a large impact on the signal-to-noise ratio. In **Figure II.23.** the signal-to-noise ratio is much larger than in **Figure II.22.** because the noise of the background signal becomes relatively larger for larger signal-to-background ratios. Also, the signal-to-background ratio becomes worse with decreasing wavelength since light scatters with an efficiency inversely proportional to λ^4. The UVA signal in **Figure II.23.b.** is not acceptable for imaging purposes since the tunneling signal is obscured by the noise of the background signal. Even though the red signal in **Figure II.23.a.** could be employed for imaging purposes, noise spikes in the background noise or other fluctuations in the background signal can easily cause probe-sample contact in feedback operation.

Figure II.24. shows data obtained under the same conditions as **Figure II.22.** except that the probe is an extreme-taper probe. The larger cone angle of the taper region of the extreme-taper probe provides a better signal-to-background ratio. As a result, the signal-to-noise ratio is also improved. As the data clearly demonstrate extreme-taper probes collect more light and offer better signal-to-background, and thereby better signal-to-noise, ratios. The choice of probe type depends on several factors, but extreme-taper probes are the clear choice for rough samples that require better tunneling signal quality.

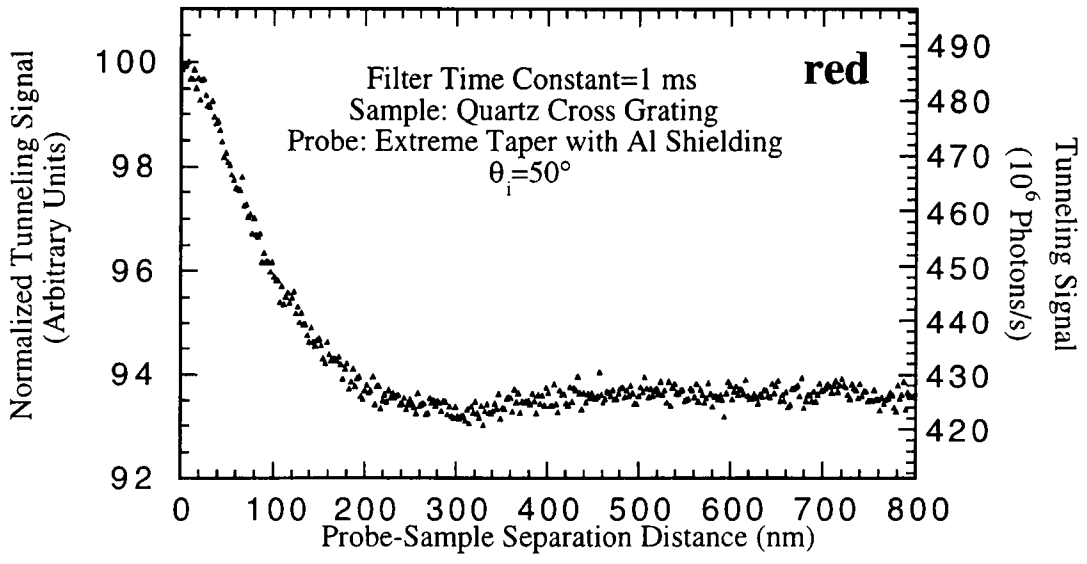


(a)

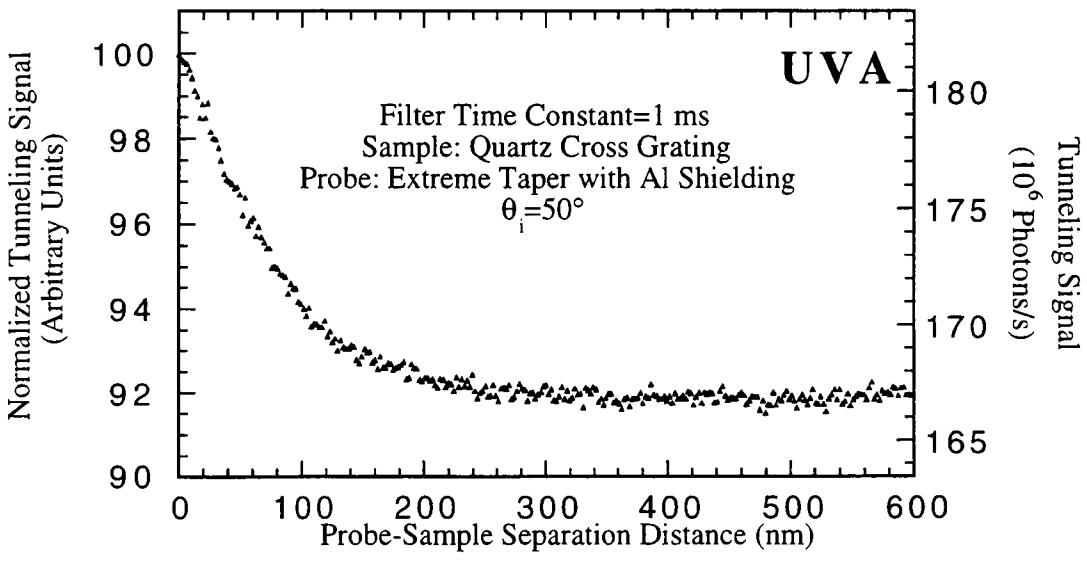


(b)

Figure II.23. Data from Long-Taper Probe without Aluminum Shielding. Tunneling signals for red(**a**) and UVA(**b**) spectra collected by a long-taper probe without Al shielding.



(a)



(b)

Figure II.24. Data from Extreme-Taper Probe with Aluminum Shielding. Tunneling signals for red(**a**) and UVA(**b**) spectra collected by an extreme-taper probe with Al shielding.

It should be noted that there is some uncertainty in the probe-sample contact position. The change in the tunneling signal when probe-sample contact occurs varies greatly with each probe, sample, and mounting position. Generally, some discontinuity exists at the point of contact; however, it is not always easy to detect the discontinuity. **Figure II.25.** shows tunneling signals for scans where the probe was allowed to make contact with the sample. The data also shows the noise level for with a filter time constant of 0.01 ms. Although the noise level of any signal can be suppressed by filters, data is normally taken with filter time constants $\leq$1 ms to insure that probe and signal response allows full data contrast. For feedback mode operation filter time constants must be $\leq$0.01 ms to avoid resonant oscillations in the control of the probe.

Theoretically calculating the tunneling signal obtained by a probe is a difficult task. The transmission from one medium to another medium is solved in a straightforward manner when the two media are separated by a planar slab. (**Appendix B.**) However, accounting for the shape of the probe makes calculations of FTIR from a planar interface to a probe difficult; the boundary conditions yield complicated equations that include complex components arising from the imaginary character of the evanescent wave. Additionally, comparisons between theoretically determined sample-to-probe transmissions and experimental tunneling signals are deceptive since a complete theoretical estimate of the tunneling signal must include the collection efficiency of the optical fiber. Nonetheless, basic calculations of probe efficiencies and effective probe diameters have been made with simple approximations.[II-13,II-4] One such calculation is presented in **Appendix C.** Although no rigorous theory has been developed, some understanding of the signals expected from certain probe geometries can be gained from these approximate theories.

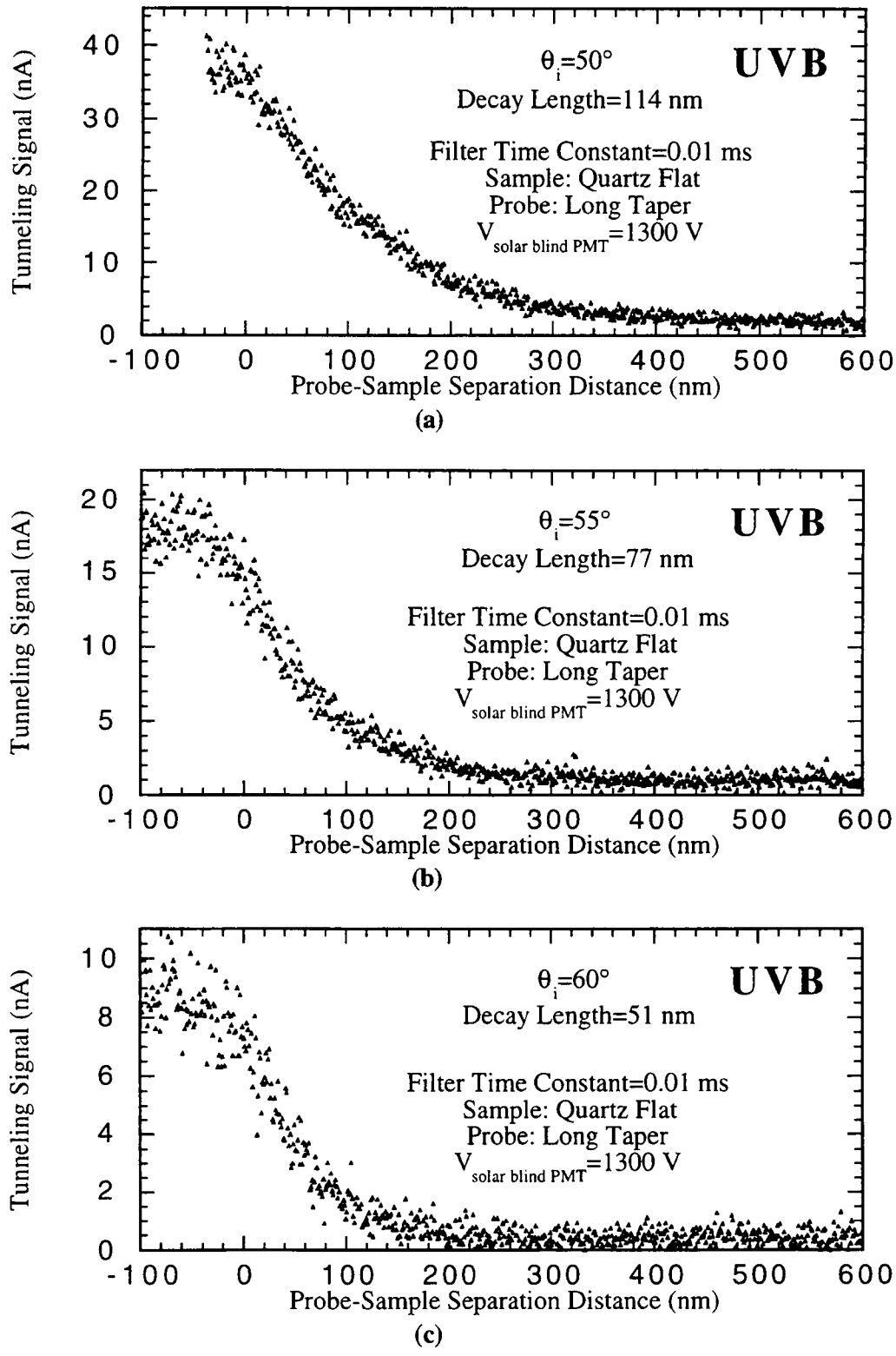


Figure II.25. Probe-Sample Contact in Tunneling Signals. UVB tunneling signals taken at **(a)** θ_i=50°, **(b)** θ_i=55°, and **(c)** θ_i=60° showing probe-sample contact.

E. Imaging

The main purpose of the study presented here is to show that the resolution of the UVPSTM depends on the wavelength of light. Images were taken of a quartz cross grating; the grating provided a consistent sample with sharp edges that gave high spatial contrast. Additionally, the index of refraction of quartz does not deviate much over the light spectrum used in this study. Thus, resolution effects from varying refractive indices are suppressed. An SEM image and an AFM image of the cross grating studied are shown in **Figures II.26. and II.27.**, respectively. The grating was coated with silver for observation in the SEM.

Since the resolution of the PSTM is dependent on probe size, comparisons between the resolution of the PSTM at different wavelengths were made using the same probe for each set of images. **Figures II.28., II.29., II.30., and II.31.** show sets of images of the cross grating taken with different spectral regions of light. Images in each set were taken with the same probe, but different probes were used for each different set of data. The images were not filtered, but the background plane was subtracted from the image. Only short-taper and extreme-taper probes were used to take data with the grating. The large scattering signal prevented the use of long-taper probes.

Each set of images in **Figures II.28., II.29., II.30., and II.31.** show resolution improvement as the wavelength of light becomes smaller. Images taken with the red spectrum do not distinguish the square shape of the grating structure well; however, images taken with the blue, red, and UVB do distinguish the square structure. Improvements in resolution are minimal for changes from the blue to UVA spectra, but some improvement in resolution does occur.

Imaging of the grating is difficult in the UVB spectral region. The increased scattered light signal makes controlling the probe in the evanescent field difficult. The noise of the arc lamp caused the probe to lose the feedback signal level as the image in

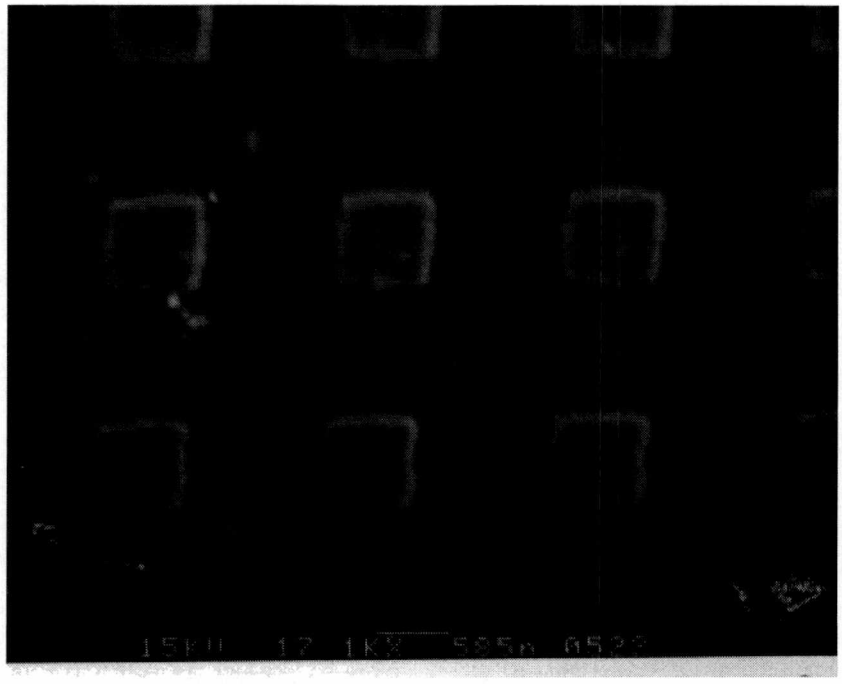


Figure II.26. SEM Image of Silver-Coated Quartz Cross Grating. Scanning electron microscope image of quartz cross grating. The bar represents 585 nm.

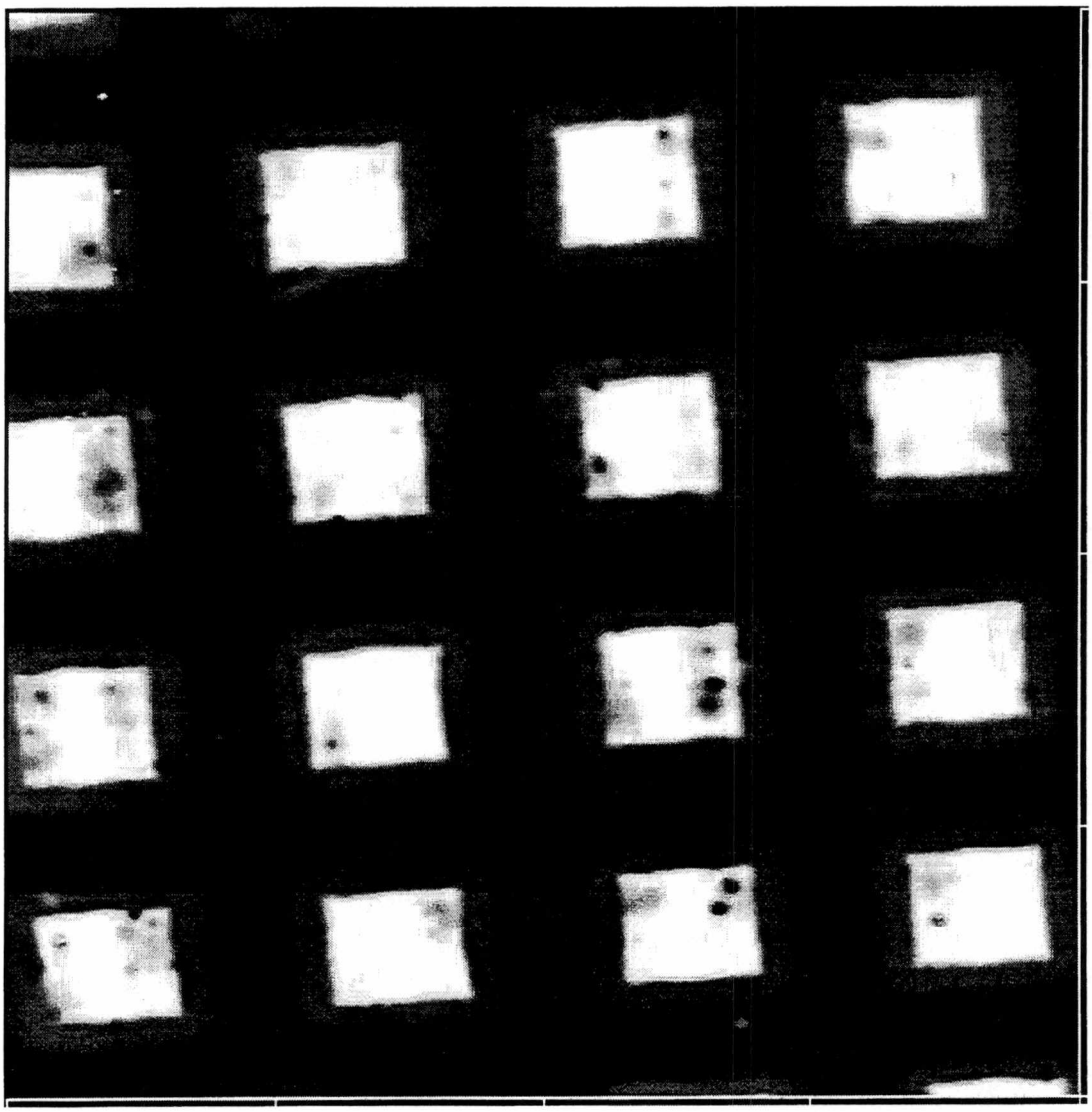
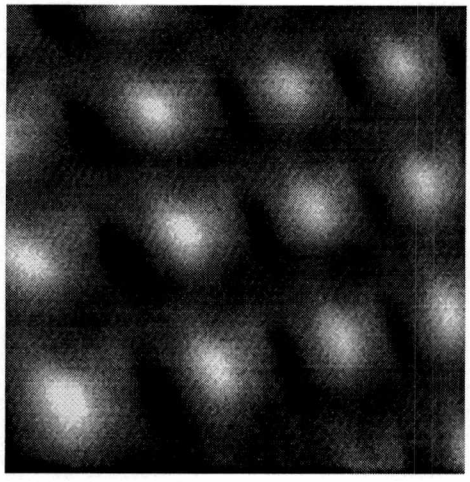
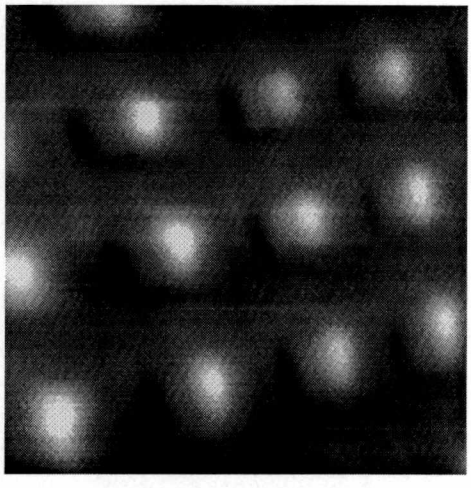


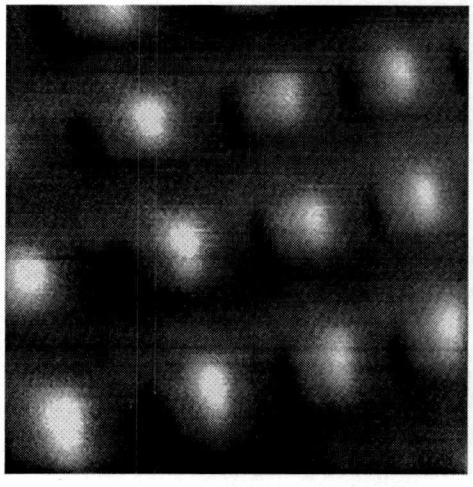
Figure II.27. AFM Image of Quartz Cross Grating. Atomic force microscope image of quartz cross grating. The image is 8 μm by 8 μm, and the gray scale ranges from 0 to 120 nm.



(a)

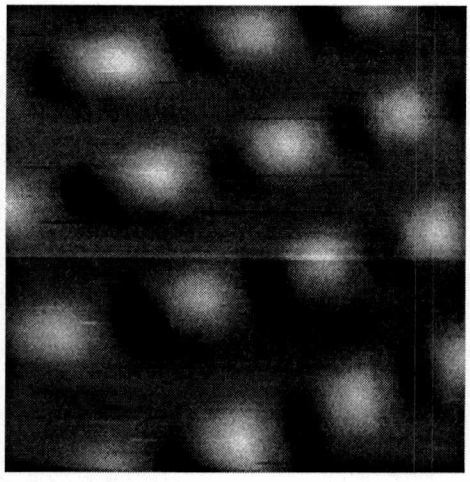


(b)

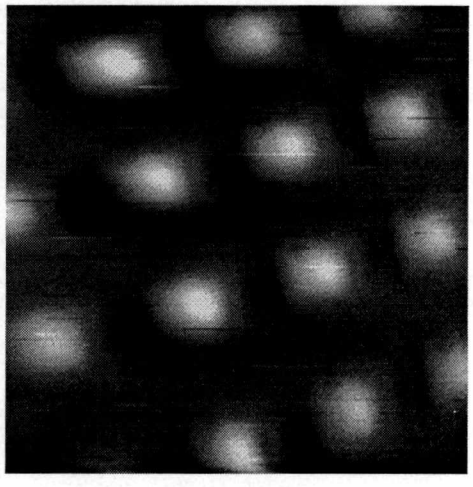


(c)

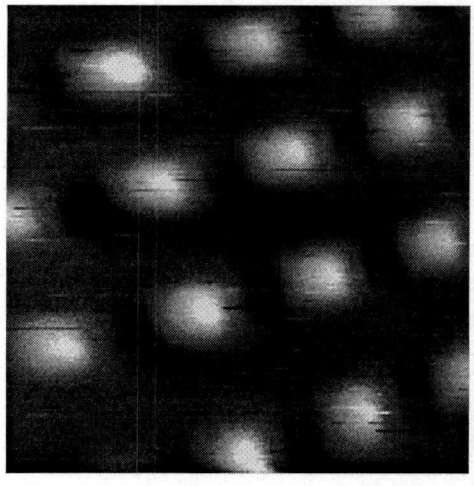
Figure II.28. Variation of Wavelength I. Raw unfiltered images in the **(a)** red, **(b)** blue, and **(c)** UVA spectral regions. θ_i=50°; short-taper probe. Each image is 7 μm by 7 μm. The square pattern of the cross grating is distinguished more clearly with decreasing wavelength.



(a)

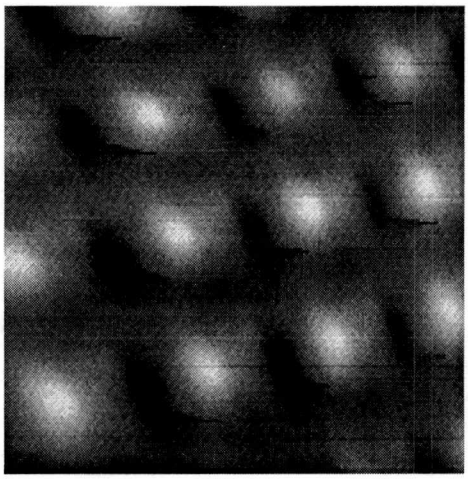


(b)

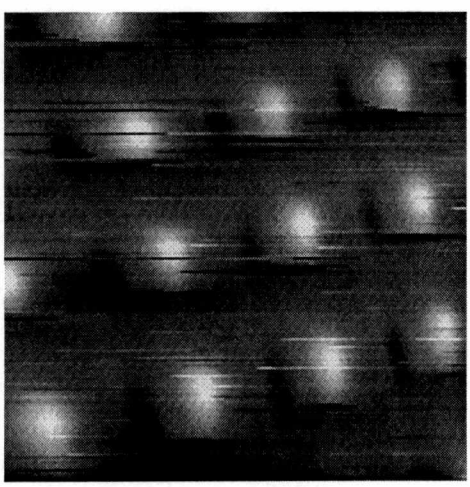


(c)

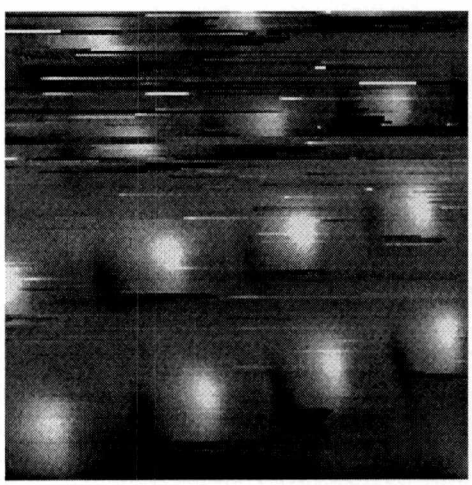
Figure II.29. Variation of Wavelength II. Raw unfiltered images in the **(a)** red, **(b)** blue, and **(c)** UVA spectral regions. θ_i=50°; extreme-taper probe. Each image is 7 μm by 7 μm. The square pattern of the cross grating is distinguished more clearly with decreasing wavelength.



(a)



(b)



(c)

<u>Figure II.30.</u> Variation of Wavelength III. Raw unfiltered images in the **(a)** red, **(b)** blue, and **(c)** UVA spectral regions. θ_i=50°; short-taper probe. Each image is 7 μm by 7 μm. The square pattern of the cross grating is distinguished more clearly with decreasing wavelength.

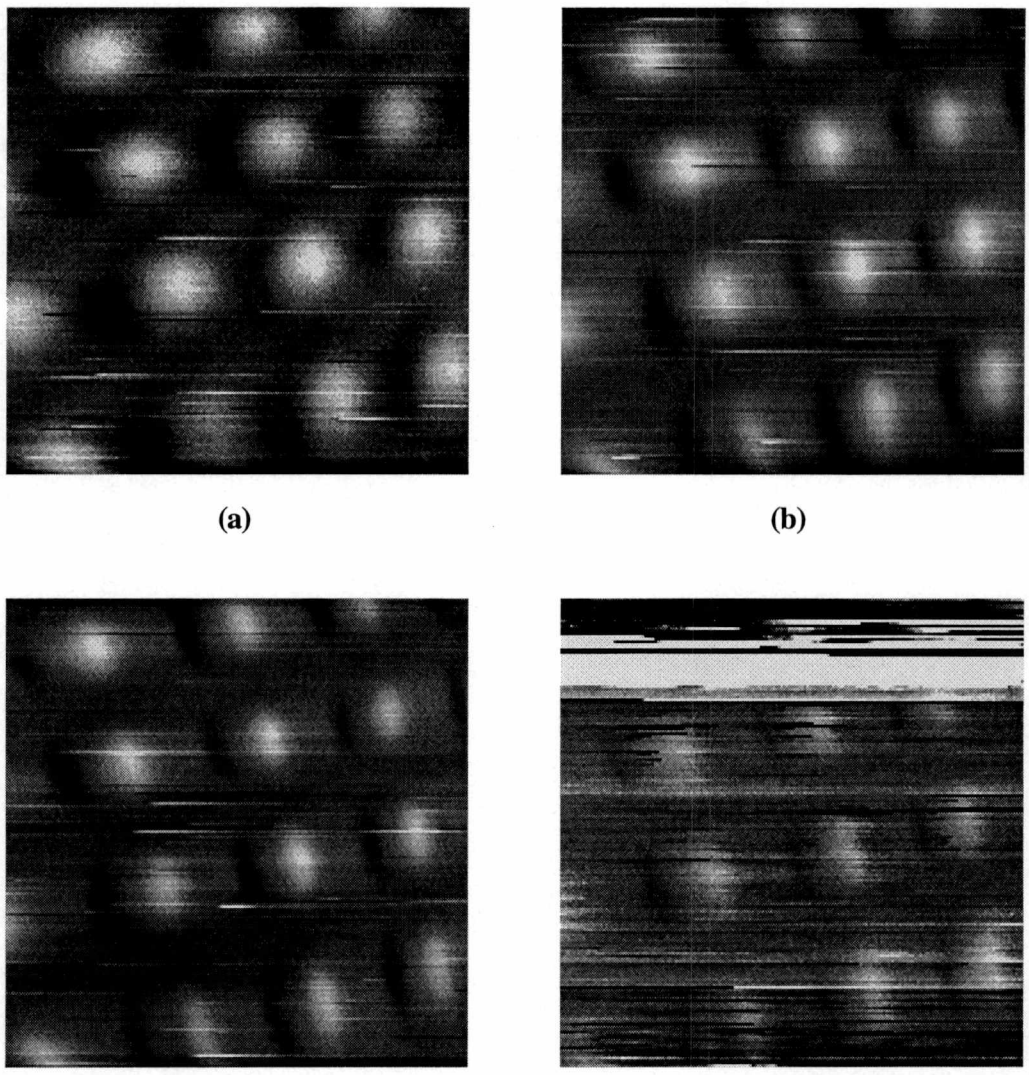


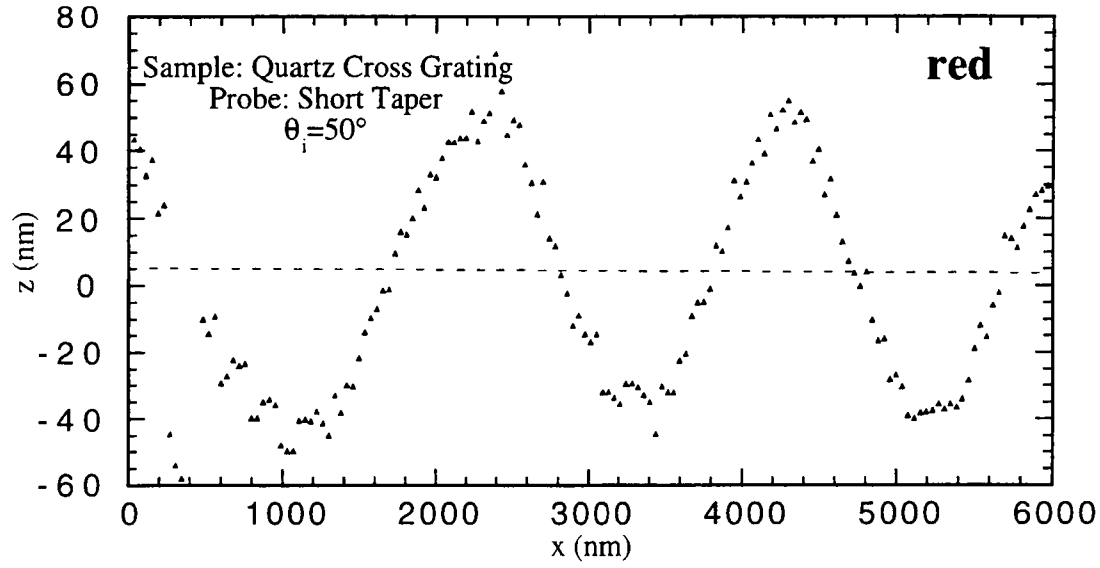
Figure II.31. Variation of Wavelength IV. Raw unfiltered images in the **(a)** red, **(b)** blue, **(c)** UVA, and **(d)** UVB spectral regions. θ_i=50°; short-taper probe. Each image is 7 μm by 7 μm. The square pattern of the cross grating is distinguished more clearly with decreasing wavelength.

Figures II.31.d. shows. Despite the abundance of noise pulses and the incomplete image, the UVB spectral image does show the best resolution.

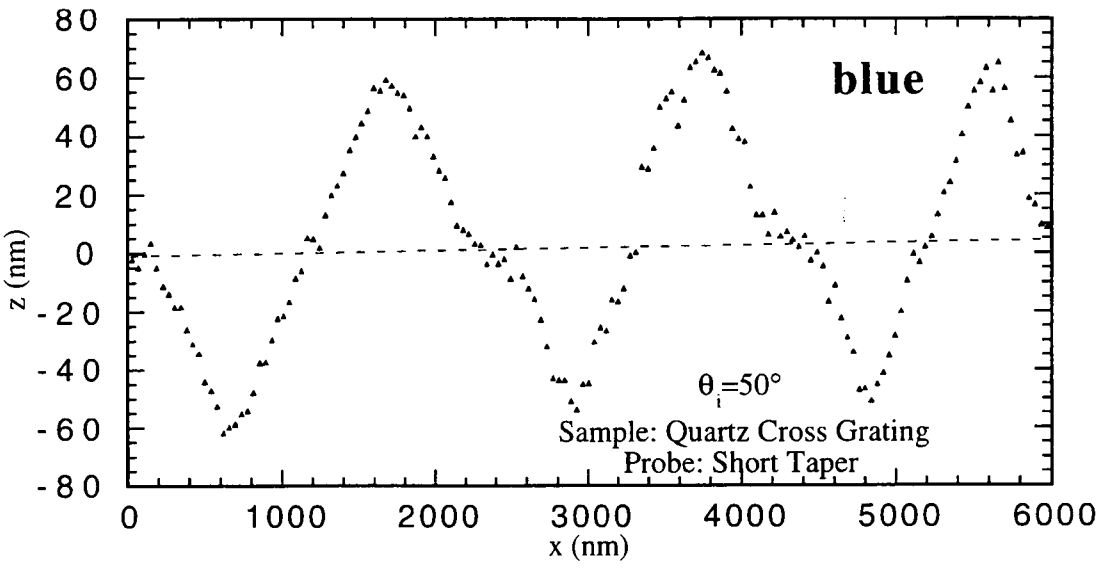
The change in resolution can be seen easier by examining cross sections of the three dimensional data. **Figures II.32., II.33., II.34., and II.35.** show height versus lateral position of the grating structure for the different spectra. The shape of the cross section changes from a sinusoidal pattern to the more accurate square well pattern as the wavelength of light changes from red to ultraviolet. Additionally, linear fits to the data shown in **Figures II.34. and II.35.** show that the imaged edge of the grating structure becomes sharper from the red to UVB spectra.

The exponentially decaying evanescent field helps to define the effective size of the probe tip. Since the decay length of the evanescent field becomes smaller as the wavelength of light becomes smaller, image resolution might improve due to smaller evanescent field decay lengths instead of, or in addition to, improvements from the smaller wavelengths. To investigate the resolution dependence on evanescent field decay length alone, images were taken with the same wavelength but at different incident angles of light. **Figure II.36.** shows images taken from θ_i=50° to θ_i=65° in the red spectral region. Some variation in the image resolution is seen for the different incident angles, but no definite improvement in resolution is observed. The decreasing signal strength with increasing incident angle may contribute to suppression of resolution improvements. Additionally, the shape of the probe tip should affect the amount of resolution improvement seen when the evanescent field decay length is changed. It is clear that improvement in resolution seen as the wavelength of light is reduced is due primarily to the higher spatial contrast of the evanescent wave which depends on the wavelength of light.

Another variable that contributes to resolution is the height of the probe above the sample surface. For large probe-sample separation distances the disturbances in the evanescent wave produced by the sample become less defined. Smaller probe-sample

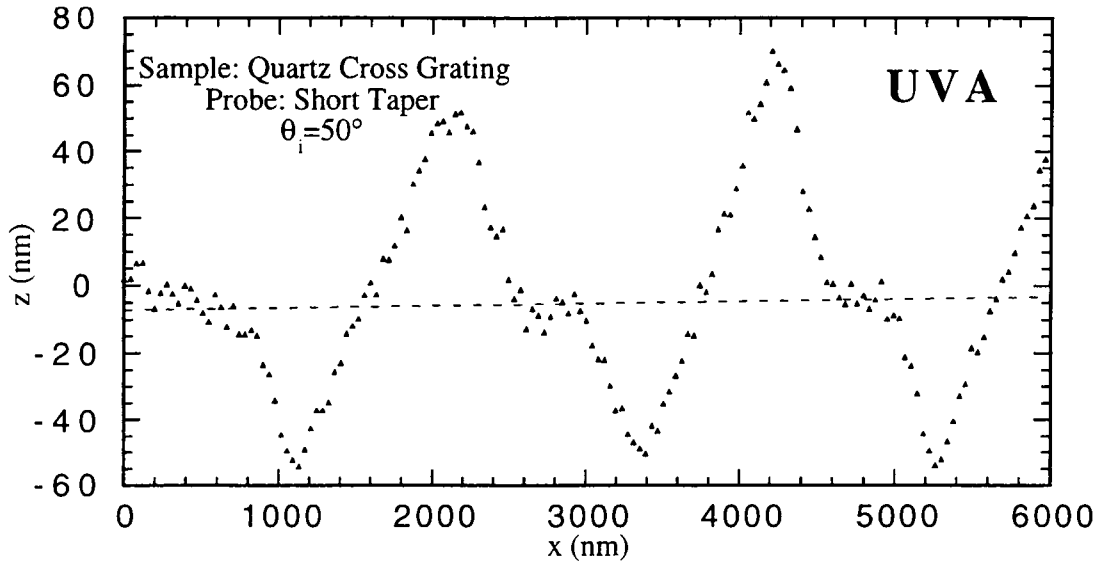


(a)

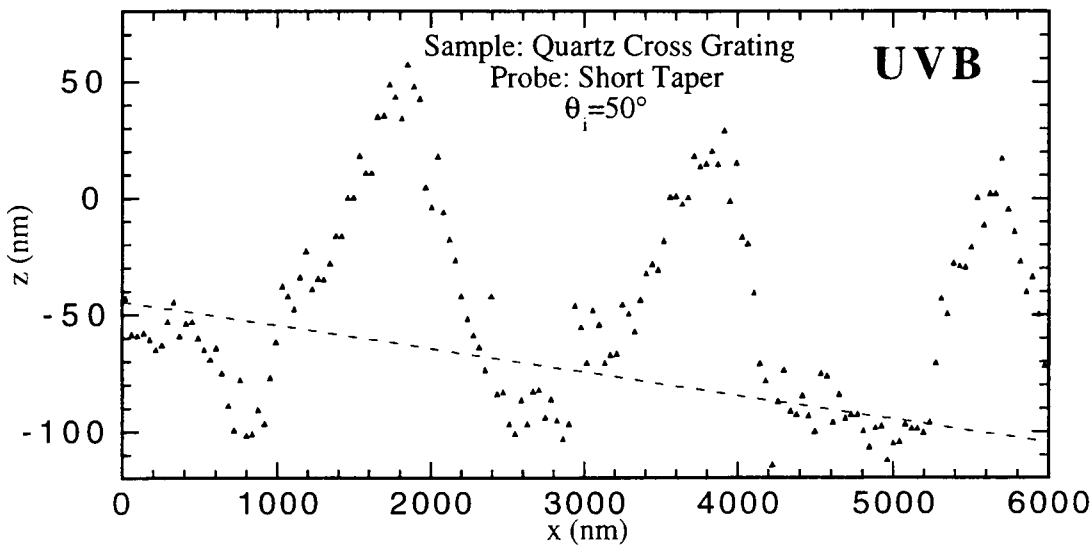


(b)

Figure II.32. Red and Blue Image Cross Sections. Cross sections of cross grating images in the **(a)** red and **(b)** blue spectra.

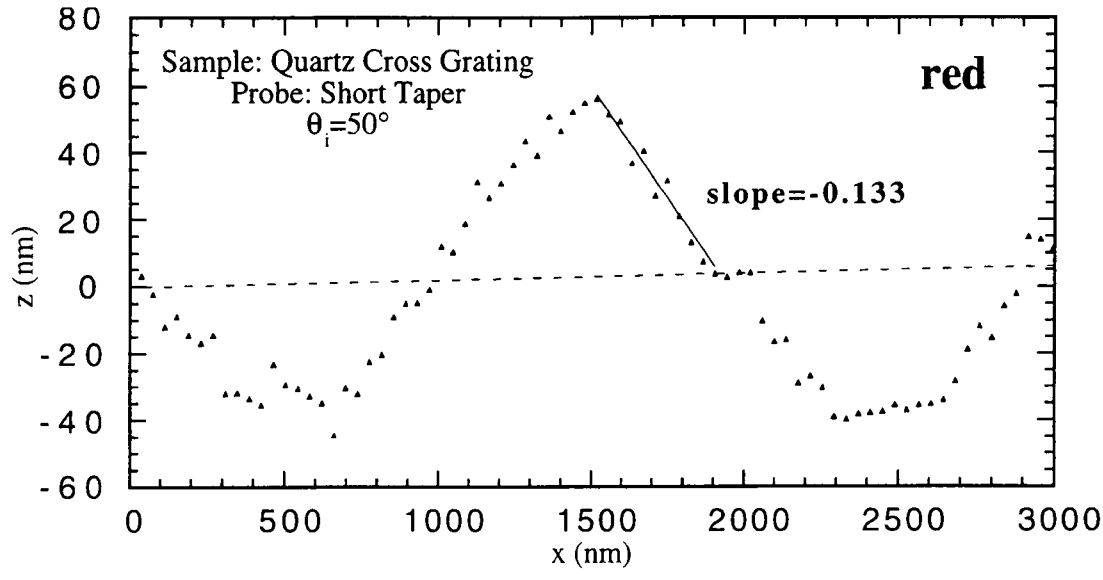


(a)

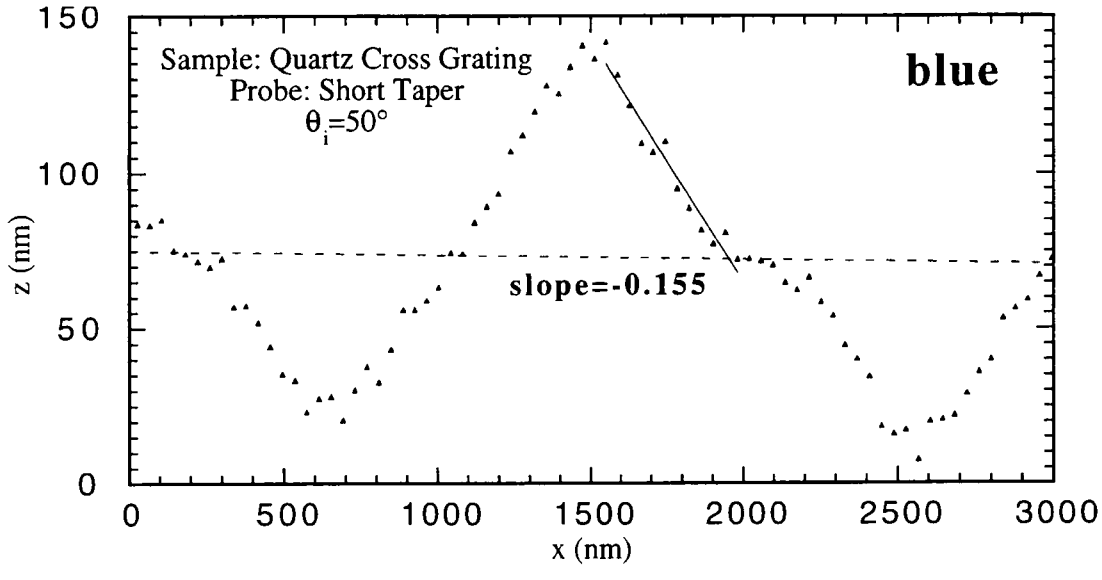


(b)

Figure II.33. UVA and UVB Image Cross Sections. Cross sections of cross grating images in the **(a)** UVA and **(b)** UVB spectra.

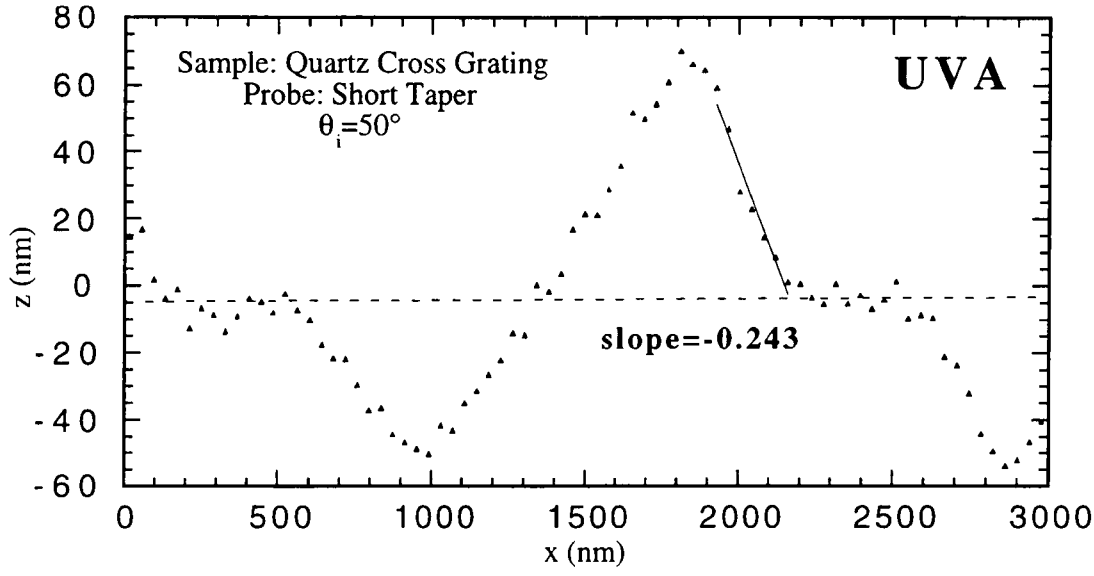


(a)

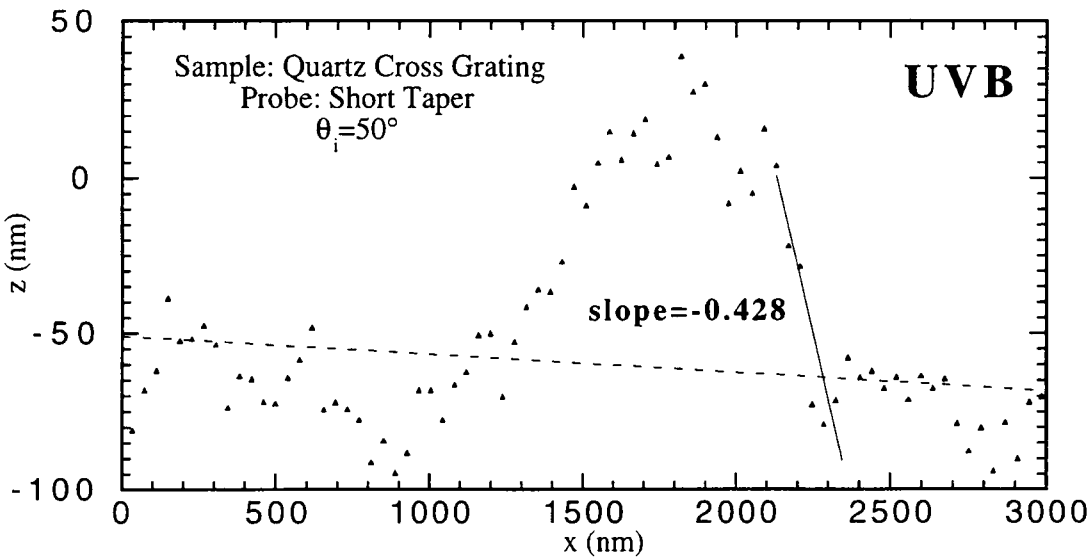


(b)

Figure II.34. Red and Blue Slope Measurements. Cross sections of cross grating images in the **(a)** red and **(b)** blue spectra with the slope of the linear fit showing the resolution of the profile.



(a)



(b)

Figure II.35. UVA and UVB Slope Measurements. Cross sections of cross grating images in the **(a)** UVA and **(b)** UVB spectra with the slope of the linear fit showing the resolution of the profile.

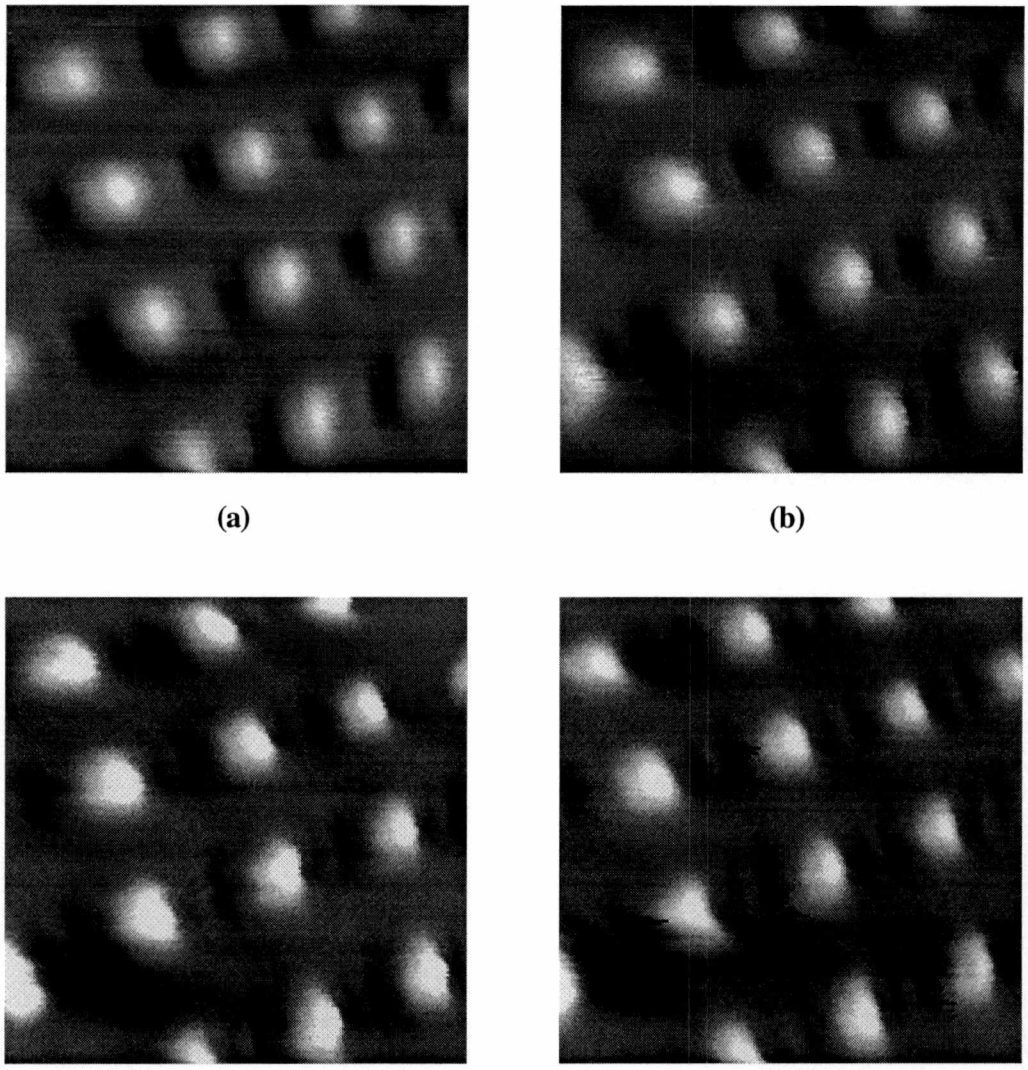


Figure II.36. Variation of Incident Angle. Raw unfiltered images in the red spectral region with incident angles(θ_i) of **(a)** θ_i=50°, **(b)** θ_i=55°, **(c)** θ_i=60°, and **(d)** θ_i=65°. Long-taper probe. Each image is 7 μm by 7 μm.

separations allow the probe to detect the modulated evanescent wave closer to the modulating source. **Figures II.37. and II.38.** show image resolution changes for different probe-sample separation distances in the red and UVA spectra, respectively. The images in the red spectral region show resolution becoming worse as the probe is scanned at distances further away from the sample. Eventually, the tunneling signal becomes too weak to compete with the background and noise signals, and the probe cannot be maintained at a constant height above the sample as **Figure II.37.d.** shows. The range of probe-sample separation for imaging in the UVA region is much smaller due to the smaller decay length of the evanescent field. Although the resolution decrease with probe-sample separation increase is not as noticeable as in the red spectrum data, there is still some decrease in the resolution. The dual capability of the UVPSTM to image with red and ultraviolet light helps to increase the useful life of probes since preliminary scans can be made with red light and larger probe-sample separation before scans in the ultraviolet with the probe closer to the sample surface are made.

F. Discussion

Determining the evanescent wave intensity on the surface of an arbitrary sample with a rigorous theoretical calculation is extremely difficult due to the complex math involved. However, close examination of UVPSTM data collected at different wavelengths of light from simple sample geometries provides insight into factors affecting the distribution of the evanescent wave on the surface of the sample. The UVPSTM images presented in **Section II.E.** reveal the evanescent wave intensity on the surface of a quartz cross grating. The simple geometry of the quartz cross grating combined with data of the evanescent wave intensity on the grating surface at different wavelengths of light provides an opportunity to speculate on the physical processes

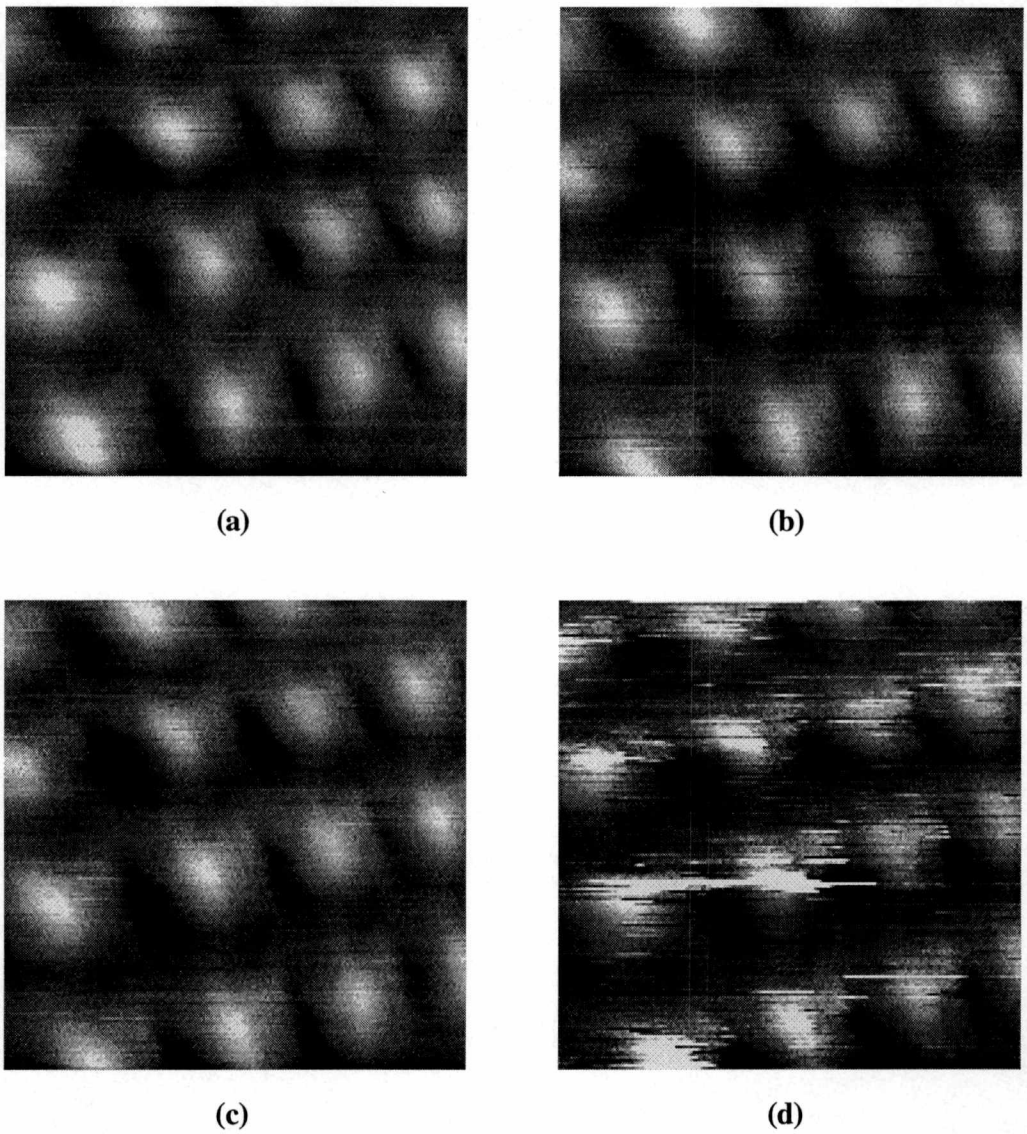


Figure II.37. Variation of Probe-Sample Separation Distance I. Raw unfiltered images in the red spectral region with probe-sample separation distances(z) of **(a)** $z=z_0$, **(b)** $z=z_0$+44 nm, **(c)** $z=z_0$+88 nm, and **(d)** $z=z_0$+210 nm. θ_i=50°; short-taper probe. Each image is 7 μm by 7 μm.

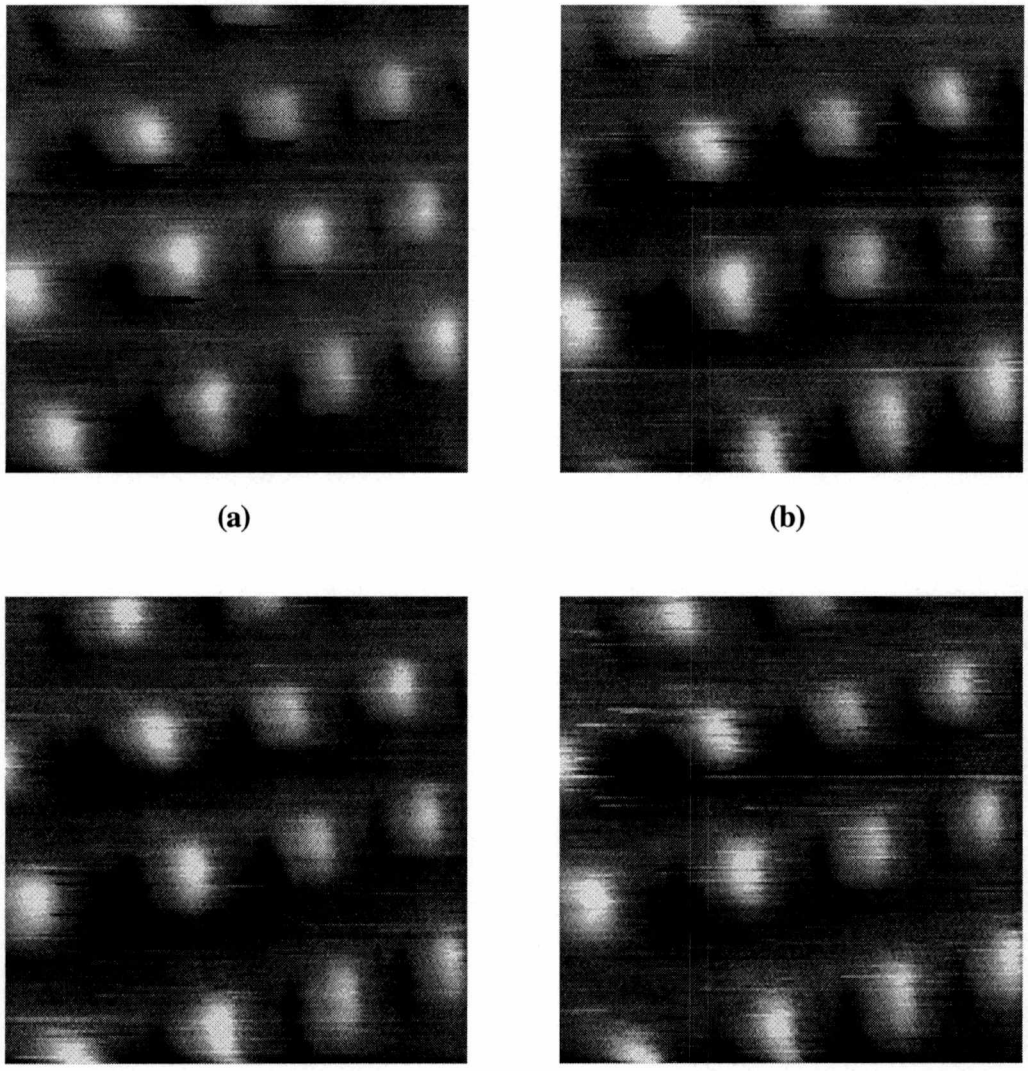


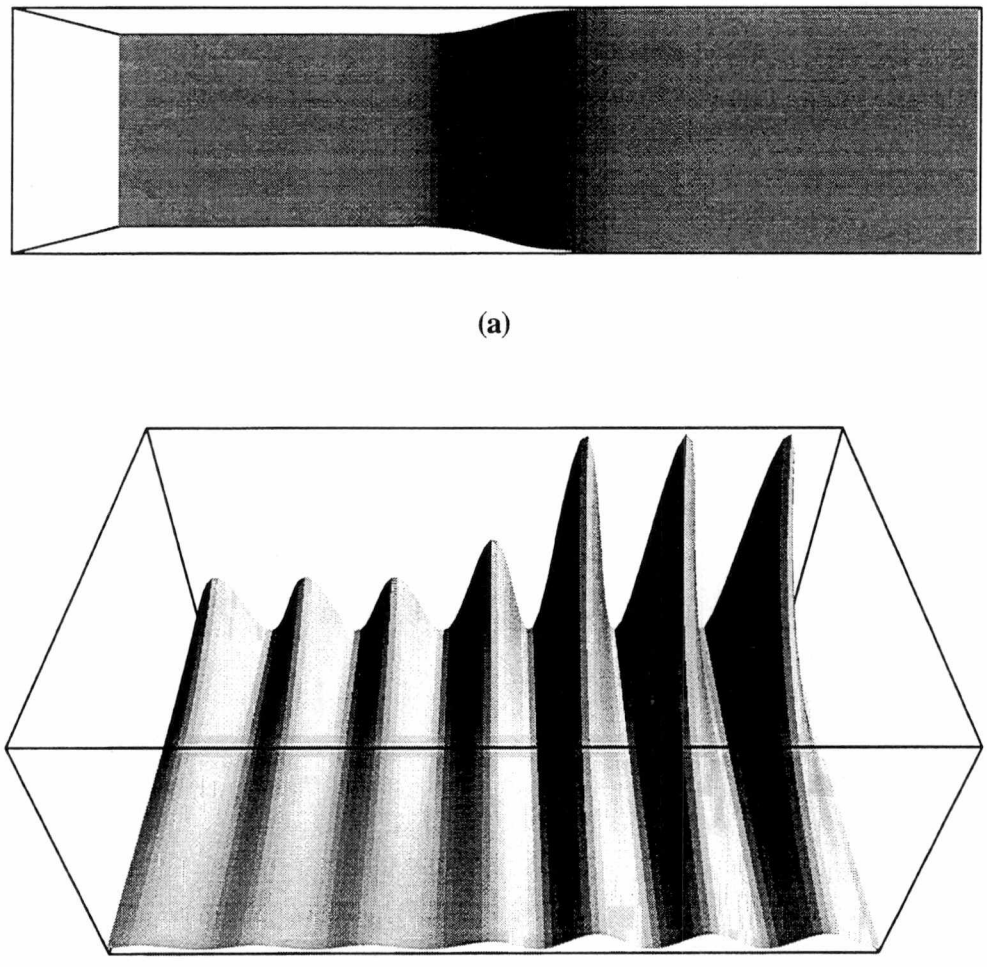
Figure II.38. Variation of Probe-Sample Separation Distance II. Raw unfiltered images in the UVA spectral region with probe-sample separation distances(z) of **(a)** $z=z_0$, **(b)** $z=z_0+22$ nm, **(c)** $z=z_0+66$ nm, and **(d)** $z=z_0+110$ nm. $\theta_i=50°$; short-taper probe. Each image is 7 μm by 7 μm.

involved in creating and changing the evanescent wave on the sample surface. Knowledge of the physical processes involved in the modulation of the evanescent wave by the sample leads to better image analysis and a better understanding of the physics of the PSTM.

Pictures showing characteristics of the evanescent wave are beneficial to understanding the evanescent wave. Once an understanding of the evanescent wave is gained, modulation of the evanescent wave by the sample surface is better understood. **Figures II.39., II.40., II.41., II.42., and II.43.** show three-dimensional images of a sample similar to the quartz cross grating and the evanescent field intensity of an evanescent wave produced on the surface. **Figures II.39.a. and II.40.a.** show a simple step-type structure generated with a hyperbolic tangent function. The step-type edge is similar to the edges of the quartz cross grating shown in **Figure II.27. Figure II.41.** shows a model sample created by combining several hyperbolic tangent functions; the model surface is similar to the actual surface of the quartz cross grating.

Figures II.39.b. and II.40.b. show "snap shots" of an evanescent wave traveling along the sample surface shown in **Figures II.39.a. and II.40.a.** These "snap shots" show the intensity of the evanescent field computed with equation **(II.1.)**. A sinusoidal function has been combined with equation **(II.1.)** to show the wave characteristic of the evanescent wave. The "snap shots" show the spatial plane that is normal to the sample surface and parallel to the lateral direction showing change in sample height; the third dimension of the plot expresses the evanescent field intensity. As expected the evanescent field intensity decreases exponentially with distance from the sample surface. The structure of the sample surface can be seen by examining a lateral cross section of the evanescent field intensity at a single point on the axis defined by the normal of the sample.

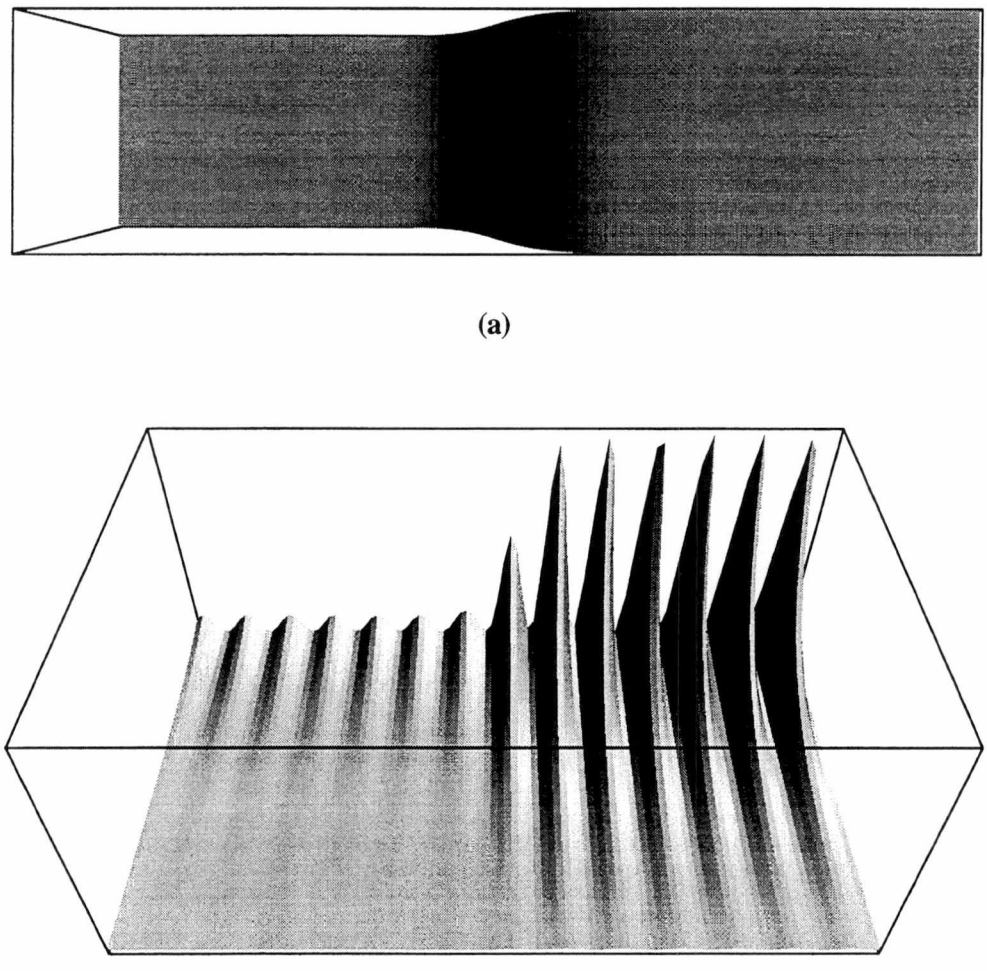
The difference between **Figures II.39.b. and II.40.b.** results from the wavelength of light used in the calculation of the evanescent field intensity. **Figure II.39.b.** was



(a)

(b)

Figure II.39. λ_e **Evanescent Wave on Step Surface.** **(a)** Three-dimensional image of a step-type surface generated with a hyperbolic tangent function, and **(b)** the intensity of an evanescent wave of wavelength λ_e produced on the surface. **(b)** shows the evanescent field intensity in a plane normal to the step-type surface. The image in **(b)** represents the evanescent wave at a single point in time. The evanescent wave travels along the surface shown in **(a)**.



(a)

(b)

Figure II.40. $\lambda_e/2$ Evanescent Wave on Step Surface. **(a)** Three-dimensional image of a step-type surface generated with a hyperbolic tangent function, and **(b)** the intensity of an evanescent wave of wavelength $\lambda_e/2$ produced on the surface. **(b)** shows the evanescent field intensity in a plane normal to the step-type surface. The image in **(b)** shows that the decay length of the $\lambda_e/2$ evanescent wave intensity in the direction normal to the surface shown in **(a)** is smaller than the λ_e case depicted in **Figure II.39.b.** Additionally, the evanescent field intensity along the surface varies more rapidly relative to the size of the structure for the shorter wavelength evanescent wave.

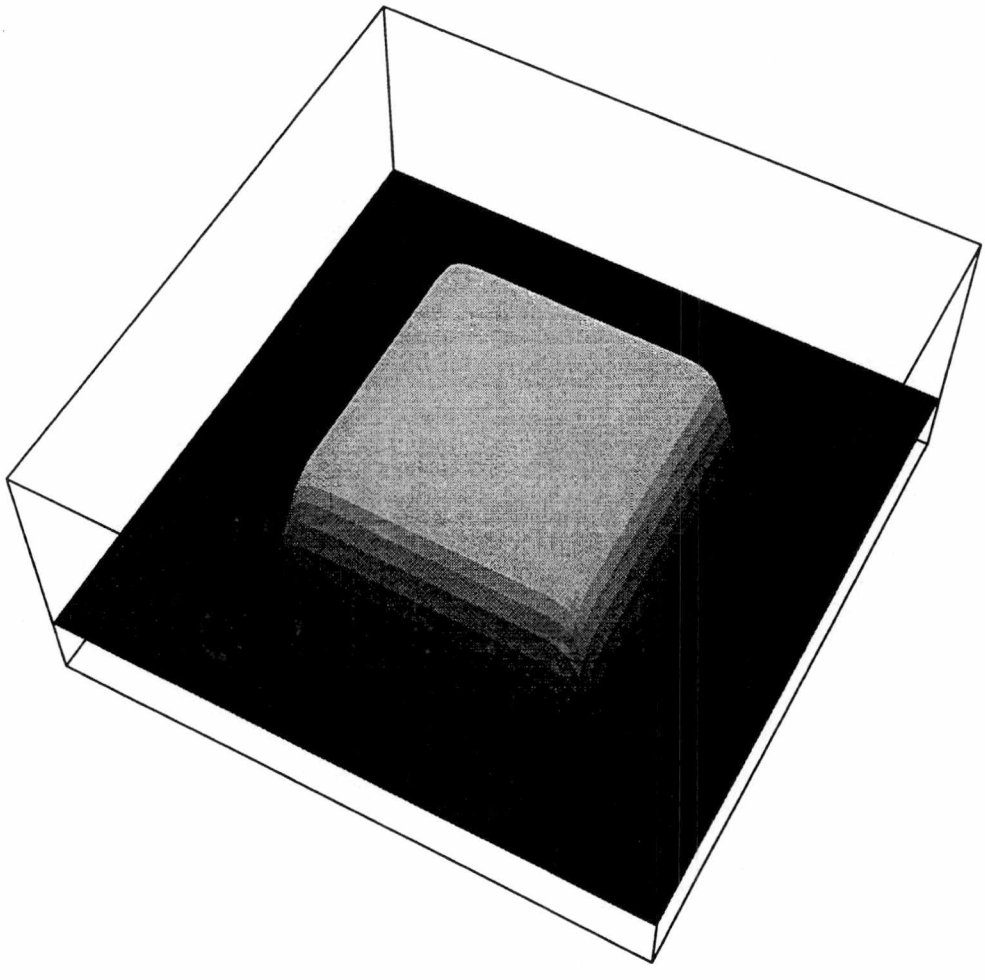


Figure II.41. Model Surface. Three-dimensional image of a surface similar to the surface of the quartz cross grating imaged with the UVPSTM.

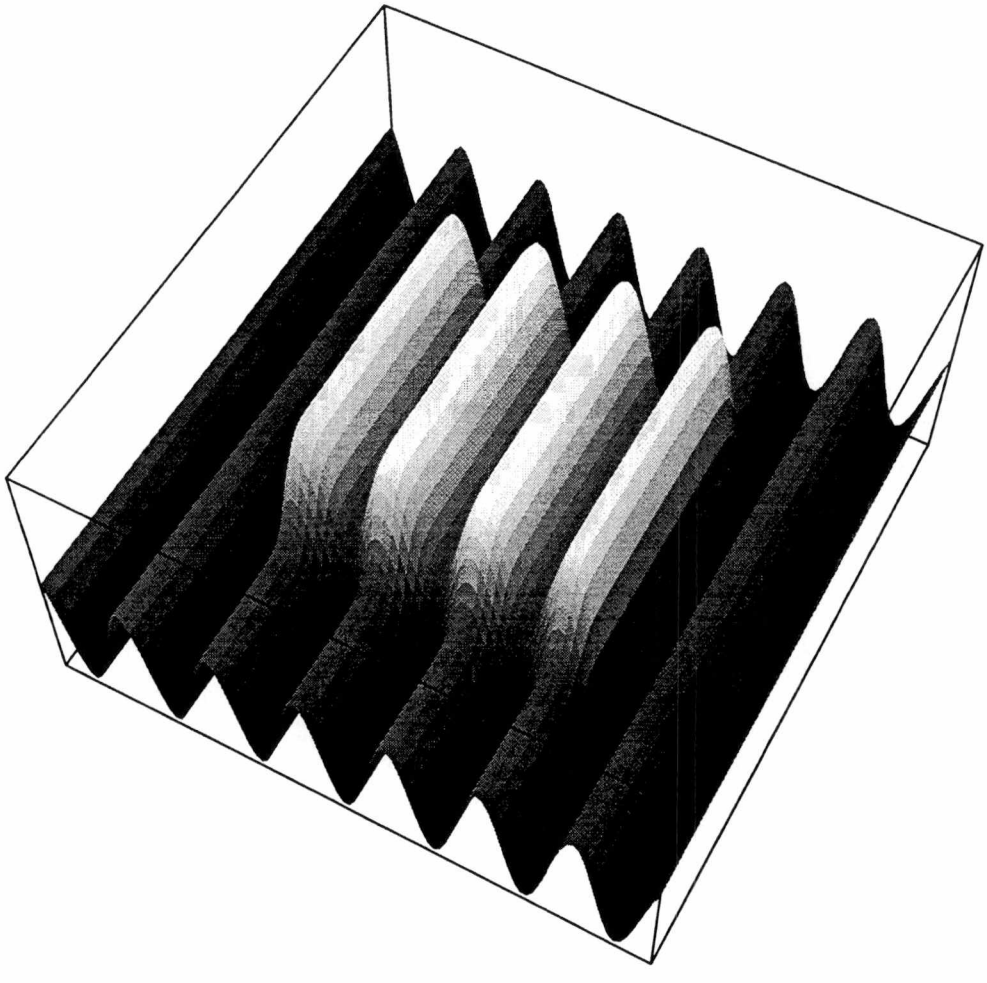


Figure II.42. λ_e **Evanescent Wave on Model Surface.** Three-dimensional image of an evanescent wave of wavelength λ_e on the model surface shown in **Figure II.41.**

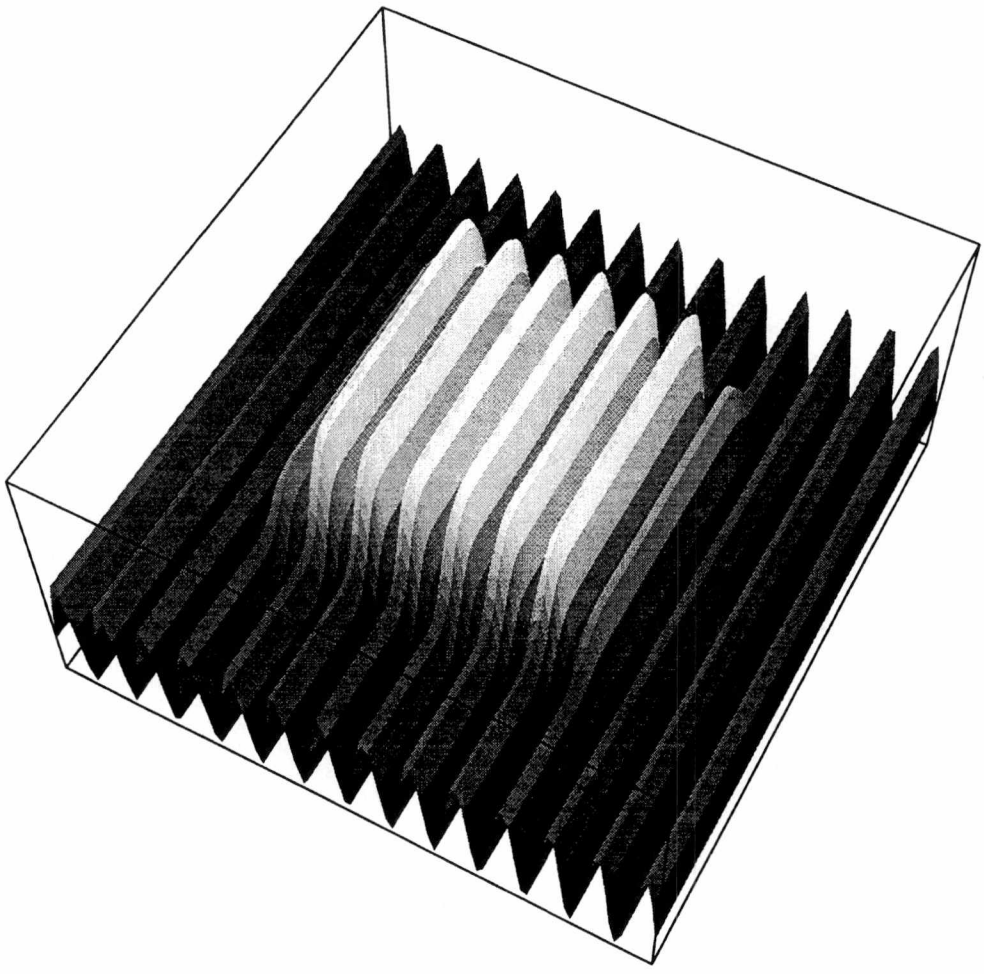


Figure II.43. $\lambda_e/2$ **Evanescent Wave on Model Surface.** Three-dimensional image of an evanescent wave of wavelength $\lambda_e/2$ on the model surface shown in **Figure II.41.** Comparison with the λ_e case shown in **Figure II.42.** demonstrates the higher spatial variation of the evanescent wave for smaller wavelength light that allows better resolution of the UVPSTM at smaller wavelengths.

generated with a wavelength of λ_e, and **Figure II.40.b.** represents a wavelength of $\lambda_e/2$. The decay length of the evanescent field is shorter for the $\lambda_e/2$ evanescent wave, and the spatial variation of the evanescent field intensity relative to the size of the sample structure is more dramatic for the $\lambda_e/2$ evanescent wave in both dimensions shown. The higher contrast of the $\lambda_e/2$ evanescent field intensity leads to better spatial resolution of structural images obtained by measurements of the evanescent field intensity.

Figures II.42. and II.43. help visualize the better spatial resolution obtained with lower wavelength light. **Figure II.42.** shows the model surface shown in **Figure II.41.** with a surface wave generated with light of wavelength λ_e superimposed on the surface. **Figure II.43.** demonstrates the same scenario for light of wavelength $\lambda_e/2$. The evanescent wave with the shorter wavelength depicts changes in the sample structure more accurately.

It is important to recall that **Figures II.39.b., II.40.b., II.42., and II.43.** represent "snap shots" of the evanescent wave produced on the surface of the sample at a single point in time. The real evanescent wave travels on the surface of the sample. Additionally, while **Figures II.39.b., II.40.b., II.42., and II.43.** show important differences between the evanescent waves produced by different wavelength light, they do not represent the actual evanescent field intensity on the sample surface. **Figures II.39.b., II.40.b., II.42., and II.43.** represent an extreme simplified case where the evanescent field intensity at any point is directly related to the height of the point above the sample surface. The actual evanescent field intensity at any point is the combination of the evanescent field intensity relating to the height of the point above the sample surface and the evanescent field intensities of evanescent waves produced at and modulated by other points on the sample surface.

Data shown in **Figures II.32., II.33., II.34., and II.35.** show cross sections of the evanescent field intensity above the quartz cross grating for different wavelengths of light. The data represent curves of constant evanescent field intensity above the structure

of the grating. Speculation on the interactions of the evanescent waves generated from and modulated by different points on the sample surface can be made from the data. Possible interactions of the evanescent wave with the surface of a sample that lead to the observed evanescent field distribution are presented here. It is important to note that the possible interactions described here are only qualitative speculation based on the data shown in **Figures II.32., II.33., II.34., and II.35.** Although no quantitative calculations or measurements were performed for the discussion presented here, the qualitative analysis of the data leads to a better understanding of the physics involved in the PSTM.

A cross section of the surface of the quartz cross grating resembles a square-well pattern; however, the data shown in **Figures II.32., II.33., II.34., and II.35.** do not exhibit square-well patterns. Data taken with the red spectrum of light resembles a sinusoidal pattern. Data taken with the blue, UVA, and UVB spectra demonstrates flat areas on the data curves becoming more apparent as the wavelength of light decreases. The sharpening of the observed structure with decreasing wavelength is expected, and in general, the data resemble a square-well pattern better for shorter wavelength light. However, the data show additional structure that prevents exact repetition of the square-well pattern. This additional structure is a decrease in the observed evanescent field intensity on one side of the raised square-well relief of the grating which leads to a false "dip" in the imaged structure of the grating. It is important to note which side of the raised structure of the grating that the "dip" occurs. Using the x-axis shown in **Figures II.32., II.33., II.34., and II.35.** as a reference, the evanescent wave propagates in the $-x$ direction, and the "dip" occurs on the $-x$ side of the raised structure of the grating.

As **Figures II.32., II.33., II.34., and II.35.** show, the lateral (x) and vertical (z) size of the "dip" decreases with decreasing wavelength. Thus, the feature representing a minimum in the evanescent field intensity is wavelength dependent. By examining the possible interactions of an evanescent wave with structure on the sample surface and

comparing predicted evanescent field distributions with the observed data, the reason for the minimum in the evanescent field intensity is determined.

To explain the interactions of the evanescent wave with the structure on the sample, **Figures II.44. and II.45.** show cross section views of an evanescent wave on the surface of model samples. **Figure II.44.** shows the evanescent wave produced on a flat sample for large and small wavelength light. The incident and evanescent waves are shown by lines representing the wavefronts of the light. A wavefront is a plane of constant phase perpendicular to the direction of propagation noted by the wave vector. The magnitude of the evanescent wave is represented by the height of the wavefront lines above the interface. Only a portion of the interface shown in **Figure II.44.** is illuminated by the incident wave. Thus, an evanescent wave only exists on a portion of the sample surface. However, the region of the sample surface where an evanescent wave exists is larger than the region illuminated by the incident wave since the evanescent wave travels along the interface. The magnitude of the evanescent field intensity increases from point ***p*** to point ***q*** as more incident light creates evanescent waves that add to the existing waves traveling across the surface. From point ***r*** to point ***s*** the evanescent field intensity decreases as the evanescent waves produced by the incident light dissipate due to scattering from sample roughness and other energy loss mechanisms. The distance along the interface between points ***p*** and ***q*** is smaller for the smaller wavelength light.

It is important to recall that the height of the wavefronts represents the magnitude of the evanescent wave at a single point on the sample surface. The intensity of the evanescent field decays with increasing distance from the surface at the same rate regardless of the magnitude of the evanescent wave. The height of the wavefronts is not to be confused with the decay length of the evanescent field intensity normal to the interface.

Figure II.45. shows the interaction of an evanescent wave with two different structures on the surface of the sample. The structures resemble edges of the square-well

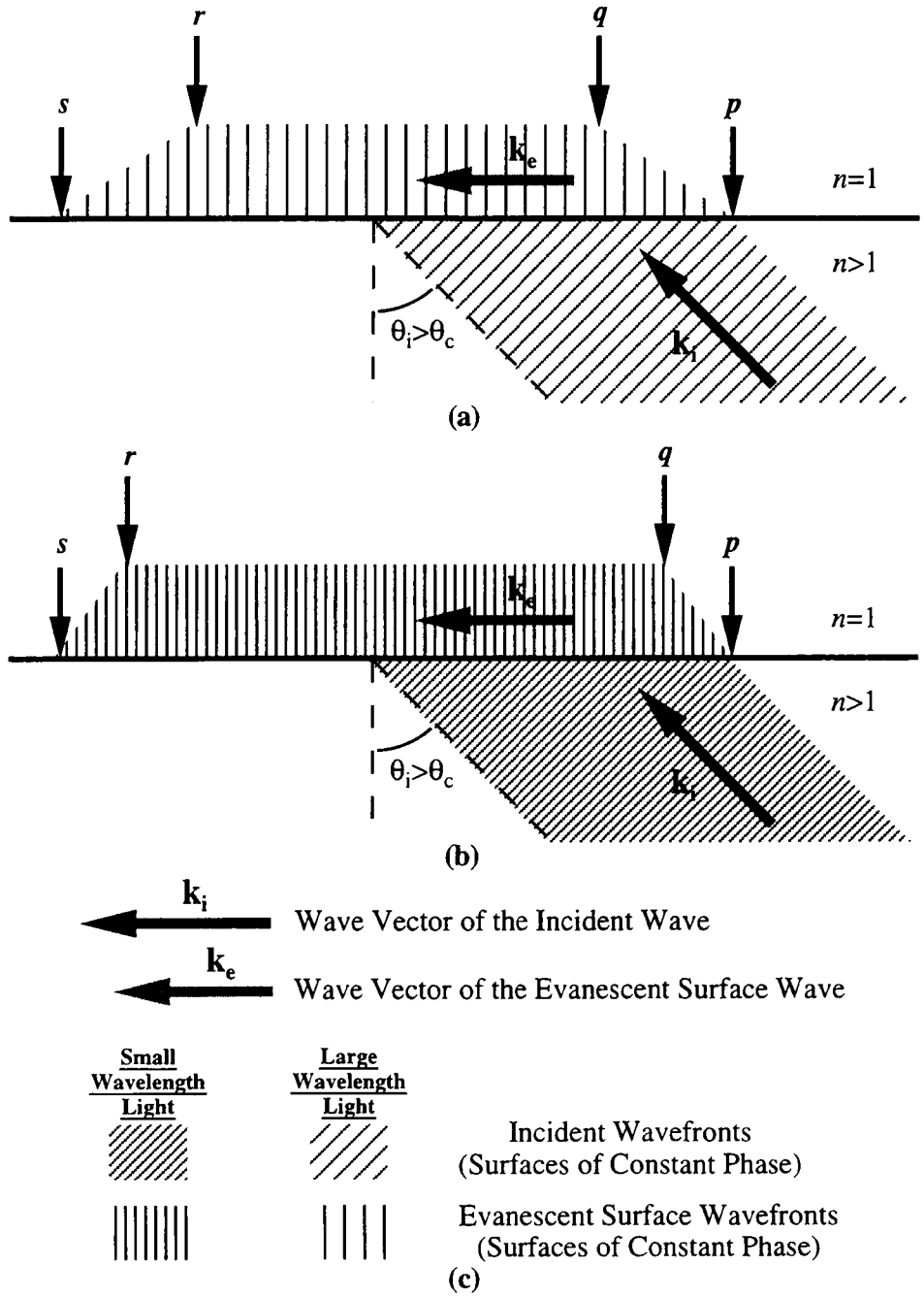
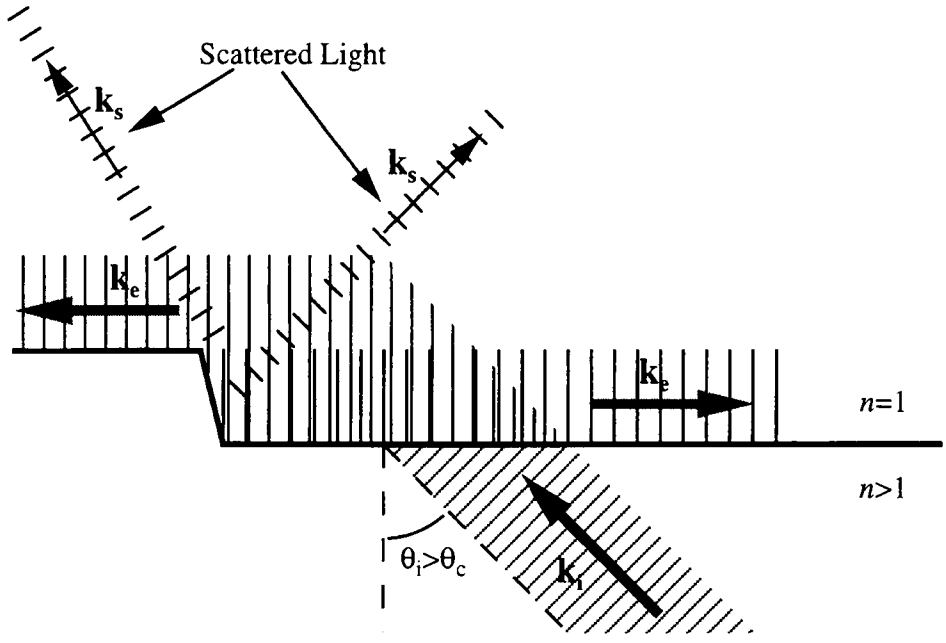
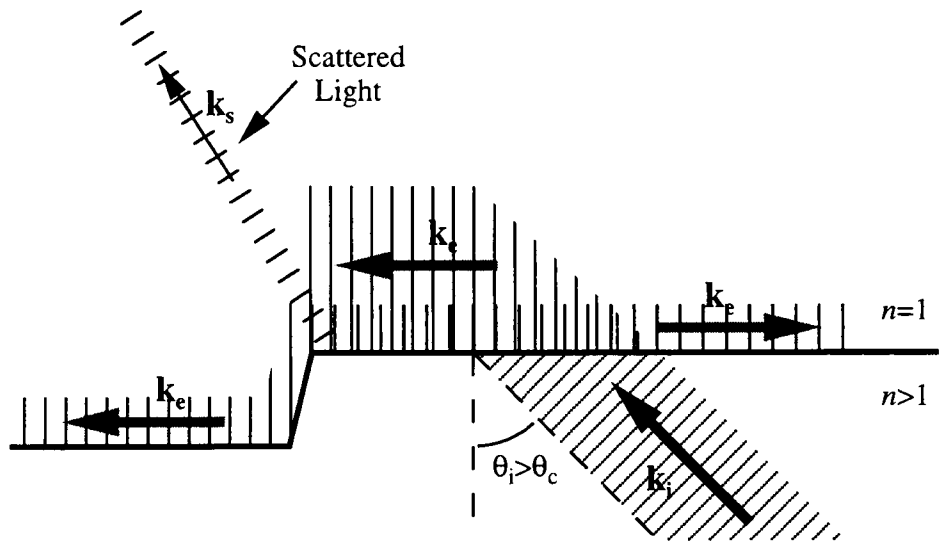


Figure II.44. Wavefronts of Incident and Evanescent Waves. The production of an evanescent wave on an interface by light incident at an angle beyond the critical angle for the interface. Cases for **(a)** large wavelength and **(b)** small wavelength light are shown. **(c)** shows the schematic of the diagrams with the amplitude of the evanescent wave expressed by the height of the wavefront pattern. The relected wave is not shown.



(a)



(b)

Figure II.45. Evanescent Wave Action at Discontinuities in the Interface. Diagrams showing possible reactions of an evanescent wave encountering a (**a**) protruding and (**b**) receding step structure on the interface. Reactions include scattering from the structure, reflection from the structure, and continuation of propagation over the structure.

relief pattern of the quartz cross grating. The evanescent wave incident on the surface discontinuity reacts in three methods. Some of the evanescent wave continues to propagate in the original direction and follows the sample structure. A portion of the evanescent wave is reflected by the structure and travels in the opposite direction where interference with the original evanescent wave may result. Finally, some light is produced at the structure by scattering of the evanescent wave from the sample structure. The fraction of evanescent wave reflecting from, scattering from, or propagating over the structure is not determined here; the magnitudes of the evanescent waves are shown for demonstration purposes only.

The basic processes involved in the production of and modulation of the evanescent wave on the sample surface combine to explain the observed evanescent field intensity distribution shown in **Figures II.32., II.33., II.34., and II.35. Figure II.46.** shows a hypothetical distribution of the evanescent wave on the surface of a sample similar to the quartz cross grating with a probe inducing frustrated total internal reflection. Illumination of the entire interface by the incident wave results in constant evanescent field intensity on the flat regions of the sample; however, discontinuities in the sample surface result in an evanescent wave distribution that does not follow the structure of the sample perfectly. In particular, the evanescent field intensity changes less rapidly than the physical structure along the interface at the edge of the sample facing the incoming evanescent wave (the protruding edge). Additionally, the evanescent field intensity reaches a minimum at the edge of the sample hidden from the incoming evanescent wave (the receding edge).

The features shown in **Figure II.46.** are the result of the interactions of the evanescent wave demonstrated in **Figures II.44. and II.45.** The size of the features is directly related to the wavelength of light since the evanescent field intensity at any point on the sample is a sum of the evanescent field intensity produced by light incident on other points on the sample. The wavefronts of large wavelength light are spaced further

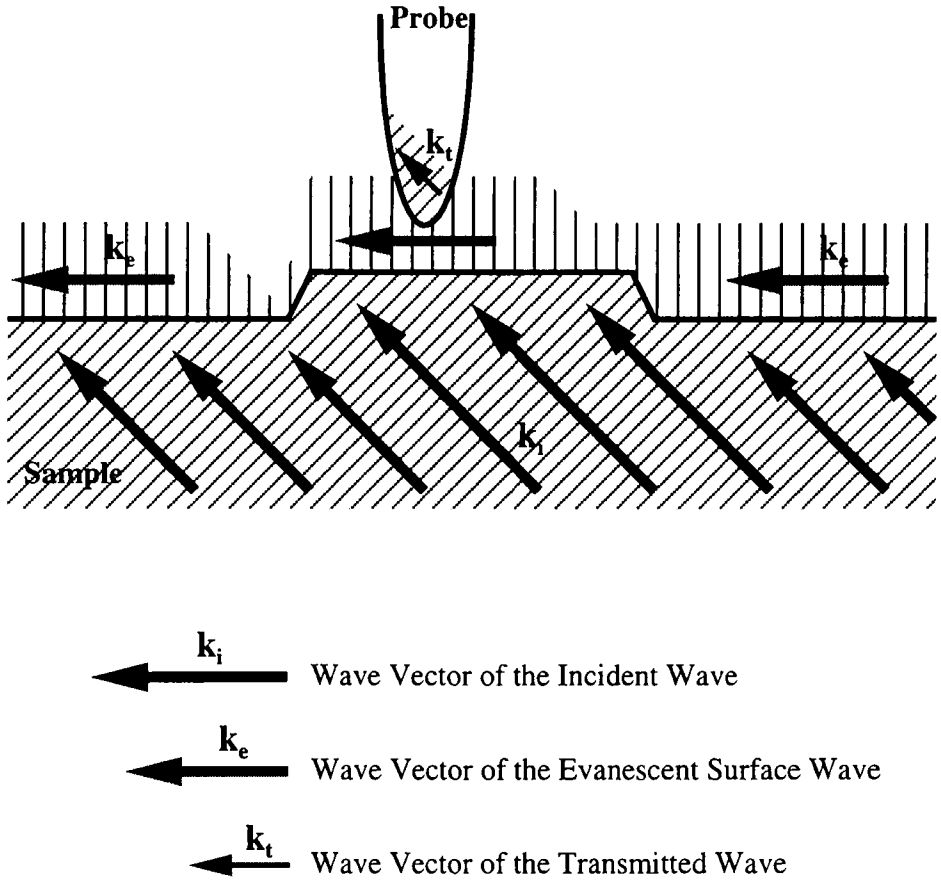


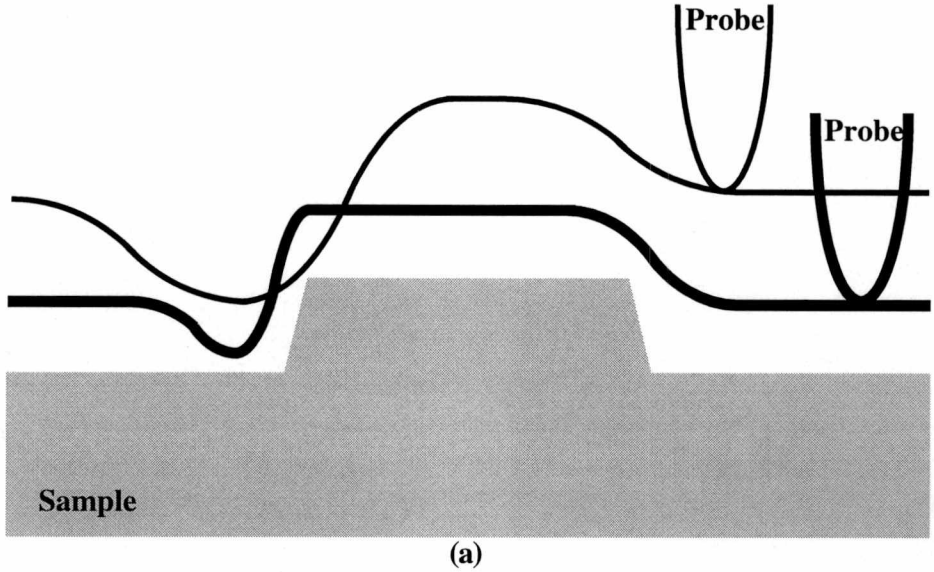
Figure II.46. Evanescent Wave Diagram for Experimental Conditions. Diagram showing the production of an evanescent wave on an interface similar to the interface of the quartz cross grating imaged with the UVPSTM. Transmission by frustrated total internal reflection to a probe occurs for the area of the probe in the evanescent field. A hypothetical distribution of the evanescent wave along the interface is shown.

apart than the corresponding wavefronts of shorter wavelength light. Thus, the features in the evanescent field intensity are spread out and exaggerated for larger wavelength light.

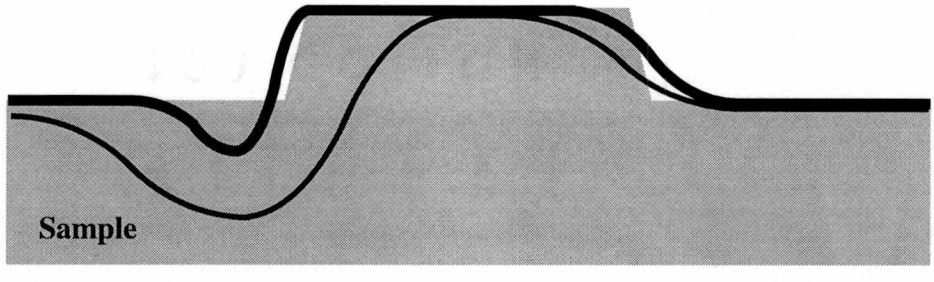
Figure II.47.a. shows scans of a probe along constant evanescent field intensity over the surface of the sample for evanescent waves produced with large wavelength (thin line) and short wavelength (thick line) light. **Figure II.47.b.** shows the corresponding image of the structure obtained by the probe scans shown in **Figure II.47.a.** The observed evanescent field intensity with changing wavelength shown in **Figures II.32., II.33., II.34., and II.35.** is similar to the changing shape of the curves in **Figure II.47.** Clearly, improvement in the lateral resolution of UVPSTM images taken with smaller wavelength light relates directly to the more rapidly varying evanescent wave intensity on the sample interface corresponding to the smaller wavelength. Additionally, when analyzing the image data obtained with the PSTM, interactions of the evanescent wave must be considered.

G. Conclusion

The visible PSTM has been improved by creating a UVPSTM. The UVPSTM allows imaging and spectroscopy over a larger range of photon energies. A UVPSTM is easily made from a visible PSTM without any elaborate modifications, and the UVPSTM can act as a visible PSTM. The manufacture of the fiber optic probe is critical to the resolution obtained with the UVPSTM, and procedures to produce probes suitable for the ultraviolet region have been developed. Data taken with the same fiber optic probe and different photon spectra show that resolution depends on the wavelength of light with resolution improving as the wavelength decreases. Comparison of data obtained at different wavelengths of light leads to a better understanding of the physical processes



(a)



(b)

Figure II.47. Probe Map of Evanescent Wave for Different Wavelengths. **(a)** Probe following a constant evanescent field intensity produced on the interface as shown in **Figure II.46.** The thin-line case represents large wavelength light, and the thick-line case represents smaller wavelength light. **(b)** The structure obtained from the evanescent wave map for large wavelength (thin line) and small wavelength (thick line) light.

involved in the production and modulation of evanescent waves on the surface of a structured interface. The UVPSTM expands the nondestructive imaging and spectroscopy capabilities of the PSTM.

CHAPTER III

Progress Toward a Soft X-Ray Scanning Tunneling Microscope

A. Introduction

The Photon Scanning Tunneling Microscope (PSTM) images samples in three dimensions with spatial resolutions superior to the diffraction limited resolutions of ordinary optical microscopes. However, the resolution of PSTMs is wavelength dependent; so, the resolution of the visible PSTM can be improved by the creation of a PSTM that operates with shorter wavelength light. Thus, we have attempted to construct a PSTM in the soft x-ray region of light, a Soft X-Ray Photon Scanning Tunneling Microscope (SXPSTM). The work described here focuses on light with a wavelength around 17.1 nm. Since lateral resolutions of $\lambda/10$ have been reported with PSTMs, lateral resolutions of 1.71 nm could be expected for a working SXPTSM.[III-1] This chapter describes the progress made toward a SXPSTM for reference during future work on the SXPSTM and in the soft x-ray region. The SXPSTM concept, the apparatus assembled, the experiments conducted, and a discussion of the progress made will be presented.

B. SXPSTM Concept

The SXPSTM operates in principle like the PSTM. The only difference between them is the wavelength, or energy, of the photons; however, this single difference in principle accounts for important differences in practice. Work in the soft x-ray region demands special soft x-ray components. Here the soft x-ray components of the SXPSTM that essentially replace the components of the visible PSTM are introduced, and the construction of the SXPSTM from the soft x-ray components is described. Later, the techniques developed to produce the SXPSTM components will be detailed.

In the visible spectrum producing total internal reflection (TIR) is straightforward. Several dielectrics meet the required TIR condition of $n_{\text{Dielectric}} > n_{\text{air}} \approx n_{\text{vacuum}}$ over broad photon energy ranges, where n is the real component of the index of refraction. The low absorption coefficients of these dielectrics permit negligible transmission loss over large ($>>\lambda$) dielectric thicknesses; thus, a simple prism allows light to enter a dielectric with $n_{\text{Dielectric}} > n_{\text{air}}$, travel through the dielectric to strike the dielectric-air interface at an incident angle (θ_i) greater than the critical angle (θ_c), and be totally internally reflected back into the dielectric **(Figure III.1.)**.

In the soft x-ray region opportunities for TIR at a sample-vacuum interface are rare. Most materials have $n<1$ over most of the soft x-ray region, and large absorption coefficients preclude using thick samples. However, in regions of anomalous dispersion, located near absorption edges, n can be greater than 1. The L_{23}-shell absorption edge of aluminum (Al) provides a small region of photon energies where $n>1$ and absorption is at a minimum **(Figure III.2.)**. In particular light just below the edge which occurs at a photon energy of 72.7 eV provides an excellent opportunity to create TIR in the soft x-ray region. For Al at 72.5 eV n=1.0247 and k, the imaginary component of the index of refraction, or the extinction coefficient, is 0.003546.[III-2] The corresponding critical angle is 77.4° and the pathlength for 1/e absorption is 383.8 nm. The large critical angle and small pathlength prevent creating TIR with an Al prism; an Al thin-film grating is

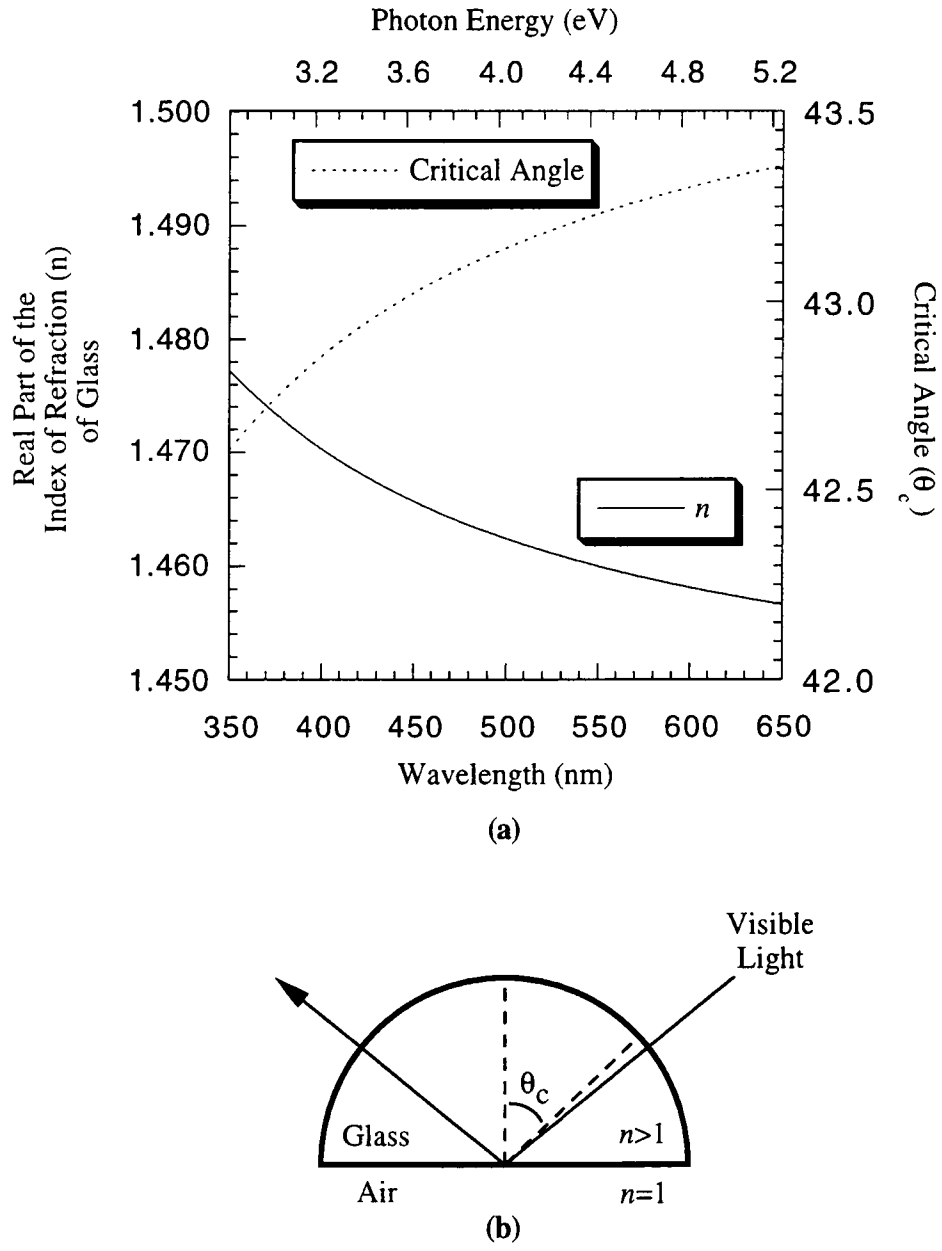
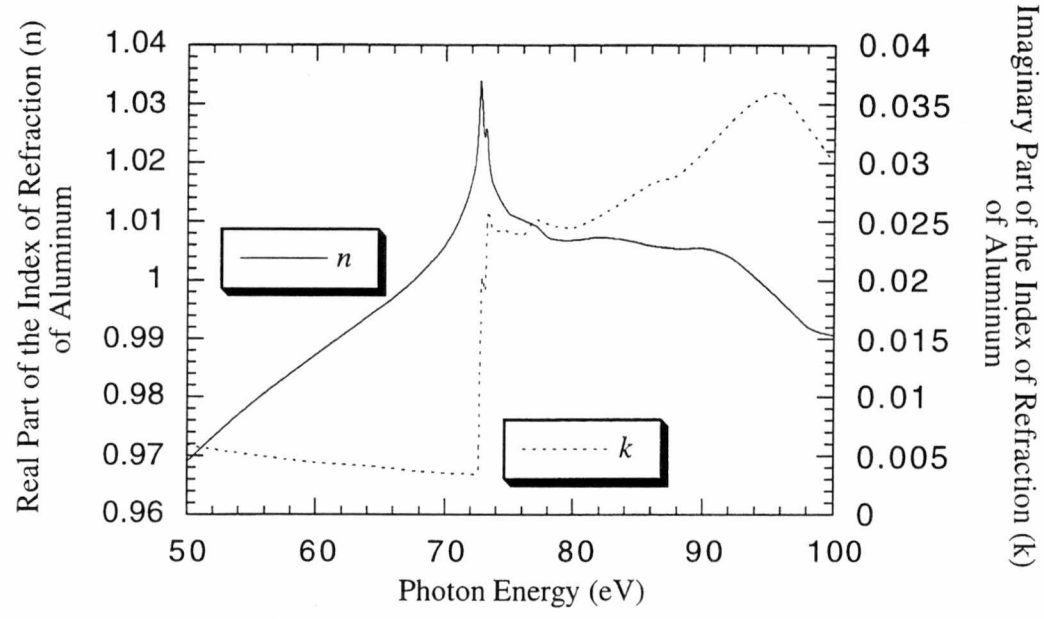
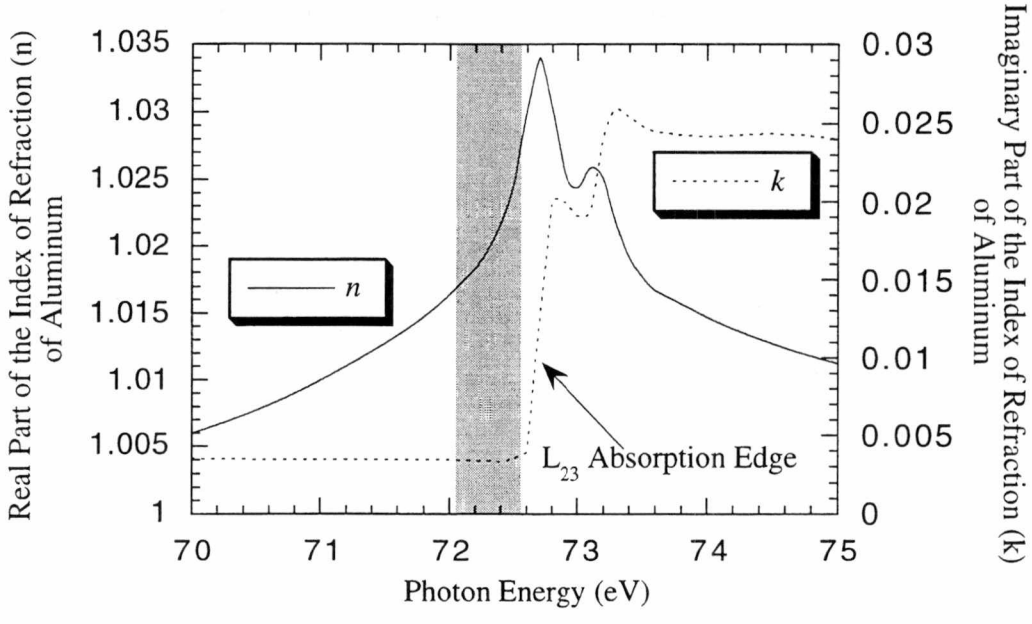


Figure III.1. Total Internal Reflection in the Visible Spectrum. The index of refraction of many dielectrics, like glass, have n greater than 1 and low absorption coefficients in the visible region of light **(a)**, and total internal reflection can be achieved easily with a semicylindrical prism **(b)**.



(a)



(b)

Figure III.2. Index of Refraction of Aluminum. The index of refraction of aluminum **(a)** in the soft x-ray region and **(b)** near the L_{23} absorption edge. The shaded region just below the absorption edge shows the target energy range.

employed instead. The Al thin-film grating performs the same task the prism performs for the visible PSTM; more specifically, the Al grating provides a means to bring light into the Al film such that the light strikes a smooth Al-vacuum interface with $\theta_i > \theta_c$.

The Al thin-film grating is a freestanding thin film approximately 80-130 nm thick. On one side of the thin film a grating relief allows light to enter the Al without significant refraction. A square-well or blazed relief pattern can perform this function; a square-well grating relief was chosen because of its easier manufacturing techniques. The square-well relief pattern must be coated with a thin layer of silver (Ag), or other opaque material, to prevent light from refracting into the Al thin film at the flat areas of the pattern and traveling through the Al-vacuum interface (since $\theta_i < \theta_c$ in this case). The opposite side of the grating structure is a flat Al-vacuum interface; thus, a planar surface acts as the SXPSTM sample substrate. The small thickness of the thin film allows enough light to reach the Al-vacuum interface without being absorbed **(Figure III.3.)**. Since aluminum oxide (Al_2O_3) forms on Al, the Al-vacuum interface is actually an Al-Al_2O_3-vacuum three layer medium, and contamination or samples on the thin film produce a four layer medium. However, for this study the thin (≈2 nm) Al_2O_3 layer and any sample or contamination material can be neglected.

The other main components of the SXPSTM are the light source and probe. Synchrotron radiation from the National Synchrotron Light Source (NSLS) at Brookhaven National Laboratory (BNL) provides the light. The synchrotron produces "white" light of many energies, but a variable line space grating monochromator gives monochromatic light from ~50-250 eV. The large synchrotron provides soft x-ray light just below the Al L_{23}-shell edge with power orders of magnitude greater than conventional x-ray tubes and other small laboratory equipment.

Since optical fibers do not transmit soft x-ray light, the visible PSTM fiber optic tip must be altered to probe the evanescent field. The most straightforward solution is to make the tunneling soft x rays create visible photons that can be transmitted down the

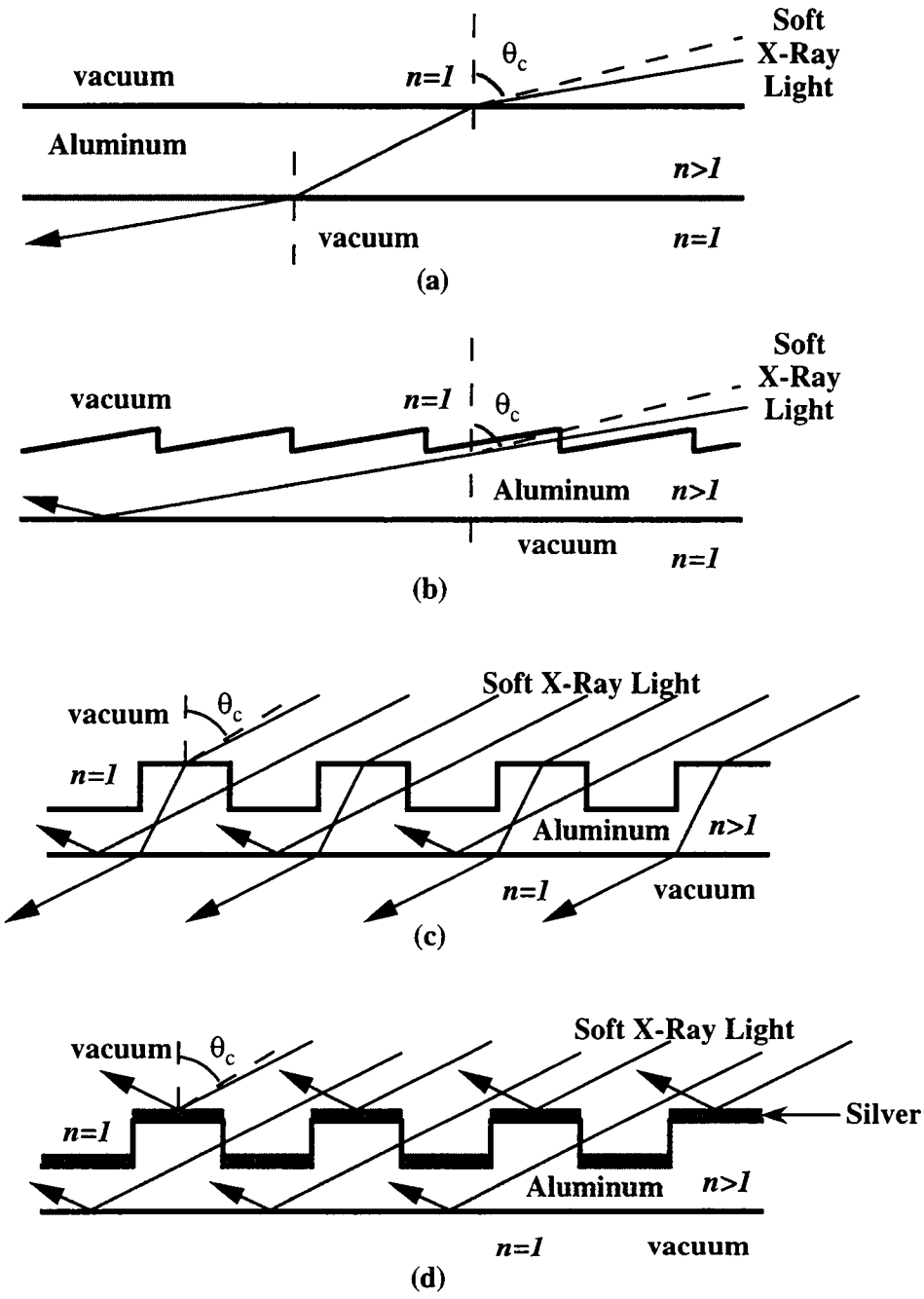


Figure III.3. Soft X-Ray Interactions with Thin Films. Soft x-ray interactions with **(a)** a plane aluminum thin film, **(b)** a sawtooth-blazed thin-film grating, **(c)** a thin-film square-well grating, and **(d)** a silver-coated thin-film square-well grating.

optical fiber to a detector; this detection technique is called "downshifting" the photon energy. Although glass or silica, the materials composing optical fibers, will create some visible photons when bombarded with soft x rays, the low photoluminescent efficiencies of glass and silica make them poor choices for this application. Phosphors are needed to provide enough downshifting to detect the evanescent field. In particular, inorganic phosphors that retain high photoluminescent efficiencies over long exposure times are applied to the tip region of the sharpened fiber optic probes. The inorganic phosphors on the probe tip detect the soft x-ray photons and create visible photons that are transmitted to a detector by the optical fiber.

The optical properties of the inorganic phosphor applied to the probe tip differ from Al. In the soft x-ray region the phosphor is highly absorbent, and the real part of the index of refraction (n) of the phosphor is less than 1. The optical properties of the phosphor create two different scenarios for probing the evanescent field. One scenario involves applying an Al coating to the phosphor-coated probe. Photon tunneling through a vacuum barrier occurs when the two surrounding media have $n>1$. To facilitate actual tunneling of soft x-ray photons, a thin Al coating can be evaporated over the phosphor on the probe; this allows photons to tunnel through the vacuum barrier between two Al media. Once the photons tunnel to the Al-coated probe they travel through the thin Al layer to the phosphor where photoluminescence takes place. Photon tunneling dominates evanescent field detection in this scenario. Another scenario for evanescent field detection involves photoluminescence excitation of the phosphor by the high energy of the evanescent field. The soft x-ray evanescent field can be sensed by a phosphor in the field when the field drives visible photon emission in the phosphor. Absorption of the energy in the evanescent field is the primary process occuring in this scenario.

In addition to altering the main components of the PSTM for soft x rays, other technical problems must be dealt with. Improved vibration isolation and damping similar to that of the electron STM must be integrated into the design of the SXPSTM to account

for the greater vibration sensitivity demanded by the shorter evanescent fields of the SXPSTM. Also, the SXPSTM must be ultrahigh vacuum (UHV) compatible for operation with the synchrotron light source.

The soft x-ray monochromator, thin-film grating, phosphor-coated fiber optic probe, and the mechanical and electrical control systems combine to form the SXPSTM. For successful SXPSTM operation several physical processes occur; each component of the SXPSTM plays a critical role in producing the central physical action of frustrated TIR at the Al-vacuum interface. The monochromator produces a high flux of soft x-ray photons of the proper energy (just below the Al L_{23}-shell edge). Light strikes the thin-film grating at an angle of incidence greater than the critical angle for the photon energy and enters the thin film via the square-well grating pattern. On the opposite side of the thin-film grating TIR occurs at the Al-vacuum interface. However, bringing the soft x-ray probe into the evanescent field frustrates TIR and causes visible photon emission in the phosphors coated on the probe. As mentioned the visible photoluminescence can occur from direct absorption of the evanescent field energy by the phosphor or from soft x rays tunneling to an Al-coated phosphor. The optical fiber carries the visible light to a cooled photomultiplier tube where an electrical current is produced that is proportional to the soft x rays detected by the probe **(Figure III.4.)**.

If the mechanical apparatus controlling the probe motion scans the probe laterally, a periodic signal relating to the spatial distribution of soft x rays will be recorded. If the probe is moved in the direction normal to the Al-vacuum interface, the evanescent field strength can be shown to decay with distance from the interface. Placing a sample of interest on the Al-vacuum interface will cause distortion of the evanescent field. The type of distortion will depend on the optical properties of the sample. The evanescent field intensity can be reduced by an absorbing sample or extended into the vacuum by an optically conducting sample. Recording the relative modulation of the evanescent field as the probe is scanned in two dimensions over the surface of the sample produces a plot

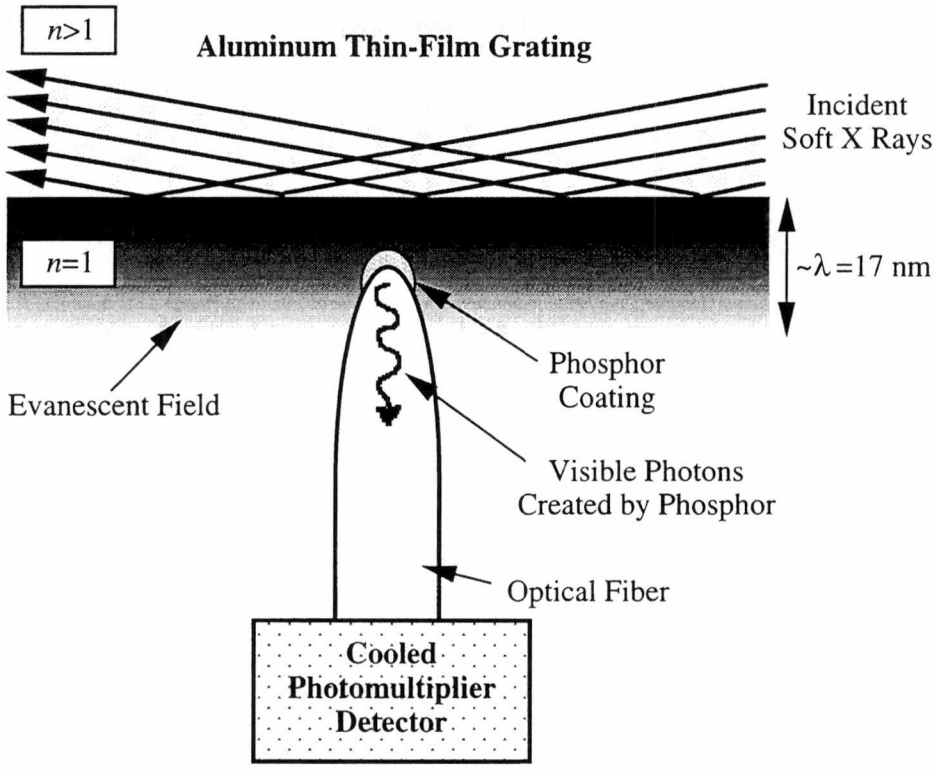


Figure III.4. SXPSTM Overview. Combination of the soft x-ray components that form the SXPSTM.

that can be analyzed to give a topographical image of the sample examined. Thus, the SXPSTM operates similar to the visible PSTM, but the visible photons and components are replaced by soft x-ray photons and components **(Figure III.5.)**.

C. SXPSTM Apparatus

Some of the components of the SXPSTM are common electron scanning tunneling microscope (STM) components. In particular, the vibration isolation system and scanning mechanisms are similar to those of STMs. The unique components of the SXPSTM are the light source, thin-film grating, and the soft x-ray probe. To avoid redundancy the vibration isolation and mechanical components of the SXPSTM will be briefly reviewed. The processes involved in manufacturing the thin-film gratings and soft x-ray probes will be discussed in detail. The design of the soft x-ray monochromator is discussed elsewhere.[III-3]

C.1. Vibration Isolation System

The SXPSTM is mounted on a suspension device that isolates the main components from vibrations and positions the probe and thin-film grating system in the soft x-ray beam. Since the SXPSTM operates on a nanometer scale, normal room vibrations can drastically affect the positioning of the probe in the evanescent field. Springs with viton o-ring dampers isolate the SXPSTM from vibrations, and a magnetic eddy current damping system quickly subdues any vibrations reaching the SXPSTM. Additionally, the entire suspension device and SXPSTM can be rotated *in situ* about the probe-grating interface to permit angles of incidence from 70° to 90°.

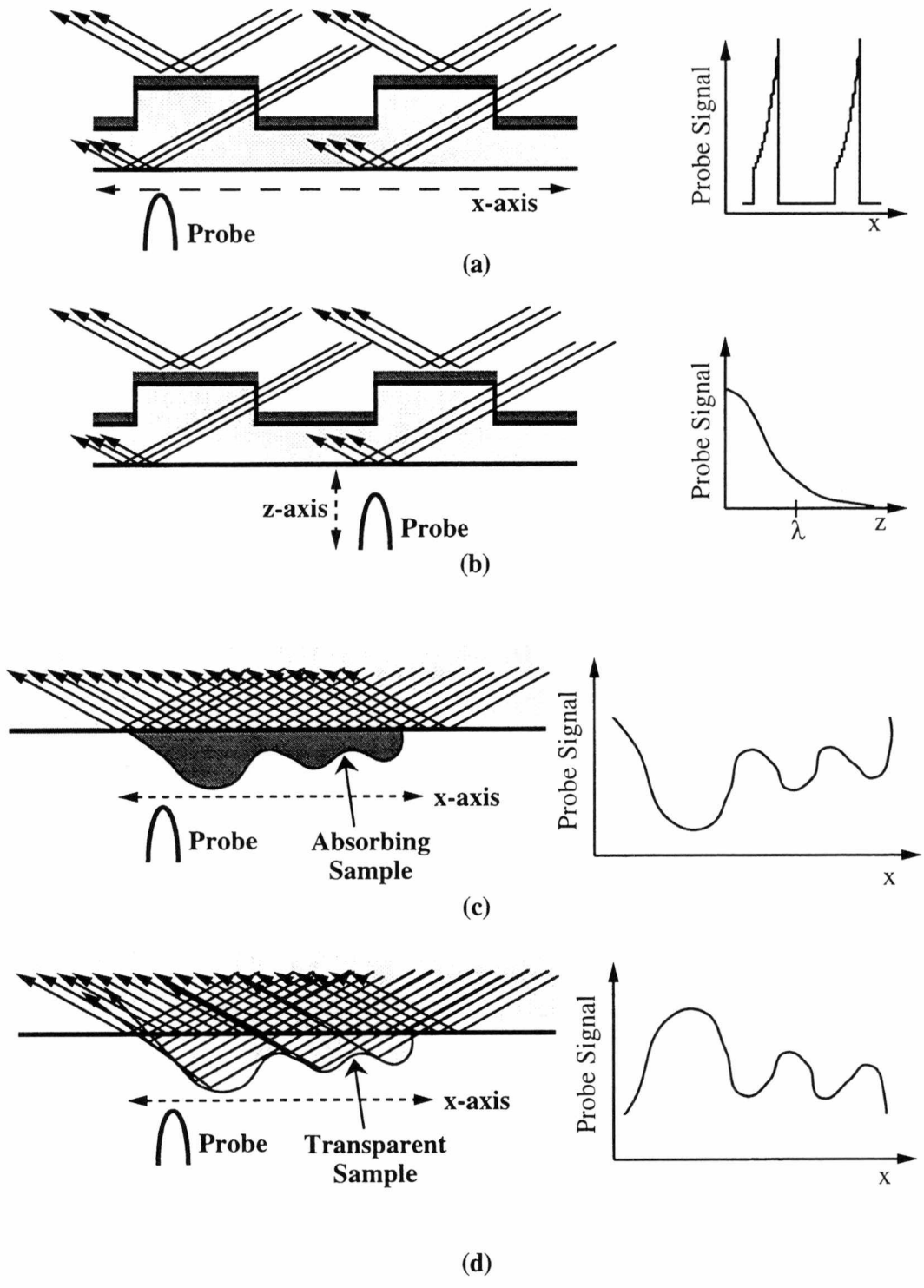


Figure III.5. Evanescent Field Intensity. Changing Intensity in the evanescent field strength detected by the soft x-ray probe as the probe is scanned **(a)** in the x direction, **(b)** in the z direction, **(c)** over an absorbing sample, and **(d)** over a transparent sample.

Several characteristics of the SXPSTM setup hampered the SXPSTM vibration isolation system, and ultimately a vibration isolation system comparable to systems of STMs is not possible. Due to the restrictions subjected by the soft x-ray monochromator, a pneumatic driven vibration isolation table could not be utilized. In most STM systems a pneumatic vibration isolation system is the first stage in vibration isolation and significantly impedes the flow of vibrations from the floor to the STM. When pneumatic systems are not employed, layers of heavy platforms with viton or silicone damping material between them provide vibration isolation in a similar fashion.[III-4] Although the large weight of the monochromator helps to isolate floor vibrations, the lack of a pneumatic system, or similar initial stage of vibration isolation, is a serious handicap in controlling vibrations of the soft x-ray probe relative to the thin-film grating. The size restrictions of the monochromator vacuum chamber and the need to rotate the SXPSTM relative to the incident light combine to restrict opportunities of placing better vibration isolation in the vacuum chamber. Placing more vibration isolation in the vacuum chamber might have compensated for the lack of a pneumatic system outside of the chamber, but the practical limitations resulted in compromising the design of the SXPSTM instead of building a new vacuum system for the monochromator. Additionally, the thin-film grating itself acts as a drumhead and vibrates much more than typical STM samples.

The fiber optic probe must be rigidly and consistently positioned within 10 nm of the thin-film grating to operate the SXPSTM. Two commercial piezoelectric devices were purchased and combined to move the fiber optic probe relative to the grating.[III-5,III-6] The probe positioning device is remotely controlled by our computer and electronics. The probe can be moved over a 10 mm range in one direction, and the probe can be scanned over 10 μm in the other directions. In the direction of the fiber probe, the probe can be moved in large steps of over 1 μm or in small steps of 0.05 nm. Thus, the probe

can be placed in the evanescent field and scanned in three directions to characterize the intensity of the evanescent field.

During operation the computer and supporting electronics control the movement of the probe and measure the light signal from the probe. The detected light is transmitted down the optical fiber to a photomultiplier tube (PMT) where the light signal is converted into a current signal.[III-7,III-8] The PMT is cooled to reduce background noise caused by thermal excitation in the photosensitive cathode. The current signal enters a picoammeter where the data can be channeled into the computer. Thus, the computer can scan the probe and monitor the probe's signal simultaneously to map the evanescent field strength as a function of position. Computer programs and electronic devices similar to the programs and devices of the visible PSTM controlled probe motion and data acquisition.

C.2. Aluminum Thin-Film Grating

Al thin-film gratings suitable for the SXPSTM have been manufactured. The following procedure was followed during grating production. A thin uniform water soluble parting layer is spincoated onto a flat glass sample, and a thin film (40 nm) of Al is evaporated over the parting layer.[III-9] The necessary smooth films were obtained with fast evaporation rates. Next, a layer of photoresist is spincoated onto the Al; photoresist is a chemical that changes chemical structure when exposed to light.[III-10] Although photoresist is normally baked, the baking step was not conducted to prevent damage to the parting layer; the photoresist was allowed to dry in air for a day to let any moisture or solvents evaporate. The photoresist is illuminated with light through a master pattern mask. When the photoresist is developed for 5 seconds, the exposed regions will dissolve, and the unexposed regions will remain.[III-11] Thus, a grating pattern can be produced in the photoresist almost identical to the master mask. A second Al layer (50

nm) is added to the grating pattern. The sample is then placed in a photoresist remover, and the remaining photoresist dissolves and carries away any Al that was coated on the photoresist, leaving strips of Al that were in contact with the first Al layer.[III-12] Next, a very thin layer (7.5 nm) of silver (Ag) is evaporated over the Al square-well structure. Finally, the Al thin film is removed from the sample by dissolving the parting layer in hot water. The glass sample is slowly lowered into the water at an angle, and as the water dissolves the parting layer, the thin film floats off onto the surface of the water. The film is then picked up with a mount designed for the SXPSTM. This process yields a thin-film grating with a smooth surface on one side and a square-well pattern with 1 μm spacing on the opposite side. The grating structure is shown in **Figure III.6.** The thin films are 97.5 nm thick at the maximum and freestanding **(Figure III.7.)**.

C.3. Soft X-Ray Probe Detector

The soft x-ray probes were manufactured by adding a phosphor layer and an Al coating to optical fiber probes typical of visible PSTM systems. The type of phosphor applied to the optical fiber is of extreme importance. Inorganic phosphors are superior to organic phosphors because the photoluminescent efficiency remains constant after long-term exposure to x-ray irradiation. Additionally, some of the most efficient phosphors are inorganic phosphors. Since only a fractional volume of one phosphor grain will be in the evanescent field, the soft x-ray probe must be coated with phosphors with high efficiencies and long-term stability. Since the soft x-ray probe's detection area sensitive to the evanescent field is extremely small (<0.01 μm^2), the photoluminescent efficiency drastically affects the magnitude of the signal detected, and if the photoluminescent efficiency of the single phosphor grain in the evanescent field decreases with long-term or high flux irradiation, the probe becomes useless.

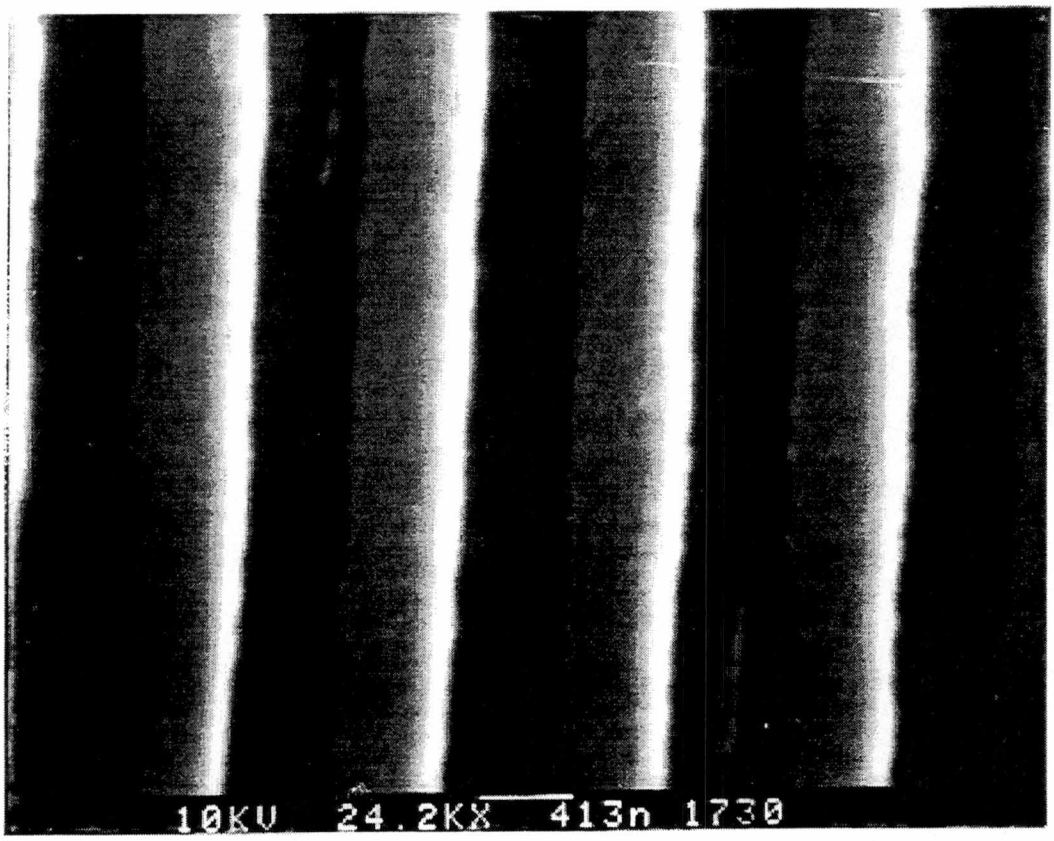


Figure III.6. Thin-Film Grating Photograph. Scanning electron microscope image of the grating structure on the aluminum thin-film grating. The image was taken at an angle of 60° to increase contrast.

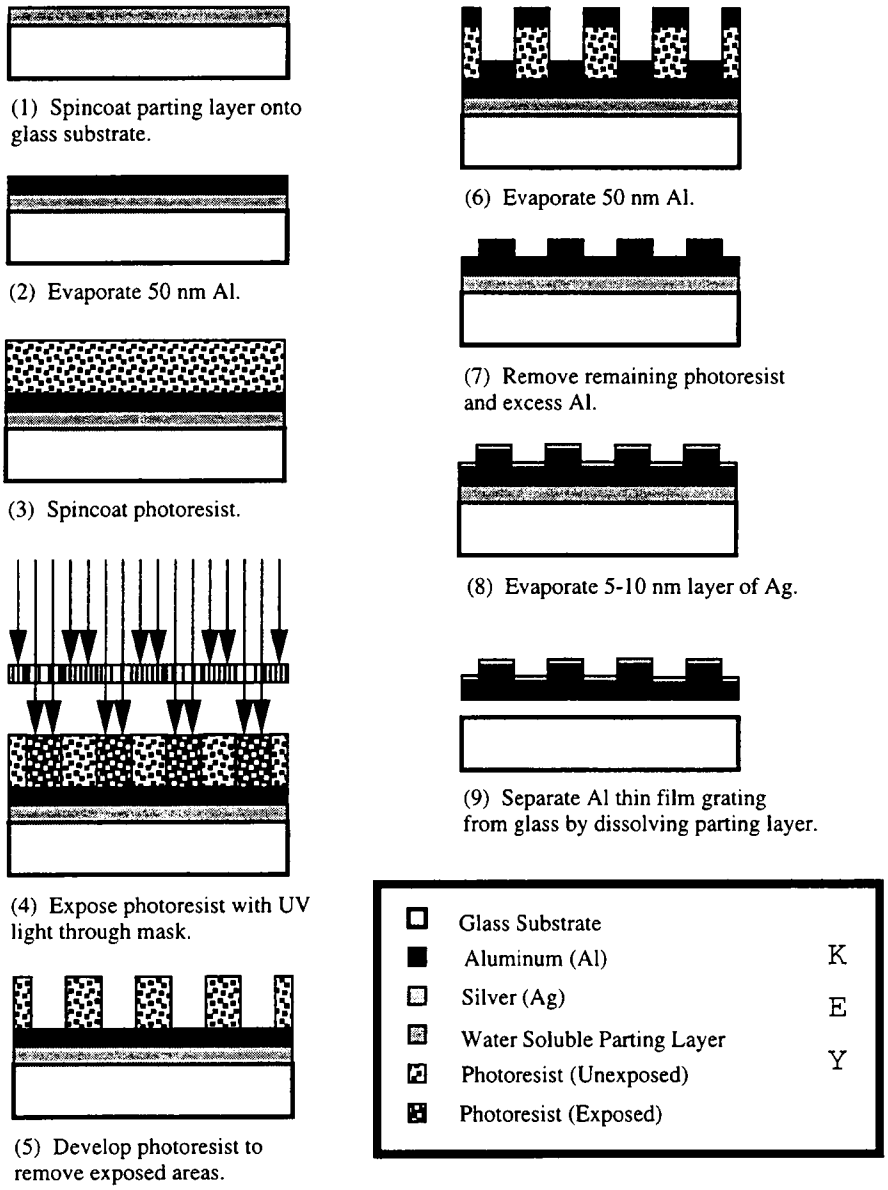


Figure III.7. Thin-Film Grating Production. Procedure for manufacturing aluminum thin-film gratings.

The inorganic phosphor chosen for the soft x-ray probes was Y_2O_2S:Eu.[III-13] The photoluminescent efficiency of Y_2O_2S:Eu at 72.5 eV is approximately 7.1%, and the amount of visible photons created is a linear function of the intensity of photons inducing photoluminescence.[III-14,III-15] When the photoluminescent efficiency of Y_2O_2S:Eu is combined with the photocathode efficiency of the photomultiplier tube for the yellow-white spectra produced by Y_2O_2S:Eu, Y_2O_2S:Eu becomes the best phosphor commercially available for application to the SXPSTM. Y_2O_2S:Eu is a powdery substance that is composed of microscopic grains with 1-5 μm diameters.

To review, the probes for the visible PSTM were formed by taking an optical fiber and pulling or etching the end of the fiber down to a point. Prior to attaining a CO_2 laser tip pulling device fiber tips were formed by acid etching. Acid etching created the pointed optical fiber for SXPSTM probes. Procedures were developed to etch the optical fibers to sharp points of different shapes and sizes.

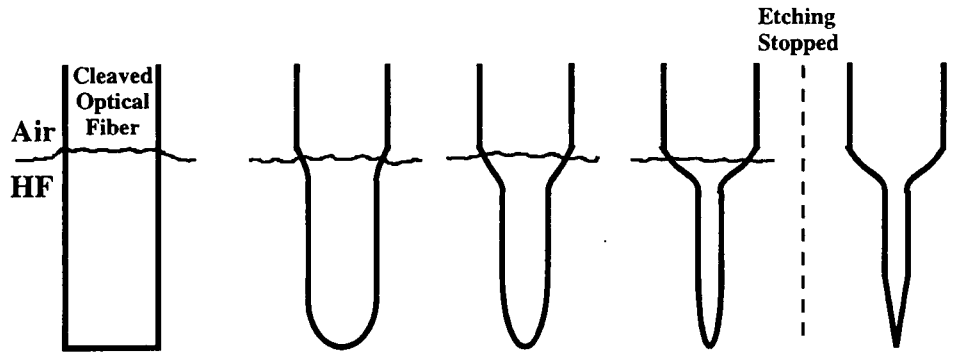
In tunneling microscopy the shape and size of the tip critically affect the resolution and performance of the microscope. A tip is characterized by its radius of curvature (tip radius), profile shape (overall macroscopic sharpness), and smoothness. Small tip radii provide better resolution, but large tip radii provide more light collection. The profile shape can affect the mechanical stability as well as the light conducting properties of the probe. A smooth probe will operate consistently; however, a rough or jagged edged probe might produce extraordinarily small tip radii. Since the phosphor material consists of grains of phosphor with diameters approximately 1-5 μm, the shape and size of the Al coated phosphor on the tip of the optical fiber determines the ultimate resolution attainable for a SXPSTM probe. The sharpened optical fiber merely acts as a base to support the phosphor and collect the light emitted by the phosphor. Therefore, optical fiber tips forming the base of a SXPSTM probe should be selected based on tip shape and profile instead of tip size. In particular, an optical fiber tip that has a short taper region and a relatively large rounded tip is better than a long tapered tip with a

small pointed end because light collection and vibration reduction are better for the short rounded tips.

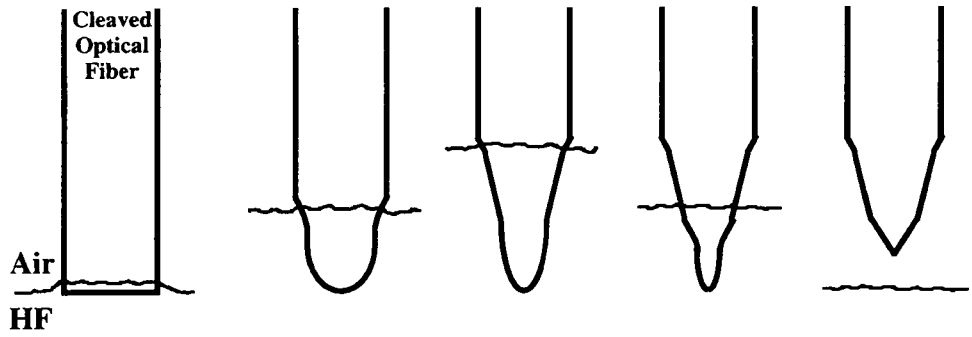
By inserting the optical fiber into the hydrofluoric (HF) acid to a certain depth for certain periods of time, procedures to etch optical fibers with tips of various radii and shape were systematically determined. Commercial optical fibers are usually composed of a core, a cladding layer, and insulation. The insulation is chemically stripped, and the fiber is placed in HF acid to etch the core and cladding. Two methods were employed to make probes suitable for the SXPSTM. An apparatus was assembled to slowly lower and raise the fiber in and out of the hydrofluoric acid; this procedure yields probes that macroscopically taper to a point over shorter fiber length than probes etched by constant imersion since the areas of the fiber closer to the tip spends more time in the HF acid than areas farther from the tip.

Another way of producing tips with short tapered profiles is by etching the optical fiber to a tip at the surface of the HF acid. An insulation stripped optical fiber is placed in the HF acid until the entire optical fiber in the acid is etched. Due to the nature of the etching process and the surface tension properties of the HF acid, the end of the etching process forms a tip with a short tapering profile. When the fiber is inserted into the HF acid, the HF acid forms a meniscus around the fiber extending up into the air. As the fiber is etched away, the amount of HF acid clinging to the fiber becomes less, and the meniscus becomes smaller. Eventually, the connection between the fiber tip and HF acid will be broken when the surface attraction between the HF acid and the dwindling area of the etched tip becomes too small to support the weight of the HF acid. After this occurrence the etching process is complete. The resulting optical fiber tip has a short tapered region corresponding to the small dimensions of the HF meniscus that performed the etching of the tip **(Figure III.8.)**.

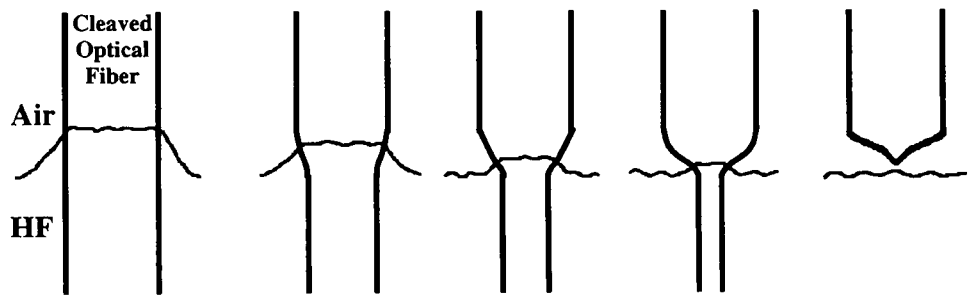
Hydrofluoric etching produces smooth optical fiber tips, but adding phosphor to the fiber tip produces a rough surface on the tip region of the soft x-ray probe. The



(a) Normal etching procedure for PSTM optical fiber probes.



(b) Short taper lengths produced by slow insertion and withdrawal of the optical fiber.



(c) Short taper lengths produced by etching in the meniscus of the acid.

Figure III.8. Optical Fiber Etching Techniques. Different procedures for manufacturing optical fiber probes.

thickness of the phosphor layer applied to the bare optical fiber tip is crucial to the operation of the soft x-ray probe. A thin layer of phosphor is superior to a thick layer of phosphor for three main reasons: better light collection by the optical fiber, less detection of background soft x rays, and fewer multiple tips.

Since the evanescent field exists only within approximately 20 nm of the Al-vacuum interface, only a phosphor grain on the extreme tip of the soft x-ray probe will be capable of detecting the evanescent field. For convenience, phosphors on the extreme tip of the soft x-ray probe capable of reaching the evanescent field will be referred to as active phosphors, and phosphor grains located between an active phosphor and the optical fiber will be referred to as intermediate phosphors. Intermediate phosphors hinder the transfer of light from the active phosphors to the optical fiber by scattering and absorbing visible light emitted by the active phosphors. Additionally, intermediate phosphors detect scattered soft x rays, soft x rays traveling through the Al thin-film grating, and any other soft x rays that are not related to the evanescent field. Detection of soft x rays not associated with the evanescent field increases the background level, and the actual tunneling signal due to the evanescent field will become more difficult to distinguish. Finally, if more than one active phosphor exists, the soft x-ray probe will be unusable in the evanescent field region since the probe would detect indistinguishable soft x-ray intensities corresponding to different physical areas near the Al-vacuum interface.

Obviously, a thick coating of phosphor on the soft x-ray probe will contain more intermediate phosphors than a thin coating of phosphor. Plus, the probability of producing multiple active phosphors will increase with the number of phosphor grains applied due to statistics and the enlargement of the macroscopic tip size by the addition of successive layers of phosphor material. Therefore, a thin layer of phosphor is superior to a thick layer of phosphor. The best amount of phosphor to apply to the tip of the probe is the least amount that definitely produces an active phosphor on the tip of the soft x-ray probe.

A procedure was developed to apply the phosphor to the optical fiber tip so that the phosphor grains stuck to the optical fiber. A solution of sodium silicate (also known as water glass) in H_2O (also known as water!) at a 1:2 ratio, respectively, is sprayed onto the optical fiber with an air powered spray gun; the water glass solution forms a thin sticky layer on the optical fiber. Before the water glass hardens, the phosphor is applied with an air powered spray gun, also. Some phosphor grains stick to the water glass, and as the water glass hardens, the phosphor grains become permanently attached to the optical fiber tip. To prepare the phosphor for application via the air gun, the phosphor is mixed with methanol at a concentration of 0.2 g Y_2O_2S:Eu per ml of methanol. Methanol serves as a fast drying liquid able to carry the phosphor through the air gun, but Y_2O_2S:Eu does not dissolve in methanol. Y_2O_2S:Eu does not retain its photoluminescent qualities when dissolved in a solvent, so the choice of a liquid to carry Y_2O_2S:Eu is critical. With practice and feedback from SEM photos the correct spraying times and distances for the water glass solution and phosphor mixture are grasped. A phosphor coated tip is shown in **Figure III.9.**

Once the phosphor layer has been added to the optical fiber tip, a layer of Al is evaporated over the phosphor and optical fiber. The purpose of this Al layer is two-fold. As mentioned before, the Al acts as a conductive medium for the soft x rays to tunnel to from the Al thin-film grating. Additionally, the Al helps to collect the light emitted from the phosphor on the probe tip. Light is emitted by the phosphor in a 4π geometry; the Al helps by reflecting light emitted away from the optical fiber back towards the optical fiber tip. Thus, more light can be launched into the conducting optical fiber. Although Al on the soft x-ray probes absorbs light, an Al coated probe was chosen. More light would probably be detected when soft x rays tunneled to an Al media and traveled directly to the phosphor instead of relying on absorption of the evanescent field by the phosphor. Additionally, an Al-vacuum-Al tunneling system closely relates to the familiar quartz-air-silica tunneling system of the visible PSTM.

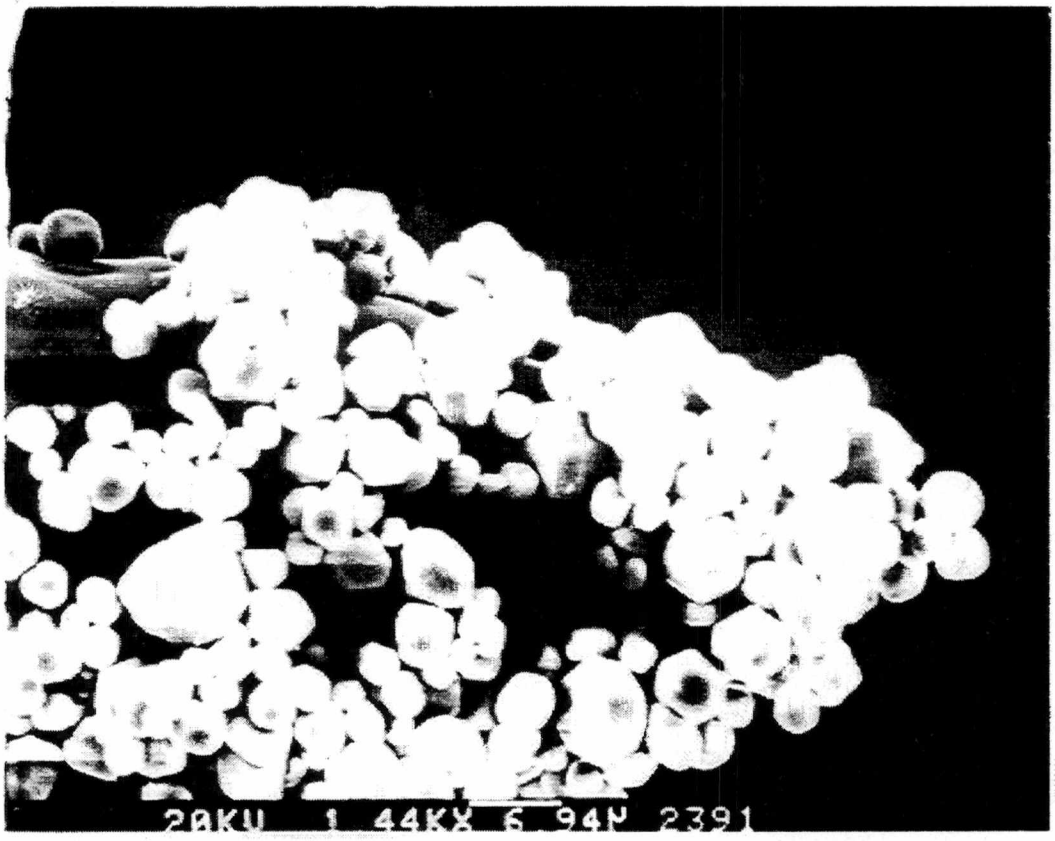


Figure III.9. Soft X-Ray Microprobe Photograph. Scanning electron microscope image of the phosphor coated tip region of a soft x-ray microprobe.

The thickness of Al applied was chosen to perform the functions of creating a medium suitable for tunneling from the Al thin film sample and increasing the efficiency of light collection by the optical fiber without absorbing too much of the actual tunneling signal. A 50 nm layer of Al was chosen; the transmission through 50 nm of Al is 0.878 at 72.5 eV. However, the pathlength of light traveling through a 50 nm thin film of Al at 80^{o} is 287.94 nm, and the transmission through 287.94 nm of Al is 0.472 at 72.5 eV. The transmission of soft x rays through the Al-vacuum-Al system of interest can be approximated by theories describing electromagnetic wave interactions at boundaries between different media (**Appendix B.**). These theories will be referred to as interface or thin film theories. The transmission through an Al-vacuum-Al system is quite different from the transmission through an Al-vacuum-absorbant system. Although the optical constants of Y_2O_2S:Eu are not known, the Al-vacuum-Y_2O_2S:Eu system can be approximated by looking at Al-vacuum-glass and Al-vacuum-Ag systems since glass and Silver are absorbants like Y_2O_2S:Eu at the photon energy of interest. Glass photoluminesses in the soft x-ray region, although at a much lower efficiency, and Silver is highly absorbent in the soft x-ray region. Y_2O_2S:Eu photoluminesses efficiently and is highly absorbent in the soft x-ray region. The sensing action of a soft x-ray probe without an Al coating can be characterized by the absorption occurring when the probe is inserted into the evanescent field. **Figure III.10.** demonstrates the advantage of using an Al-coated tip to facilitate better coupling into the evanescent field.

The soft x-ray probes manufactured for this study were large compared to probes that could achieve the ultimate resolutions of a SXPSTM. Since the amount of soft x rays needed for a SXPSTM were questionable, larger probes were chosen to obtain as large a tunneling signal as possible. Resolution was sacrificed for signal strength. The only criteria for resolution in this study was that the soft x-ray probes must be able to resolve the periodic pattern of evanescent waves on the Al-vacuum interface. The phosphor grains on the extreme tip of the soft x-ray probes determined the probe radius, but the

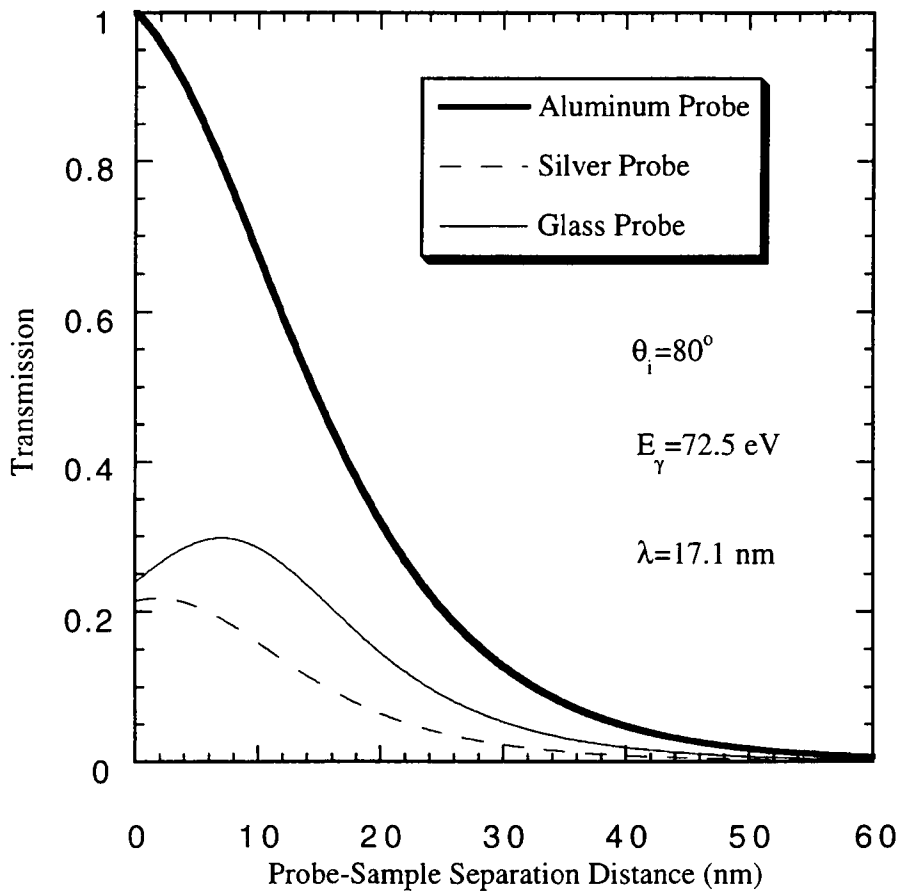


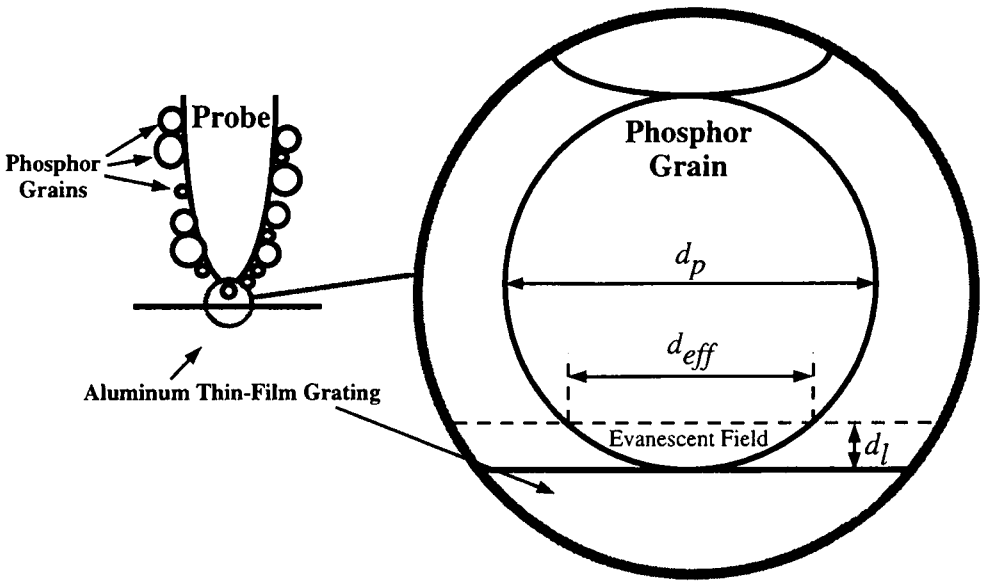
Figure III.10. Probe Material Comparison. Transmission vs. probe-sample separation distance for different probe materials.

spatial resolution of the probe is determined by the combination of the tip radius and the decay length of the tunneling signal. The exponential decay of the tunneling signal dominates the resolution of tunneling microscopes, and resolutions much less than the tip radii can be obtained. The resulting effective size of the soft x-ray probes can be obtained with simple geometry (**Figure III.11.**). For a probe tip, the effective phosphor grain, with a diameter of 1 μm in an evanescent field with a decay length of 20 nm, the effective tip diameter is less than 280 nm. The soft x-ray probes were microscopically inspected before use to assure only phosphor grains with diameters less than 1 μm were on the tip of the probe; thus, spatial resolutions capable of mapping the 2 μm spaced evanescent field regions on the sample could be obtained.

D. Total Internal Reflection in the Thin-Film Grating

The Al thin-film gratings developed for the SXPSTM were designed to perform one specific function: to create a soft x-ray evanescent field at an Al-vacuum interface. Two experiments were conducted to determine if the thin-film gratings performed this function. The first experiment involved observing the transmission of soft x rays through the Al thin-film gratings; the second experiment involved detecting the evanescent field with the soft x-ray probe. The combined experiments provide both a macroscopic and microscopic test of the performance of the thin-film gratings. Additionally, since both experiments were conducted with the soft x-ray probe acting as the detector, the quantity of soft x rays needed for a SXPSTM can be inferred by the number of photons detected by the probe.

An evanescent field is created at an interface when light from one medium is totally internally reflected back into that medium; therefore, the observance of total internal reflection (TIR) indicates the presence of an evanescent field. By monitoring the



$$d_{eff} = d_p \sin\left[\frac{\cos^{-1}\left(\frac{d_p}{2} - d_l\right)}{\frac{d_p}{2}}\right]$$

d_p=phosphor diameter

d_l=evanescent field decay length

d_{eff}=effective probe diameter

Figure III.11. Probe Size Calculation. Effective tip diameters are related to the actual diameter of the phosphor on the probe tip and the decay length of the evanescent field.

transmitted intensity of soft x rays as a function of incident angle TIR can be detected. In this section the transmission of soft x rays through an Al thin-film grating will be theoretically calculated and experimentally shown. The results will be analyzed to determine the performance of the Al thin-film gratings.

D.1. Theoretical Transmission through the Thin-Film Grating

Monitoring the transmitted intensity of soft x rays through the Al-vacuum interface as a function of incident angle provides a means of detecting TIR. However, the angle of incidence at the Al-vacuum interface of the thin-film grating is not exactly the angle of incidence associated with the angle formed between the grating and incident beam of soft x rays. When soft x rays enter the thin-film grating, refraction causes the light beam to change directions since the surface of the grating pattern on the thin film is not normal to the incident beam of light. Additionally, the modified direction and transmitted intensity of a light beam varies with the area on the thin-film grating that the light beam strikes. In contrast to the familiar semicylindrical prism the thin-film grating functions in a complicated manner. The operation of the thin-film grating will be detailed as the theory describing the grating is introduced. Then the experimental data will be compared with the theoretical model to determine if TIR was observed.

To describe the intensity of soft x rays transmitted through the Al thin-film grating, a theory was developed that combines Fresnel's equations, multilayer media formulae, and basic geometry. For convenience the side of the Al thin-film grating with the square-well grating pattern on it will be referred to as the grating side or grating, and the flat Al-vacuum interface will be the sample side or sample. Also, the grating will be treated as being composed of three regions; the regions of interest can be viewed with a two dimensional cross section showing the square-well pattern. The first two regions are the flat areas parallel to the sample side. One will be the high flat region and the other

will be the low flat region relative to the sample side of the thin film. The other region is the area between the high and low flat regions; this will be referred to as the step region (**Figure III.12.**). Only the step region facing the incident light will be important since the other step region will be shielded from the incident light by the high flat region. To match experimental parameters calculations for the transmission through a thin-film grating were made for a thin-film grating structure with dimensions given in **Section III.C.2.**

The light transmission through the high and low flat regions will be treated as a standard four-medium layered system. The transmission of light through two thin films is a four-media layered system. For the high and low flat regions of the thin-film gratings the four media in the apparent order to the incident light are vacuum (vac), Ag, Al, and vacuum (vac). The transmitted intensity of light through the four-media system is a function of the media's refractive indices, the incident angle of light to the vacuum-Ag interface, the energy or wavelength of light, and the thicknesses of the Ag and Al thin films. The transmittance of the system can be calculated by standard theories for optical thin film systems (**Appendix B.**). A different result for the transmission through the four-media system is obtained for the high and low flat regions due to the differences in the thickness of the Al film. The respective transmissions will be referred to as T_{high} and T_{low}.

The light entering the step region will be treated in three simple stages: transmission through the vacuum-Al interface, absorption by the Al thin film, and transmission through the Al-vacuum interface. When light enters the step, a small amount of reflection and refraction will occur at the vacuum-Al interface. After accounting for absorption occurring as light travels through the thin film, the problem becomes a simple case of transmission through an Al-vacuum interface. The transmitted intensities through the high flat, low flat, and step regions will be weighted according to

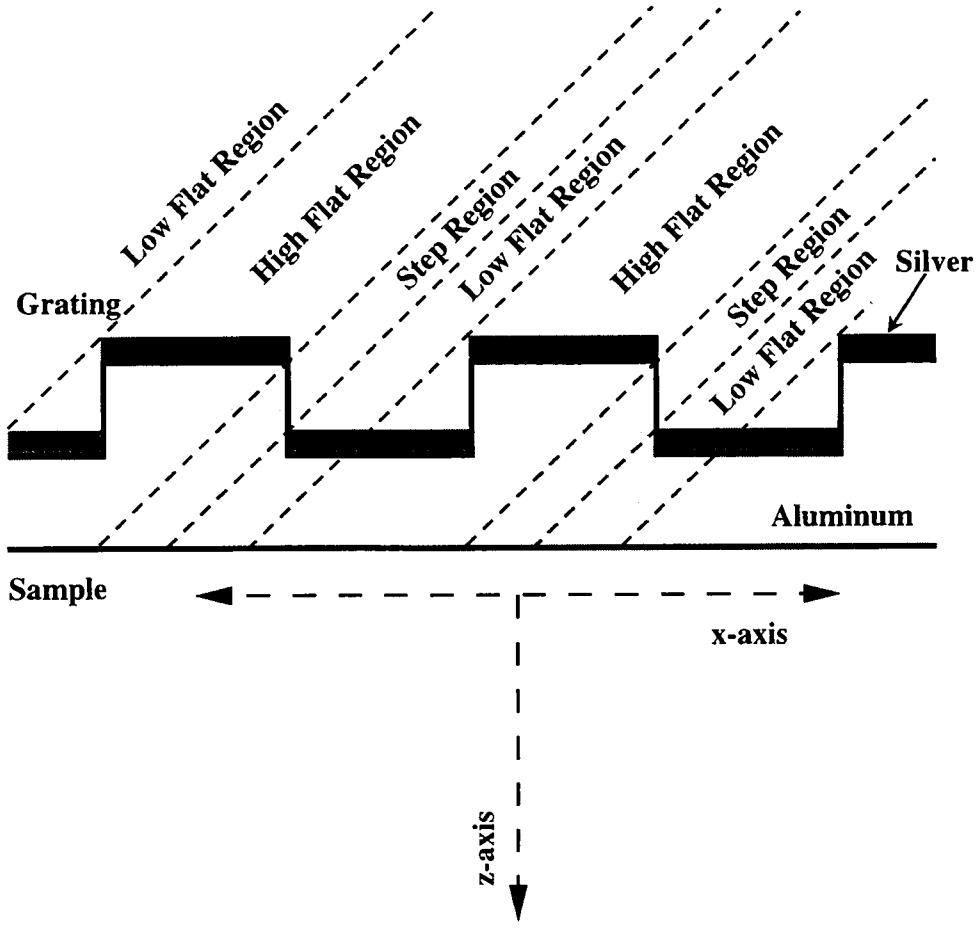


Figure III.12. Thin-Film Grating Regions. Soft x-ray light will interact differently with the different regions of the aluminum thin-film grating. For reference, the regions will be referred to as the high flat, low flat, and step regions as shown in the diagram.

the flux of light incident on each region and then summed to provide the total transmission through the thin film.

Light striking the step region of the thin-film grating is refracted at the vacuum-Al interface, travels through the Al thin film, and strikes an Al-vacuum interface. The transmissions through the vacuum-Al and Al-vacuum interfaces are obtained by standard Fresnel equations (**Appendix B.**). A fraction of the light traveling through the Al thin film is absorbed. The fraction of light not absorbed is obtained by considering the absorption coefficient of Al at the particular photon energy of interest:

$$T_{film} = e^{-\left(\frac{4\pi k}{\lambda}\right)\ell}. \qquad \textbf{(III.1.)}$$

Here the pathlength of light, ℓ, is determined by geometry. To simplify the theory an average pathlength traversed by the light entering the step region of the grating was substituted for the actual range of pathlengths. The complete transmission through the step region of the thin-film grating is expressed as the product of the transmission through the vacuum-Al interface, the Al thin film, and the Al-vacuum interface:

$$T_{step} = T_{vac-Al} T_{film} T_{Al-vac}. \qquad \textbf{(III.2.)}$$

The flux of light striking the three regions of the thin-film grating changes with the angle between the light beam and thin-film grating. In general, the flux of light hitting the high and low flat regions decreases with increasing angle, but the flux of light hitting the step region increases with increasing angle. However, additional shadowing effects occur as angles close to grazing incidence are approached; the high flat region shadows the low flat and step regions. The relative incident light flux associated with each region can be expressed in terms of the angle of incidence and the dimensions of the square-well relief pattern on the thin-film grating. The resulting relative light flux hitting the different regions are:

$$f_{high} = \cos(\theta_i), \qquad \textbf{(III.3.)}$$

$$f_{low} = \frac{[l_1 - h_2 \tan(\theta_i)]l_1}{l_1^2}\cos(\theta_i), \qquad \textbf{(III.4.)}$$

and

$$f_{step} = \frac{l_1(h_2 - d_1)}{l_1^2}\sin(\theta_i). \qquad \textbf{(III.5.)}$$

A portion of the light hitting the high flat region will travel through the step region shaded from the incoming light and then strike the shaded region of the low flat region. This light is treated by the theory as though it traveled through only one Ag layer and the thickest part of the Al thin film The transmission through two Ag layers is <0.04% at 72.5 eV and an angle of incidence of 80°; this increases the theoretical background signal slightly.

The transmissions of the three regions of the thin-film grating are weighted by the relative flux of light incident on each region. The total transmission through the thin-film grating is expressed as the sum of these weighted transmissions through the three regions:

$$T_{total} = f_{high}T_{high} + f_{low}T_{low} + f_{step}T_{step}. \qquad \textbf{(III.6.)}$$

The total transmission is a function of the photon energy and the incident angle of light. **Figure III.13.** shows the calculated transmission as a function of the angle of incidence and photon energy.

This theory neglects several physical processes and assumes certain conditions. As mentioned earlier, the oxide layer and any contamination on the Al thin film are neglected. In general, an aluminum oxide layer will suppress the TIR seen in the transmission, and the amount of suppression will increase with oxide thickness. **Figure III.14.** shows the suppressing affect that the oxide layer has on TIR at the Al-vacuum interface. The oxide thickness on the Al thin-film grating is unknown. Typical oxide layers range from 2.0 to 5.5 nm, but thickness and composition of oxide layers vary widely.[III-2] The chemical treatments used in the manufacturing of the grating structure might have created an unusually thick oxide layer.

The theory also neglects the scattering of light by the thin film surface and the grating structure. The thin films and their interfaces are considered perfectly smooth; however, the actual surface may be rough when compared with the wavelength of light.

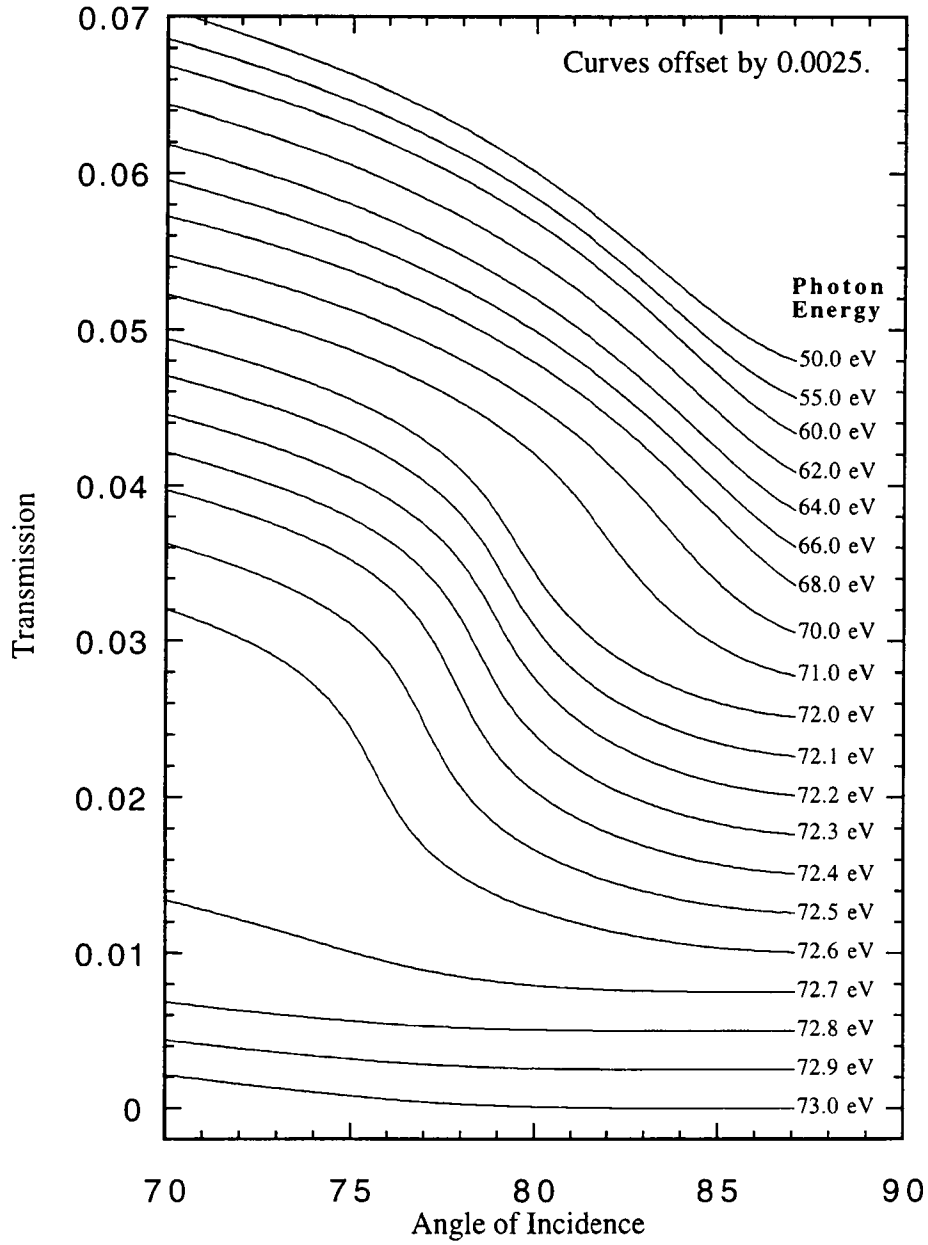


Figure III.13. Theoretical Thin-Film Grating Transmission. Theoretical transmission of the aluminum thin-film grating vs. angle of incidence for different photon energies.

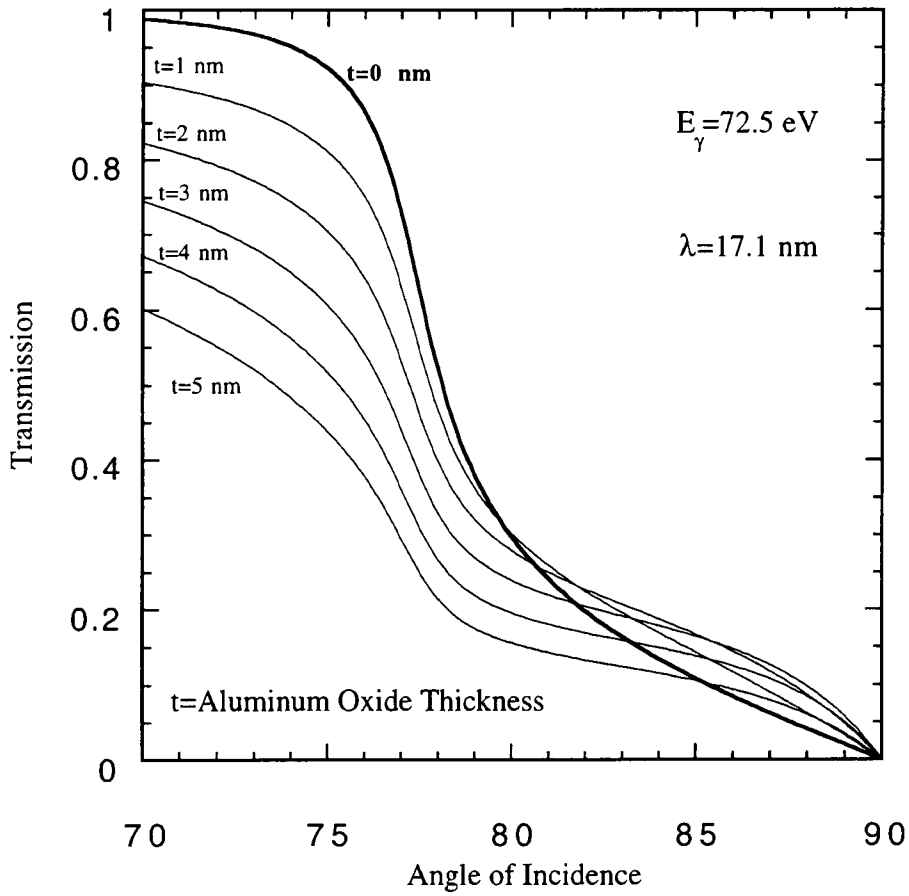


Figure III.14. Aluminum Oxide Suppression. Transmission vs. angle of incidence for an aluminum-vacuum interface with different aluminum oxide thicknesses.

Fast evaporation rates were used to obtain the smoothest films possible. The nature of gratings is to diffract and scatter light; however, any diffraction or scattering of light into the thin-film grating is neglected. In particular, the step region may act as a slit since the adjacent flat regions are opaque to soft x rays, but diffraction at the step region is neglected. The incident beam of soft x rays is assumed to be collimated, and the light is assumed to strike the grating in the plane formed by the normal to the thin film and the perpendicular to the grating lines.

D.2. Experimental Transmission through the Thin-Film Grating

The transmission of soft x rays through the Al thin-film gratings as a function of photon energy and angle of incidence was observed experimentally with the SXPSTM apparatus. The soft x-ray monochromator controlled the photon energies employed, and a micrometer attached to the SXPSTM provided a means of changing the angle of incidence of light by rotating the thin-film grating and soft x-ray probe system. The setup allowed a limited range of angular motion, but the region of interest ($70^{o}<\theta_{i}<90^{o}$) was easily attained. The soft x-ray probe acted as the detector, but the probe was positioned far ($>>\lambda$) away from the sample side of the thin-film grating to insure that the transmission of soft x rays through all three regions described in the previous section were viewed equally.

In normal operation of the soft x-ray monochromator a spectrometer allows precise measurement of the photon energy exiting the monochromator. Because of space restrictions in the vacuum chamber the spectrometer was not operable while experiments with the SXPSTM apparatus were conducted. Therefore, the photon energy had to be obtained by another means. The monochromator changes photon energy by scanning and rotating a mirror that reflects the light coming from a variable line spaced grating, and the motors controlling the scanning and tilting of the mirror contain decoders that provide

numbers relating to the position of the motors. These motor positions provided a means of knowing the photon energy produced by the monochromator. Prior to installing the SXPSTM apparatus the scan and tilt motor positions were recorded as the spectrometer recorded the photon energies produced by the monochromator. If the synchrotron beam of electrons moves, the photon energy produced by the monochromator changes because the monochromator lacked an entrance slit. An Al thin film filter in the monochromator provided a means of detecting photon energy shifts due to synchrotron beam motion. By observing the change in photon output when the filter was inserted and withdrawn from the monochromator beam, the Al L_{23}-shell edge could be detected, and the edge became a reference point to detect shifts in the photon energy. Although the motor positions did not provide accuracy of the photon energy comparable to the spectrometer, the motor positions coupled with the Al thin film filter proved adequate for the studies involved here.

Changes in the total light output of the monochromator occurred for different measurements due to the changing efficiency of the monochromator with photon energy and the continually decreasing power emitted by the synchrotron. The changing flux of light was compensated by monitoring the light power emitted from the monochromator. The light detected by the soft x-ray probe was recorded as the angle of incidence was varied with adjustments of the micrometer.

Figure III.15. shows the observed transmission for the Al thin-film grating over an energy range from 64.4 eV to 73.2 eV. Total internal reflection is seen in the data for energies between 71.0 eV and 72.6 eV. For energies below 71.0 eV the TIR curve begins to fade into the background signal. The TIR is strongest at 71.5 eV and 71.7 eV.

Certain features of the experimental curves differ from the theoretical curves shown in **Figure III.13.** The most notable and significant difference is the angle of incidence at which TIR occurs, the critical angle. Theory suggests that the critical angle should occur between $\approx 76^{\circ}$ and $\approx 82^{\circ}$ for energies from 72.6 eV to 71.0 eV; however, the

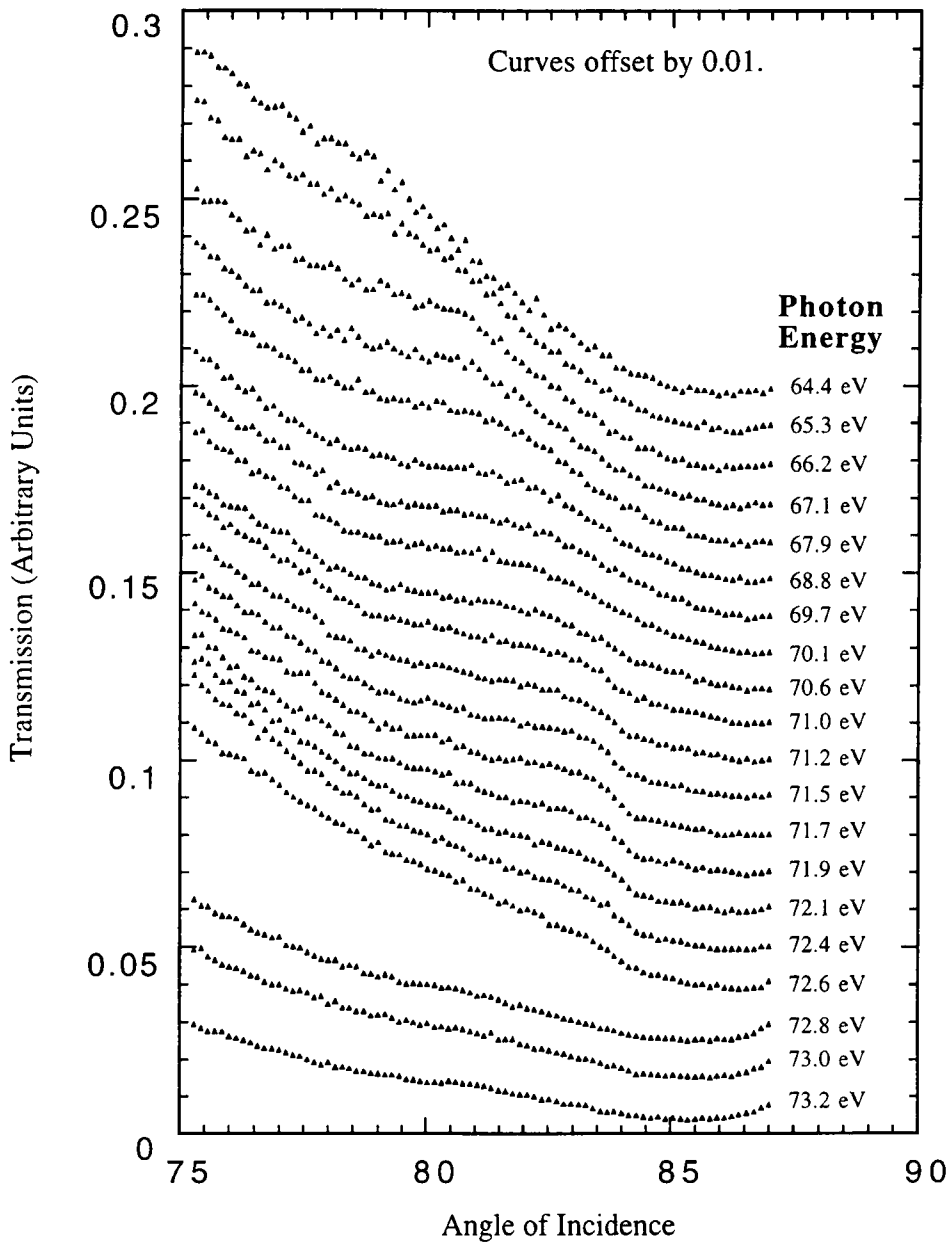


Figure III.15. Experimental Thin-Film Grating Transmission. Experimental transmission of aluminum thin-film grating vs. angle of incidence for different photon energies.

data only shows critical angles close to 84°. Additionally, the critical angle does not seem to move much with varying photon energy. However, the general shape of the experimental curves matches the theory well. The transmission at energies greater than the L_{23} absorption edge is significantly smaller due to the associated higher absorption coefficient. The background signal from x rays transmitted through the Ag reflecting layer on the grating side of the thin film follows the expected slow taper in transmission strength as the angle of incidence increases, and the TIR curve is seen superimposed on the background signal.

Although the experimental data clearly shows total internal reflection, there is concern over the position of the critical angle. Two possible explanations exist for the exceptionally high critical angle. The background signal may have been too high at low angles of incidence. This would cause any TIR signal to be drowned out by the slowly tapering background signal. The experimental curves at 72.4 eV and 72.6 eV suggest that the magnitude of the background signal might have been a problem. The TIR curves for 72.4 and 72.6 eV are not as steep as curves for lower energies. Since the critical angles at 72.4 and 72.6 eV should be less than the critical angles for lower energies, the TIR curve may have been covered by the background signal except for the tail end of the TIR curve.

Another explanation for the high critical angles might lie in the material composition of the thin film. Al is subject to extremely rapid oxidation even under ultrahigh vacuum. It is possible that Al in the thin-film grating is contaminated with aluminum oxide (Al_2O_3). Base pressures for the evaporation of Al during thin film production were $\approx 2\times10^{-6}$ Torr, and fast evaporation rates increased the probability of smooth and pure Al films. However, the reported base pressures needed to obtain ultra pure Al films is 10^{-8} Torr, and oxidation in bulk Al can occur after deposition.[III-16,III-17] Additionally, theoretical absorption coefficients 14% smaller than experimental measurements for the L_{23} edge have been reported that suggest bulk oxidation leads to high absorption coefficients.[III-18] Thus, undoubtedly there is some amount of Al_2O_3

contamination in the Al. Additionally, other contaminants might be in the Al, also. For instance, tungsten (W) coils are used to heat the Al, but when Al melts, Al reacts with W and erodes the W coil. Thus, W could be a possible contaminant in the film, too.

The amount of Al_2O_3 contamination and the effect of the contamination on the optical constants of the thin-film grating cannot be precisely determined. However, the Bruggeman effective medium theory for the dielectric constant of impure materials can be used to calculate the effect of contamination.[III-19,III-20] The effective dielectric constant, ε, of Al with a dielectric constant ε_{Al} with a volume fraction, f, of Al_2O_3 with dielectric constant ε_{Ox} is related by :

$$\frac{\varepsilon-\varepsilon_{Al}}{\varepsilon+2\varepsilon_{Al}} = f\frac{\varepsilon_{Ox}-\varepsilon_{Al}}{\varepsilon_{Ox}+2\varepsilon_{Al}}. \qquad \textbf{(III.7.)}$$

A graph of the effective optical constants for Al with different fractional volumes of Al_2O_3 is shown in **Figure III.16.** As expected, the large fractional volumes of Al_2O_3 reduce the real part of the index of refraction to the point where TIR cannot occur at some energies, and the critical angle is increased over all energy levels.

It should be noted that the resolution of the soft x-ray monochromator is more than sufficient to observe the detailed structure of the optical properties of Al at the L_{23} edge. The monochromator was designed for Soft X-Ray Emission Spectroscopy which requires detailed resolution precise enough to monitor emission changes at sharp absorption edges. With an 1250 μm exit slit, the largest slit width available, the resolution of the monochromator is 0.27 eV at 72.1 eV. However, since the wavelength dispersion occurs in a plane perpendicular to the slit, the resolution of the SXPSTM is dependent on the size of the soft x-ray probe. For a 1 μm diameter probe the resolution should be (1 μm/1250 μm)0.27 eV; this gives a resolution of ≈0.2 meV. The actual resolution is not that small since the resolution for the monochromator is limited by the resolving efficiency of the grating and the source size. The source size is ≈200-300 μm;

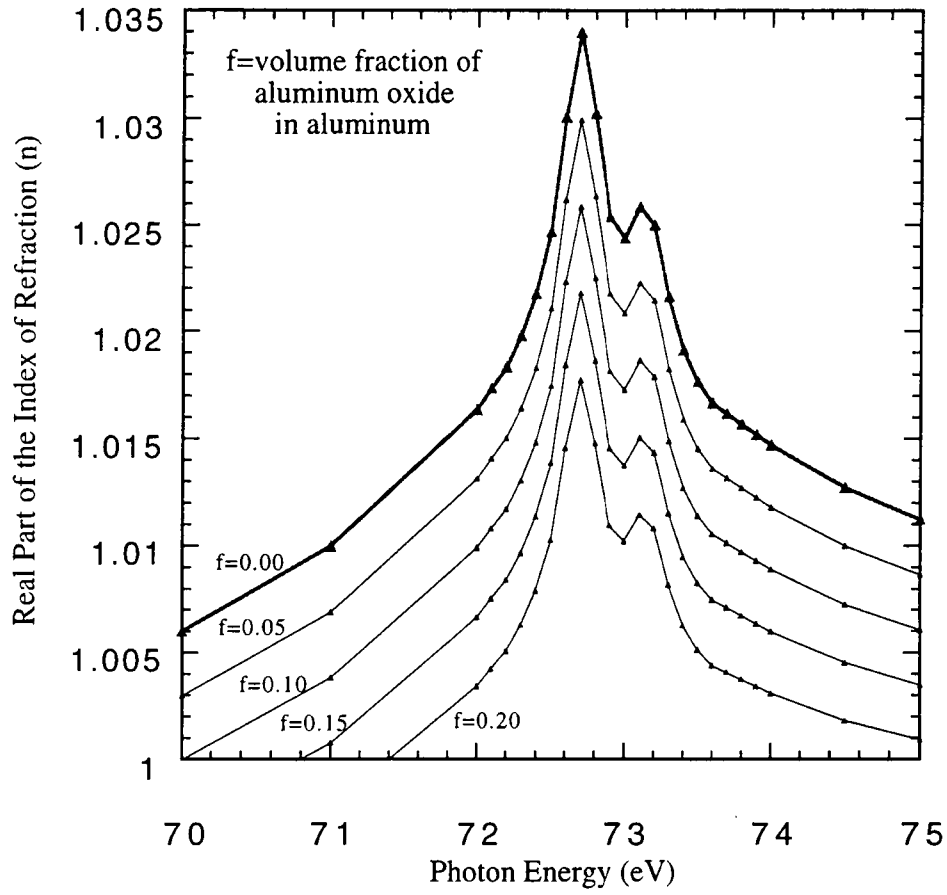


Figure III.16. Bruggeman Approximation. Real part of the index of refraction vs. photon energy for aluminum with aluminum oxide contamination based on Bruggeman approximation.

so, the resolution seen by the probe detector is roughly (250 μm/1250 μm)0.27 eV, or ≈0.05 eV. The observed low values for the real part of the index of refraction of Al cannot be attributed to the resolving properties of the monochromator.

Although the experimental critical angles for total internal reflection in the Al thin-film grating were higher than theoretical angles, TIR was clearly observed. The discrepancy between theory and experiment is most likely explained by a combination of excessive background signal at low angles of incidence and Al_2O_3 contamination in the Al thin film. In addition to showing the performance of the Al thin-film grating, the transmission curves show that the soft x-ray probe detects the soft x rays since the data was obtained using the soft x-ray probe as the detector. The magnitude of the light signal collected by the probe in the geometry of the transmission experiment can be seen from typical transmission data **(Figure III.17.)**.

E. Probing the Evanescent Field

Successful operation of the SXPSTM depends on the capability to probe and characterize the evanescent field produced at the Al-vacuum interface on the sample side of the Al thin-film grating. An experiment was conducted to characterize the evanescent field by scanning the soft x-ray probe close ($<\lambda$) to the sample surface. Variations in the intensity of light detected by the probe as it is scanned indicate the presence of an evanescent field. The variation observed in the light intensity will depend on the direction that the probe is scanned relative to the sample surface of the thin-film grating. Scanning the probe in a lateral direction parallel to the Al-vacuum interface and perpendicular to the grating lines should produce a periodic signal relating to the periodic regions of evanescent waves. However, scanning the probe in the direction normal to the Al-vacuum interface should produce an exponential signal relating to the decaying

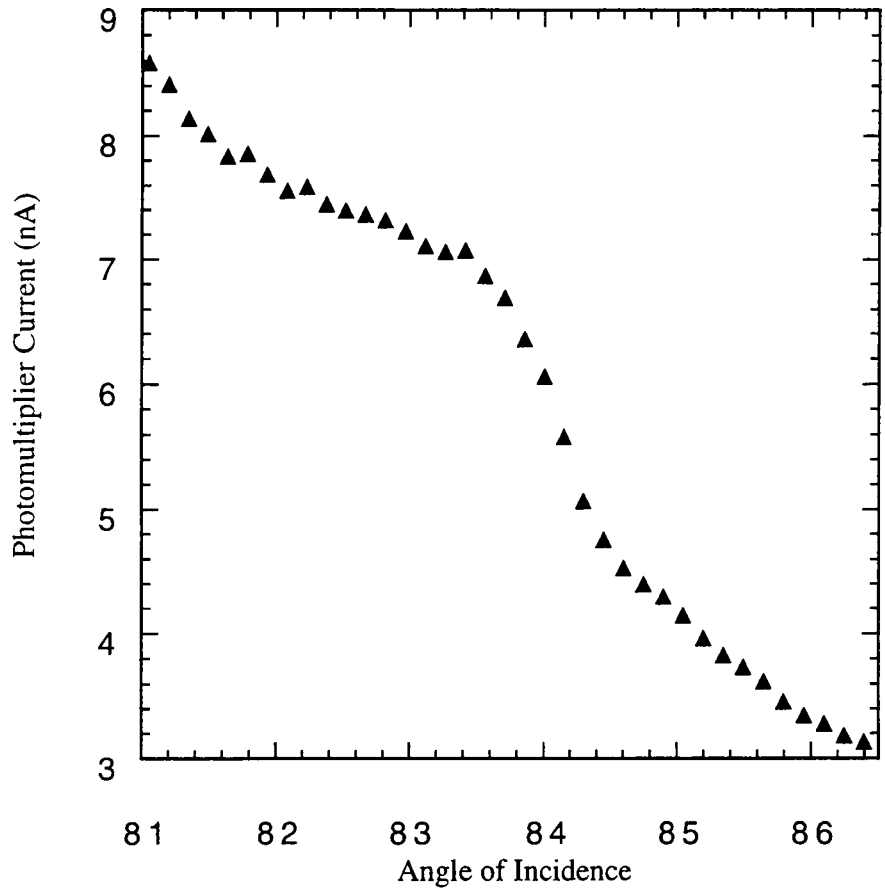


Figure III.17. Typical Transmission Data. Total internal reflection curve for aluminum thin-film grating obtained with soft x-ray microprobe.

strength of the evanescent field. The lateral and normal scan directions will be referred to as the x and z directions, respectively, as shown in **Figure III.12.** In this section we generate theoretical signals and show experimental data of probe scans corresponding to the x and z directions.

E.1. Theoretical Generation of Signals from Probe Scans

The intensity of the evanescent field varies exponentially in the z direction and periodically in the x direction; the signal detected by the soft x-ray probe as it scans the evanescent region will deviate accordingly. Here the intensity of soft x rays striking a theoretical probe scanned in the x and z directions is described. The probe will be treated as an Al detector with dimensions $<<\lambda$. Additionally, the theory will be limited to the description of soft x rays traveling from the Al thin-film grating to the Al probe; the soft x-ray collection or detection efficiencies associated with the probe and detection system will not be included. First, the intensity of soft x rays detected when the probe is scanned in the z direction will be studied; then, the intensity detected when the probe is scanned in the x direction will be presented.

If soft x-ray light strikes the Al-vacuum interface on the sample side of the Al thin-film grating, the light will be totally internally reflected into the Al thin film, and an evanescent wave will be created at the interface. The intensity of the evanescent field in the vacuum region decays exponentially with increasing distance from the interface. The decay length (γ) is described by:

$$\gamma = \frac{4\pi}{\lambda}\sqrt{\left(\frac{\tilde{n}_{Al}}{\tilde{n}_{vac}}\right)^2 \sin^2(\theta_i) - 1}\,.^{\text{III-1}} \qquad \textbf{(III.8.)}$$

The decay length depends on the indices of refraction of the two media, the wavelength of light, and the incident angle of the light. The dependence of the decay length on angle of incidence and the real part of the index of refraction, n, is shown in **Figure III.18.**

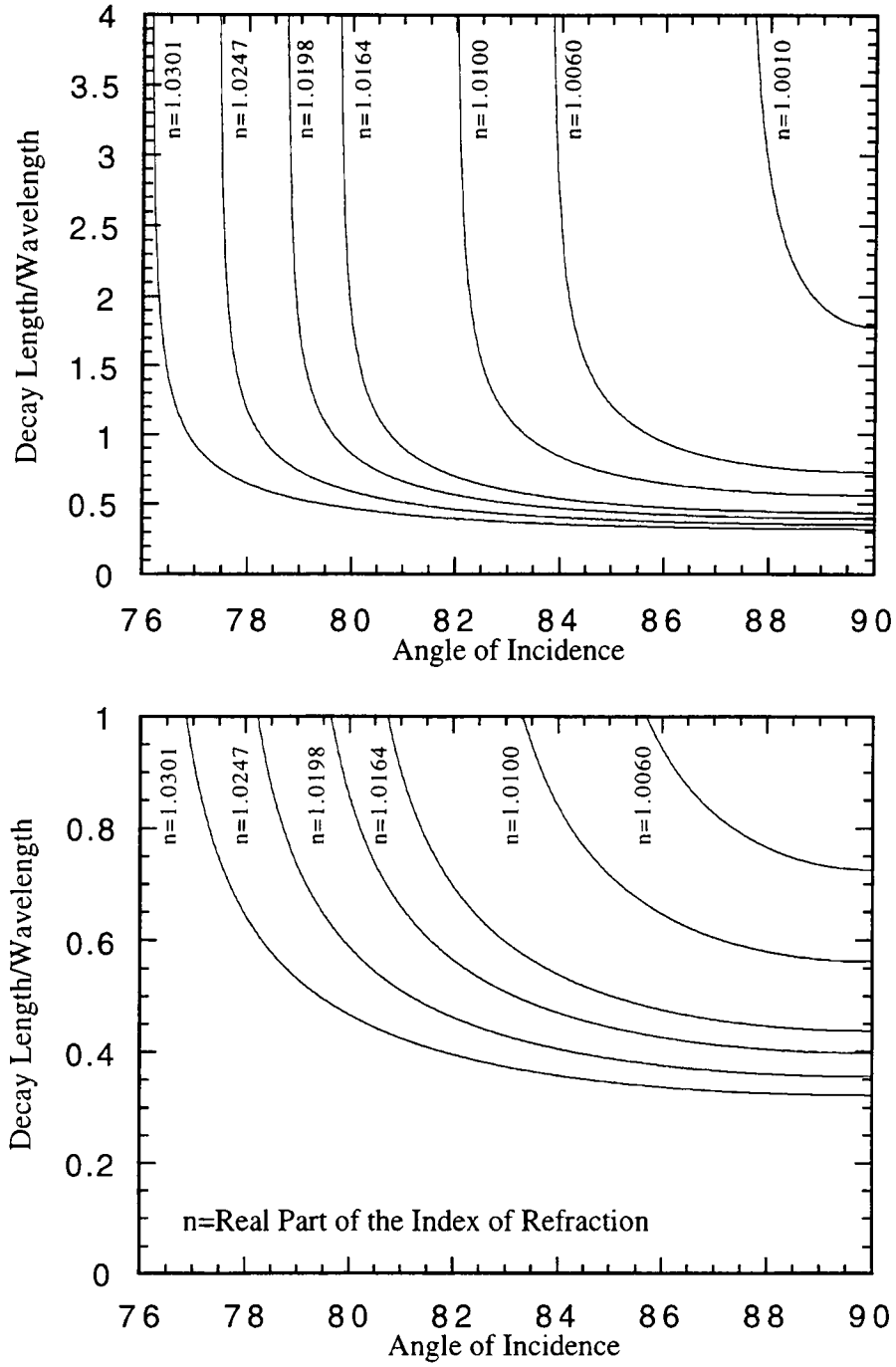


Figure III.18. Evanescent Field Decay Length. Decay length/wavelength of the evanescent field vs. angle of incidence for different *n*.

If a soft x-ray probe is inserted into the evanescent field region, frustrated TIR will occur, and light will tunnel from the Al thin film to the probe. The intensity of light tunneling from the Al thin film sample to the probe decreases as the separation distance between the probe and sample increases. The decrease of the tunneling signal is similar to, but not exactly the same as, the decay of the evanescent field. The intensity of tunneling soft x rays as a function of probe-sample separation can be described as a three-media layered system similar to the layered systems describing the operation of the Al thin-film grating (**Appendix B.**). The transmission of soft x rays from the sample to probe depends on the angle of incidence and the probe-sample separation distance. Also, the transmission depends on the photon energy since the index of refraction and the wavelength of light are functions of photon energy. **Figure III.19.** shows the theoretical transmission for an Al-vacuum-Al system for different angles of incidence to the Al-vacuum interface.

The transmission of soft x rays from the sample to probe as a function of position on the x-axis will depend on the probe-sample separation distance. However, if the probe is in the evanescent field region, the transmission will be a periodic function of x. The periodic relationship arises from the geometry of the square-well pattern on the grating side of the Al thin film. As described in the section concerning the Al thin-film gratings, light incident on different regions of the grating will interact differently with the thin-film grating. Light incident on the high and low flat regions of the grating will not create an evanescent wave on the sample side of the thin-film grating, but light incident on the step region of the grating can create an evanescent wave on the sample. As shown in **Figure III.12.** for $\theta_i > \theta_c$, some regions of the sample have evanescent waves, and the rest of the sample has a small amount of light transmitted through the Al-vacuum interface.

The regions of evanescent waves are a direct result of light hitting the step region of the grating, and the regions of transmitted light result from light hitting the flat regions of the grating. Since absorption increases exponentially with increasing pathlength, the

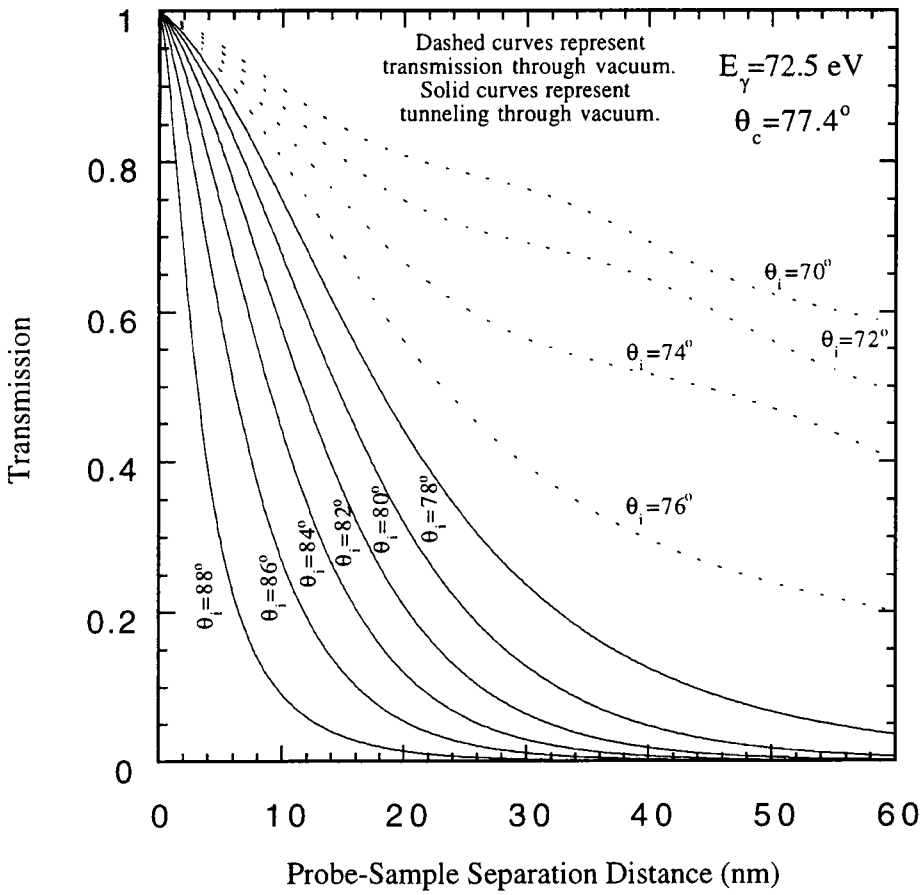


Figure III.19. Theoretical Tunneling Signal for Z Scans. Theoretical transmission of tunneling soft x rays from thin-film grating to probe vs. probe-sample separation distance for different angles of incidence.

amount of light coming from the step region and hitting the sample interface decreases exponentially with the position on the x-axis. Consequently, the evanescent field strength will decay exponentially as a function of position on the x-axis, too. The exponential decay in the x direction is not as strong as the exponential decay of the evanescent field in the z direction because the decay constant for absorption below the Al L_{23}-shell edge is much smaller than the decay constant for the evanescent field.

The intensity of soft x rays detected by the probe as a function of position on the x-axis can be generated easily by combining the theories describing the thin-film gratings and tunneling soft x rays. The sample side of the thin-film grating can be divided into regions corresponding to the regions of the grating side. The region on the sample where incident light comes from the step region of the grating will be referred to as the step region of the sample. Likewise, high and low flat regions on the sample will correspond to light coming from the high and low flat regions of the grating.

The amount of light emitted from the high flat regions into the vacuum will essentially be $f_{high}T_{high}$; likewise, the light emitted from the low flat region will be $f_{low}T_{low}$. Here f_{high} and f_{low} are determined by equations **(III.3.)** and **(III.4.)**, and T_{high} and T_{low} are calculated with the thin film theory described in **Appendix B.** To simplify the theory the transmission of light through the high and low flat regions of the sample to the probe will be considered independent of the probe-sample separation distance.

The amount of light transmitted through the step regions of the sample will depend on the probe-sample separation distance as well as the thin-film grating conditions. By using thin film theory from **Appendix B.** with equations **(III.2.)** and **(III.5.)** the transmission signal of the SXPSTM can be written:

$$T_{SXPSTM} = f_{step}T_{vac-Al}T_{film}T_{sample-probe}. \qquad \textbf{(III.9.)}$$

However, to describe the transmission to a small probe close to the sample surface, the transmission through the Al thin film, T_{film}, must be calculated for each position of the probe on the x-axis. Previously, in the theory describing the thin-film gratings the

pathlength of light, ℓ, of equation **(III.1.)** was averaged to simplify the theory, but for the calculation of T_{SXPSTM} , ℓ will be written as a function of position on the x-axis.

Figures III.20., III.21., and **III.22.** show the calculated transmission from sample to probe for scans in the x direction. **Figure III.20.** shows the variation of the transmitted signal for different probe-sample separation distances, and the periodic function of the transmission is shown over a 10 μm range. The period of the signal is 2 μm. **Figure III.21.** shows the spreading of the evanescent field region as the angle of incidence is increased. Finally, **Figure III.22.** shows theoretical transmission curves for scans in the z and x directions for conditions that are most closely related to the experimental conditions.

Because of assumptions made in the theoretical calculations, the theory represents an ideal sample-probe system that is impossible to duplicate in the laboratory, and actual data should differ from the theoretical calculations. In particular, the assumption that all surfaces on the Al thin-film grating are smooth should cause an underestimate for the transmission of soft x rays through the high and low flat regions of the thin-film grating. The surfaces of the thin-film gratings cannot be perfectly smooth when compared with the small wavelength of light involved in this experiment. Thus, the background signal detected by the probe will be much stronger than theoretically predicted. In addition to the assumption of ideally smooth surfaces, the assumption of an infinitesimally small soft x-ray probe causes the theoretical curves to be more defined than an actual probe could produce. Although the probes envisioned for the SXPSTM would be small enough to resolve the 2 μm spaced evanescent field pattern with similar resolution to the theoretical predictions, this study involves probes with larger diameters, and the actual transmission data should show a rounded image of the theoretical calculations. Although the theory does not predict the actual experimental results, the theory describes the dependence of the expected transmission signal on the physical dimensions of the probe-sample system.

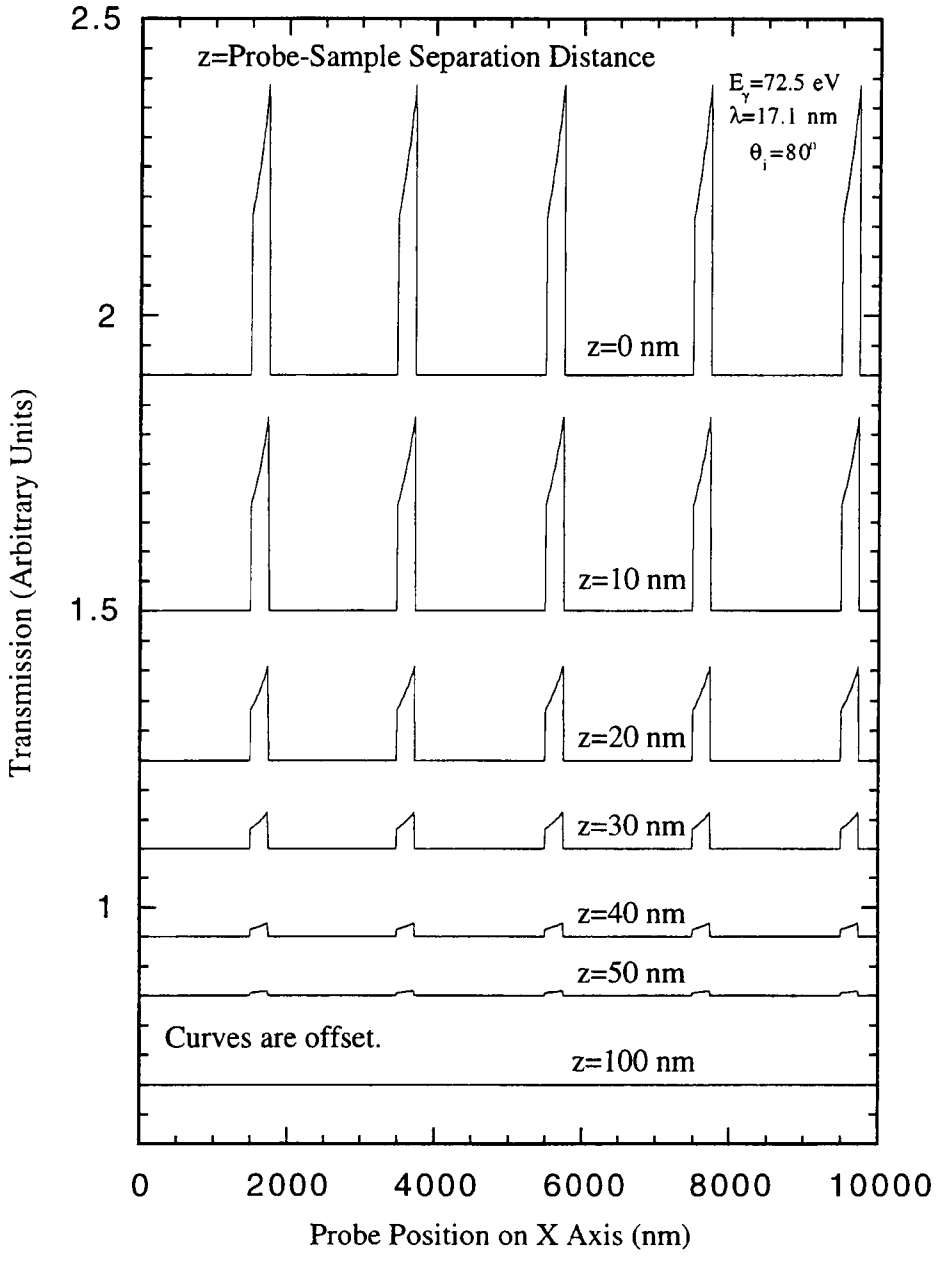


Figure III.20. Theoretical Periodic Signal of X Scans. Theoretical probe signal vs. probe position on the x axis for different probe-sample separation distances.

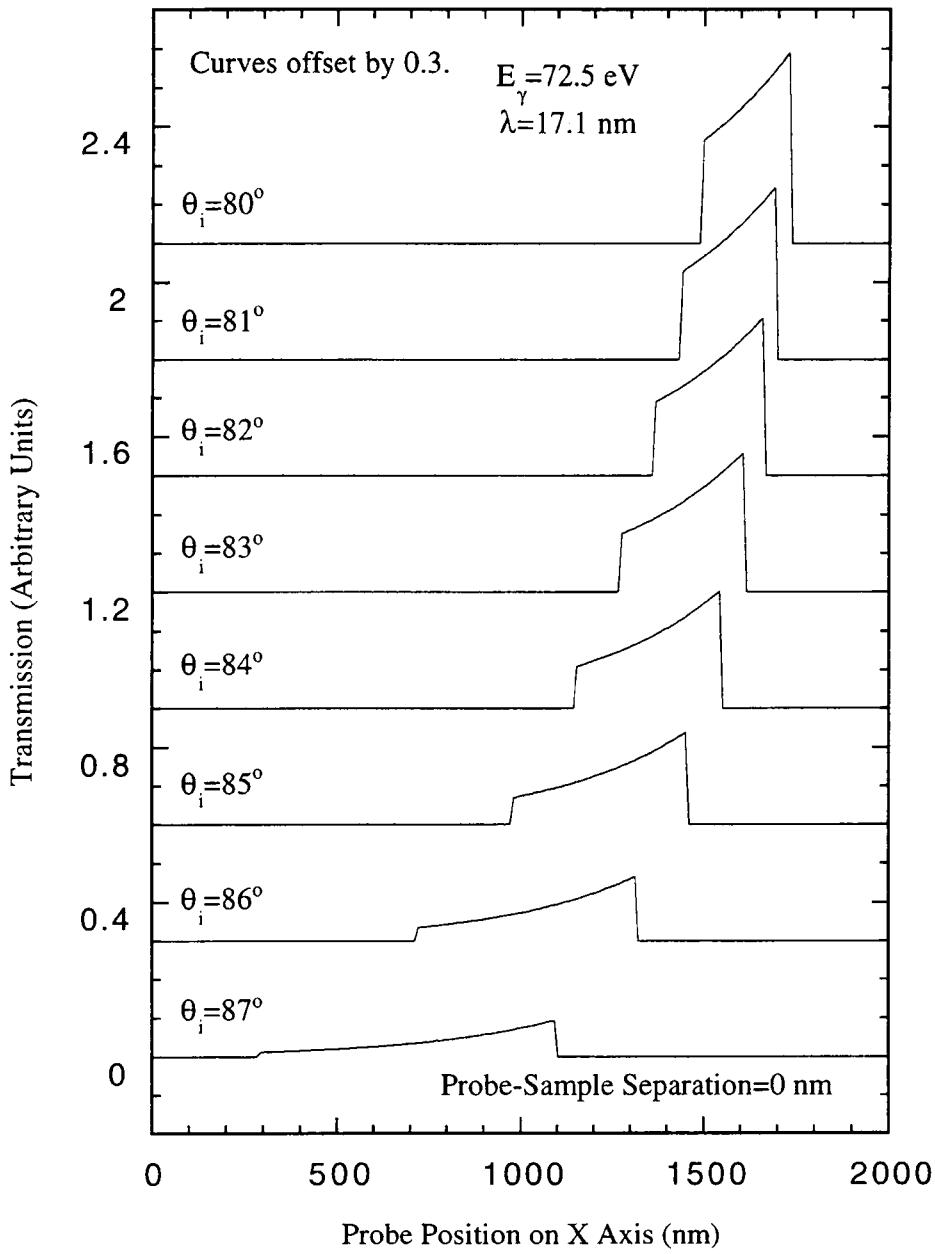


Figure III.21. Spreading of Evanescent Field Region. Theoretical probe signal vs. probe position on the x axis for different angles of incidence.

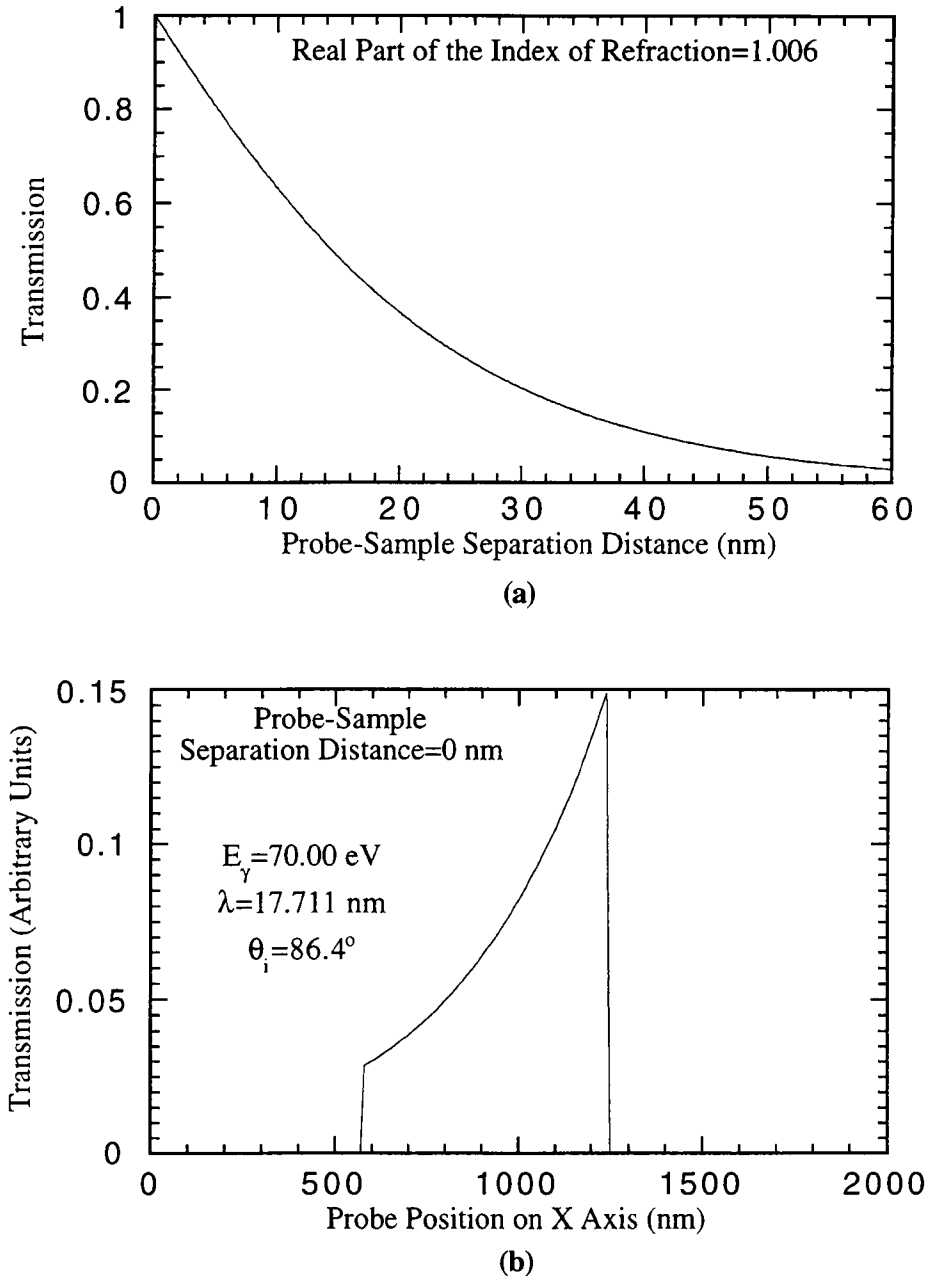


Figure III.22. Theoretical Signals for Experimental Conditions. Theoretical probe signal vs. **(a)** probe-sample separation distance and **(b)** probe position on x axis for experimental conditions.

E.2. Experimental Data from Probe Scans

The evanescent field was examined experimentally with the SXPSTM setup. Preliminary experiments were conducted to determine the best conditions for sampling the evanescent field; then, the soft x-ray probe was moved into the evanescent field region and scanned to detect signals relating to the varying evanescent field strength. First the preliminary experiments will be reviewed; then, the data for scans in the x and z directions will be presented.

The probe was moved toward the Al-vacuum interface of the Al thin-film grating with the Inchworm motor. With each step of the Inchworm motor, the probe was scanned in the x direction, and the photomultiplier signal was monitored. The computer controlled the Inchworm motion, probe scanning, and signal monitoring. This allowed the computer to stop the Inchworm motor and pull the probe back with the piezoelectric tube if a signal was detected that suggested the probe was near or on the surface of the thin-film grating. Periodically, the Inchworm was stopped and a transmission vs. angle of incidence curve was obtained as described in **Section III.D.2.** This was done to assure that beam motion in the synchrotron ring did not cause an energy shift in the light output from the monochromator. Once the evanescent field was detected, the piezoelectric clamps of the Inchworm motor were secured. The piezoelectric tube provided 4 μm of motion in the z direction and 10 μm of motion in the x direction. Scans for various times and dimensions were recorded.

The angle of incidence for the light incident on the Al thin-film grating was 86.4°. **Figure III.17.** shows the TIR curve obtained for the energy and corresponding index of refraction utilized. The angle of incidence was chosen based on the TIR curve of **Figure III.17.** to reduce the background signal and obtain the best conditions for signal detection based on the parameters of the grating and the expected parameters for the dimensions of the evanescent field. All of the data presented here was obtained with these conditions.

Once the probe entered the evanescent field region and was scanned in the x direction, the periodic signal relating to the grating structure helped determine the position of the probe relative to the sample surface. **Figure III.23.** shows two x-axis scans taken at different probe-sample separation distances. The periodic structure of the evanescent field distribution across the x-axis of the sample is apparent in the scans where the probe is near the surface of the sample; however, at larger probe-sample separation distances no periodic signals relating to the evanescent field are seen.

The periodic distribution associated with the grating structure provided a test pattern to compare with the experimental data. **Figures III.24., III.25., III.26.,** and **III.27.** all show various x scans of the surface of the sample; the scans were taken under various conditions. The primary feature that all of the scans show is the repeating structure expected from the periodic distribution of the evanescent field. The period of the data matches the expected period of the grating structure well. Peaks corresponding to photon tunneling in the evanescent field are approximately 2 μm apart, and peak widths are between 500 and 1000 nm.

It should be noted that several factors prevent producing perfectly spaced data. The deflection of the piezoelectric scan tube is not a perfect linear function of the voltage applied, and there is a short delay of motion after a scan is started. In fact, some curvature is expected in x scans for piezoelectric tubes; z motion will accompany x deflection to some degree. The piezo tube was assembled and mounted by hand, and the "homemade" control electronics were simple circuits with non-perfect linear gain. The "homemade" nature of the system coupled with the non-rigid freestanding thin film results in non-perfect linear scans across axes that are not perfectly orthogonal to the sample-vacuum interface. The piezoelectric tube was calibrated with a highly sensitive feeler gauge, and the probe positions on the z and x axes should be approximately 10% and 20% accurate, respectively.[III-21]

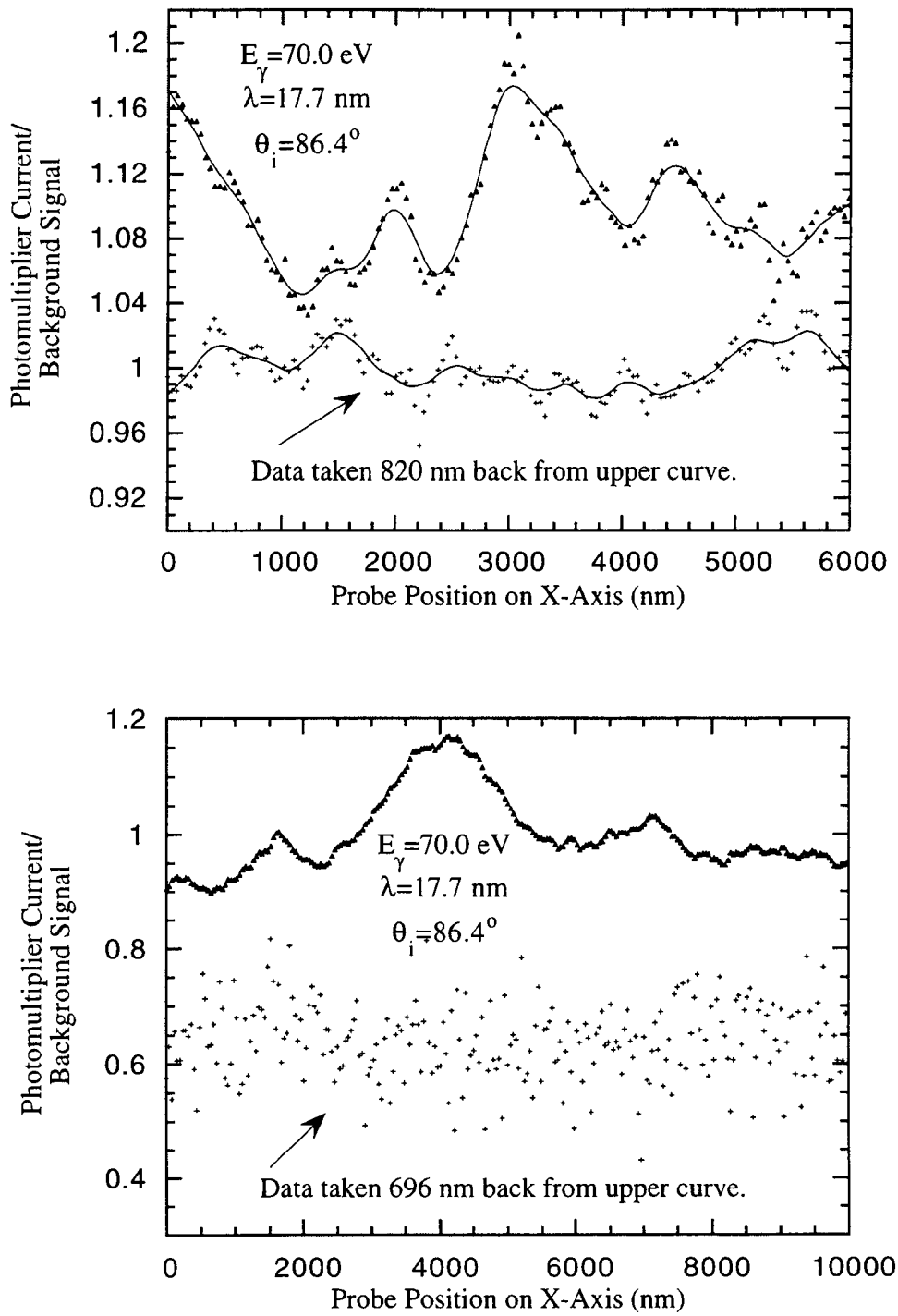


Figure III.23. X Scan Data I. Data for probe scans in the x direction.

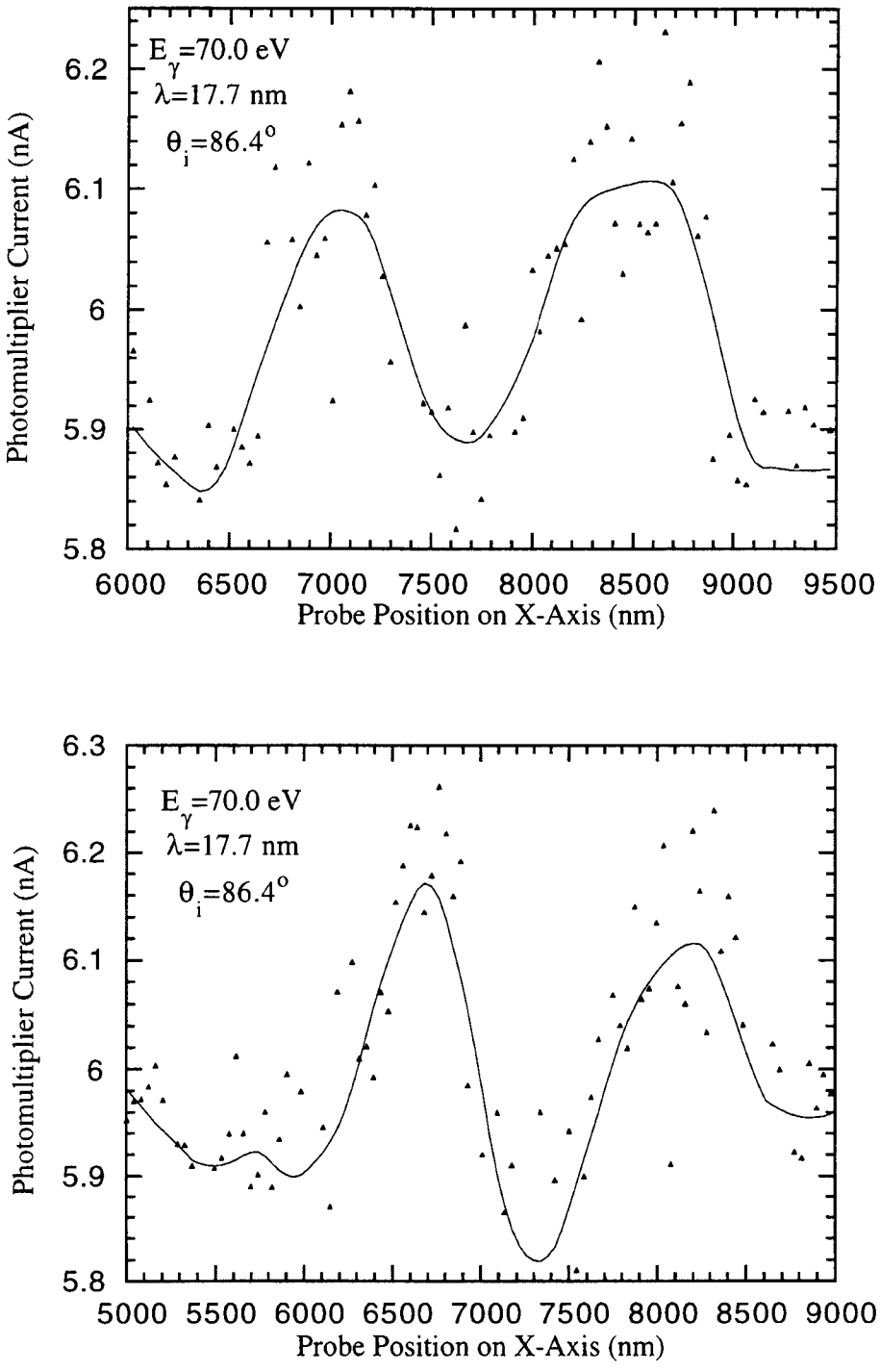


Figure III.24. X Scan Data II. Data for probe scans in the x direction.

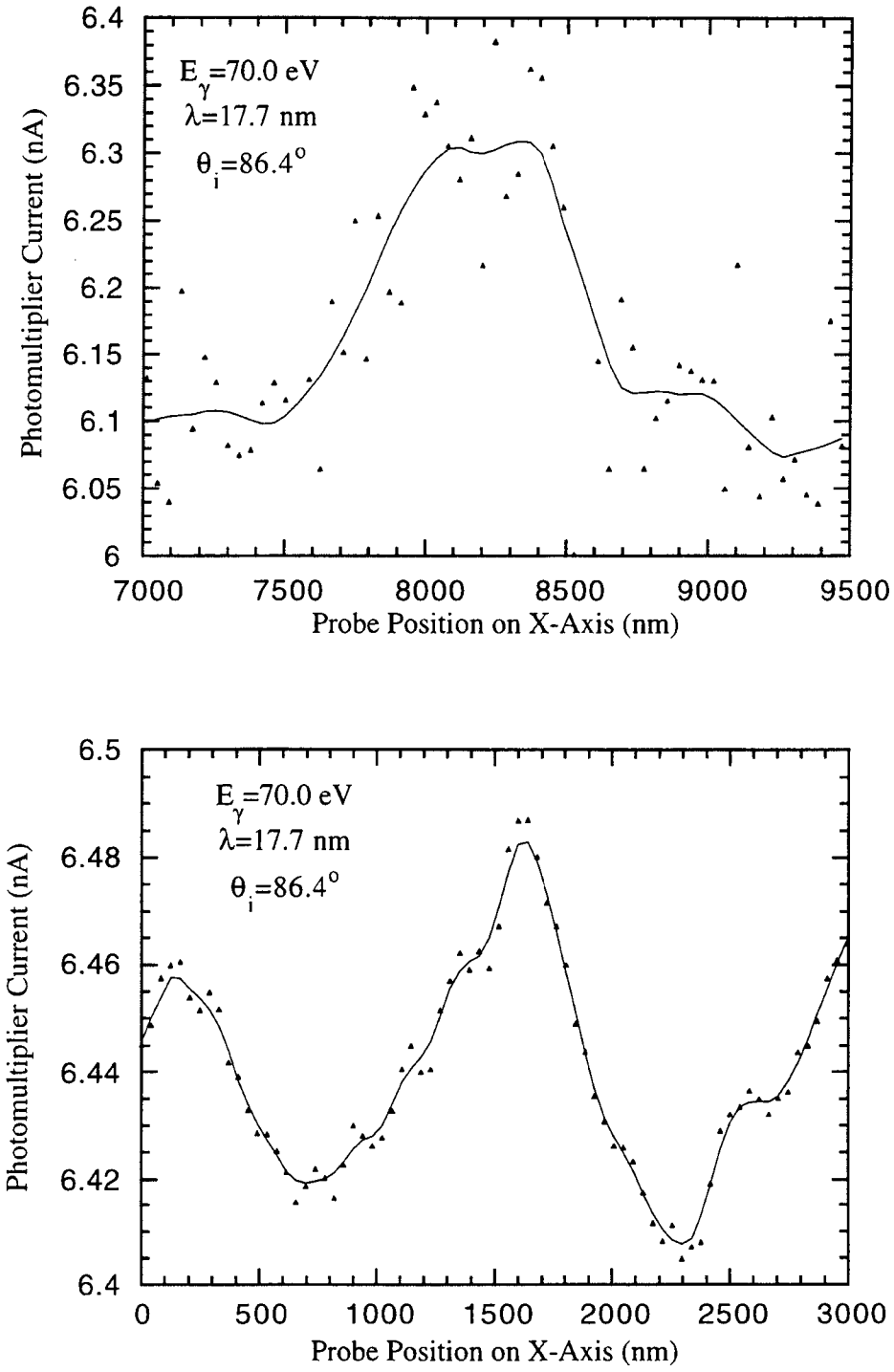


Figure III.25. X Scan Data III. Data for probe scans in the x direction.

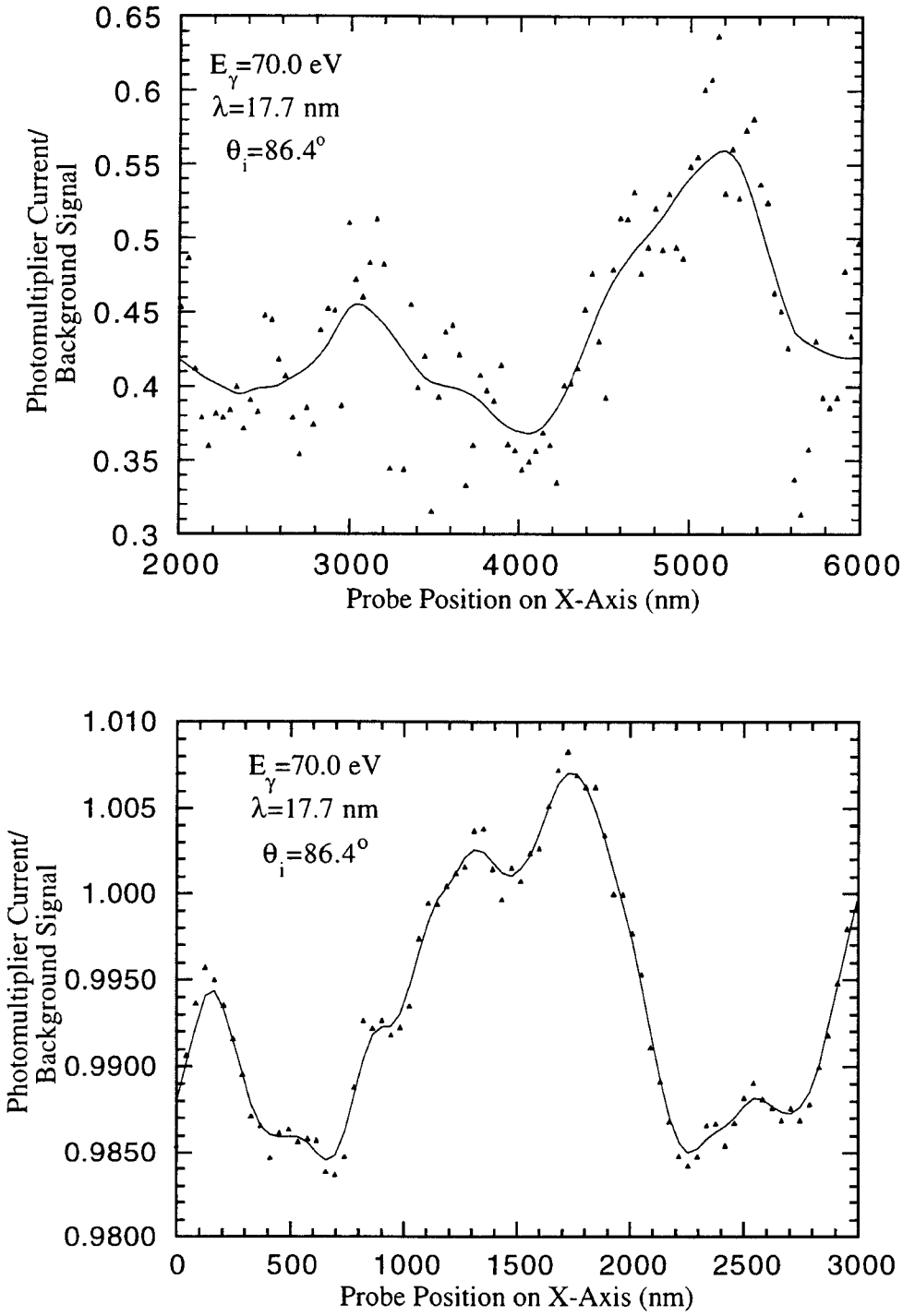


Figure III.26. X Scan Data IV. Data for probe scans in the x direction.

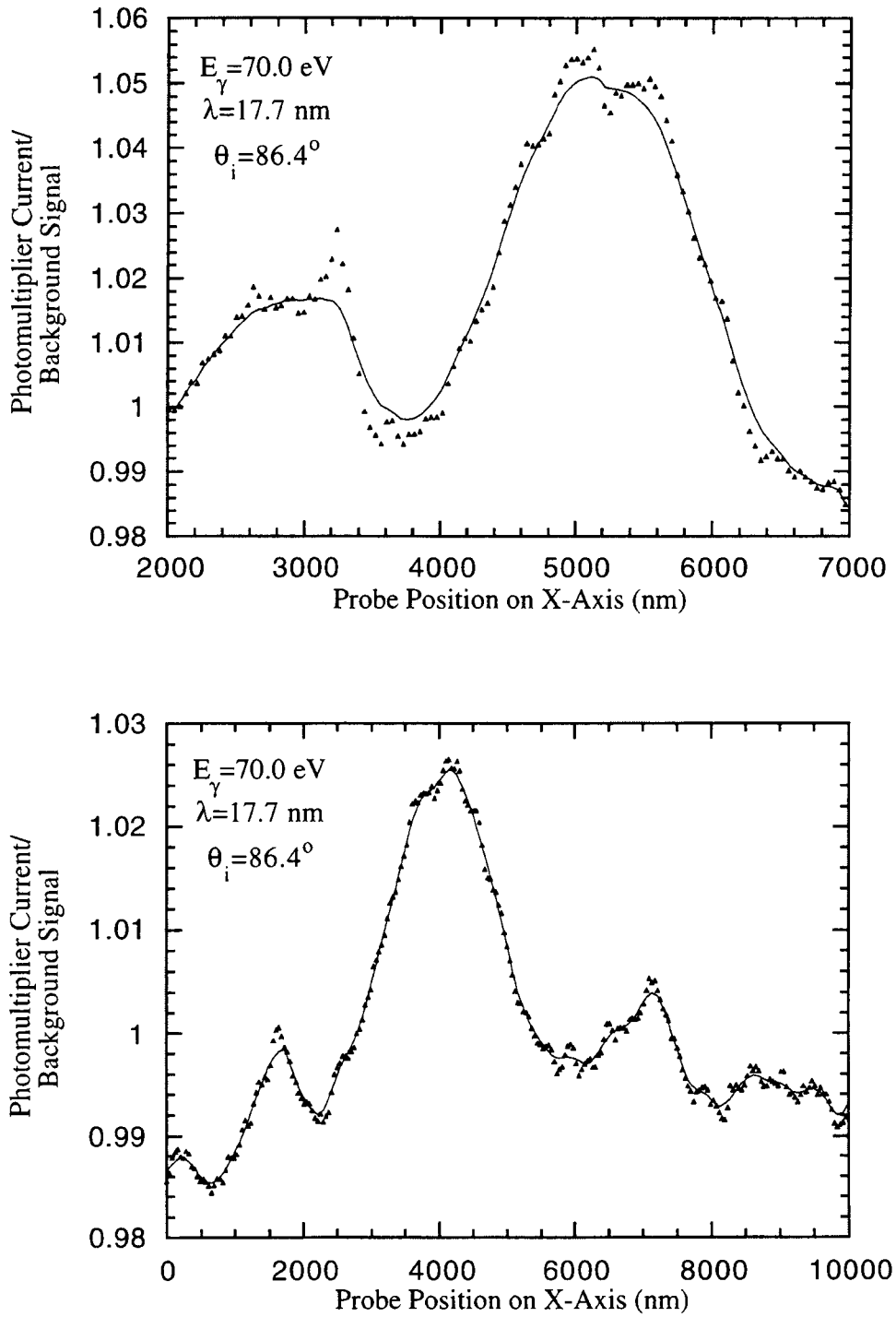


Figure III.27. X Scan Data V. Data for probe scans in the x direction.

The relative signal to background ratio can be seen by the data in **Figures III.24.** and **III.25.** As expected, the background signal is larger than theoretically predicted. Typical signal to background ratios were 0.01 to 0.07. The background is primarily due to soft x-ray light scattering through the high and low flat regions of the grating. Dark current and stray visible light detection were minimized by cooling the photomultiplier tube and shielding the vacuum system and the optical fiber leading to the photomultiplier tube housing. The signal from dark current and stray visible light is negligible when compared with the signal from soft x-ray light transmitted through the grating.

The different relative heights of the peaks is attributed to several factors. Any inconsistency in the grating structure at the small step region that is responsible for transmitting the soft x-ray light to the evanescent field region will cause varying peak heights and profiles in the tunneling signal detected by the probe. Of course, the peak heights will vary with probe-sample separation and the varying light output from the monochromator over time. If the scan axis is not parallel to the sample surface, the probe-sample separation variations will cause exponentially varying peak heights. In the large peaks shown in **Figure III.27.**, the probe was most likely touching the thin film surface. The height and width of these peaks when compared with the rest of the data suggest that the probe was in contact with the thin film and moving or stretching the thin film as the probe was scanned. No damage to the thin film or probe was detected when this occurred. In fact, the probe could be moved into the thin film over 10 μm and more without damage occurring to either the probe or thin film. Apparently, the phosphor grains are rigidly adhered to the optical fiber with the sodium silicate as described in Section III.C.3.

Although the flexibility of the thin film eased problems of "tip crashing" commonly associated with scanning probe microscopy, the movement of the thin film caused problems in determining the evanescent field decay length and location of the thin film relative to the tunneling signal. Consistent results for tunneling signals during z-axis

scans were hard to obtain. Moving the probe both toward and away from the sample interface caused movement of the thin-film grating. Additionally, the oxide layers on the probe and sample surfaces prevented Al-Al contact that would provide the maximum tunneling signal. The limited data obtained is shown in **Figures III.28.** and **III.29.**

Figure III.28. is an example of the uncertainty in probe position created by the movable thin film. There are two regions (probe position=0 and 500 nm) in the large scan that could be considered evanescent field decay. However, it is uncertain whether the rise in the signal at 0 or 500 nm relates to the evanescent field region. Probe-sample contact might have occurred at 500 nm. If so, the probe might have moved along the thin film laterally until an evanescent field region was crossed giving rise to the peak at 0 nm. Or, the probe might have deformed the grating in a localized region around the probe position so that more light was transmitted through the grating. Either case is plausible.

Because of the problems created by the movable thin film, the scans in the z direction were limited to scans over small ranges that would not cause significant movement of the thin film. **Figure III.29.** shows scans of this nature. The oxide layers and problems of thin film movement reduce the signal strength observed; however, exponential curves were fitted to the data to obtain decay lengths for the signals. The decay lengths of 28.6 and 12.5 nm are close to the predicted value of approximately 20 nm.

The experimental data show the expected tunneling signals for scans in the x and z directions. For x scans, the dimensions of the periodic evanescent field regions observed in the data correspond well with the expected dimensions within the accuracy of the experimental conditions. The general variations in the tunneling signal observed during scans in the z direction also match theoretically expected results. Although complications arose from the flexibility of the thin-film grating, experimental decay constants for the evanescent field are close to the expected constant of 20 nm. The magnitude of the signals obtained with the large (≈200-300 nm) probe were small when

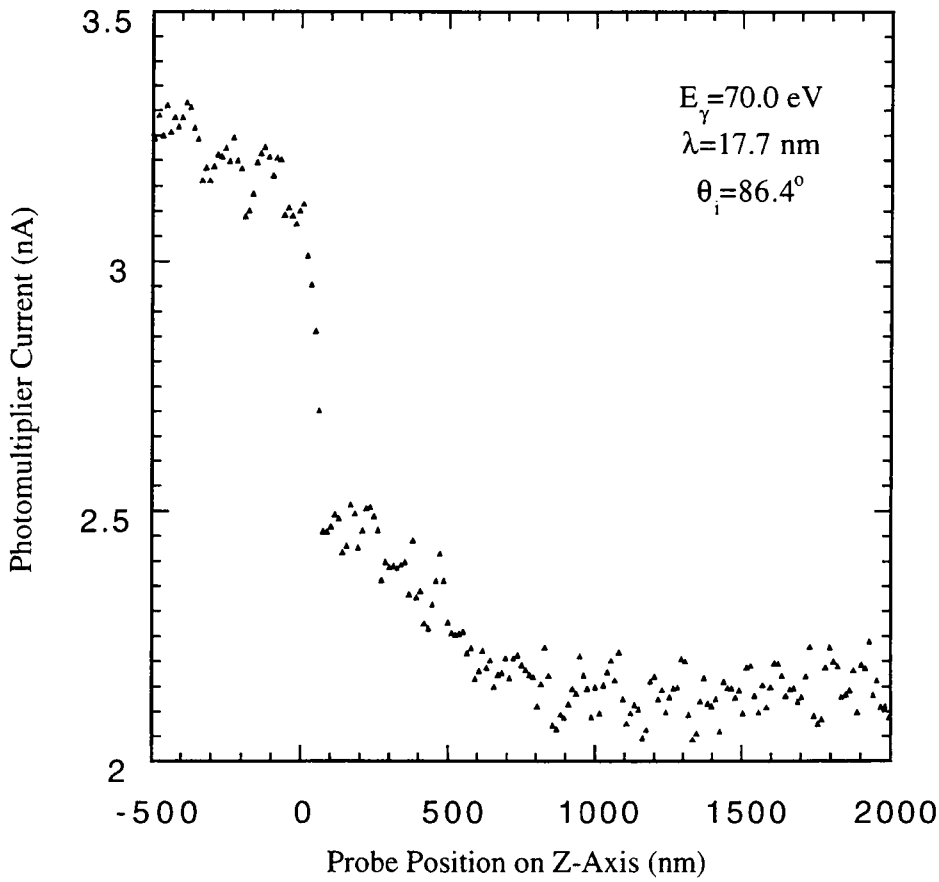


Figure III.28. Z Scan Data I. Data for a probe scan in the z direction.

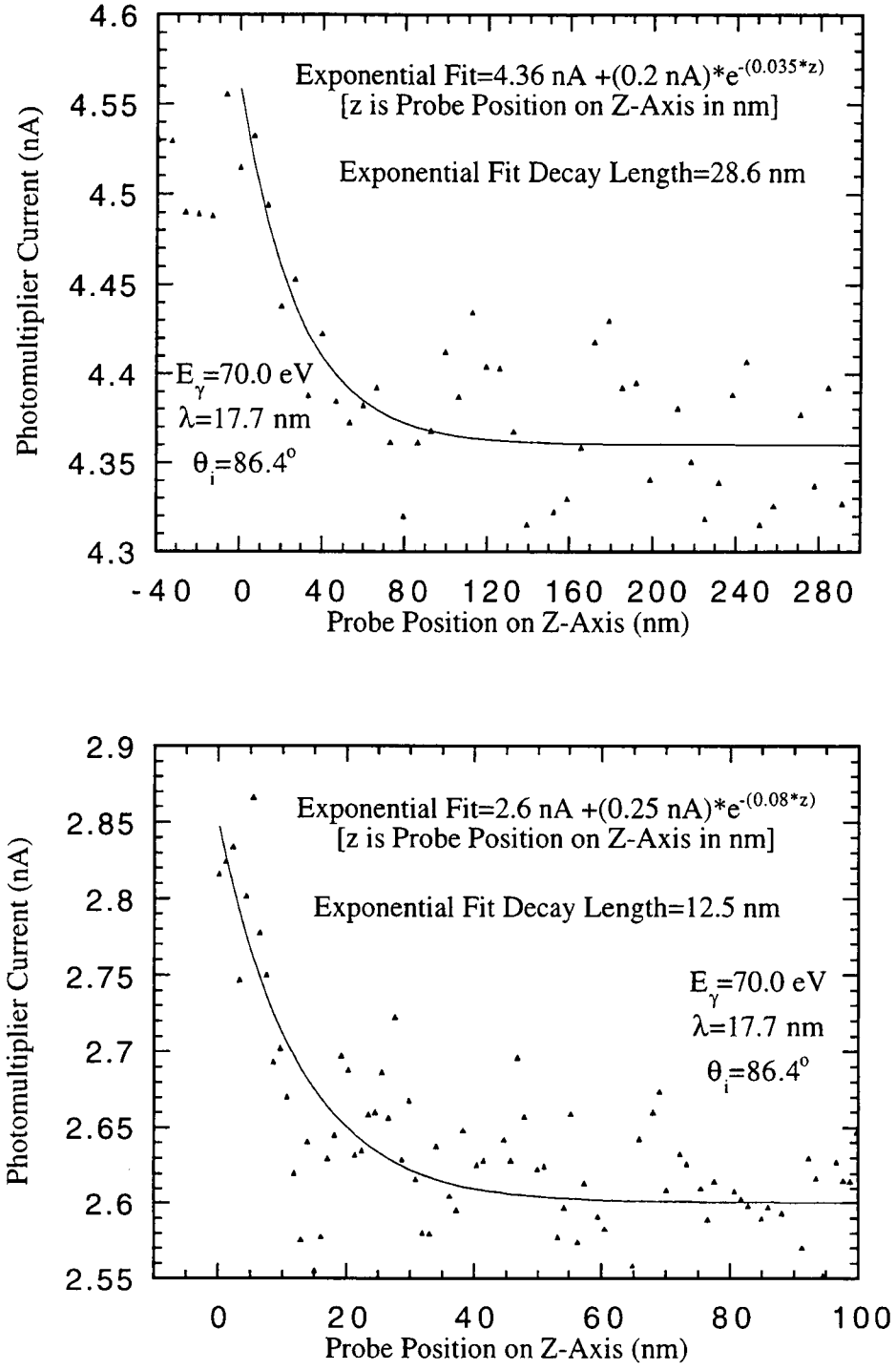


Figure III.29. Z Scan Data II. Data for probe scans in the z direction.

compared with the background signal from light scattered through the high and low flat regions of the thin-film grating. Al_2O_3 in the Al thin film and on the surfaces of the thin film and probe created problems by reducing the index of refraction of the thin film and decreasing the tunneling signal at probe-sample contact. Additionally, the flexibility of the thin-film grating made the probe-sample system more susceptible to vibration, and problems in determining the absolute position of the sample relative to the probe occurred. The data show evanescent fields produced on an Al-vacuum interface in the soft x-ray region, and the evanescent fields produced have been probed and characterized by soft x-ray tunneling to a sub micron detector scanned within 100 nm of the Al-vacuum interface.

F. Conclusion

Technologies relating to the PSTM and science in the soft x-ray region have been advanced by producing a soft x-ray version of the PSTM, the SXPSTM. For soft x-ray light just below the L_{23} absorption edge of Al, the real part of the index of refraction of Al is greater than 1 and absorption is at a minimum. Soft x rays in this region have been employed to create a soft x-ray version of the familiar prism and fiber optic probe detector used in visible photon scanning tunneling microscopy. Al thin-film gratings and soft x-ray probes suitable for creating and detecting a soft x-ray evanescent field have been developed. An evanescent field has been created on an Al-vacuum interface and probed with a soft x-ray microprobe.

TIR at an Al-vacuum interface in the soft x-ray region has been detected by observing the transmitted intensity of soft x rays through an Al thin-film grating. The observed TIR in the soft x-ray region indicates the presence of a soft x-ray evanescent field. The critical angle for TIR observed was larger than expected; Al_2O_3 in the Al thin

film is suspected of reducing the index of refraction of the Al. The soft x-ray evanescent field created by an Al thin-film grating has been probed by observing the transmitted signal of soft x rays from the Al thin film to a soft x-ray probe inserted into the evanescent field. As the probe was scanned laterally across the Al thin film sample, periodic variations in the intensity of the detected signal were observed. The variations in the observed signal correspond to periodic regions of evanescent waves on the Al thin film sample. Variations in the detected signal occurred when the probe was scanned in the direction normal to the Al thin-film grating, also. The flexibility and movement of the thin-film grating caused problems in determining the exact position of the Al-vacuum interface, but tunneling signals that decay sharply with probe motion on the order of the wavelength of light (17.7 nm) were detected.

Total internal reflection in an Al thin-film grating has been demonstrated with soft x-ray light. The evanescent wave created at the Al-vacuum interface has been probed and characterized with a soft x-ray microprobe. The information obtained and physical processes observed are important resources for future work in the soft x-ray region and with the SXPSTM.

List of References

List of References

[I-1]Binnig, et. al.

[I-2]US Patent 5018865 (Nov. 1986).

[I-3]R. C. Reddick, R. J. Warmack, and T. L. Ferrell, *Phys. Rev. B* **39**, 767 (1989).

[I-4]R. C. Reddick, R. J. Warmack, D. W. Chilcott, S. L. Sharp, and T. L. Ferrell, *Rev. Sci. Instrum.* **61**, 3669 (1990).

[I-5]S. L. Sharp, "Substrates for Combined Surface Enhanced Raman Spectroscopy and Photon Tunneling Measurements", Ph. D. Dissertation, University of Tennessee, Knoxville (1992).

[I-6]T. L. Ferrell, S. L. Sharp, and R. J. Warmack, *Ultramicroscopy* **42-44**, 408 (1992).

[II-1]Handbook of Optical Solids, ed. E. D. Palik, 1985.

[II-2]S. L. Sharp, R. J. Warmack, J. P. Goudonnet, I. Lee, and T. L. Ferrell, *Acc. Chem. Res.* **26**, 377 (1993).

[II-3]Hg arc lamp, model #6281,Oriel Corporation, 250 Long Beach Blvd., P. O. Box 872, Stratford, CT 06497.

[II-4]PMT model #9412, Thorn EMI Electron Tubes Inc., 100 Forge Way, Unit F, Rockaway, NJ 07866.

[II-5]Fiber #16-105S, General Fiber Optics, Inc., 98 Commerce Rd., Cedar Grove, NJ 07009.

[II-6]PMT model #9524B, Thorn EMI Electron Tubes Inc., 100 Forge Way, Unit F, Rockaway, NJ 07866.

[II-7]Power supply model #304 with optical feedback unit model #TX5, Photochemical Research Associates Inc., 45 Meg Drive, London, Ontario, Canada N6E 2V2.

[II-8]F. Defornel, P. M. Adam, L. Salomon, J. P. Goudonnet, and P. Guerin, *Optics Letters* **19**, 1082 (1994).

[II-9]T. L. Ferrell, S. L. Sharp, and R. J. Warmack, *Ultramicroscopy* **42-44**, 408 (1992).

[II-10]Matching fluid code 06350, R. P. Cargille Laboratories, Inc., 55 Commerce Rd., Cedar Grove, NJ 07009.

[II-11]P-2000 Laser Based Micropipette Puller, Sutter Instrument Co., 40 Leveroni Court, Novato, CA 94949.

[II-12]Fused silica indices of refraction obtained by interpolation of values given by Newport Corporation in the *1994 Newport Catalog*, p. 2.99.

[II-13]S. Jiang, H. Ohsawa, K. Yamada, T. Pangaribuan, M. Ohtsu, K. Imai, and A. Ikai, *Jpn. J. Appl. Phys.* **31**, 2282 (1992).

[III-1]R. C. Reddick, R. J. Warmack, D. W. Chilcott, S. L. Sharp, and T. L. Ferrell, *Rev. Sci. Instrum.* **61**, 3669 (1990).

III-2Handbook of Optical Solids, ed. E. D. Palik, 1985.

III-3T. A. Callcott, W. L. O'Brien, J. J. Jia, Q. Y. Dong, D. L. Ederer, R. N. Watts, and D. R. Mueller, *Nucl. Instrum. and Methods A* **319**, 128 (1992).

III-4M. Okano, K. Kajimura, S. Wakiyama, F. Sakai, W. Mizutani, and M. Ono, *J. Vacuum. Sci. Technol. A* **5**, 3313 (1987).

III-5Coarse z motion obtained with Burleigh Instruments, Inc. UHVE-025 Inchworm Motor.

III-6Fine x, y, and z motion obtained with Staveley Sensors, Inc. EBL#2 Piezoceramic Tube Actuator.

III-7Corning 50/125 CPC3 Multimode Optical Fiber.

III-8RCA Photomultiplier Tube #C31034-02.

III-9MicroSi, Inc. Altilith Barrier Coating #CEM BC5.

III-10Shipley Microposit Photoresist #1811.

III-11Shipley Microposit Developer #MF-319.

III-12Shipley Microposit Remover #1165.

III-13USR Optonix Phosphor #WRE1150.

III-14D. E. Husk and S. E. Schnatterly, *J. Opt. Soc. Am. B* **9(5)**, 660 (1992).

III-15D. E. Husk and S. E. Schnatterly, *J. Opt. Soc. Am. B* **7(11)**, 2226 (1990).

III-16J. H. Halford, F. K. Chin, and J. E. Norman, *J. Opt. Soc. Am.*, **63**, 786 (1973).

III-17E. T. Hutcheson, G. Hass, and J. K. Coulter, *Optics Comm.*, **3**, 213 (1971).

III-18E. Shiles, T. Sasaki, M. Inokuti, and D. Y. Smith, *Phys. Rev. B* **22**, 1612 (1980).

III-19D. A. G. Bruggeman, *Ann. Phys.* **24**, 636 (1935).

III-20R. Jansson and H. Arwin, *Optics Comm.* **106**, 133 (1994).

III-21Federal Products Corporation, Model #432.

A-1S. J. B. Reed, Electron Microprobe Analysis, *Cambridge Univ. Press*, 1975.

A-2Novascan 30, SEMCO Instruments Co. Ltd., Ottawa, Canada, K2C OA7.

A-3Handbook of Optical Constants, Ed. E. D. Palik, *Academic Press*, 1985.

A-4Model 4028, Galileo Electro-Optics Corp., Galileo Park, Sturbridge, MA. 01518.

A-5N. A. Dyson, X-rays in Atomic and Nuclear Physics, *Cambridge Univ. Press*, 1990.

A-6W. J. McConnell, R. D. Birkhoff, R. N. Hamm, and R. H. Ritchie, *Radiat. Res.* **33**, 216 (1968).

A-7M. Gryzinski, *Phys. Rev.* **138**, A336 (1964).

A-8C. Feldman, *Phys. Rev.* **117**, 455 (1960).

A-9S. Thomas and E. P. Pattison, *J. Phys. D: Appl. Phys.* **3**, 349 (1970).

A-10H. J. Fitting, *Phys. Stat. Sol.* a**26**, 525 (1974).

C-1T. L. Ferrell, ORNL Notebook #A102885G, 94 (1992).

Appendices

Appendix A

Scanning Electron Microscope Soft X-Ray Spectrometry

A. Introduction

The scanning electron microscope (SEM) has been one of the most important tools for scientists in the twentieth century. By monitoring the back scattered electrons produced when an electron beam is scanned across a sample of interest the SEM produces an image of the sample down to resolutions <1 nm. While the scattering of electrons from the sample surface gives structural information about the sample, other physical processes occurring when the electron beam bombards the sample produce more information about the sample. One such process of interest is the emission of x rays. The work described here demonstrates that the detection of characteristic soft x rays with a wavelength dispersive spectrometer provides a means of determining the spatial concentration of light elements in a SEM sample.

The technique of using characteristic x-ray emission to perform spectroscopy on SEM samples has already been investigated to a great extent. In fact, commercial x-ray spectrometers exist that are capable of detecting most of the atomic elements. These spectrometers operate as energy dispersive spectrometers. X rays emitted by the SEM sample are passed through a thin window and collected by a solid state detector. With each x ray absorbed by the solid state detector an electronic pulse is created and sent to

analyzing electronics. By measuring the size of the electronic pulse the energy of the absorbed x ray can be determined. Thus, by counting and analyzing electronic pulses created by characteristic x rays the relative concentration of atomic elements in a SEM sample can be mapped. This method of SEM x-ray spectroscopy works extremely well for most elements; however, difficulties occur when analyzing elements with low atomic numbers, or light elements. The x-ray energies of light elements are relatively low, while a solid state detector works best with high energy x rays. Three main factors reduce the performance of solid state detectors at low energies. The transmission of x-ray windows becomes smaller, the size of the electronic pulse from the low energy x ray is smaller, and background noise becomes stronger. As the number of x rays detected becomes smaller and the size of the pulses relative to the noise level becomes smaller, the detection capability gets worse.

The work presented here explores a different approach to the problem of detecting characteristic x rays of light elements during SEM operation. Instead of detecting x rays with an energy dispersive spectrometer, x rays have been detected with a wavelength dispersive spectrometer. A soft x-ray spectrometer that uses a Au-coated spherical grating at grazing angles of incidence to disperse light has been designed for use with a SEM. The light elements Li, Be, B, C, Mg, Al, and Si have been detected with the soft x-ray spectrometer. By using this soft x-ray spectrometer, elemental spectroscopic images have been simultaneously obtained with structural images taken by the SEM.

Although the overall objective of an energy dispersive spectrometer and the soft x-ray spectrometer is the same, their operation differs both in procedure and benefit. The most notable difference is the region of the x-ray spectrum in which the detectors operate. An energy dispersive detector only detects hard x rays; the soft x-ray spectrometer presented here detects soft x rays. The main differences between hard and soft x rays are the penetration capabilities of the x ray and the energy of the x ray. Hard x rays penetrate deep into matter, but soft x rays only penetrate ~1 μm into matter before the x ray is

absorbed. The energy of x rays is associated with the definition of "hard" and "soft" x rays. Hard x rays range from ~200 eV to 10^5 eV, and soft x rays range from ~50 eV to ~200 eV. The photon energy range between 50 eV and 100 eV is defined by some to be the extreme ultraviolet. Since the work here involves photons created by movements of inner shell electrons which is characteristic of x rays, the 50 eV to 100 eV range will be referred to as soft x rays.

The primary x rays detected by the energy dispersive detector are K-shell x rays. K-shell x rays are the x rays produced when an electron hole is created in the innermost electron shell, the K shell, and an electron from the conduction band fills the hole by moving into the K-shell orbit. A photon corresponding to the energy difference between the conduction band and the K shell is emitted. The soft x-ray spectrometer detects some K-shell x rays and some L-shell x rays. L-shell x rays are x rays produced when an electron fills a vacancy in the L electron shell in a similar fashion to the production of a K-shell x ray. The L shell is the second inner most electron shell. For Li, Be, and C, K-shell x rays were detected by the soft x-ray spectrometer; for Mg, Al, and Si, L-shell x rays were detected.

Although an energy dispersive detector becomes less efficient as photon energy decreases, the soft x-ray spectrometer increases in efficiency with decreasing photon energy. The main factor contributing to better efficiencies at lower photon energies is the increase in reflectance of the grating surface at lower photon energies. Additionally, the background noise level of the soft x-ray spectrometer, due primarily to bremsstrahlung radiation, becomes higher at shorter wavelengths, or higher energies. These factors make the soft x-ray spectrometer suitable for elemental spectroscopy of the light elements with the SEM.

Certain spatial and compositional resolution limits exist for elemental spectroscopy with electron excitation. When an energetic electron enters a solid, the electron scatters through interactions with electrons in the solid. The electron can

produce electron holes, and thereby produce x rays, all along its path of travel. Additionally, secondary electrons produced by the primary electron can produce x rays. The resulting volume of solid where x rays can be produced is the volume occupied by scattered electrons. The spatial resolution of x-ray spectrometers is limited to the largest cross sectional area of this volume. Since the pathlength of electrons varies with different materials and electron energies, spatial resolution depends on the properties of the material and the electron energy employed. The pathlength of electrons in low density materials is larger than pathlengths in high density materials; therefore, x-ray spectrometry of low density materials, which includes materials with light elements, will have larger spatial resolution. The spatial resolution, σ, in μm can be expressed by the empirical relation

$$\sigma = 0.231\frac{E_e^{3/2} - E_\gamma^{3/2}}{\rho}, \qquad \textbf{(A.1.)}$$

where E_γ is the x-ray energy in keV, E_e is the primary electron energy in keV, and ρ is the density of the solid in g cm^{-3}.[A-1] Using this relation spatial resolution limits of 5.0 μm for Al L_{23}-shell soft x-ray detection and 7.2 μm for Be K-shell soft x-ray detection are obtained for 15 keV electron excitation. The compositional resolution limit depends on the signal-to-background level; bremsstrahlung is the primary constituent of the background signal.

With the exception of the elements Li, Be, and B, energy dispersive spectrometers have reached resolutions that compare with the spatial and compositional resolution limits. The soft x-ray spectrometer presented here is not capable of obtaining the compositional resolutions comparable to the resolution limits of the light elements; however, spatial resolutions comparable to the spatial resolution limits have been obtained. The small solid angle of collection prevents the spectrometer from reaching the compositional resolution limits, but the data obtained from this study is useful for the consideration and design of multilayer mirror spectrometers that may reach these limits. Additionally, since the soft x-ray spectrometer detects low energy x rays, soft x-ray

emission data from electron excitation is important information in the consideration of using soft x-ray spectrometry with soft x-ray microscopes to determine spatial elemental composition and spatial electron density of states.

The main purpose of this study was to determine the efficiency of the soft x-ray spectrometer, to determine the yield and mechanism of soft x-ray emission from electron excitation, and to obtain elemental spectroscopic images with the soft x-ray spectrometer. The mechanical design and detection efficiency of the soft x-ray spectrometer will be presented. Then experimental yields of soft x rays will be compared with theoretical calculations to determine the physical processes leading to soft x-ray emission of light elements. Finally, elemental spectroscopic images will be presented.

B. Soft X-Ray Spectrometer for the Scanning Electron Microscope

The soft x-ray spectrometer was attached to a scanning electron microscope (SEM)[A-2] capable of imaging with 15 keV and 1 to 5 keV electrons. The electrons were incident on an Al sample 45° from the normal of the sample surface. Soft x-rays emitted perpendicular to the incident electrons (-45° from the sample normal) entered the spectrometer (**Figure A.1.**). Typical beam currents for soft x-ray spectrometry were 1.0-25.0 μA.

The soft x-ray spectrometer utilized the Rowland circle geometry for grazing incidence spherical gratings. Soft x rays passed through a slit and baffle arrangement and illuminated a Au-coated 600 grooves/mm spherical grating at an incident angles between 78° and 87°. The grating efficiency was measured to be 0.15 at 82° at 50 eV. Grating efficiencies at other angles were extrapolated from the value at 82° and 50 eV based on the reflectance of Au.[A-3] Once the soft x rays strike the grating, a certain fraction will be focused and diffracted into a spectrum. The spectrum of soft x rays was detected by a

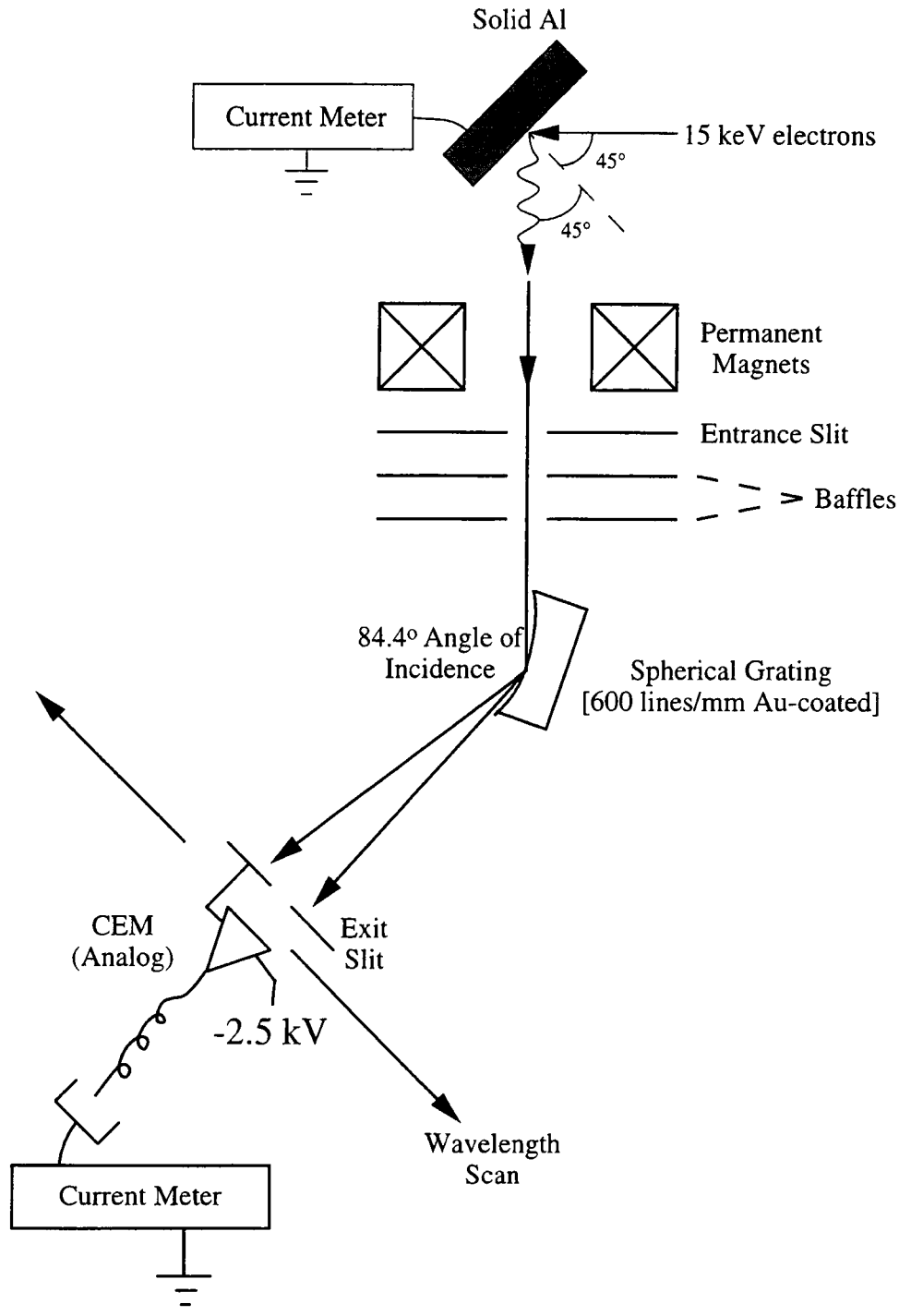


Figure A.1. Soft X-Ray Spectrometer. Wavelength dispersive soft x-ray spectrometer designed to collect x rays emitted from a sample illuminated by an electron beam from a scanning electron microscope.

channeltron electron multiplier (CEM)[A-4] with a 0.72 mm slit. The CEM was operated in the analog mode with a -2.5 kV potential on the photocathode, and the gain of the channeltron was measured to be 3×10^4. The quantum efficiency of the CEM photocathode was measured at the National Synchrotron Light Source at Brookhaven National Laboratory. The CEM quantum efficiency was measured by comparing the photocurrent emitted by the CEM photocathode with the photocurrent generated by a calibrated Au photodiode with a known efficiency. The resulting quantum efficiency is shown in **Figure A.2.**

By scanning the exit slit and CEM across the spectrum, the entire soft x-ray region could be examined. Peaks of interest were integrated to determine the total number of x rays detected from that wavelength region. The combination of slits and baffles, a negative 2.5 kV bias on the CEM, and bending magnets eliminated spurious signals by preventing scattered electrons from reaching the CEM. Thus, the spectrometer signal only consisted of characteristic x rays and bremsstrahlung background radiation.

C. Soft X-Ray Yield from Electron Bombardment

The amount of characteristic soft x rays emitted from a sample is a critical quantity in elemental spectroscopy. The total number of x rays emitted from a solid into the vacuum region per incident electron is called the yield. Although yields are well known for hard x rays, yields for soft x rays are not well defined. Detector and grating efficiencies in the soft x-ray region are not well documented, and theoretical calculations are difficult due to uncertainties in the fluorescent yield, range values, and emission processes of light element soft x-ray emission. In this section the efficiency of the soft x-ray spectrometer will be used to measure the yield of characteristic soft x rays emitted

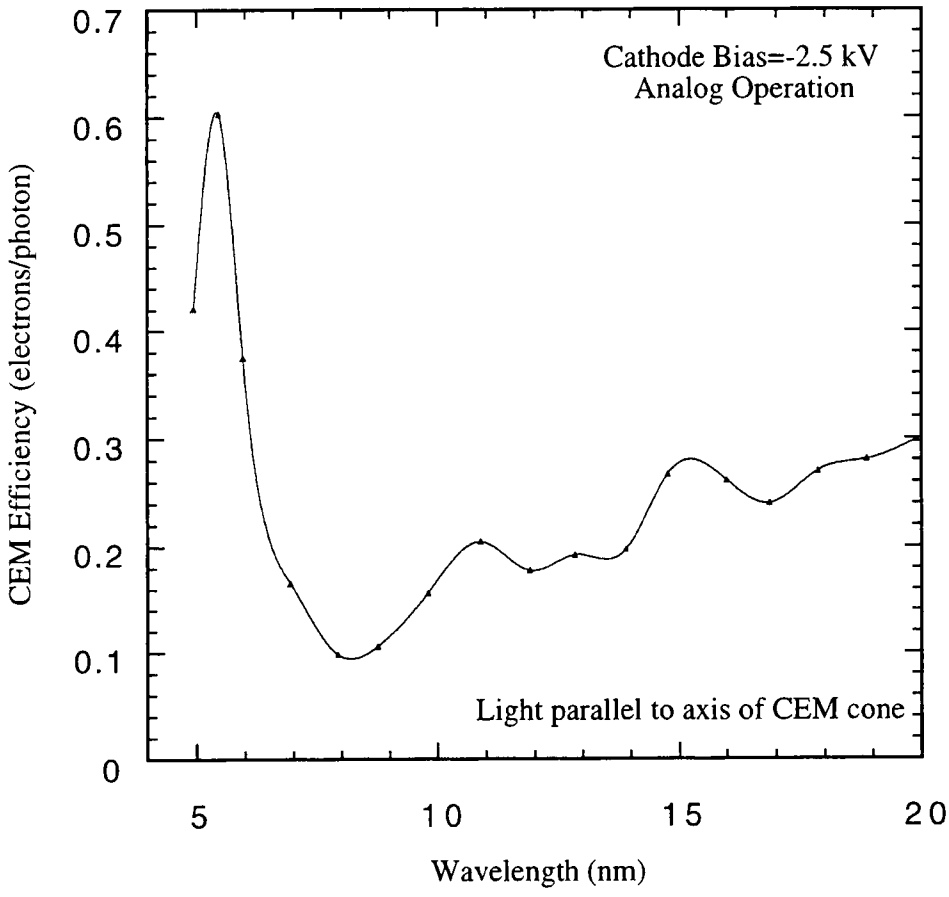


Figure A.2. Channeltron Electron Multiplier Efficiency. Efficiency of the channeltron electron multiplier as a function of wavelength. The decrease in efficiency at the lowest wavelengths may be due to absorption from carbon contamination on the cathode surface.

from samples. Additionally, the yield will be theoretically calculated for the element Al to help determine the physical processes involved in soft x-ray emission.

C.1. Element Spectra and Yield Measurements

The experimental yield of soft x rays produced per electron can be determined by the equation

$$Y = \frac{N_\gamma \Omega}{N_e \Delta\Omega \varepsilon} \qquad \textbf{(A.2.)}$$

where N_γ is the number of photons detected by the CEM, N_e is the number of incident electrons, $\Delta\Omega$ is the solid angle examined by the spectrometer, Ω is the relative total angle photon emission assuming a $\cos^2$ distribution of photons, and ε is the grating efficiency.

Figures A.3., **A.4.**, **A.5.**, **A.6.**, **A.7.**, **A.8.**, and **A.9.** show emission data for the light elements observed. The yield of characteristic soft x-ray photons per incident electron is given for materials that allowed accurate measurement of N_e. Yields are not given for LiF and BN because the sample current from these materials could not be determined. The stated yield for Be may be high due to a possible inaccuracy of N_e. The Be sample was a thin film of Be on a glass substrate, and electron bombardment of the Be thin film causes the Be to evaporate. To insure that Be was being bombarded and that no emission was lost in holes created by the evaporated Be, the thin film sample was constantly moved during data collection. The conductivity of the Be thin film during electron bombardment (and thereby evaporation) may not be suitable for transfer of the electrons to the current meter input. Thus, the sample current for the Be data may be too low which would make the stated yield too high.

Yield=0.027 Si L_{23}-Shell Soft X-Ray Photons per 15 keV Electron

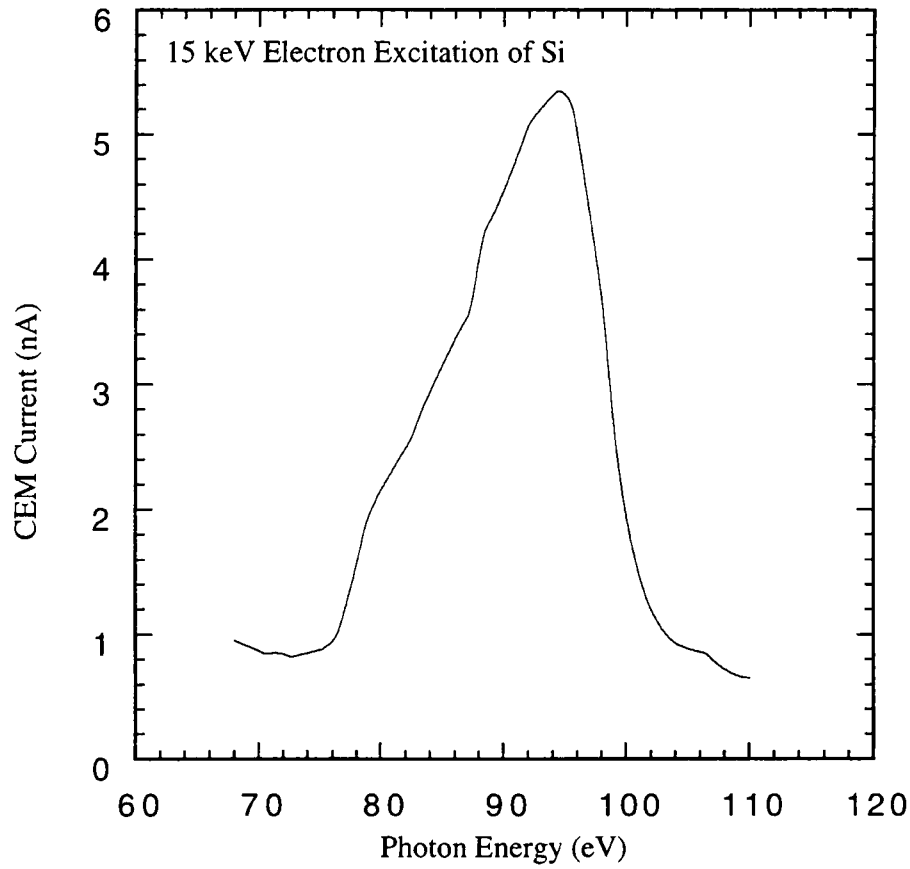


Figure A.3. Si Soft X-Ray Emission. Characteristic L_{23}-shell soft x-ray emission of Si bombarded with 15 keV electrons.

Yield=0.021 Al L_{23}-Shell Soft X-Ray Photons per 15 keV Electron

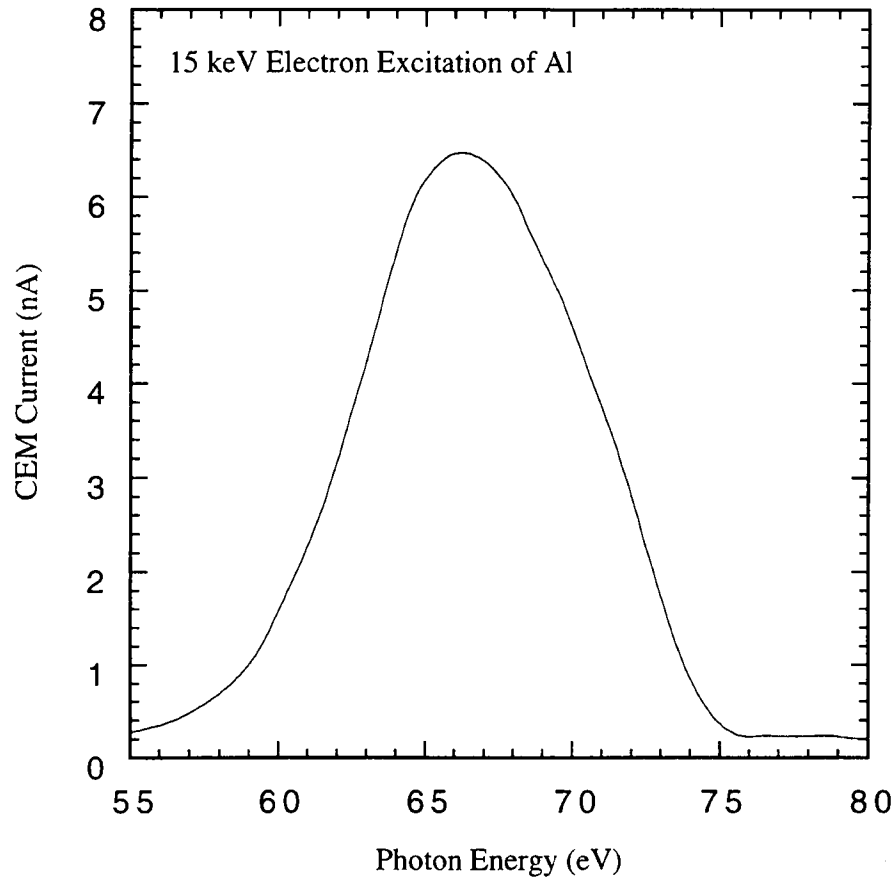


Figure A.4. Al Soft X-Ray Emission. Characteristic L_{23}-shell soft x-ray emission of Al bombarded with 15 keV electrons.

Yield=0.028 Mg L_{23}-Shell Soft X-Ray Photons per 5 keV Electron

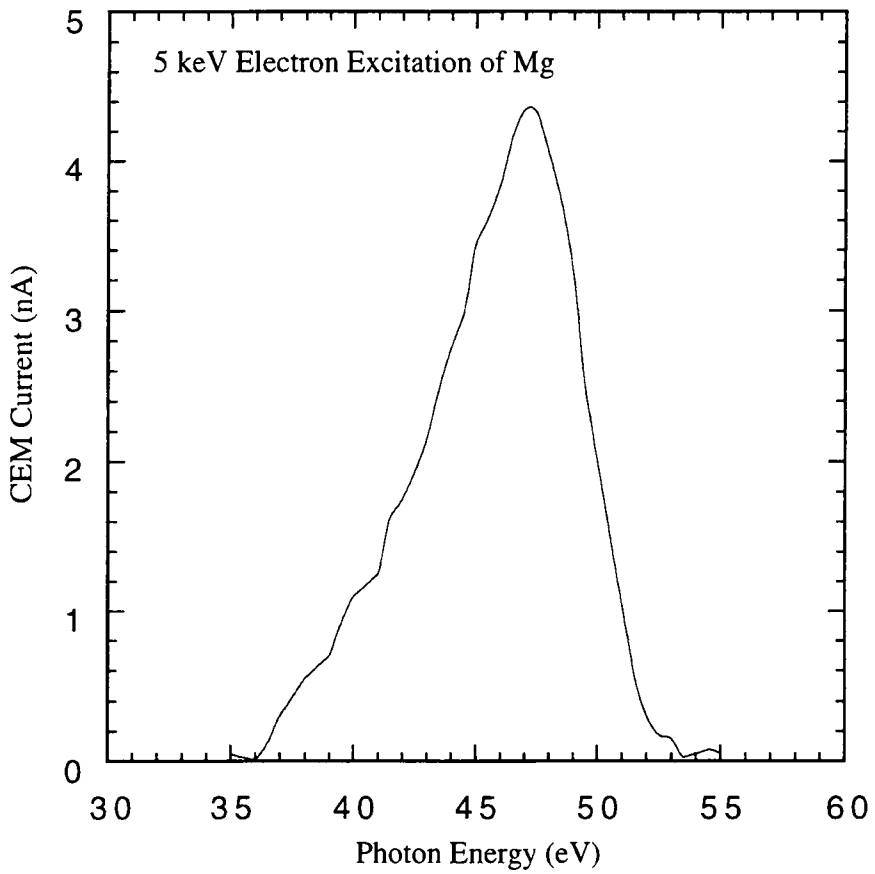


Figure A.5. Mg Soft X-Ray Emission. Characteristic L_{23}-shell soft x-ray emission of Mg bombarded with 5 keV electrons.

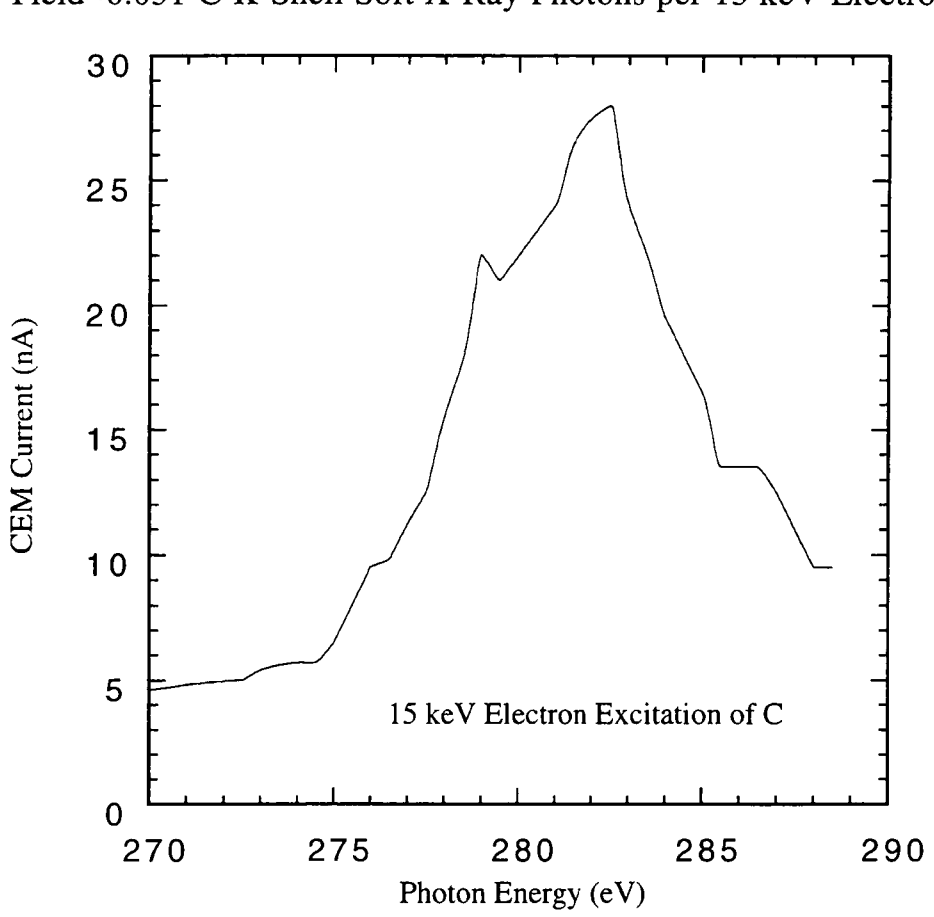


Figure A.6. C Soft X-Ray Emission. Characteristic K-shell soft x-ray emission of C bombarded with 15 keV electrons.

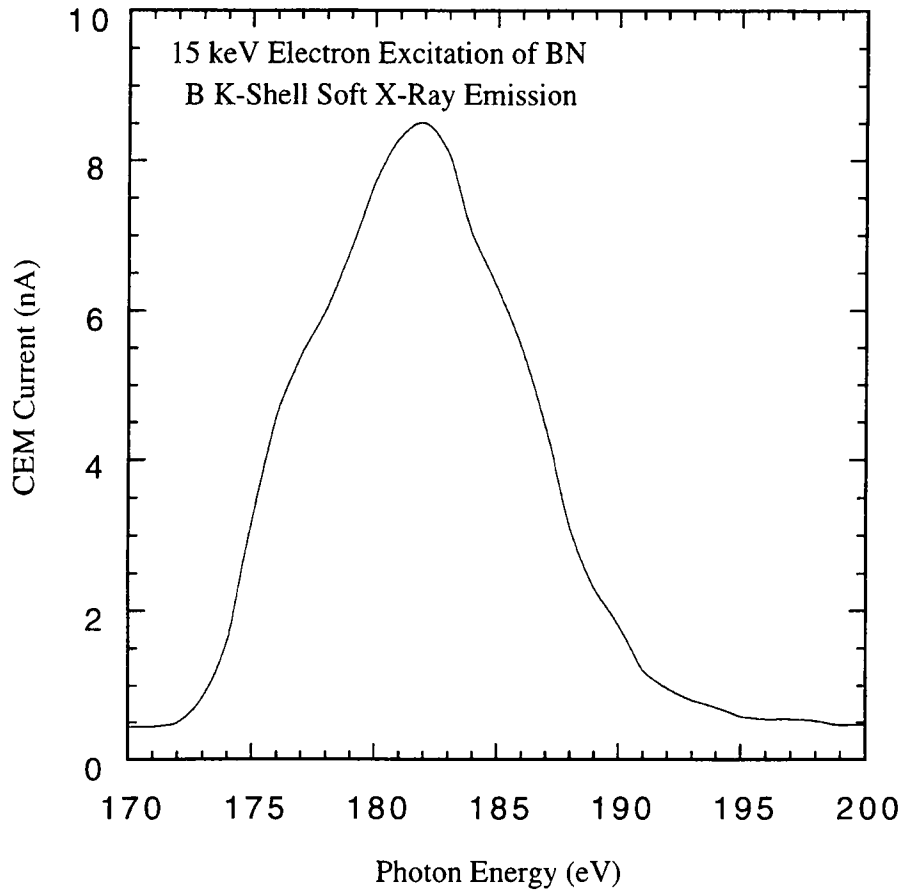


Figure A.7. B Soft X-Ray Emission. Characteristic K-shell soft x-ray emission of B from BN bombarded with 15 keV electrons.

Yield=0.0426 Be K-Shell Soft X-Ray Photons per 15 keV Electron

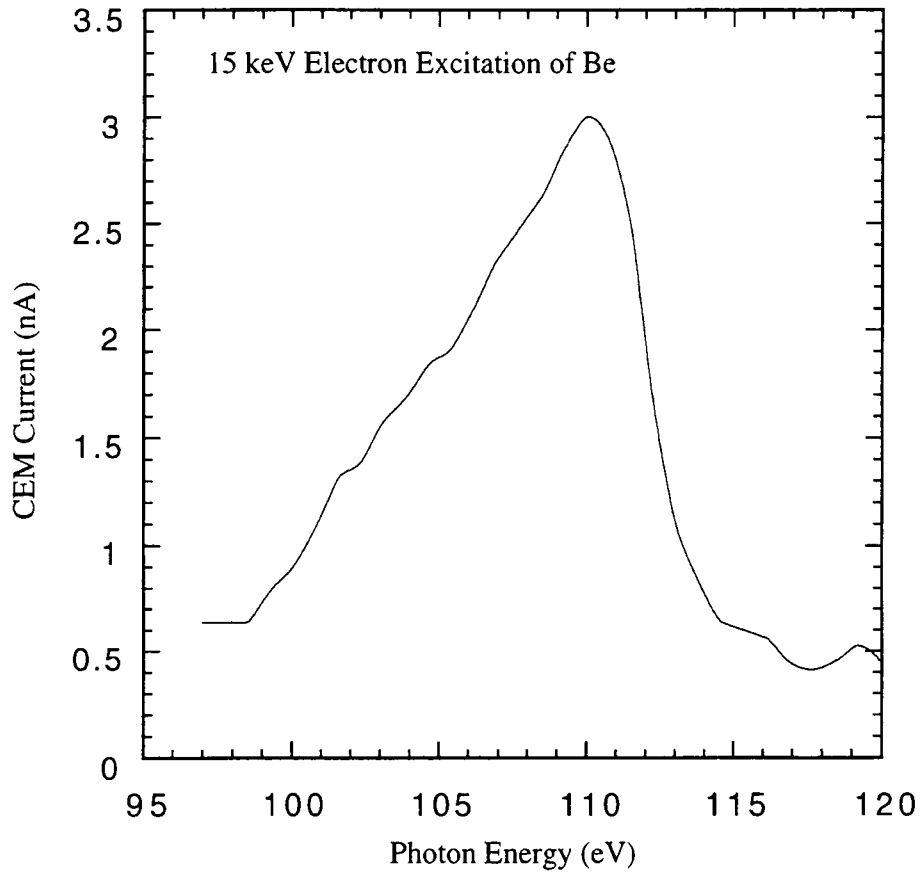


Figure A.8. Be Soft X-Ray Emission. Characteristic K-shell soft x-ray emission of Be bombarded with 15 keV electrons.

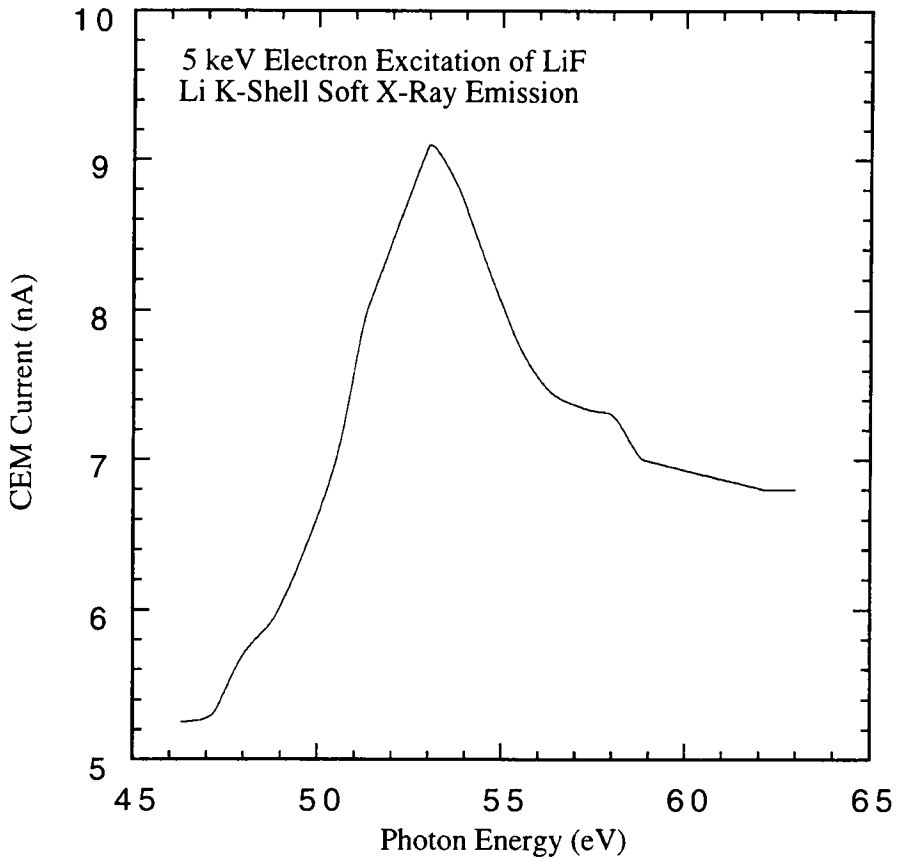


Figure A.9. Li Soft X-Ray Emission. Characteristic K-shell soft x-ray emission of Li from LiF bombarded with 5 keV electrons.

C.2. Theoretical Calculation of Yield

Standard theories can be used to calculate the soft x-ray yield from electron excitation; however, several factors make the theory inaccurate. Specifically, uncertainties in the fluorescent yield, uncertainties in the range of electrons in light elements, and contributions to the yield from secondary electrons make reliable theoretical calculations difficult. Nevertheless, theoretical calculations can be used to help describe the physical processes that lead to soft x-ray emission; therefore, the yield of Al L_{23}-shell soft x rays from 15 keV electron excitation will be calculated. Al provides the best illustrative model of the emission processes of interest since the L_{23}-shell soft x-ray energy (72.5 eV) is in the center of the soft x-ray energies of the light elements. Additionally, the stopping power and range of electrons in Al have been reported by many sources. The yield of soft x rays induced by the primary electron will be calculated using standard theories; then, the yield induced by secondary electrons will be calculated.

The yield from the primary electron can be calculated by the formula

$$Y_{primary} = \int_U^{E_0} 6N\omega_L\sigma(E)\left[\frac{1}{4\pi}\int_0^{2\pi}\int_0^{\pi/2} e^{-\mu x\frac{\cos\alpha}{\cos\phi}}\sin\phi d\phi d\theta\right]\left[\frac{dx}{dE}\right]dE \qquad \textbf{(A.3.)}$$

where N is the density of atoms and $\sigma(E)$ is the cross section for ionization per L-shell electron. The limits of integration are the binding energy of the L_{23}-shell electrons (U) and the energy of the incident electron (E_0); the factor of six corresponds to the six electrons in the L_{23} shell. The fluorescent yield[A-5] ω_L is given by

$$\omega_L = \frac{Z^4}{1.02\times10^8 + Z^4}. \qquad \textbf{(A.4.)}$$

The double integration of the exponential term in equation **(A.3.)** accounts for the average x-ray absorption in the sample, with the normalization factor $1/4\pi$. The inverse of the stopping power (dx/dE) is an empirical fitting to the stopping power calculated by Ritchie.[A-6]

The ionization cross section per L-shell electron as a function of the excitation electron energy (E) and the binding energy of the emitted electron (U) is given by Gryzinski[A-7] as

$$\sigma(E) = \frac{\sigma_0}{U^2} g\left(\frac{E}{U}\right). \qquad \textbf{(A.5.)}$$

If the bombarding particle is an electron, σ_0 is 6.56×10^{-14} eV^{2}cm^2. The function $g(E/U)$ is a maximum at ~$4U$ as shown in **Figure A.10**.

The limits of integration for the inner double integral limit the solid angle of emission to 2π since x rays emitted into the sample will be completely absorbed. μ is the mass absorption coefficient for Al L_{23} soft x-rays in Al, α is the incidence angle for the electrons (45°), and ϕ is the angle of exit for the x-rays relative to the sample normal. μ is $4\pi k/\lambda$, where k is the extinction coefficient of Al.[A-3] The distance x traversed by the electrons in the sample as a function of energy is given by

$$x(E) = R(E_0) - R(E), \qquad \textbf{(A.6.)}$$

where R is the range of an electron in Al.

There are discrepancies in the range of electrons in Al in the literature for electron energies of interest here. Three different range-energy expressions were used. Feldman gives

$$R(E) = 257E^{1.77} \qquad \textbf{(A.7.)}$$

where R is in 10^{-8} cm and E is the electron energy in keV.[A-8] Thomas and Pattison give

$$R(E) = 256.5 \times 10^{-5} E^{1.3} \qquad \textbf{(A.8.)}$$

where R is in μg cm^{-2} and E is the electron energy in eV.[A-9] Finally, Fitting gives

$$R(E) = 900\rho^{-0.8} E^{1.3} \qquad \textbf{(A.9.)}$$

where R is in 10^{-8} cm, ρ is the density in g cm^{-3}, and E is the electron energy in keV.[A-10] The formulae of Feldman, Thomas and Pattison, and Fitting give a range of 3.10 μm, 2.64 μm, and 1.37 μm for a 15 keV electron in Al, respectively. These range expressions represent the maximum range of an electron in the solid. The average range of a number of electrons should be smaller. The discrepancy in the ranges causes a significant

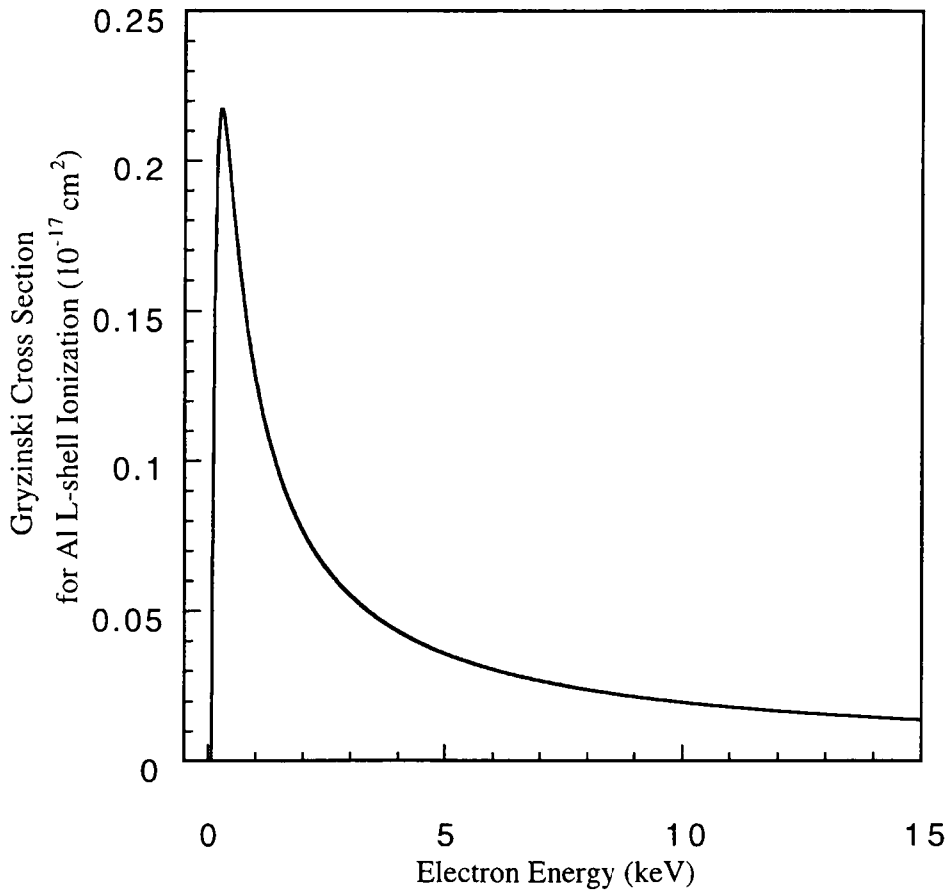


Figure A.10. Gryzinski Cross Section. Theoretical cross section for Al L-shell ionization given by Gryzinski[A-7].

variation in the yield calculations due to the short penetration depths of the soft x rays. Evaluation of equation **(A.3.)** with the above parameters gives yields of 0.00023, 0.00037, and 0.00070 photons/electron for the primary 15 keV electron using the range-energy expressions of Feldman, Thomas and Pattison, and Fitting, respectively.

The yield from the secondary electrons created in the solid by the primary electron can be calculated in a similar fashion. If *S(e,E)* is a function that describes the secondary electron distribution created in Al by an electron with energy *E*, the yield from secondary electrons can be written as:

$$Y_{2nd} = \int_U^{E_0} 6N\omega_L \frac{\int_U^E S(e,E)\sigma(e)de}{\int_{E_{min}}^E S(e,E)de}\left[\frac{1}{4\pi}\int_0^{2\pi}\int_0^{\pi/2} e^{-\mu x\frac{\cos\alpha}{\cos\phi}}\sin\phi d\phi d\theta\right]\left[\frac{dx}{dE}\right]dE. \quad \textbf{(A.10.)}$$

Here the cross section for ionization by the primary electron in equation **(A.3.)** is replaced by the integral of the secondary electron distribution multiplied by the cross section for ionization by the secondary electron; the integral of the secondary electron distribution alone in the denominator serves to normalize the integral in the numerator. The limits of integration for the numerator are the binding energy of the L_{23}-shell electrons (U) and the degraded energy of the primary electron (E). The limits of integration for the denominator are E_{min} and E, where E_{min} represents the minimum energy of the secondary electrons.

S(e,E) was chosen to be *1/e* for all primary energies (E) based on the measurements by McConnell *et al.*[A-6] Since *1/e* goes to infinity at e =0, 10 eV was used as E_{min}. This includes the Al volume plasmon energy of 15 eV. Evaluation of equation **(A.8.)** with the above parameters gives yields of 0.0013, 0.0020, and 0.0034 photons/primary electron from the secondary electrons produced by the primary electron using the range-energy expressions of Feldman, Thomas and Pattison, and Fitting, respectively. The total yield is the sum of the yield from the primary electron and the yield from the secondary electrons produced in the solid. The total calculated yield, *Y*, becomes $Y_{primary}+Y_{2nd}$ or 0.0015, 0.0024, and 0.0041 photons/primary electron using the

corresponding range formulae. Approximately 85% of this yield is due to the soft x rays created by the secondary electrons in the solid. **Figures A.11., A.12.,** and **A.13.** show the relative contribution to the yield by primary and secondary electrons for calculations using the Feldman, Thomas and Pattison, and Fitting range-energy expressions.

The theoretically determined yields differ from the experimental value by factors between five and ten. The primary uncertainties in the theory are the fluorescent yield, the approximate secondary electron distribution, and the range of the electrons in the solid. The theory does not include soft x-ray emission from secondary fluorescence or soft x-ray emission from electrons that enter the solid, create L-shell ionizations, and then exit the solid. Any of these processes or combinations of these processes could account for the difference between experimental and theoretical results. These uncertainties indicate the difficulty of theoretically calculating the soft x-ray yield for light elements. However, the theory clearly shows that secondary electrons play a significant role in the electron excited emission of soft x rays from light elements.

C.3. Discussion of Soft X-Ray Emission Mechanism

The theoretical calculations for the Al L_{23}-shell soft x-ray emission from 15 keV electron excitation show that the emission process from electron excitation is not simple. Several factors can lead to increased or decreased soft x-ray yields. For high-energy soft x-ray emission secondary electron-induced emission will not contribute as much to the total yield since the number of secondary electrons decreases rapidly with increasing energy. Additionally, lower primary electron energies will result in increased contributions to the yield from primary electron-induced emission since the ionizations produced by the primary electrons will not be too deep in the solid to result in emitted soft x rays. Other critical factors in the emission process are backscattered electrons and secondary fluorescence. Backscattered primary electrons and the secondary electrons

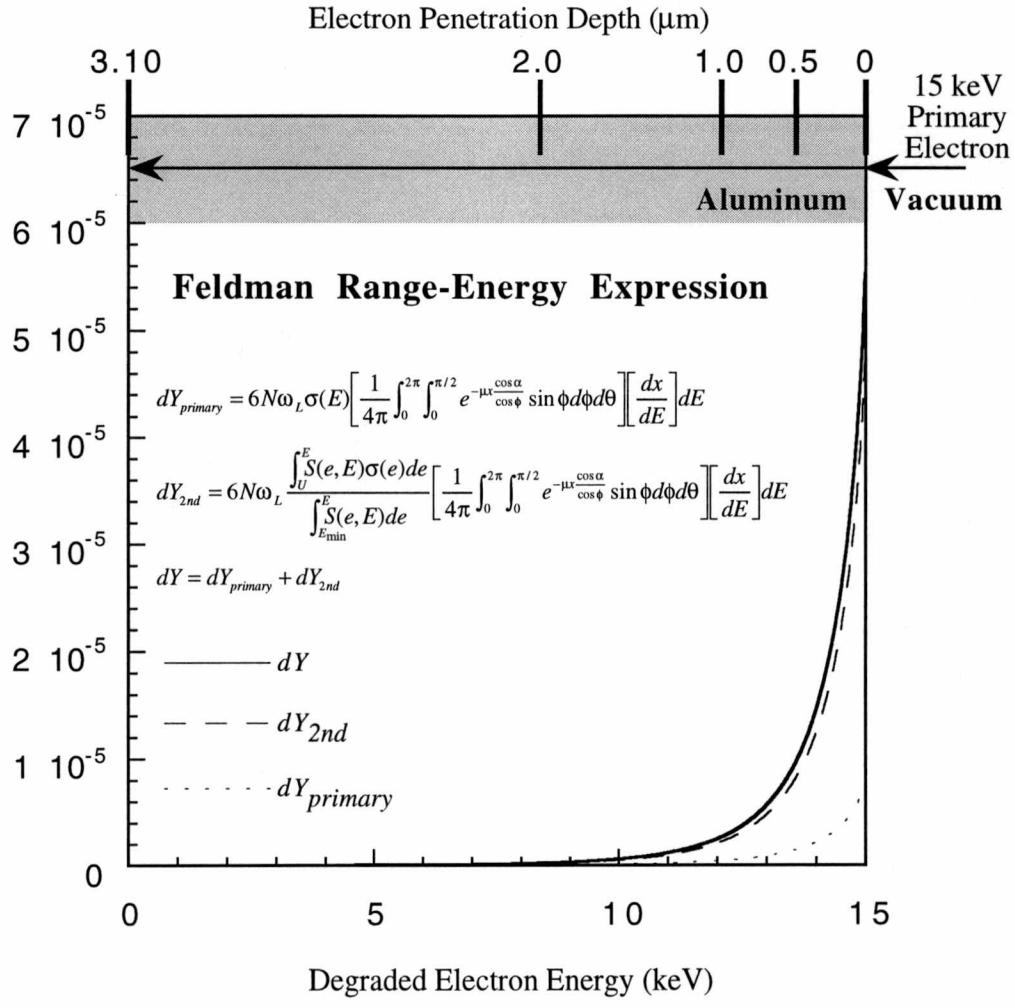


Figure A.11. Yield Theory with Feldman Expresssion. The contribution to the Al L_{23}-shell soft x-ray yield by the primary 15 keV electron and the secondary electrons in terms of the degraded energy of the primary electron and the penetration depth of the primary electron according to Feldman.

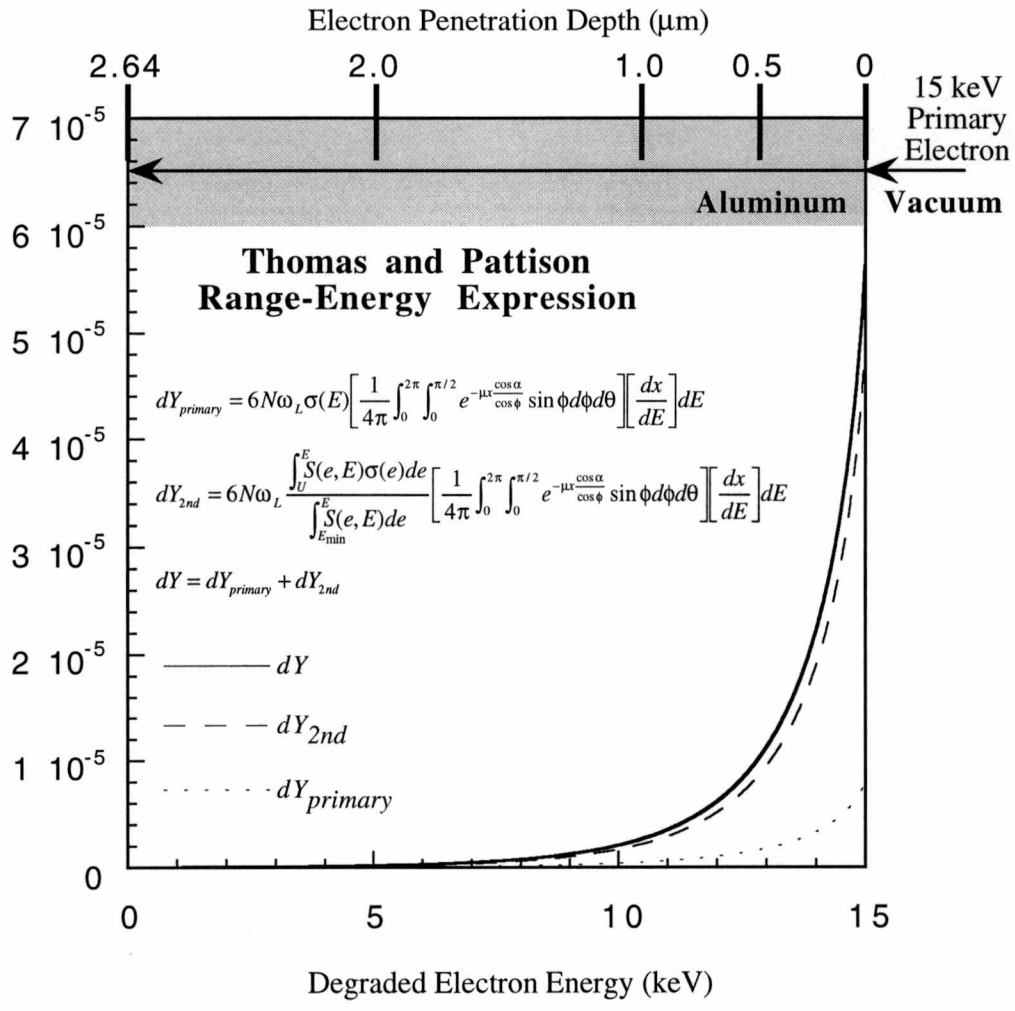


Figure A.12. Yield Theory with Thomas and Pattison Expresssion. The contribution to the Al L_{23}-shell soft x-ray yield by the primary 15 keV electron and the secondary electrons in terms of the degraded energy of the primary electron and the penetration depth of the primary electron according to Thomas and Pattison.

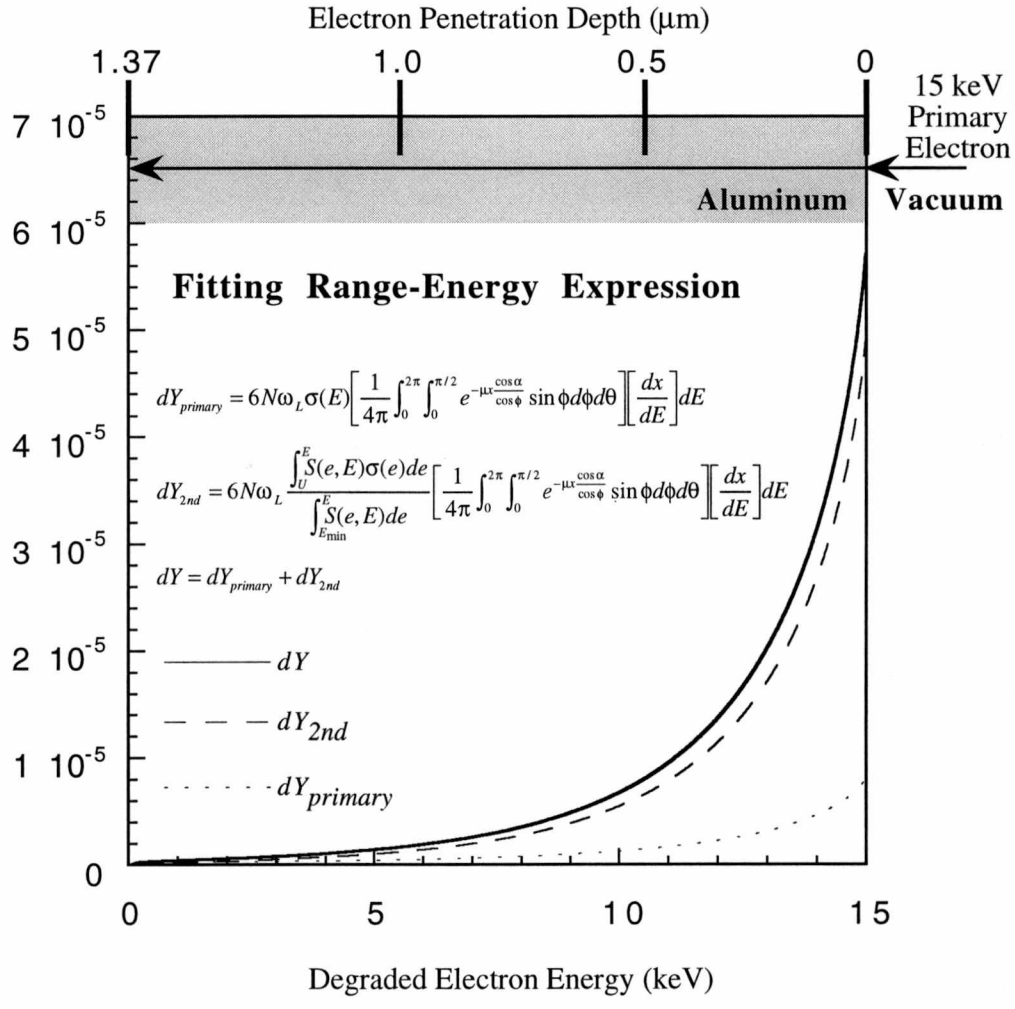


Figure A.13. Yield Theory with Fitting Expresssion. The contribution to the Al L_{23}-shell soft x-ray yield by the primary 15 keV electron and the secondary electrons in terms of the degraded energy of the primary electron and the penetration depth of the primary electron according to Fitting.

they create in the solid can create ionizations near the surface of the solid; soft x rays created from these ionizations will have a high probability of being emitted into the vacuum. Secondary fluorescence provides a means of transporting photons created deep in the solid to the surface of the solid. To correctly calculate the yield a Monte Carlo type simulation would be needed to account for all of the random variations in electron and soft x-ray interactions, and an exact value for the fluorescent yield would be needed.

Even though the exact yield cannot be calculated the data and theory provide important information for the elemental spectroscopy of light elements using soft x-ray emission. In particular, when using electron excitation the yield of soft x rays is much larger than the small values of fluorescent yield suggest for light elements. Even though the probability of creating an x ray from a vacancy in the electron shell is small, there are many more ionizations being produced due to the low ionization energies for the light elements. Since a significant number of secondary electrons have enough energy to create ionizations, the number of ionizations per primary electron is dramatically increased. The theory for the Al L_{23}-shell soft x-ray emission suggests that the yield of soft x rays can be increased by a factor of ten. The increase of the yield by secondary electrons makes light element spectroscopy with the SEM more feasible, and the distinctive role that the secondary electrons play in soft x-ray emission allows for the selection of the ideal electron excitation energy for maximum soft x-ray yield.

The increased yield from secondary electron excitation in light element spectroscopy with the SEM should be noted in the consideration of light element spectroscopy with soft x-ray excitation. For soft x-ray excitation secondary electrons will not increase the yield appreciably. Instead, the yield will be dependent on the cross section of ionization by soft x rays and the fluorescent yield. Secondary fluorescence is one possible mechanism to increase the yield from soft x-ray excitation. Although the soft x-ray yields from soft x-ray excitation are not as large as the yields from electron

excitation, soft x-ray emission is still the preferred method for reaching the lowest possible compositional resolutions due to the absence of significant bremsstrahlung.

D. Microanalysis Images

The soft x-ray emission signal from a sample examined with the SEM can be collected simultaneously with the scattered electron signal produced by the SEM. While the scattered electron signal of the SEM produces a structural map of the sample of interest, the soft x-ray emission signal produces an elemental composition map of the sample. The spectrometer presented here is only capable of collecting one soft x-ray photon energy at one time and, therefore, can only map the concentration of one element per SEM scan; however, with the addition of an area sensitive channelplate detector and multichannel analyzing electronics all of the elements with characteristic soft x-ray emission could be mapped in one SEM scan. The data presented here results from setting the soft x-ray spectrometer at a particular photon energy and then scanning the electron beam across the sample and collecting the scattered electron and soft x-ray emission signals simultaneously. When more than one spectroscopic image is presented with a single SEM image, one or more of the spectroscopic images were obtained during a different SEM scan.

The spectroscopic images do not represent the exact volume concentration of the element of interest. Instead, the spectroscopic images display the relative volume concentration of the element in the sample. It is important to note that the soft x rays are emitted from any place in the sample that the incident electron and the secondary electrons reach. Spectroscopic images may be deceiving due to the low penetration of soft x rays. A heavy concentration of an element deep in the sample may not produce a

large emission signal because of the small number of electrons reaching the element and the high absorption of the x rays produced.

Bremsstrahlung radiation will be detected by the spectrometer and creates a background signal for all elements under investigation. The amount of bremsstrahlung produced is slightly dependent on the material being irradiated. Additionally, some elements may have overlapping emission peaks that add to the background signal and cause false concentration in the spectroscopic image. Confusion due to bremsstrahung and overlapping emission can be reduced by further investigation at different photon energies.

Another factor that affects the spectroscopic imaging is the structure of the sample. Shadowing and other effects can prevent the emitted x rays from reaching the spectrometer or prevent the electrons from reaching a section of the sample. By analyzing the spectroscopic image in comparison with the SEM structural image or taking additional data with the sample rotated or tilted, the properties of sample can be obtained.

Figure A.14. shows the variation in the soft x-ray emission signal with the changing volume concentration of the sample. The sample investigated here is a Si wafer with layers of C on the surface. As the electron beam from the SEM is moved from pure Si to Si with a 10 nm C overlayer, the Si L_{23}-shell soft x-ray emission signal decreases. As the thickness of the C overlayer increases in steps of 10 nm the Si emission signal decreases in a step-like fashion, also.

Figures A.15., A.16., A.17., and **A.18.** show SEM images and spectroscopic images of LiF, Mg, and Al with a Ni grid laid over the material. The spectroscopic images were obtained by monitoring the soft x-ray emission signal at photon energies corresponding to Li K-shell, Mg L_{23}-shell, and Al L_{23}-shell emission, respectively. Bright areas represent high signals and high concentrations of the element under investigation. Scan times were from 1 to 30 minutes, and beam currents were from 1 to

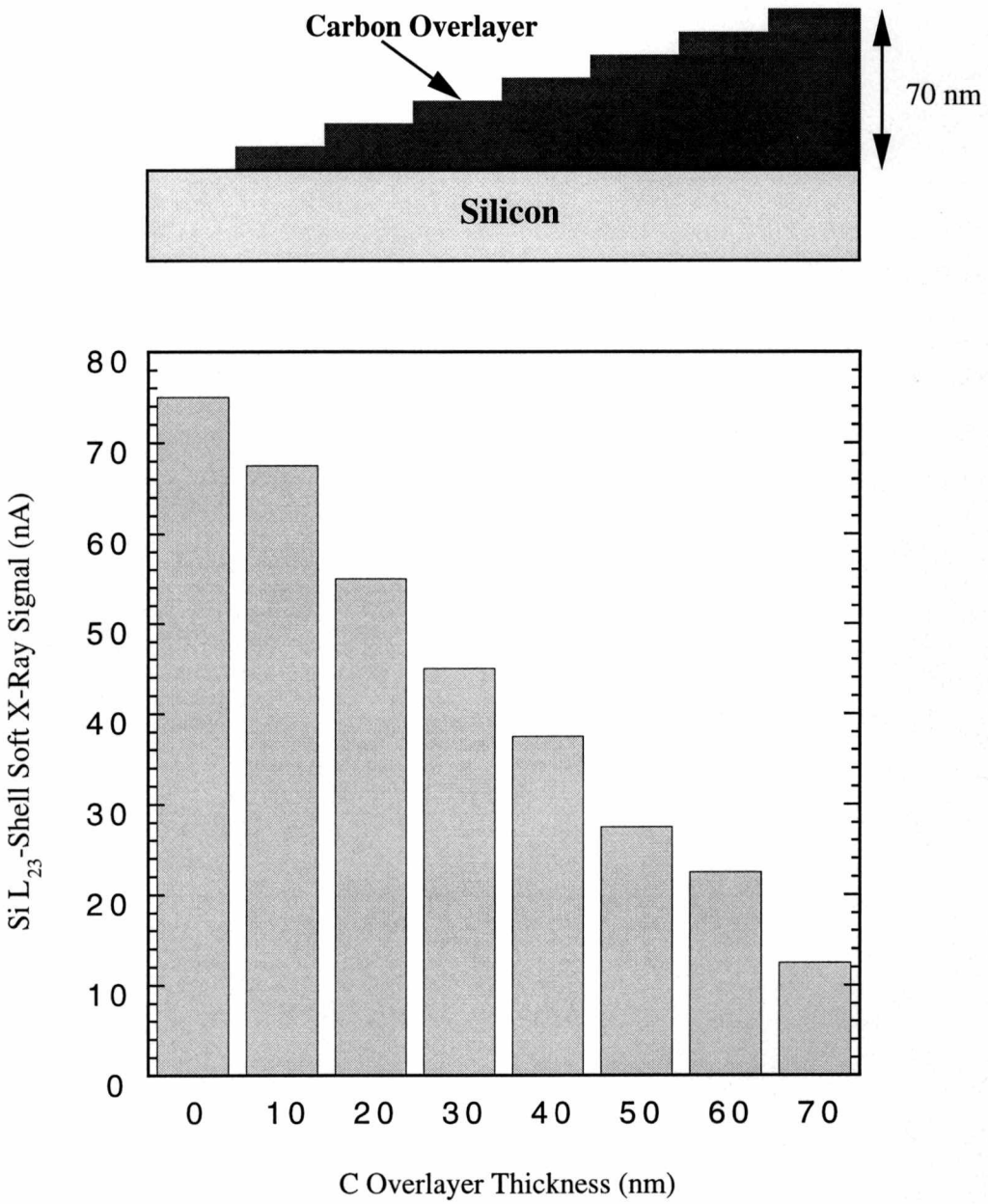


Figure A.14. Si Soft X-Ray Signal from Si with C Overlayer. Si L_{23}-shell soft x-ray emission signal from pure Si with a C overlayer of varying thickness. The decreasing Si signal with increasing C thickness indicates the dwindling volume concentration of Si.

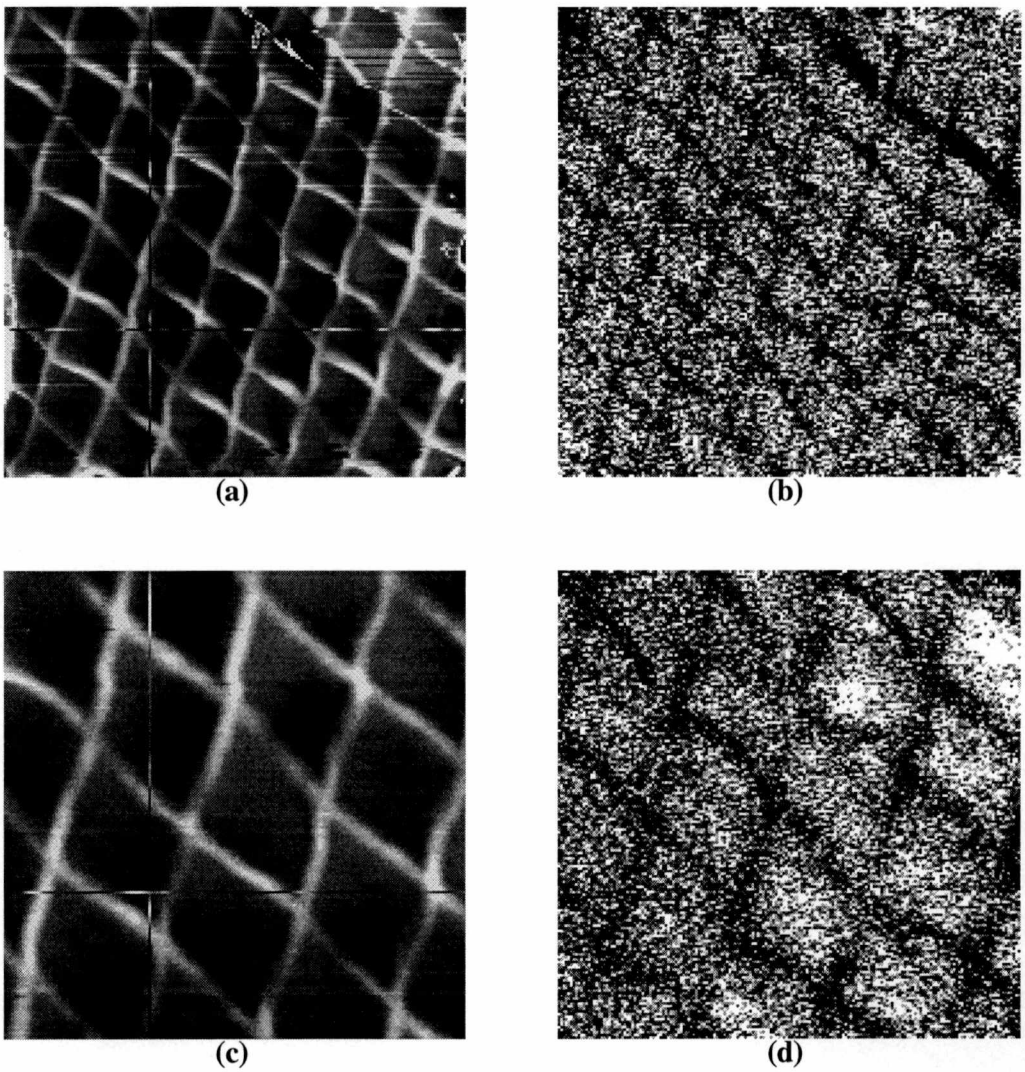
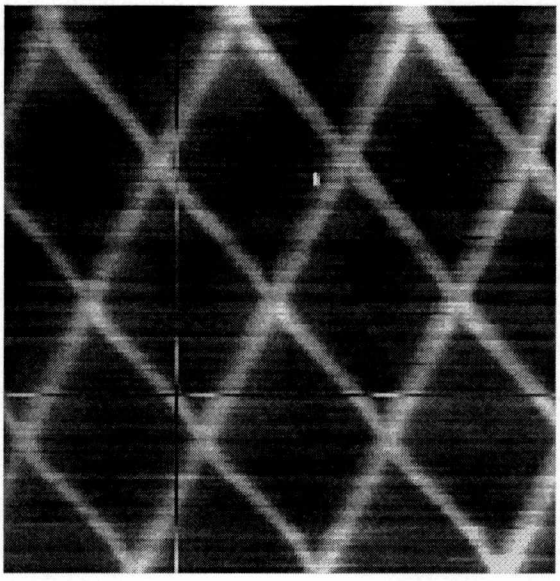
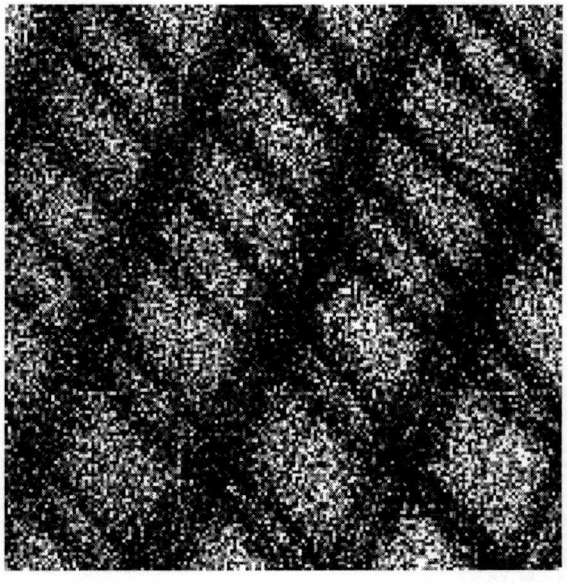


Figure A.15. SEM and Li Images. **(a)** and **(c)** SEM images and **(b)** and **(d)** corresponding Li K-shell soft x-ray emission spectrocopic images of a LiF crystal covered with a Ni grid. The grid lines are spaced 317.5 μm apart.



(a)



(b)

Figure A.16. SEM and Mg Images. **(a)** SEM image and **(b)** corresponding Mg L_{23}-shell soft x-ray emission spectroscopic image of Mg covered with a Ni grid. The grid lines are spaced 317.5 μm apart.

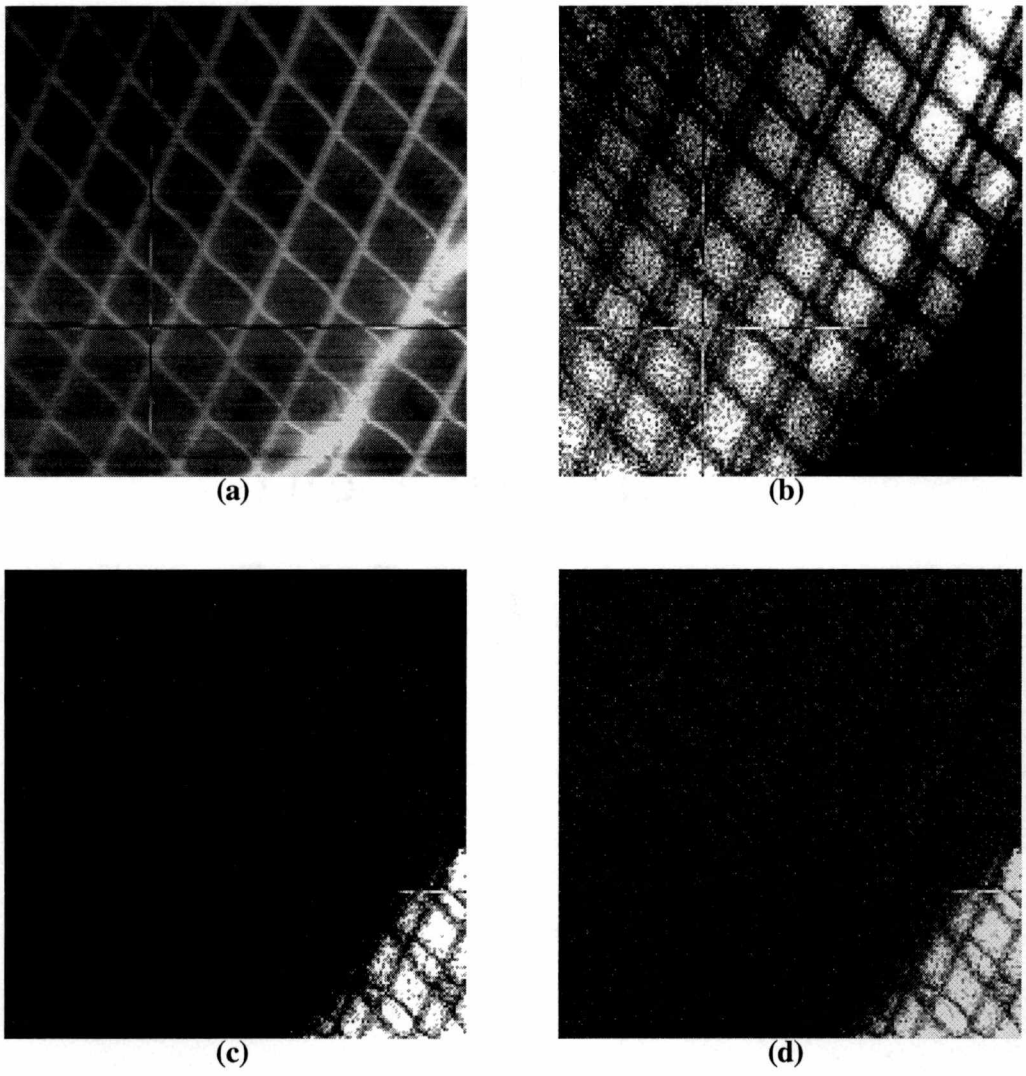


Figure A.17. SEM, Mg, and Al Images. **(a)** SEM image and corresponding **(b)** Mg L_{23}-shell and **(c)** and **(d)** Al L_{23}-shell soft x-ray emission spectroscopic images of Mg and Al covered with a Ni grid. **(d)** is the same image as **(c)** except the brightness and constrast have been adjusted to show the faint shadows of the Ni grid on the Mg section of the sample. The shadows seen on the Mg section indicate that bremsstrahlung does contribute to the detected signal of the spectrometer. The grid lines are spaced 317.5 μm apart.

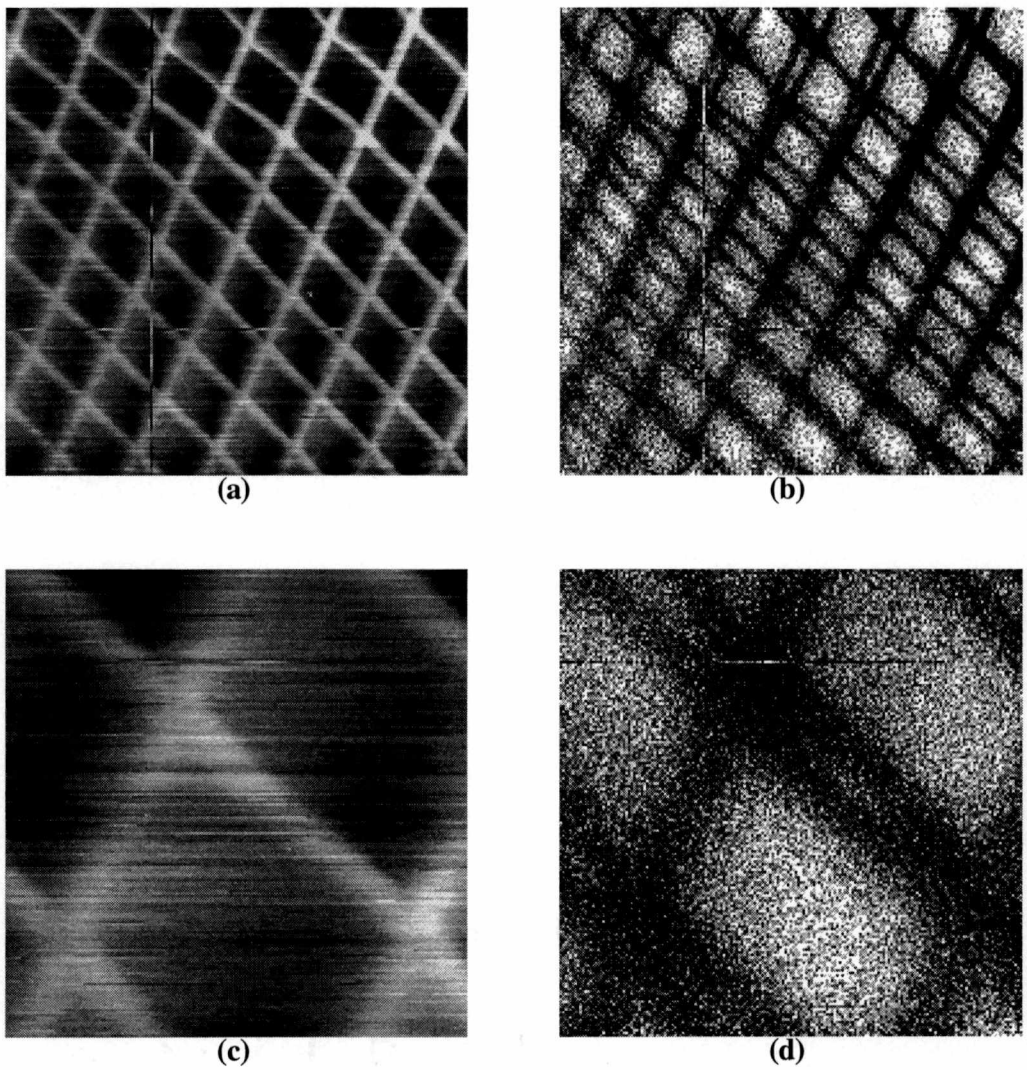


Figure A.18. SEM and Al Images. **(a)** and **(c)** SEM images and **(b)** and **(d)** corresponding Al L_{23}-shell soft x-ray emission spectrocopic images of Al covered with a Ni grid. The grid lines are spaced 317.5 μm apart.

20 μA. The necessary scan time and beam current were dependent on the signal strength. Shadowing effects can be seen when the Ni grid was not in good contact with the surface of the sample. The grid is composed of squares with 317.5 μm sides, but the square structure appears diamond shaped because the electron beam is hitting the sample at a 45° angle. The faint dark lines in **Figure A.17.(d).** are most likely due to bremsstrahlung radiation being blocked by the Ni grid structure; this shows that bremsstrahlung is detected as a background signal.

E. Conclusion

A grazing incidence soft x-ray spectrometer has been constructed for use with a scanning electron microscope. Soft x-ray emission from electron excitation of the light elements Li, Be, B, C, Mg, Al, and Si has been observed. By monitoring the signal of characteristic soft x rays emitted from the SEM sample during SEM imaging, elemental spectroscopic images have been obtained. By measuring the efficiency of the spectrometer, values for the yield of soft x rays emitted per incident electron have been determined. Analysis of theoretical computations of the soft x-ray yield shows that soft x-ray emission from vacancies produced by secondary electrons in the solid contribute significantly to the soft x-ray yield; in some cases secondary electron-induced emission is the dominant mechanism of emission. The technique of using wavelength dispersive spectrometry is an important alternative to energy dispersive spectrometry in microanalysis of samples containing light elements.

Appendix B

Optical Theory of Layered Thin Films

When light traversing through one medium is incident on a second medium, some light will be transmitted into the second medium and some light will be reflected back into the first medium. The percentage of incident light transmitted and reflected at the interface can be calculated with standard electromagnetic theories. The same techniques that determine the reflected and transmitted intensities for this simple two-media (or single interface) case provide the reflected and transmitted intensities for multimedia cases. Fresnel showed how to calculate these reflected and transmitted intensities, and calculations are found in almost all undergraduate and graduate textbooks on electromagnetism and optics. These standard theories are generally known as the optical theories of layered thin film systems. In this appendix we show the method of determining the transmitted intensity of p-polarized light through a two-media system, a three-media system, and a four-media system.

First, we consider the two-media system. An equation expressing the transmitted intensity of light can be obtained by writing the incident, reflected, and transmitted light at the interface as plane waves. The electric field of the plane wave takes the form :

$$\vec{E}_a = E_a e^{-i(\vec{k}_a \bullet \vec{r} - \omega t)} \hat{a} . \qquad \textbf{(B.1.)}$$

Here the electric field strength of a plane wave oscillates with a frequency (ω) associated with the photon energy. The medium in which the incident and reflected waves reside will be called medium 0, and the medium in which the transmitted wave travels will be called medium 1. The interface between the two media will be called the 01 interface. If we let the 01 interface lie in the xy-plane and consider the xz-plane the plane of incidence, the y-component of the electric field will be zero.**(Figure B.1.)**

At the 01 interface the plane waves must obey the laws of electromagnetic radiation. Specifically, for z=0, the tangential component of the electric and magnetic fields of the plane waves must be continuous. The continuous electric field gives us one equation relating the electric field strengths of the light waves. We let the subscripts i, r, and t denote the incident, reflected, and transmitted waves, and the subscripts 0 and 1 denote the media 0 and 1. If θ_i, θ_r, and θ_t represent the angles that the respective waves make with the normal to the 01 interface, we have :

$$E_{0i}\cos\theta_i e^{-i(\vec{k}_i\bullet\vec{r}-\omega t)} - E_{0r}\cos\theta_r e^{-i(\vec{k}_r\bullet\vec{r}-\omega t)} = E_{1t}\cos\theta_t e^{-i(\vec{k}_t\bullet\vec{r}-\omega t)}. \qquad \textbf{(B.2.)}$$

Since all of the light is of the same frequency, the time dependent terms in the exponential should all be equivalent. We then have :

$$\theta_i = \theta_r, \qquad \textbf{(B.3.)}$$

$$\vec{k}_i \sin\theta_i = \vec{k}_t \sin\theta_t, \text{ and} \qquad \textbf{(B.4.)}$$

$$E_{0i}\cos\theta_i - E_{0r}\cos\theta_r = E_{1t}\cos\theta_t. \qquad \textbf{(B.5.)}$$

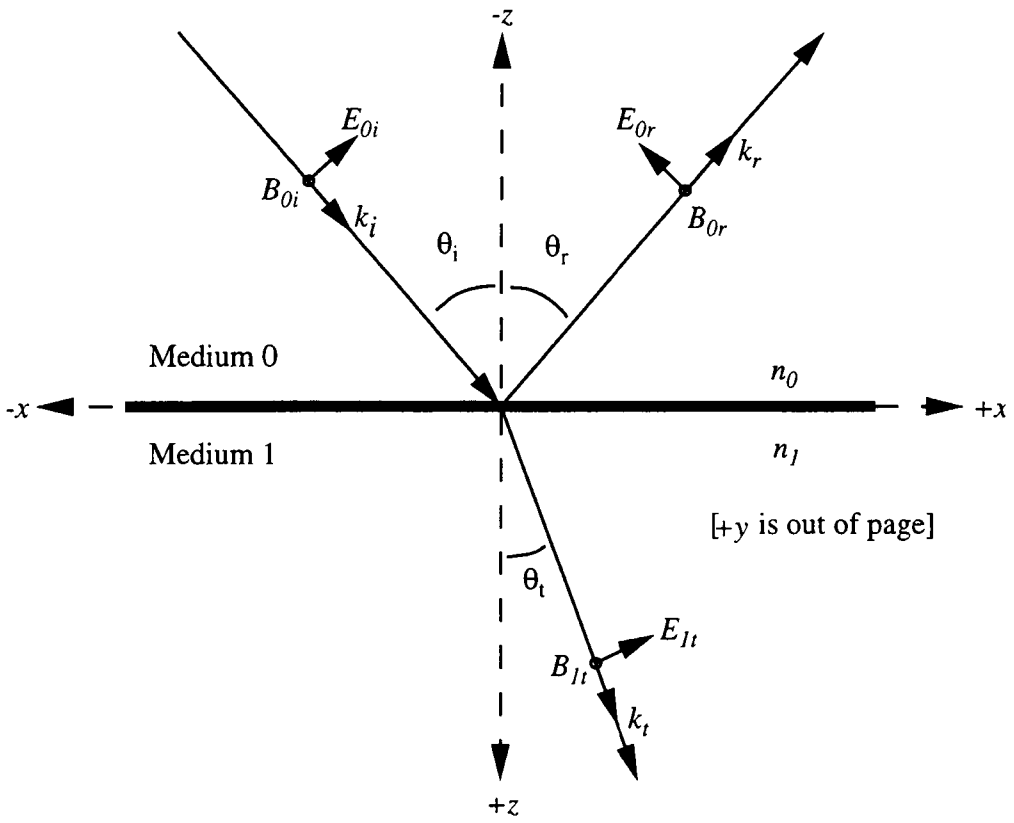


Figure B.1. Two-Media System. Optical system consisting of two media and one interface.

Since $\tilde{k}_a = 2\pi n_a/\lambda$, equation **(B.4.)** becomes Snell's Law :

$$\tilde{n}_i \sin\theta_i = \tilde{n}_t \sin\theta_t . \qquad \textbf{(B.6.)}$$

Snell's Law and equation **(B.3.)** determine the direction of the reflected and transmitted light waves from the direction of the incident wave and the refractive indices of the media. Here the refractive index, $\tilde{n}$, is complex and contains the real part of the index of refraction, n, and the extinction coefficient, k, which is the imaginary part of the index of refraction.

Since the permeability of medium 0 and medium 1 are essentially equivalent at optical frequencies, the continuity of the magnetic field at the 01 interface gives another equation relating the electric field strengths of the waves:

$$\frac{E_{0i}}{v_i} + \frac{E_{0r}}{v_r} = \frac{E_{1t}}{v_t} \qquad \textbf{(B.7.)}$$

or

$$\tilde{n}_0 E_{0i} + \tilde{n}_0 E_{0r} = \tilde{n}_1 E_{1t} . \qquad \textbf{(B.8.)}$$

Here v is the velocity of the wave. Equations **(B.3.)**, **(B.5.)**, **(B.6.)** and **(B.8.)** and the refractive indices of the media give the electric field strengths and directions of the reflected and transmitted waves in terms of the electric field strength and incident angle of the incident wave :

$$\left(\frac{E_{0r}}{E_{0i}}\right) = r_{01} = \frac{\tilde{n}_1 \cos(\theta_i) - \tilde{n}_0 \cos(\theta_t)}{\tilde{n}_1 \cos(\theta_i) + \tilde{n}_0 \cos(\theta_t)} \qquad \textbf{(B.9.)}$$

and

$$\left(\frac{E_{1t}}{E_{0i}}\right) = t_{01} = \frac{2\tilde{n}_0 \cos(\theta_i)}{\tilde{n}_1 \cos(\theta_i) + \tilde{n}_0 \cos(\theta_t)} . \qquad \textbf{(B.10.)}$$

r_{01} and t_{01} are called the Fresnel coefficients for reflection and transmission of p-polarized light from a single interface (interface 01).

While equations **(B.9.)** and **(B.10.)** give the electric field strengths of the reflected and transmitted light, the reflected and transmitted power per unit area is defined by the Poynting vector :

$$\vec{S} = c^2 \varepsilon_0 \vec{E} \times \vec{B}. \qquad \textbf{(B.11.)}$$

The magnitude of the Poynting vector is the average power per unit area or irradiance (I) :

$$I = \langle S \rangle = \frac{c\varepsilon_0}{2} E^2. \qquad \textbf{(B.12.)}$$

The reflected and transmitted fluxes at the 01 interface then become :

$$R_{01} = \frac{I_{0r} \cos\theta_r}{I_{0i} \cos\theta_i} = \left| \left(\frac{E_{0r}}{E_{0i}} \right) \right|^2 = {r_{01}}^2 \qquad \textbf{(B.13.)}$$

and

$$T_{01} = \frac{I_{1t} \cos\theta_t}{I_{0i} \cos\theta_i} = \frac{\tilde{n}_1 \cos\theta_t}{\tilde{n}_0 \cos\theta_i} \left| \left(\frac{E_{1t}}{E_{0i}} \right) \right|^2 = \frac{\tilde{n}_1 \cos\theta_t}{\tilde{n}_0 \cos\theta_i} {t_{01}}^2, \text{ respectively.} \qquad \textbf{(B.14.)}$$

R_{01} and T_{01} are called the reflectance and transmittance of the 01 interface.

The same method of determining the reflectance and transmittance of the two-media system can be used to determine the reflectance and transmittance of three and four-media systems. For the three-media system the three media will be media 0, 1, and 2. The two interfaces will be 01 and 12. Interface 01 will be the plane where z=0, and interface 12 will be the plane where $z=d_1$. Here d_1 is the thickness of medium 1.**(Figure B.2.)**

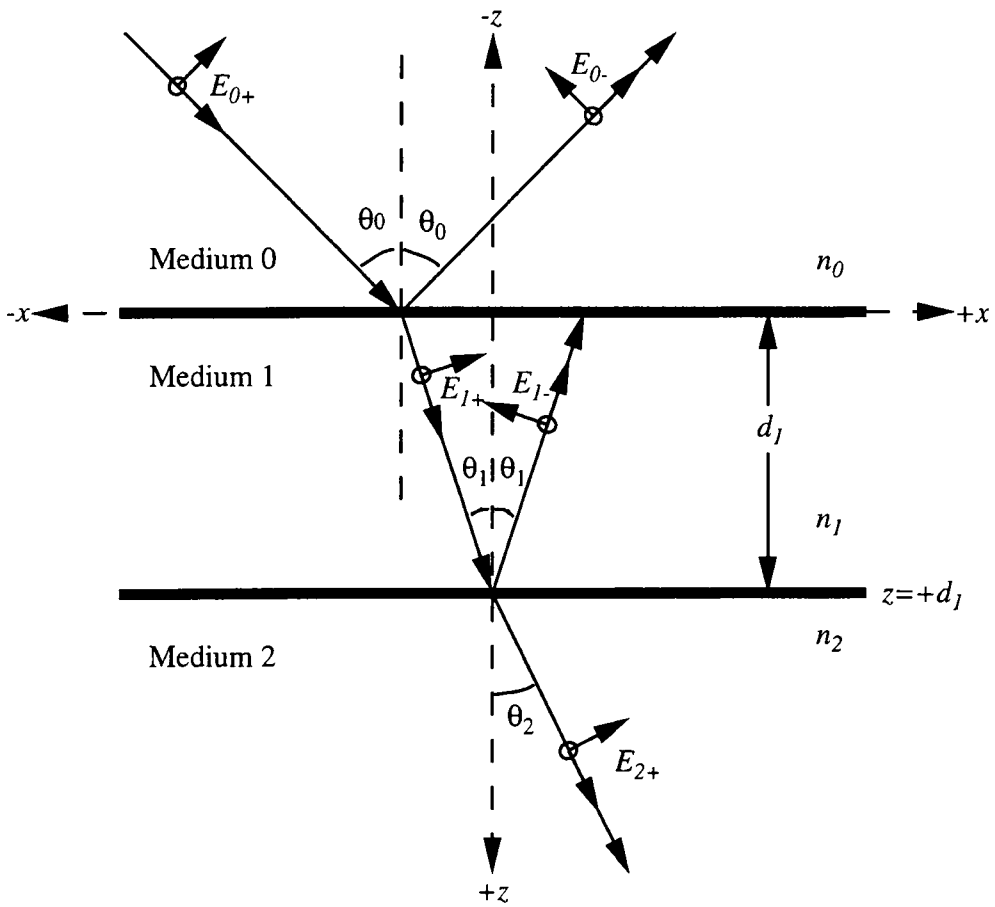


Figure B.2. Three-Media System. Optical system consisting of three media and two interfaces.

The procedure for determining the transmittance from medium 0 to medium 2 follows the same procedure for the two-media case, only the math is a little more complicated. We write the light in each medium as a plane wave. Solving the boundary condition for the electric and magnetic fields at interface 01 (z=0) gives :

$$E_{0+}\cos\theta_0 - E_{0-}\cos\theta_0 = E_{1+}\cos\theta_1 - E_{1-}\cos\theta_1 \qquad \textbf{(B.15.)}$$

and

$$\tilde{n}_0 E_{0+} + \tilde{n}_0 E_{0-} = \tilde{n}_1 E_{1+} + \tilde{n}_1 E_{1-}. \qquad \textbf{(B.16.)}$$

Here the subscripts i , r, and t have been replaced by subscripts + and -. The + denotes waves traveling in the positive z direction; the - corresponds to waves traveling in the negative direction. This convention is necessary since light will successively reflect off of both the 01 and 12 interfaces in medium 1. The electric fields of the plane waves merely represent the total amount of light traveling in the given direction and medium.

For interface 12 (z=d_1) we have :

$$E_{1+}\cos\theta_1 e^{-i\tilde{k}_1 d_1\cos(\theta_1)} - E_{1-}\cos\theta_1 e^{+i\tilde{k}_1 d_1\cos(\theta_1)} = E_{2+}\cos\theta_2 e^{-i\tilde{k}_2 d_1\cos(\theta_2)} \qquad \textbf{(B.17.)}$$

and

$$\tilde{n}_1 E_{1+} e^{-i\tilde{k}_1 d_1\cos(\theta_1)} + \tilde{n}_1 E_{1-} e^{+i\tilde{k}_1 d_1\cos(\theta_1)} = \tilde{n}_2 E_{2+} e^{-i\tilde{k}_2 d_1\cos(\theta_2)}. \qquad \textbf{(B.18.)}$$

Here $\tilde{k}_a$is the magnitude of the wave vector in medium a. $\tilde{k}_a$ can be written in terms of the refractive index of the medium and the wavelength of light in a vacuum (λ) :

$$\tilde{k}_a = \frac{2\pi\tilde{n}_a}{\lambda}. \qquad \textbf{(B.19.)}$$

Solving equations **(B.17.)** and **(B.18.)** for E_{2+} and E_{1-} in terms of E_{1+} we get :

$$\left(\frac{E_{1-}}{E_{1+}}\right) = r_{12}e^{-2i(2\pi/\lambda)\tilde{n}_1 d_1 \cos(\theta_1)} \qquad \textbf{(B.20.)}$$

and

$$\left(\frac{E_{2+}}{E_{1+}}\right) = t_{12}e^{-i(2\pi/\lambda)\tilde{n}_1 d_1 \cos(\theta_1)}e^{+i(2\pi/\lambda)\tilde{n}_2 d_1 \cos(\theta_2)}, \qquad \textbf{(B.21.)}$$

where r_{12} and t_{12} are the Fresnel coefficients shown in equations **(B.9.)** and **(B.10.)**. Using equations **(B.15.)**, **(B.16.)**, and **(B.20.)** we can solve for E_{1+} in terms of E_{0+} :

$$\left(\frac{E_{1+}}{E_{0+}}\right) = \frac{t_{01}}{1 + r_{01}r_{12}e^{-2i(2\pi/\lambda)\tilde{n}_1 d_1 \cos(\theta_1)}}. \qquad \textbf{(B.22.)}$$

Equations **(B.21.)** and **(B.22.)** give us the electric field strength transmitted into medium 2 in terms of the incident electric field strength :

$$\left(\frac{E_{2+}}{E_{0+}}\right) = \frac{t_{01}t_{12}e^{-i(2\pi/\lambda)\tilde{n}_1 d_1 \cos(\theta_1)}e^{+i(2\pi/\lambda)\tilde{n}_2 d_1 \cos(\theta_2)}}{1 + r_{01}r_{12}e^{-2i(2\pi/\lambda)\tilde{n}_1 d_1 \cos(\theta_1)}}. \qquad \textbf{(B.23.)}$$

The transmittance from medium 0 to medium 2 is determined as in equation **(B.14.)** of the 2 media case :

$$T_{02} = \frac{\tilde{n}_2 \cos\theta_2}{\tilde{n}_0 \cos\theta_0}\left|\left(\frac{E_{2+}}{E_{0+}}\right)\right|^2. \qquad \textbf{(B.24.)}$$

With a little more patience and math the case of four media follows in the same manner. The media are referred to as media 0, 1, 2, and 3; the interfaces between the media are interfaces 01, 12, and 23. The thickness of medium 1 will be d_1; the thickness of medium 2 will be d_2. A schematic of this scenario is shown in **Figure B.3.** For the

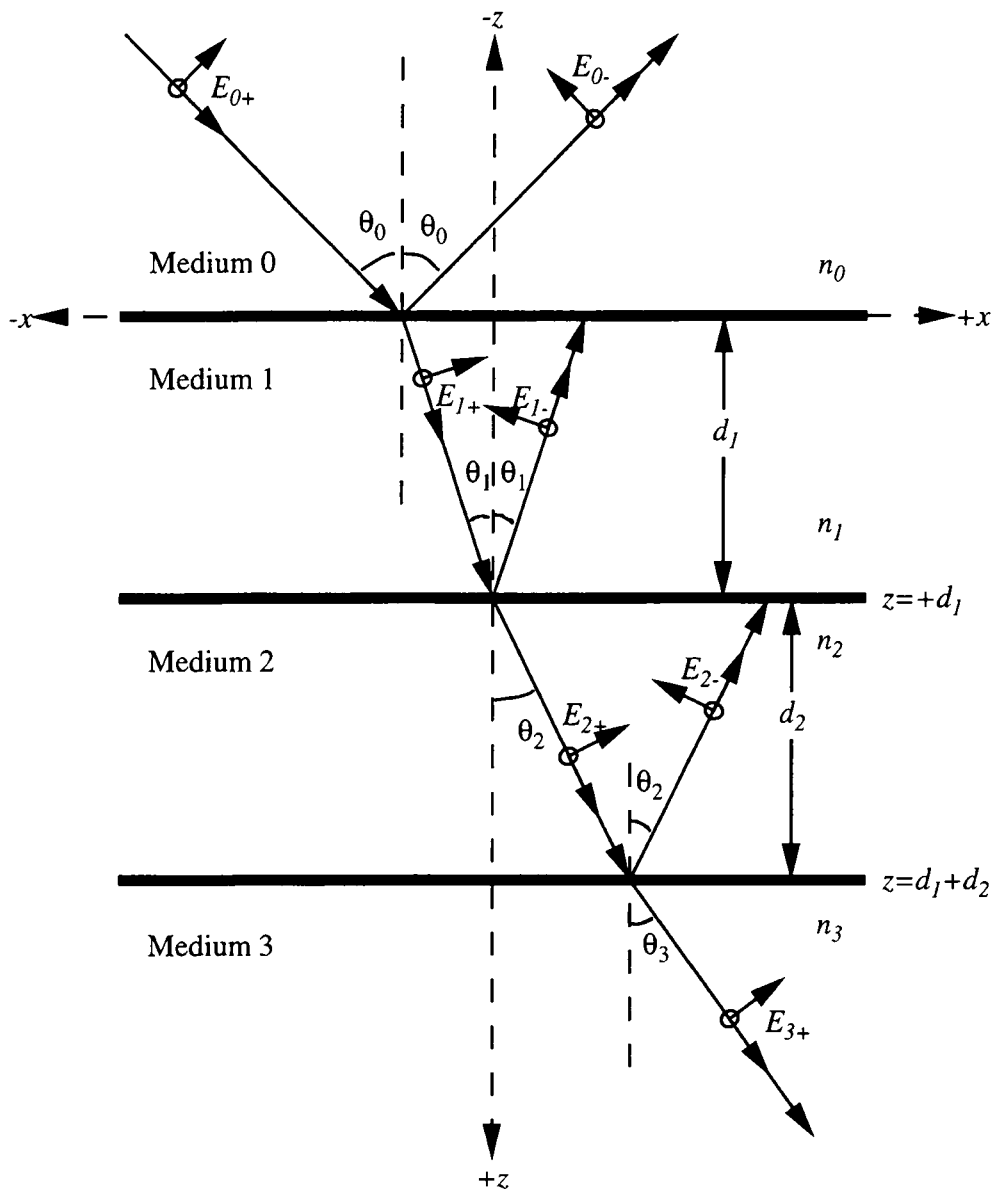


Figure B.3. Four-Media System. Optical system consisting of four media and three interfaces.

four-media case there are six unknown electric field strengths and six equations obtained from the boundary conditions at the three interfaces. All six unknowns can be obtained from the six equations.

The six equations obtained from the boundary conditions at interfaces 01, 12, and 23 are :

$$E_{0+}\cos\theta_0 - E_{0-}\cos\theta_0 = E_{1+}\cos\theta_1 - E_{1-}\cos\theta_1, \qquad \textbf{(B.25.)}$$

$$\tilde{n}_0 E_{0+} + \tilde{n}_0 E_{0-} = \tilde{n}_1 E_{1+} + \tilde{n}_1 E_{1-}, \qquad \textbf{(B.26.)}$$

$$\begin{aligned} &E_{1+}\cos\theta_1 e^{-i\tilde{k}_1 d_1\cos(\theta_1)} - E_{1-}\cos\theta_1 e^{+i\tilde{k}_1 d_1\cos(\theta_1)} = \\ &E_{2+}\cos\theta_2 e^{-i\tilde{k}_2 d_1\cos(\theta_2)} - E_{2-}\cos\theta_2 e^{+i\tilde{k}_2 d_1\cos(\theta_2)} \end{aligned}, \qquad \textbf{(B.27.)}$$

$$\begin{aligned} &\tilde{n}_1 E_{1+} e^{-i\tilde{k}_1 d_1\cos(\theta_1)} + \tilde{n}_1 E_{1-} e^{+i\tilde{k}_1 d_1\cos(\theta_1)} = \\ &\tilde{n}_2 E_{2+} e^{-i\tilde{k}_2 d_1\cos(\theta_2)} + \tilde{n}_2 E_{2-} e^{+i\tilde{k}_2 d_1\cos(\theta_2)} \end{aligned}, \qquad \textbf{(B.28.)}$$

$$\begin{aligned} &E_{2+}\cos\theta_2 e^{-i\tilde{k}_2(d_1+d_2)\cos(\theta_2)} - E_{2-}\cos\theta_2 e^{+i\tilde{k}_2(d_1+d_2)\cos(\theta_2)} = \\ &E_{3+}\cos\theta_3 e^{-i\tilde{k}_3(d_1+d_2)\cos(\theta_3)} \end{aligned}, \text{ and} \qquad \textbf{(B.29.)}$$

$$\begin{aligned} &\tilde{n}_2 E_{2+} e^{-i\tilde{k}_2(d_1+d_2)\cos(\theta_2)} + \tilde{n}_2 E_{2-} e^{+i\tilde{k}_2(d_1+d_2)\cos(\theta_2)} = \\ &\tilde{n}_3 E_{3+} e^{-i\tilde{k}_3(d_1+d_2)\cos(\theta_3)} \end{aligned}, \text{ respectively.} \qquad \textbf{(B.30.)}$$

Form these six equations we obtain the following relations by working from equation **(B.30.)** to equation **(B.25.)** :

$$\frac{E_{3+}}{E_{2+}} = t_{23} e^{-i\tilde{\kappa}_2(d_1+d_2)} e^{+i\tilde{\kappa}_3(d_1+d_2)}, \qquad \textbf{(B.31.)}$$

$$\frac{E_{2-}}{E_{2+}} = r_{23} e^{-2i\tilde{\kappa}_2(d_1+d_2)}, \qquad \textbf{(B.32.)}$$

$$\frac{E_{2+}}{E_{1+}} = \frac{t_{12}e^{-i\tilde{\kappa}_1 d_1}e^{+i\tilde{\kappa}_2 d_1}}{1 + r_{12}r_{23}e^{-2i\tilde{\kappa}_2 d_2}}, \tag{B.33.}$$

$$\frac{E_{1-}}{E_{1+}} = e^{-2i\tilde{\kappa}_1 d_1}\left(\frac{r_{23}e^{-2i\tilde{\kappa}_2 d_2} + r_{12}}{1 + r_{12}r_{23}e^{-2i\tilde{\kappa}_2 d_2}}\right), \text{ and} \tag{B.34.}$$

$$\frac{E_{1+}}{E_{0+}} = \frac{t_{01}\left(1 + r_{12}r_{23}e^{-2i\tilde{\kappa}_2 d_2}\right)}{1 + r_{01}r_{12}e^{-2i\tilde{\kappa}_1 d_1} + r_{01}r_{23}e^{-2i\tilde{\kappa}_1 d_1}e^{-2i\tilde{\kappa}_2 d_2} + r_{12}r_{23}e^{-2i\tilde{\kappa}_2 d_2}}, \tag{B.35.}$$

where $$\tilde{\kappa}_a = \tilde{k}_a \cos(\theta_a) = \left(\frac{2\pi\tilde{n}_a}{\lambda}\right)\cos(\theta_a). \tag{B.36.}$$

From these equations we obtain the electric field strength transmitted into medium 3 in terms of the incident electric field strength :

$$\frac{E_{3+}}{E_{0+}} = \left(\frac{E_{3+}}{E_{2+}}\right)\left(\frac{E_{2+}}{E_{1+}}\right)\left(\frac{E_{1+}}{E_{0+}}\right) \text{ gives} \tag{B.37.}$$

$$\frac{E_{3+}}{E_{0+}} = \frac{t_{01}t_{12}t_{23}e^{-i\tilde{\kappa}_1 d_1}e^{-i\tilde{\kappa}_2 d_2}e^{-i\tilde{\kappa}_3(d_1+d_2)}}{1 + r_{01}r_{12}e^{-2i\tilde{\kappa}_1 d_1} + r_{01}r_{23}e^{-2i\tilde{\kappa}_1 d_1}e^{-2i\tilde{\kappa}_2 d_2} + r_{12}r_{23}e^{-2i\tilde{\kappa}_2 d_2}}. \tag{B.38.}$$

As before the transmittance of the four-media system becomes :

$$T_{03} = \frac{\tilde{n}_3 \cos\theta_3}{\tilde{n}_0 \cos\theta_0}\left|\left(\frac{E_{3+}}{E_{0+}}\right)\right|^2. \tag{B.39.}$$

Appendix C

Transmission through a Wedge-Shaped Gap

Although calculations of the transmission of light from a planar interface to another nonplanar interface are difficult, careful approximations and appropriate geometrical conventions can lead to simple, effective, and informative theories. One such theory is presented here. The transmission from a planar interface to a conical probe resting on the planar interface is considered. The angle of incidence to the planar interface is greater than the critical angle; so, the transmission of light results from frustrated total internal reflection. The problem is worked in two-dimensions with an wedge-shaped air gap of angle α defining the geometry of the system. The problem is solved by expressing light as a wave function and determining the flux of light in each region by examining the probability current of the wave function in the respective region. This eloquent approach is valid for s-polarized light and interfaces with no curvature.[C-1]

Figure C.1. shows a general schematic of the geometry and coordinate systems defining the wedge-shaped gap. Media 0 and 2 have an index of refraction equal to n ($n_0=n_2=n$), and medium 1 is air with $n_1=1$. Light is incident on the $y=0$ interface between media 0 and 1. The angle of incidence to the $y=0$ interface (θ_i) is greater than the critical angle for the interface; θ represents angles with respect to the xy-coordinate system. Frustrated total internal reflection occurs between medium 0 and medium 2. Medium 2 represents a probe defined by α, the angle of the wedge-shaped air gap region. Rotation

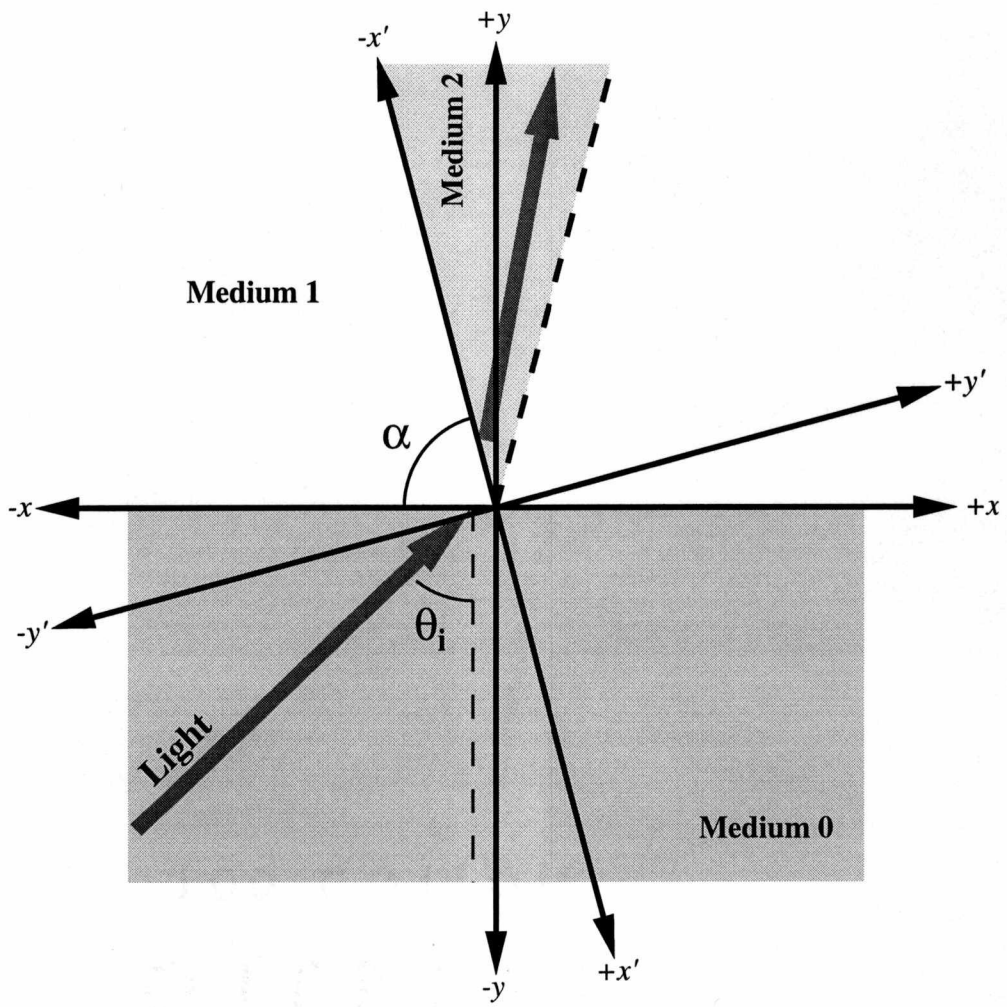


Figure C.1. Geometry of the Wedge-Shaped Gap. The coordinate system and the physical geometry of the wedge-shaped gap used for the theoretical calculation of the transmission from medium 0 to medium 2 (a conical shaped probe).

of the system about the y-axis produces a conical probe with a half angle of $\pi/2-\alpha$. The x' and y' axes define a second coordinate system that allows easier computation of the boundary conditions along the x' axis.

The amount of light transmitted between medium 0 and medium 2 can be calculated by writing the plane waves in media 0 and 2 as wave functions and comparing the probability currents associated with the wave functions of each medium. This approach is valid for s-polarized light. To simplify the theory, only light interactions on the $-x$ and $-x'$ axes will be considered, and multiple reflections between the interfaces defined by these axes will be neglected. For large α, these assumptions are valid. Using the probability current to compute the transmission is geometrically convenient since the transmitted light flux in one direction can be computed.

The wave function of light in medium 0 is written as

$$\Psi_0 = A_0 e^{inkx\sin\theta_0 + inky\cos\theta_0}. \qquad \textbf{(C.1.)}$$

Here A_0 is a constant representing the magnitude of the original wave, and $\theta_0=\theta_i$. Only the light traveling in the $+y$ direction is included in this wave function. To calculate the probability current in medium 0, the conjugate and the partial derivative of equation **(C.1.)** must be calculated. The conjugate is expressed by

$$\Psi_0^* = A_0^* e^{-inkx\sin\theta_0 - inky\cos\theta_0}. \qquad \textbf{(C.2.)}$$

The partial derivative,

$$\frac{\partial\Psi_0}{\partial y} = A_0\left[ink\cos\theta_0\right]e^{inkx\sin\theta_0 + inky\cos\theta_0}, \qquad \textbf{(C.3.)}$$

is taken with respect to y since the transmission of light in the $+y$ direction is of interest here. The probability current of light traveling in the $+y$ direction is

$$\mathrm{Im}\left[\Psi_0^*\frac{\partial\Psi_0}{\partial y}\right] = A_0^* A_0\left[nk\cos\theta_0\right]. \qquad \textbf{(C.4.)}$$

The wave function in medium 2 is more complex because of the geometry of the system. The wave function is written as

$$\Psi_2 = A_0 t_{01} t_{12} e^{inkx'\sin\xi'_2 + inky'\cos\xi'_2}, \qquad \textbf{(C.5.)}$$

where the angle ξ' is determined with respect to the $x'y'$-coordinate system. The terms t_{01} and t_{12} are the Fresnel transmission coefficients for the 01 and 12 interfaces, respectively. For s-polarized light incident on an ij interface the transmission coefficient is

$$t_{ij} = \frac{2n_i \cos\theta_i}{n_i \cos\theta_i + n_j \cos\theta_j}. \qquad \textbf{(C.6.)}$$

The wave function must be written in terms of the incident angle (θ_0=θ_i) and the angle of the wedge (α). Snell's Law gives

$$n\sin\theta_0 = \sin\theta_1 \qquad \textbf{(C.7.)}$$

and

$$\sin\xi'_1 = n\sin\xi'_2. \qquad \textbf{(C.8.)}$$

The equation

$$\xi'_1 = \theta_1 - \alpha \qquad \textbf{(C.9.)}$$

relates angles in the xy-coordinate and $x'y'$-coordinate systems. Equations **(C.7.)**, **(C.8.)**, and **(C.9.)** combine to form

$$n\sin\xi'_2 = \sin\xi'_1 = \sin(\theta_1 - \alpha) \qquad \textbf{(C.10.)}$$

and

$$n\cos\xi'_2 = n\sqrt{1-\sin^2\xi'_2} = \sqrt{n^2 - \sin^2(\theta_1 - \alpha)}. \qquad \textbf{(C.11.)}$$

With equations **(C.10.)** and **(C.11.)**, equation **(C.5.)** becomes

$$\Psi_2 = A_0 t_{01} t_{12} e^{ikx'\sin(\theta_1-\alpha)+iky'\sqrt{n^2-\sin^2(\theta_1-\alpha)}}. \qquad \textbf{(C.12.)}$$

Since the transmission of light in the $+y$ direction is of interest here, equation **(C.12.)** must be converted to the xy-coordinate system. x and y are written in terms of x' and y' as

$$x = x'\cos\alpha + y'\sin\alpha \qquad \textbf{(C.13.)}$$

and

$$y = -x'\sin\alpha + y'\cos\alpha, \text{ respectively.} \qquad \textbf{(C.14.)}$$

From these equations

$$x' = x\cos\alpha - y\sin\alpha \tag{C.15.}$$

and

$$y' = x\sin\alpha + y\cos\alpha \tag{C.16.}$$

are obtained. Substituting equations **(C.15.)** and **(C.16.)** into equation **(C.12.)** gives

$$\Psi_2 = A_0 t_{01} t_{12} e^{ik[x\cos\alpha - y\sin\alpha]\sin(\theta_1-\alpha) + ik[x\sin\alpha + y\cos\alpha]\sqrt{n^2 - \sin^2(\theta_1-\alpha)}}. \tag{C.17.}$$

To make calculation of the conjugate of **(C.17.)** easier, the following substitutions are made:

$$\rho e^{i\gamma} = \sin(\theta_1 - \alpha) \tag{C.18.}$$

and

$$\eta e^{i\phi} = n^2 - \sin^2(\theta_1 - \alpha). \tag{C.19.}$$

Equation **(C.17.)** now becomes

$$\Psi_2 = A_0 t_{01} t_{12} e^{ik[x\cos\alpha - y\sin\alpha]\rho e^{i\gamma} + ik[x\sin\alpha + y\cos\alpha]\eta^{1/2} e^{i(\phi/2)}}, \tag{C.20.}$$

and the conjugate of **(C.20.)** is written as

$$\Psi_2^* = A_0^* t_{01}^* t_{12}^* e^{-ik[x\cos\alpha - y\sin\alpha]\rho e^{-i\gamma} - ik[x\sin\alpha + y\cos\alpha]\eta^{1/2} e^{-i(\phi/2)}}. \tag{C.21.}$$

The partial derivative of equation **(C.20.)** with respect to y is

$$\frac{\partial \Psi_2}{\partial y} = A_0 t_{01} t_{12}\left[-ik(\sin\alpha)\rho e^{i\gamma} + ik(\cos\alpha)\eta^{1/2} e^{i(\phi/2)}\right] \times$$
$$e^{ik[x\cos\alpha - y\sin\alpha]\rho e^{i\gamma} + ik[x\sin\alpha + y\cos\alpha]\eta^{1/2} e^{i(\phi/2)}}. \tag{C.22.}$$

Finally, equations **(C.21.)** and **(C.22.)** combine to give the probability current in the y direction in medium 2:

$$\mathrm{Im}\left[\Psi_2^* \frac{\partial \Psi_2}{\partial y}\right] = A_0^* A_0 t_{01}^* t_{01} t_{12}^* t_{12}\left[-k(\sin\alpha)\rho(\cos\gamma) + k(\cos\alpha)\eta^{1/2}\cos(\phi/2)\right] \times$$
$$e^{-2k[x\cos\alpha - y\sin\alpha]\rho\sin\gamma - 2k[x\sin\alpha + y\cos\alpha]\eta^{1/2}\sin(\phi/2)}. \tag{C.23.}$$

The transmission (T) from medium 0 to medium 2 of the light flux in the y direction is determined by the ratio of the probability current in medium 2 to the

probability current in medium 0. Thus, equation **(C.23.)** divided by equation **(C.4.)** yields

$$T = t_{01}^{*} t_{01} t_{12}^{*} t_{12} \left[\frac{-(\sin\alpha)\rho(\cos\gamma) + (\cos\alpha)\eta^{1/2}\cos(\phi/2)}{n\cos\theta_0} \right] e^{-2kx'\rho\sin\gamma} e^{-2ky'\eta^{1/2}\sin(\phi/2)} \quad \textbf{(C.24.)}$$

Taking $y'=0$ gives the transmission to points along the $-x'$ axis:

$$T|_{y'=0} = t_{01}^{*} t_{01} t_{12}^{*} t_{12} \left[\frac{-(\sin\alpha)\rho(\cos\gamma) + (\cos\alpha)\eta^{1/2}\cos(\phi/2)}{n\cos\theta_0} \right] e^{-2kx'\rho\sin\gamma} \quad \textbf{(C.25.)}$$

Any point along the $-x'$ axis can be expressed in terms of the distance from the 01 interface (y=0). **Figure C.2.** shows the transmission expressed by equation **(C.25.)** as a function of distance from the 01 interface for different α. The transmission was computed for n=1.5, λ=600 nm, and $\theta_0=\theta_i=45°$.

As **Figure C.2.** shows, the transmission becomes zero when α becomes 90°, as expected. The transmission becomes constant for $\alpha=0°$ since medium 2 joins medium 0 in that case. The constant should be unity, but since multiple reflections of the light were neglected the magnitude of the transmission is not unity at small α. However, for large angles of α, the approximation neglecting multiple reflections is valid. The decay length of the transmission for all α shown in **Figure C.2.** is the same as the decay length for the evanescent field intensity computed with the same conditions. Only the magnitude of the transmitted signal varies with changing α. Effective diameters of the conical probe formed by α are shown in **Figure C.2.** As expected, the larger diameter probes provide larger transmission magnitudes.

This theory demonstrates several important points. As expected, the theory shows that the magnitude of transmission becomes smaller as the angle of the wedge-shaped gap becomes larger. However, the transmission to various points on the interface defined by the x' axis follows the evanescent field intensity produced by the 01 interface for all wedge angles. Perhaps the most important point is brought forward by this consistency of the decay length of the signals for different wedge angles. The magnitude of the transmission of light through air gaps with different wedge angles varies greatly for

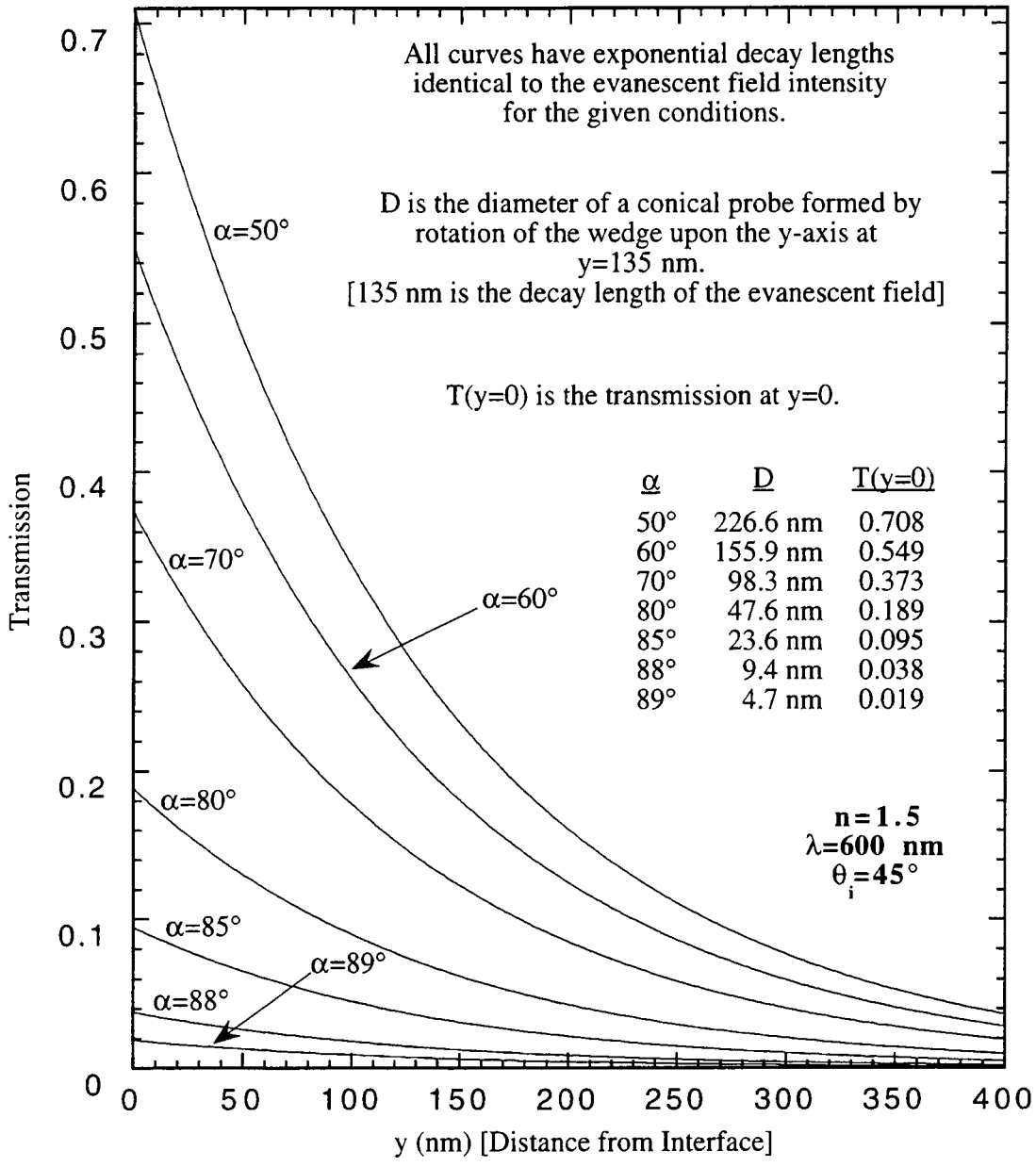


Figure C.2. Transmission for Varying Wedge Angle. The transmission from medium 0 to medium 2 as a function of distance from the 01 interface for different wedge angles. The magnitude of the transmission for any distance from the 01 interface decreases as the wedge angle increases; however, the decay lengths of the signal for each wedge angle are identical to the decay length of the evanescent field intensity computed for the given conditions.

sections of the 12 interface that are the same distance from the 01 interface. Thus, the efficiency with which the evanescent wave traveling along the 01 interface couples to the 12 interface depends heavily on the angle of the 12 interface with respect to the evanescent wave, and the amount of light being transmitted into medium 2 such that the light travels in the $+y$ direction decreases with increasing wedge angle.

Vita

James Edgar Parks II was born on December 18, 1967 in Lexington, Kentucky to Dr. James Edgar Parks and Mrs. Barbara Catron Parks. He graduated Oak Ridge High School in Oak Ridge, Tennessee in 1985. He received a B. S. in Physics from North Carolina State University in 1989. During summer breaks at North Carolina State University he practiced research in the Health and Safety Research Division (presently the Health Sciences Research Division) of Oak Ridge National Laboratory. He continued research at Oak Ridge National Laboratory from his enrollment in the Graduate School of the University of Tennessee, Knoxville until he received his Doctor of Philosophy in August, 1995.

On March 5, 1994 James Edgar Parks, II married the former Cheryl Edwina Dixon. They currently reside in Knoxville, Tennessee.